**University of Plymouth**

**PEARL** **https://pearl.plymouth.ac.uk**

04 University of Plymouth Research Theses 01 Research Theses Main Collection

1996

# THE STRUCTURE AND DYNAMICS OF A CONVERGENT ESTUARINE FRONT

REDBOURN, LISA JANE

http://hdl.handle.net/10026.1/1809

http://dx.doi.org/10.24382/4145
University of Plymouth

*All content in PEARL is protected by copyright law. Author manuscripts are made available in accordance with publisher policies. Please cite only the published version using the details provided on the item record or document. In the absence of an open licence (e.g. Creative Commons), permissions for further reuse of content should be sought from the publisher or author.*

# THE STRUCTURE AND DYNAMICS OF A CONVERGENT ESTUARINE FRONT

by

**LISA JANE REDBOURN**

A thesis submitted to the University of Plymouth
in partial fulfillment for the degree of

**DOCTOR OF PHILOSOPHY**

Institute of Marine Studies
Faculty of Science

**October 1996**

LIBRARY STORE

REFERENCE ONLY

UNIVERSITY OF PLYMOUTH
Item No. 900318291 6
Date - 8 MAY 1997 S
Class No. T 551.4609 REO
Contl. No. X703473254
LIBRARY SERVICES

90 0318291 6

## ABSTRACT

### The Structure and Dynamics of a Convergent Estuarine Front

**L.J. Redbourn**

This thesis considers the structure and dynamics of a convergent front, which forms at the confluence of the Tamar and Lynher rivers during the ebb tide, in the Tamar Estuary, South West England. Temperature, salinity and velocity were sampled at high frequency in the region of frontogenesis, and these data are used to assess the evolution and development of a front during the course of an ebb tide. The equation of continuity and the horizontal equations of motion are applied to the data set in order to evaluate the dynamic regime operating in the vicinity of the front, and its spatial and temporal variation. Mixing within the region is appraised from a consideration of the vertical eddy viscosity and diffusivity, and the gradient Richardson number.

Results suggest that the evolution of the front occurs in two distinct stages: the first being the formation of a convergent, near-horizontal interface between denser Tamar water flowing south-westwards, and less dense Lynher water flowing south-eastwards, such that this first stage can be described as a plume front. The interface has an increased degree of shear-induced turbulence and vertical mixing associated with it. In the later stages of the ebb tide, the front evolves into a turbulent, buoyant jet of Lynher water which extends over most of the area surveyed, and the less turbulent Tamar water is entrained into the Lynher jet. In both the longitudinal and lateral directions, the Lynher flow is found to be primarily accelerated by the barotropic pressure gradient, whereas the Tamar flow is mainly accelerated baroclinically. A markedly more variable and complex dynamic regime in the lateral direction appears to be influenced by daily variations in fresh water run-off and tidal range to a greater extent than the longitudinal dynamics.

## LIST OF CONTENTS


| Contents | Page Number |
|---|---|
| Copyright statement | i |
| Title page | ii |
| Abstract | iii |
| List of contents | iv |
| List of tables and figures | vii |
| Acknowledgements | xii |
| Author's declaration | xiii |
| **Chapter 1 Introduction and literature review** | 1 |
| 1.1 Overview of estuarine circulation and mixing | 1 |
| 1.2 Estuarine fronts | 5 |
| *1.2.1 Plume fronts* | 6 |
| *1.2.2 Tidal mixing fronts* | 9 |
| *1.2.3 Shear fronts* | 11 |
| 1.3 The Tamar Estuary | 13 |
| 1.4 The equations of motion | 17 |
| 1.5 Stratification and mixing processes | 21 |
| **Chapter 2 Field work and data processing** | 26 |
| 2.1 Rationale | 26 |
| 2.2 Equipment | 26 |
| 2.3 Surveying method | 32 |
| 2.4 Data processing | 33 |
| 2.5 Data accuracy | 36 |
| **Chapter 3 Description of initial results** | 37 |
| 3.1 T-S bridge results | 37 |
| 3.2 ETS results | 42 |
| 3.3 ADCP results | 50 |
| **Chapter 4 The application of the equation of continuity** | 56 |
| 4.1 Derivation of the equation of volume continuity | 56 |

4.2 Application of the equation of volume continuity 58
4.3 Derivation of the equation of salt continuity . 63
4.4 Application of the equation of salt continuity . 65
4.5 Cross-frontal transport . . . . 68
**Chapter 5 The application of the equations of motion . . 74**
5.1 Derivation of the equation of motion . . 74
5.2 Application of the equation of motion . . 77
*5.2.1 Temporal accelerations . . 78*
*5.2.2 Advective accelerations . . 78*
*5.2.3 Pressure terms . . . . 80*
*5.2.4 Coriolis accelerations . . . 83*
*5.2.5 Frictional forces (Reynold's stress terms)* 83
5.3 Solving the equations of motion . . . 84
**Chapter 6 Results and discussion . . . . . 88**
6.1 Qualitative interpretation of results . . 90
*6.1.1 The northern survey box . . 90*
*6.1.2 The southern survey box . . 102*
*6.1.3 Summary of frontal evolution . . 105*
*6.1.4 Cross-frontal transport. . . 107*
*6.1.5 Mixing across the fronts . . 109*
*6.1.6 Salt fluxes . . . . 110*
6.2 Primary momentum balance . . . 112
*6.2.1 The primary longitudinal and lateral momentum balances for each box . 113*
*6.2.2 Temporal variations in the primary momentum balances . . . 126*
*6.2.3 Overview of the dynamics of a generalised ebb tide . . . . . 134*
6.3 Richardson number, vertical mixing coefficient and flux Richardson number analysis. . . 151

*6.3.1 The overall Richardson number and vertical mixing coefficient* . . . 151

*6.3.2 Flux Richardson number analysis* . 159

**Chapter 7 Conclusions and future work** . . . . 165

7.1 Background conditions within the survey area . 165

7.2 Evolution of the front and its characteristics . 166

7.3 The momentum balance . . . . 167

7.4 Mixing . . . . . 169

7.5 Recommendations for future work . . 171

References . . . . . 173

Appendix . . . . . 180

## LIST OF TABLES AND FIGURES

**Tables and figures** **Page Number**


Figure 1.1 Schematic diagram of a plume front . . . 8

Figure 1.2 Schematic diagram of a tidal intrusion front . . 8

Figure 1.3 Schematic diagram of an axial convergent front . 12

Figure 2.1 Map of Tamar Estuary showing survey area . . 27

Figure 2.2 Equipment deployment configuration on "Catfish" . 29

Figure 2.3 Equipment deployment configuration on "Tamaris" . 30

Table 2.1 Tidal conditions for the detailed surveys . . 32

Figure 2.4 Tamar-Lynher confluence and figure-of-eight survey grid 34

Table 3.1 Tidal conditions during surveying . . . 37

Figure 3.1 Temperature and salinity data for all surveys . . 39

Figure 3.2 T-S data at 1m and 4m depths, 20.04.94 survey . 41

Figure 3.3 T-S data at 1m and 5m depths, 22.04.94 survey . 41

Figure 3.4 T-S data at 1m and 5m depths, 25.04.94 survey . 41

Figure 3.5 3-D temperature surface plot of transect AB2 . 43

Figure 3.6 3-D temperature surface plot of transect AB3 . 44

Figure 3.7 3-D temperature surface plot of transect CB2 . 45

Figure 3.8 3-D temperature surface plot of transect BA3 . 46

Figure 3.9 Colour plot of salinity for transect AB3 . . 48

Figure 3.10 Colour plot of salinity for transect AB4 . . 49

Figure 3.11a Colour plot of east-west velocity ($ms^{-1}$) for transect AB3 . . . . . 51

Figure 3.11b Colour plot of north-south velocity ($ms^{-1}$) for transect AB3 . . . . . 52

Figure 3.12a Colour plot of east-west velocity ($ms^{-1}$) for transect BA3 . . . . . 54

Figure 3.12b Colour plot of north-south velocity ($ms^{-1}$) for transect BA3 . . . . . 55

Figure 4.1 Volume element with velocity and density . . 56

Figure 4.2 Schematic of depth slices in survey grid . . . 59

Figure 4.3 Depth slice with respect to x y z axes . . . 60
Figure 4.4 Volume element with velocity and salinity . . 63
Figure 4.5 Diagram of re-sampling strategy . . . . 66
Figure 4.6 Plan view of survey boxes containing front . . 68
Figure 4.7 Depth slice with front for boxes 2N, 3N and 4N . . 70
Figure 4.8 Depth slice with two fronts for box 7N . . . 71
Figure 5.1 Volume element with pressure . . . . 74
Figure 5.2 Depth slice with average and fluctuating velocity components 77
Figure 5.3 Depth slice with average vertical velocities . . 79
Figure 5.4 Hydrostatic pressure for a stack of depth slices . . 81
Figure 6.1a FA1, east-west velocity . . . . 91
Figure 6.1b FA1, north-south velocity . . . . 91
Figure 6.2a AB1, east-west velocity . . . . 91
Figure 6.2b AB1, north-south velocity . . . . 91
Figure 6.3a BC1, east-west velocity . . . . 91
Figure 6.3b BC1, north-south velocity . . . . 91
Figure 6.4a CF1, east-west velocity . . . . 91
Figure 6.4b CF1, north-south velocity . . . . 91
Figure 6.5a FA2, east-west velocity . . . . 91
Figure 6.5b FA2, north-south velocity . . . . 91
Figure 6.6a AB2, east-west velocity . . . . 91
Figure 6.6b AB2, north-south velocity . . . . 91
Figure 6.7a BC2, east-west velocity . . . . 91
Figure 6.7b BC2, north-south velocity . . . . 91
Figure 6.8a CF3, east-west velocity . . . . 92
Figure 6.8b CF3, north-south velocity . . . . 92
Figure 6.9a FA3, east-west velocity . . . . 92
Figure 6.9b FA3, north-south velocity . . . . 92
Figure 6.10a AB3, east-west velocity . . . . 92
Figure 6.10b AB3, north-south velocity . . . . 92
Figure 6.11a FC1, east-west velocity . . . . 92
Figure 6.11b FC1, north-south velocity . . . . 92

Figure 6.12a CB1, east-west velocity . . . . 92
Figure 6.12b CB1, north-south velocity . . . . 92
Figure 6.13a BA1, east-west velocity . . . . 92
Figure 6.13b BA1, north-south velocity . . . . 92
Figure 6.14a AF1, east-west velocity . . . . 92
Figure 6.14b AF1, north-south velocity . . . . 92
Figure 6.15a FC2, east-west velocity . . . . 93
Figure 6.15b FC2, north-south velocity . . . . 93
Figure 6.16a BA2, east-west velocity . . . . 93
Figure 6.16b BA2, north-south velocity . . . . 93
Figure 6.17a AF2, east-west velocity . . . . 93
Figure 6.17b AF2, north-south velocity . . . . 93
Figure 6.18a FC3, east-west velocity . . . . 93
Figure 6.18b FC3, north-south velocity . . . . 93
Figure 6.19a CB2, east-west velocity . . . . 93
Figure 6.19b CB2, north-south velocity . . . . 93
Figure 6.20a FE1, east-west velocity . . . . 93
Figure 6.20b FE1, north-south velocity . . . . 93
Figure 6.21a ED1, east-west velocity . . . . 93
Figure 6.21b ED1, north-south velocity . . . . 93
Figure 6.22a DC1, east-west velocity . . . . 94
Figure 6.22b DC1, north-south velocity . . . . 94
Figure 6.23a CF2, east-west velocity . . . . 94
Figure 6.23b CF2, north-south velocity . . . . 94
Figure 6.24a CD1, east-west velocity . . . . 94
Figure 6.24b CD1, north-south velocity . . . . 94
Figure 6.25a DE1, east-west velocity . . . . 94
Figure 6.25b DE1, north-south velocity . . . . 94
Figure 6.26b EF1, north-south velocity . . . . 94
Figure 6.27a FC4, east-west velocity . . . . 94
Figure 6.27b FC4, north-south velocity . . . . 94
Figure 6.28 Schematic of frontal wedge . . . . 97

Figure 6.29 Schematic of retreating tongue of Tamar water . . 99
Figure 6.30 Schematic of Lynher jet . . . . . 100
Figure 6.31 Admiralty Chart of survey area . . . . . 103
Figure 6.32 Time-scale of frontal evolution . . . . . 107
Figure 6.33 Time and duration of survey boxes from all three days . 114
Figure 6.34a Longitudinal and lateral barotropic pressure gradients vs. time (northern survey box) . . 135
Figure 6.34b Longitudinal and lateral barotropic pressure gradients vs. time (southern survey box) . . 135
Figure 6.35a Longitudinal and lateral baroclinic pressure gradients vs. time (northern survey box) . . 138
Figure 6.35b Longitudinal and lateral baroclinic pressure gradients vs. time (southern survey box) . . 138
Figure 6.36a Longitudinal Reynold's stress terms vs time (northern survey box) . . . . . 141
Figure 6.36b Longitudinal Reynold's stress terms vs time (southern survey box) . . . . . 141
Figure 6.37a Lateral Reynold's stress terms vs time (northern survey box) . . . . . 142
Figure 6.37b Lateral Reynold's stress terms vs time (southern survey box) . . . . . 142
Figure 6.38a Longitudinal and lateral Coriolis acceleration vs. time (northern survey box) . . . 144
Figure 6.38b Longitudinal and lateral Coriolis acceleration vs. time (southern survey box) . . . 144
Figure 6.39a Longitudinal and lateral depth averaged total acceleration vs. time (northern survey box) . . 146
Figure 6.39b Longitudinal and lateral depth averaged total acceleration vs. time (southern survey box) . . 146
Figure 6.40a Longitudinal spatial acceleration terms vs. time (northern survey box) . . . 147
Figure 6.40b Longitudinal spatial acceleration terms

vs. time (southern survey box) . . . 147
Figure 6.41a Lateral spatial acceleration terms
vs. time (northern survey box) . . . 148
Figure 6.41b Lateral spatial acceleration terms
vs. time (southern survey box) . . . 148
Figure 6.42a Ri vs. depth, box 1N . . . . . 152
Figure 6.42b Ri vs. depth, box 2N . . . . . 152
Figure 6.42c Ri vs. depth, box 3N . . . . . 152
Figure 6.42d Ri vs. depth, box 4N . . . . . 152
Figure 6.42e Ri vs. depth, box 5N . . . . . 152
Figure 6.42f Ri vs. depth, box 6N . . . . . 154
Figure 6.42g Ri vs. depth, box 7N . . . . . 154
Figure 6.42h Ri vs. depth, box 1S . . . . . 154
Figure 6.42i Ri vs. depth, box 2S . . . . . 154
Figure 6.42j Ri vs. depth, box 3S . . . . . 154
Figure 6.43a Ev/E0 vs. depth, box 1N . . . . 156
Figure 6.43b Ev/E0 vs. depth, box 2N . . . . 156
Figure 6.43c Ev/E0 vs. depth, box 3N . . . . 156
Figure 6.43d Ev/E0 vs. depth, box 4N . . . . 156
Figure 6.43e Ev/E0 vs. depth, box 5N . . . . 156
Figure 6.43f Ev/E0 vs. depth, box 6N . . . . 157
Figure 6.43g Ev/E0 vs. depth, box 7N . . . . 157
Figure 6.43h Ev/E0 vs. depth, box 1S . . . . 157
Figure 6.43i Ev/E0 vs. depth, box 2S . . . . 157
Figure 6.43j Ev/E0 vs. depth, box 3S . . . . 157
Figure 6.44 $K_z/N_{zu}$ vs. $Ri_u$ . . . . . 161
Figure 6.45 Ellison's curve of $K_z/N_z$ vs. Ri . . . 162
Figure 6.46 $K_z/N_{zv}$ vs. Riv . . . . . 163

## ACKNOWLEDGEMENTS

Firstly, many thanks to my supervisor, Keith Dyer for his invaluable guidance and patience throughout the course of this project. I am also very grateful to David Huntley for always managing to find the time to answer any queries, especially during the final stages of writing up.

I would like to offer my thanks to the following people, without whom the completion of the project would have been impossible;

Dr. Rocky Geyer and Craig Marquette from W.H.O.I. for allowing us to use their ADCP and for all their help and advice

Kevin Hammond, Becky Matthews and Trevor Parrott for their assistance with the fieldwork

Bablu Sinha, Tim O'Hare, Jon Miles, Dave Simmonds, Paul Chatwin, Malcolm Christie, Karen Stapleton and James Smith for many valuable discussions about the project

N.E.R.C. for supporting the studentship and for funding the trip to the I.A.P.S.O. conference in Hawaii

Dr. Bram Murton for kindly allowing me the time to finish writing up whilst working at the S.O.C.

All those onboard the Charles Darwin during cruise CD102 for their advice and suggestions on the final draft, and for the viva horror stories...

On a more personal note, my time in Plymouth was made very enjoyable by the many members of the Coffee Club. Those who will be particularly hard to forget (try as I might) are Babbers, Chatters, Malcolm, Jon, Karen, Yo, Adam, the two Jo's, "Safe Hands" Sands, Paul, Pauline, Mike, Andy and the Pillsbury Dough Boy.
Thanks to all my mates in London and Crowborough for staying there...
I would also like to thank Hels sincerely for "winging it" with me during the final three days of preparing the thesis.

Finally, my love and thanks to Mum, Dad and Billy for everything.

## AUTHOR'S DECLARATION

At no time during the registration for the Degree of Doctor of Philosophy has the author been registered for any other University award.

This study was financed with the aid of a studentship from the Natural Environment Research Council.

A programme of advanced study was undertaken, which included final year honours courses in physical oceanography, modelling and estuarine oceanography.

Relevant scientific seminars and conferences were regularly attended at which work was often presented.

Presentations and Conferences Attended:

Papers have been presented at two departmental seminars and at the International Association of Physical Sciences in the Ocean Conference, Honolulu, Hawaii, August 1995. A poster was presented and gained first place at the Institute of Marine Studies poster competition, July 1994.

Signed.....

Date 10th April 1997

# CHAPTER 1

# INTRODUCTION AND LITERATURE REVIEW

An estuary has been defined by Cameron and Pritchard (1963) as "a semi-enclosed coastal body of water which has a free connection with the open sea and within which sea water is measurably diluted with fresh water derived from land drainage". The combined effects of the tidal regime, the topography of the estuary and the buoyancy introduced by freshwater run-off produce often complex patterns of circulation and mixing within the estuary. Many estuaries are host to industry, shipping and recreation, and consequently to the pollution associated with these activities, as well as being important sites for wildlife. Therefore, in order to effectively protect and manage estuarine environments, it is necessary to understand the circulation and mixing processes affecting them. These processes occur over a range of temporal and spatial scales, varying from those lasting a few seconds and acting over a few metres such as short-period turbulence, to long-period effects lasting for days and effective over several kilometres e.g. fluctuations in run-off (Dyer, 1982). Examples of intermediate scale processes, extending for hundreds of metres and lasting several hours, are internal waves, intense mixing periods and estuarine fronts. Each of these processes has an effect on localised circulation and mixing which may have wider implications for, as an example, the dispersal of solute or pollutant in the estuary as a whole. Hence, it is the aim of this project to study the structure and dynamics of one such intermediate feature, a front in the Tamar Estuary, South-West England, using quasi-synoptic measurements of current velocity, temperature and salinity. The overall objective of the project is to study the localised dynamic regime, and its effect on mixing and circulation in the vicinity of the front. The temporal and spatial variations in the frontal structure and dynamics will be assessed throughout the course of an ebb tide. Mixing processes and the cross-frontal transport of water and salt will also be quantified.

## 1.1 OVERVIEW OF ESTUARINE CIRCULATION AND MIXING

Estuaries can be classified into three types by considering their hydrodynamic regimes which are largely controlled by tidal range, topography and fresh water inflow. Salt wedge estuaries develop where a river discharges into a virtually tideless sea. The less

dense river water spreads out over the surface of the denser, saline sea water which can be thought of as a salt wedge penetrating and thinning upstream. Sharp salinity and density gradients define the interface between fresh water and sea water. As the fresh water flows over the saline water, shear stresses occur on the interface producing turbulence and generating internal waves on the interface which break, causing the salt water to be entrained into the overlying fresh water. In contrast, a well-mixed estuary is one in which the tidal range is high and the tidal currents are strong relative to the river flow. Salinity hardly varies with depth but may vary laterally across the estuary. The dominant mixing mechanism is turbulence generated by friction between tidal currents and the estuary bed which is a more effective mixing process than internal waves along the interface. Salt wedge and well-mixed estuaries represent the end members of the classification. Turbulence produced by internal velocity shear is the dominant mixing mechanism in highly stratified estuaries whereas turbulence generated by bottom friction is dominant in well-mixed estuaries (Dyer, 1988). Between these two extremes are partially mixed estuaries in which both mixing mechanisms are important. In partially mixed estuaries such as the Tamar in South West England, rivers discharge into a sea with a moderate tidal range. Salt water is mixed upwards and fresh water is mixed downwards causing the interface or halocline to become less well-defined. As a consequence, the fresher water flowing seawards now has a higher salinity, therefore the flow in this upper layer, which is required to discharge fresh water at a rate equal to river flow, is increased so that the compensating landwards flow in the lower layer from the sea is stronger than in a salt wedge estuary (Wilson, 1988). These residual currents are typically less than 10% of the magnitude of the tidal currents superimposed on them, but they are still an important aspect of estuarine circulation. In a more general sense, tidal mixing increases horizontal density gradients which in turn produce horizontal pressure gradients of sufficient magnitude to drive the residual circulation which acts both longitudinally and laterally in an estuary.

Another feature of estuarine circulation is the marked tidal asymmetry. As the tidal wave propagates into the estuary, the wave crest (i.e. high water) travels faster than the wave trough (low water) because the speed of propagation is dependent on water depth. Also, as the tide rises, a large volume of water must flow through a decreasing cross-sectional area as it moves up the estuary. Hence the speed of flood currents is greater

than ebb currents, and there is a slower turn of tide at high water with a longer period of slack water, compared to low water.

Superimposed on this general pattern of circulation and mixing in estuaries are a number of smaller-scale processes which act locally for shorter periods of time. For example, as the tide floods, a body of water may be trapped by a headland, or an embayment, where it undergoes different mixing processes to the water in the main part of the estuary. As the tide ebbs, the patch of water with different temperature and salinity characteristics may be entrained back into the main flow. The presence of bends, tributaries and tidal flats can also cause separation of the flow and formation of intermediate scale patches which become entrained and advected by tidal flow and gradually undergo turbulent mixing (Dyer, 1982). Internal waves have been observed in many estuaries (Gargett, 1976, Farmer and Smith, 1977,1980, Haury *et al.*, 1979, Chereskin, 1983, New *et al.*, 1986, Sturley, 1990) and are capable of locally modifying the mixing regime. They are generated by the interaction of stratified tidal flow with the estuarine topography, as would occur in a surface seiche (New and Dyer, 1987) or where there is a steeply sloping depression in the bottom topography (Sturley, 1990). The internal waves increase mixing in two ways. Firstly, long wavelength internal waves cause stretching of the fresh water/salt water interface which enhances the shear at the wave crests and troughs. This process is parameterised using the Richardson number, which is given by:

$$Ri = \frac{-g\left(\frac{\partial \rho}{\partial z}\right)}{\rho\left(\frac{\partial u}{\partial z}\right)^2} \qquad (1.1)$$

where g is gravitational acceleration, ρ is density, u is velocity and z is depth.

For a Richardson number less than 0.25, the shear is sufficient to overcome the stability, and turbulence and mixing ensue, whereas at a value greater than 0.25, stability reduces turbulence. The stretching of the salt water/fresh water interface effectively reduces the Richardson number locally to increase mixing. Internal waves can also increase mixing when they break. This process is quantified by the Froude number, defined as the ratio between the tidal velocity and the phase velocity of long, small amplitude waves on the given density distribution. For example, a stratified ebb fl;ow over a topographic depression may generate internal waves with an unpstream phase velocity. If the mean

ebb current exceeds this phase velocity, the waves will break generating turbulence. Both of these processes will eventually produce an intense mixing period (New *et al.*, 1986,1987) which can be recognised as an intermediate scale patch of water with more homogeneous temperature and salinity characteristics than the ambient, more stratified flow.

Density-driven secondary flow may also be an important process in terms of mixing in the estuary. For example, in the presence of a linear density stratification (such as would be expected on the ebb tide in a partially mixed estuary), sidewall irregularities cause vertical mixing at the sides of the channel which sets up transverse horizontal density and thus pressure gradients. These drive a secondary transverse circulation pattern across the estuary (Parsons, 1987). Differential longitudinal advection, caused by depth variations and hence variable velocities across a channel, will set up transverse salinity and density gradients in the presence of an initial longitudinal density gradient. The associated pressure gradients produce a transverse secondary flow (Parsons, 1987, Huzzey, 1988). This type of circulation may ultimately lead to the generation of an estuarine front (Nunes and Simpson, 1985, Simpson and James, 1986, Simpson and Turrell, 1986, Huzzey and Brubaker, 1988, Turrell, 1989). Fronts themselves have a significant effect on localised circulation and mixing processes which may be relevant in terms of the overall estuarine hydrodynamics, and they will be discussed more fully in the following section.

Much of the previous work in estuaries has been done using tidally averaged values of temperature, salinity and velocity. The process of tidally averaging these data masks smaller-scale processes such as those mentioned above, which, whilst being localised and generally short-lived (i.e. less than a tidal cycle) may still have an important effect on the mixing and circulation patterns within particular regions of the estuary. This project attempts to make a detailed study of one such feature, using temperature, salinity and velocity data collected during several ebb tides in one localised region of the Tamar Estuary. The feature in question is the convergent front that forms as the Lynher river discharges into the Tamar Estuary during the ebb. A combination of qualitative interpretation and quantitative analysis of the results is used to study the formation of the front, its structure and dynamics and the variation of these characteristics both temporally and spatially. The mixing processes, dynamic regime and circulation

patterns operating in the region of frontal formation can then be assessed, thus giving an insight into some of the more complex, small-scale processes which occur in estuaries, and which have received less attention than larger-scale processes in much of the previous work on estuarine hydrodynamics.

The remainder of this literature review will introduce several different types of estuarine front, summarise the findings of previous work done in the Tamar Estuary, consider some of the applications of the equations of motion in estuarine environments (which comprises the major part of the quantitative analysis in this project) and describe in more detail some of the smaller-scale processes which have been observed in estuaries and which may be significant in this study.

## 1.2 ESTUARINE FRONTS

A front can be defined as a region characterised by an anomalous local maximum in the horizontal gradient of some water property such as temperature or salinity (Largier, 1993) i.e. it is a region of intensified gradients in which ocean properties change more rapidly with horizontal distance than in the surrounding waters (Simpson and James, 1986). This means, therefore, that two differing water masses have to be brought in to juxtaposition, or there has to be a strong lateral gradient in mixing processes which would change the characteristics of the water mass (Huzzey and Brubaker, 1988). As an example, fronts are frequently located at the transition between a vertically well-mixed and a partially stratified regime. While some fronts can be thought of as "passive" in that they are merely a delineation between two different water types of similar density (the water type being defined by nutrient concentration, for example), most fronts are dynamically active in that there is a convergent water flow, usually at the surface, and a vertical circulation in addition to whatever variation there may be in water properties (Largier, 1993). This frontal circulation is usually associated with a density difference between the two waters and maintains the front as a sharp transition approximating an interface. Despite the sharp transition, fronts are not necessarily a barrier to horizontal exchange. In fact, they may experience strong cross frontal fluxes of properties through the operation of horizontal mixing processes on the large gradients that occur there (Simpson and James, 1986). Fronts occur on a range of spatial and temporal scales, varying from oceanic fronts which are thousands of kilometres in length and persist for

several months, to estuarine fronts with length and time scales comparable to the tidal excursion and tidal period respectively.

The presence of a front can often be detected at the surface from the change in water colour, lines of foam and flotsam and a change in sea state. As mentioned previously, vertical circulation is usually enhanced at a front which is especially important in a stratified regime where this type of circulation is minimal. It allows increased vertical transport of momentum, heat and salt and more efficient exchange of nutrients. Accumulations of plankton are often associated with fronts, either due to their *in situ* production at the front or because of passive convergent transport towards it (Largier, 1993). Hence, increased biological productivity often occurs in frontal zones. The convergent surface flow also acts as a barrier to the dispersion of fine sediments, and concentrates pollutants and toxins.

It can be seen that the study of the formation and dynamics of estuarine fronts is not only interesting scientifically, it is also very relevant for protecting and managing the estuarine environment.

O'Donnell (1993) has broadly classified estuarine fronts into three categories; plume fronts, tidal mixing fronts and shear fronts. The following is a brief review of some previous work done on fronts in each category.

### *1.2.1 Plume Fronts*

Plume fronts are essentially the result of the juxtaposition of two different water types. They occur where fresher, less dense river water discharges into more saline, denser water. The fresh water spreads out and flows over the denser water in a layer usually no more than a few metres thick, so that its free surface slopes down towards the leading edge where the plume front forms (Garvine, 1974, Pinckney and Dustan, 1990). The front propagates into the ambient, saline water at a velocity $U=\sqrt{g'D}$ where g' is reduced gravity and D is the depth of the fresh water layer (Simpson and Turrell, 1986). The frontal dynamics are controlled by surface pressure gradients, interfacial friction and entrainment across the frontal interface (Bowman, 1988). One of the earliest detailed studies of this type of front was conducted by Garvine and Monk (1974) on the Connecticut River plume which discharges into Long Island Sound on the east coast of the USA. They determined the hydrography and horizontal current field in the vicinity of the front and referenced these measurements to a co-ordinate system attached to the

front itself, which was observed from surface marker drogue experiments. Their observations showed strong density gradients delineated by sloping isopycnals in the frontal zone. The horizontal pressure gradients induced by these sloping isopycnals and by the free surface slope, generated strong surface convergence from both sides of the front. The denser salt water is driven beneath the lens of fresher water. It entrains the lighter water and mixes it downwards, resulting in a downward vertical mass flux which is supplied by the horizontal inflow towards the front of fresher water from more remote regions of the plume. Conservation of mass requires that water which converges and sinks at the front is swept away from near the front along a path above the interface (Garvine, 1974) (see figure 1.1).

The distinct colour changes and foam and flotsam lines associated with plume fronts allows them to be effectively surveyed using remote sensing as well as *in situ* hydrographic measurements. Klemas and Polis (1977a, b) demonstrated the usefulness of this technique for mapping fronts in Delaware Bay.

If an estuary has a strong, reversing tidal flow then plume fronts will typically form only during the ebb tide (Bowman and Iverson, 1977). As the flood tide begins in the estuary, the surface slope across the plume is reversed causing the fronts to rapidly dissipate in most cases. However, where tidal currents are sufficiently strong, the advancing plume front may be swept back into the estuary to form a tidal intrusion front such as that in the Seiont Estuary, North Wales (Simpson and Nunes, 1981). Tidal intrusion fronts will be prominent only in estuaries which exhibit the right range of tidal inflow in relation to the fresh water discharge i.e. large enough currents to drive the fresh water outflow back into the estuary but not so large that the density structure is disrupted by vertical mixing (Simpson and Turrell, 1986). The front exhibits a 'V' configuration with an isolated point convergence at its apex and an associated gyre system (see figure 1.2). There are rapid sinking motions occurring at the point convergence where the two frontal arms meet, and surface flow relative to the front is towards it on both sides. A similar type of intrusion front has also been observed in Port Hacking Estuary, Australia during the flood tide by Huzzey (1982). This front separates the brackish, ambient water within the deep estuarine basin from the incoming oceanic water, which can be thought of as a density current plunging beneath the less dense water. The plunge point and hence the position of the front occurs when the incoming

*Figure 1.1 Schematic diagram of a plume front*

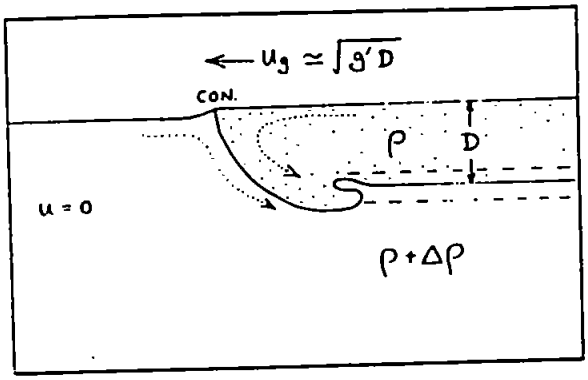


*Schematic of a density current in which lighter water advances at speed $U_g$ into denser stationary fluid. Flow within the surface layer towards the head of the density current is required to replace water entrained in mixing waters behind the head. The partially mixed waters produced are left behind the advancing flow in a layer indicated by the dashed line.*

(from Simpson and Turrell. 1986)

*Figure 1.2 Schematic diagram of a tidal intrusion front*

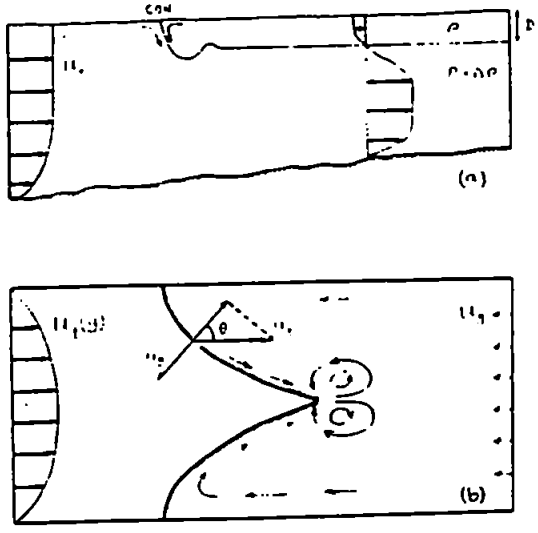


*Schematic of tidal intrusion fronts: (a) the competition of the gravity current with the tidal current into the estuary; (b) interaction of tidal intrusion front with the lateral shear to produce a V front with a single point convergence at the apex and attendant gyres.*

(from Simpson and Turrell. 1986)

down-slope tidal density current becomes critical in terms of its densimetric Froude number. The frontal position and dynamics are therefore controlled by the bathymetry, the local water depth and the difference in density between the two water masses. The front remains almost stationary for the duration of the flooding tide, in contrast to Simpson and Nunes' tidal intrusion front which moves upstream with the flooding tide, primarily controlled by the relative magnitudes of the river discharge and range of tidal elevation, and is not strongly tied to the bathymetry.

### *1.2.2 Tidal Mixing Fronts*

The characteristics of the stratification in estuaries are the result of competition between vertical mixing and buoyancy stratification. In estuaries, the horizontal buoyancy flux due to fresh water sources generally dominates solar heating, which is the more important factor inducing stratification on the continental shelf (O'Donnell, 1993). The estuarine Richardson, $R_{EST}$, number can be used to classify estuaries in terms of the results of the stratification *vs.* mixing competition;

$$R_{EST} = \frac{g \Delta\rho Q_f}{\rho W u_T^3} \qquad (1.2)$$

where $u_T$ is the typical tidal current amplitude, W is the width of the estuary and $Q_f$ is the flux of fresh water. On a local scale, the stratification-mixing competition can result in fronts which form in shoaling regions where tidally generated turbulent stirring is just sufficient to mix away the buoyancy in the surrounding deeper, stratified water (Bowman, 1988).

Simpson and Hunter (1974) observed a front in the Irish Sea which marked the boundary between stratified and vertically mixed regimes. The relative consistency of the observed position of the front suggested that the transition between stratified and unstratified regimes is essentially controlled by the level of tidal mixing. For a given rate of heat input (which is largely responsible for inducing stratification in shelf seas) Simpson and Hunter considered the energy balance between the potential energy required to maintain mixing and the energy lost from the tidal motion via frictional bottom forces. Assuming that the work required to maintain homogeneity is provided by the bottom stress, then it should equal the fraction of the power (per unit volume) dissipated in the bottom boundary layer that is used for mixing. From this balance, they derived that the locus of the front should be defined by a critical value of $h/u^3$, where h

is the water depth and u is the velocity. It was found that the Irish Sea front is approximately parallel to the contours of $h/u^3$ at a value between 65 and 100. Fearnheard (1975) used this Simpson-Hunter parameter in a model to predict the formation of fronts by tidal mixing around the British Isles with some success. Yanagi and Tamaru (1990) also used $h/u^3$ to model frontogenesis in the Bungo Channel of the Seto Inland Sea, Japan. They found that Simpson and Hunter's theory worked well, except that it could not predict the frontal position in early spring. This limitation was ascribed to the fact that horizontal heat transport plays an important role in the generation of stratification at this time, which is not accounted for in the theory. Another example of a tidal mixing front was observed by Sharples and Simpson (1993) in Liverpool Bay. The frontogenesis here is driven by a relaxation of a fresh water induced horizontal density gradient following the decrease in tidal range at neap tides. It results in an area of Liverpool Bay being stratified for a period of eight days before the increase in tidal mixing as the spring tide approaches returns the region to its initial, vertically mixed state.

Although these ideas were developed for mixing on continental shelves, they should be applicable in estuaries, even though the effects of the unsteady intensity of tidal stirring and the advection of fresh water by buoyancy-driven currents dominate the evolution of stratification in this environment (O'Donnell, 1993). For an estuarine frontal zone separating well-mixed from stratified water, an energy balance can be formulated as;

$$h/u^3 = b\, L\, \varepsilon\, k\, \rho / \beta\, g\, S_b\, Q_f \qquad (1.3)$$

where h is the local water depth, u is the r.m.s. tidal velocity, b is the estuary width, L is the cross-frontal width scale, $\varepsilon$ is the mixing efficiency, k is a quadratic dimensionless drag coefficient associated with tidal currents, $\rho$ is the water density, $\beta$ is a proportionality constant between density and salinity, g is the acceleration due to gravity, $S_b$ is the salinity in the lower layer of the water column and $Q_f$ is the discharge of fresh water into the estuary (Bowman and Esaias, 1981, Bowman, 1988). The idea behind this equation is that in an estuarine frontal zone, a balance exists between the rate of production of tidally generated turbulent kinetic energy available for vertical mixing, and the horizontal flux of buoyancy within the gravitational circulation, which tends to stratify the water column (Bowman, 1988). Lateral shear is important in maintaining these fronts. They are often observed to be stronger on ebb tide when faster

flowing currents in deeper, offshore water advect lower salinity upstream water past higher salinity shoal waters. This shear increases the horizontal density contrast across the front as well as sharpening the frontal interface (Bowman and Iverson, 1977).

### *1.2.3 Shear Fronts*

This brings us to the third category of estuarine fronts suggested by O'Donnell (1993). Shear fronts are the result of differences in the rate of horizontal advection in the direction of the local density gradient and they have been observed in many estuaries. Huzzey (1988) found that the density distribution across the York River, Chesapeake Bay is characterised by distinct inhomogeneities for most of the tidal cycle. The estuary is laterally homogeneous only at times of maximum flood and ebb current. At other times, the density of water in the shoal and channel regions differs, which is caused by the longitudinal density gradient being advected at different velocities as the tidal current magnitude varies over shoals and channels. These density differences result in horizontal pressure gradients which may, at certain times, be strong enough to generate localised lateral circulations. In a continuation of this work, Huzzey and Brubaker (1988) studied longitudinal estuarine fronts aligned parallel to the axis of the York River estuary. Longitudinal fronts are formed when differential advection of the longitudinal density gradient generates distinct differences in the density of the shoal and channel waters. At such times, the resultant horizontal pressure gradients drive lateral circulations. The associated lateral flows, although small, may be of sufficient magnitude to generate surface convergence in the form of a front. This phenomena has been previously observed in the Conwy Estuary, North Wales (Nunes and Simpson, 1985, Simpson and James, 1986, Simpson and Turrell, 1986, Turrell, 1989). An axial convergence front forms during the flood phase of the tide and is maintained by a transverse circulation which results from an interaction between the vertical and lateral shear in the flood current and the longitudinal density gradient. As such, in a channel with a longitudinal density gradient, denser fluid will be swept upstream in the centre of the channel by the swifter tidal current in this deeper region. At the edges of the channel, the peripheral flow is retarded by frictional forces, tending to create an unstable density distribution (see figure 1.3), and the resultant pressure gradients drive a two-celled circulation with convergence and sinking in mid-channel. The front is observed

*Figure 1.3 Schematic diagram of an axial convergence front*

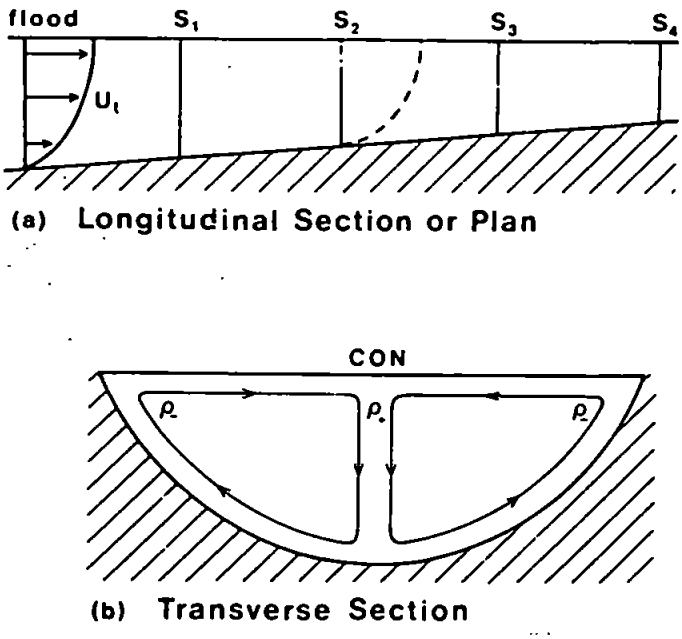


Conceptual model of the transverse circulation. Vertical and horizontal shear in the flood currents distort the isohalines ($S_1$ etc) to produce lateral gradients which drive a transverse circulation with strong convergence and sinking along the main axis of the current.

(from Nunes and Simpson, 1985)

along this longitudinal axis. Convergence only occurs in regions with a significant longitudinal density gradient, and the dependence of frontogenesis on an initial horizontal density gradient has been confirmed with laboratory tank experiments by Simpson and Linden (1989).

Sarabun (1993) made observations of the Chesapeake Bay tidal front. He found that the change in depth between the shoal and channel in this area results in a difference in magnitude and phase for tidal currents in the shallows relative to those in the channels. The tidal currents, combined with a density gradient in the axial direction results in the formation of a pronounced lateral density gradient at the shoal edge, in agreement with Huzzey's results. Hence, frontal formation depends largely on the longitudinal density gradient, the sharpness of the lateral bathymetric variation and the tidal current.

One additional category of fronts is included in Bowman's review of estuarine fronts (1988). Headland fronts are formed in association with flow around headlands, promontories, banks, shoals and islands (Pingree *et al.*, 1977). The influence of coastline configurations on gross tidal flow causes increased tidal streaming off headlands, and weaker tidal velocities in adjacent bays. This strong tidal streaming in the neighbourhood of headlands will cause a local minimum in the value of the $h/u^3$ stratification parameter. Therefore, if stratified conditions exist offshore, an abrupt transition to well-mixed conditions may occur in the vicinity of the headland and a front will form.

It should be noted that estuarine fronts often exhibit characteristics from more than one of the categories described above, so the formation of fronts is likely to result from an interaction of several processes.

## 1.3 THE TAMAR ESTUARY

In this section, the physical characteristics of the Tamar estuary will be introduced, followed by brief definitions of the some of the processes which have been studied in the estuary. The results of these studies are then reviewed chronologically.

The Tamar Estuary extends 31 km from its seaward boundary with Plymouth Sound to the limit of its salinity intrusion at Weir Head. The estuary carries fresh water run-off from three rivers, the Tamar, the Tavy and the Lynher. The Tamar river carries the largest fresh water flows, with typical monthly averaged flows decreasing from 38 $m^3s^{-1}$

in January to 5 $m^3s^{-1}$ in June. On average, the Tavy contributes about 30% of the Tamar input and the Lynher about 20% (Uncles *et al.*, 1983). Tides are semi-diurnal with mean neap and spring ranges of 2.2 m and 4.7 m (George, 1975), such that the estuary is macrotidal. A Hansen and Rattray type of analysis shows the estuary to be well-mixed or transitional in the upper reaches and partially mixed in the lower reaches (Uncles *et al.*, 1985a).

Much of the work that has been done previously in the Tamar Estuary has used tidally-averaged velocity and salinity data to examine the residual transport of water and salt. The processes found to be primarily responsible for these residual transports are now briefly described.

The residual (non-tidal) circulation in the Tamar is generated by the gravitational circulation, Stoke's drift, fresh water input and density gradients. The gravitational circulation is a simple process whereby salinity causes gravity to play a dominant role in vertically stratifying the fluid according to its density (Rattray and Dworski, 1980). Stoke's drift is more complex; it is essentially the result of frictional forces distorting the tidal ellipse thereby causing a partially progressive tidal wave which gives rise to non-zero correlations between tidal fluctuations in water depth and velocity. This generates a residual inflow of water into the estuary, which is balanced by a residual flow in the opposite direction when the set-up gradient caused by the up-estuary Stoke's drift is sufficient to overcome frictional forces (Uncles and Jordan, 1980). The fresh water input into the estuary produces a residual flow by generating an axial surface slope (Uncles *et al.*, 1986), and finally, density gradients arising from the salinity distribution generate horizontal pressure gradients and thus a residual flow.

The residual flux of salt in the estuary is the result of both advective processes such as tidal pumping, and transverse and vertical shear dispersion. Tidal pumping arises because of frictional forces distorting the tidal curve such that slack water lags high water, causing a residual, up-estuary flux of salt. Essentially, it is caused by Stoke's drift, which results in a higher discharge per unit velocity at high tide than at low tide, because of variations in the cross-sectional area of the estuary.

The transport of salt due to transverse shear dispersion is associated with correlated spatial variations in salinity and longitudinal velocity across the width of the estuary. Similarly, vertical shear dispersion transport is associated with correlated spatial

variations in salinity and longitudinal velocity through the depth of the water column. Both types of shear transport are due to steady residual currents (with gravitational circulation being particularly important in the case of vertical shear dispersion) and oscillatory tidal currents (Uncles and Stephens, 1990).

The significance of these processes in various regions of the Tamar Estuary has been assessed using the results from several surveys. Uncles *et al.* (1983) computed flushing times and axial dispersion coefficients during low run-off, spring tide conditions when the estuary was comparatively well-mixed. The flushing time under these extreme conditions was found to be three weeks, although one week is quoted as a more typical value, and vertical shear dispersion was found to be small throughout the estuary. The transverse shear dispersion coefficient was dependent on the cross-estuary mixing time-scale: if the only cross-estuary mixing mechanism was turbulence, then the time-scale for this transverse mixing greatly exceeded the flushing time, such that salt and other solutes would be washed out of the estuary before being mixed, and the transverse shear dispersion coefficient would be negligible. This was not found to be the case and Uncles *et al.* concluded that the process of transverse oscillatory shear must be acting in the upper estuary in addition to turbulence, to explain the calculated coefficients. In the lower reaches of the estuary, tidal trapping was the single most important process. Tidal trapping occurs when patches of water and solute become 'trapped' in the sub estuaries and embayments of the lower estuary during the course of a tidal excursion, effectively dispersing the solute.

Uncles *et al.* (1985a) examined the transverse and vertical structure of water, salt and sediment transport in the upper reaches of the estuary. They found that the transport of salt due to vertical shear was always directed up-estuary in this region. However, the total residual salt transport was up-estuary in the deeper, central channel but down-estuary over the shallow, inter-tidal mud flats and hence, the down-estuary advection of salt by residual flow dominates the transport by vertical shear in these areas. Tidal pumping was also found to contribute significantly the salt transport. Vertical shear dispersion dominated that due to transverse shear at the landward end of the estuary, but the two types of shear dispersion were of comparable magnitudes in the wider, lower reaches of the estuary.

A more extensive survey of the estuary by Uncles *et al.* (1985b) revealed that residual flow and salt fluxes in the upper estuary were primarily the result of tidal pumping, Stoke's drift and freshwater inputs. In the lower estuary, the vertical shear dispersion and gravitational circulation were the most significant contributions to the residual flow. These observations were expanded upon by Uncles *et al.* (1986). They attributed the distribution of lateral, tidally-averaged currents in the upper estuary to three factors: (1) differential density gradient forcing generated by variations in the longitudinal salinity gradient over a cross-section, (2) the interaction of the tidal flow with lateral variations in topography and (3) the response to fresh water inputs to the upper estuary, which produced axial surface slopes. The second factor is effectively the Stoke's drift, which was found to be up-estuary in the deeper, central channel and down-estuary over the shallow, inter-tidal mud flats. This lateral structure in the residual flow is the result of varying frictional effects between the shallow and deeper regions of the cross-sectional topography which distort the tidal currents. The residual flow due to density gradients was seen to enhance that due to Stoke's drift.

The intra-tidal behaviour of vertical shear dispersion, again in the upper estuary, was investigated by Uncles and Stephens (1990). They defined a parameter, $\psi$, proportional to the negative salt flux due to the vertical shear divided by the tidally averaged longitudinal salinity gradient. During spring tides, $\psi$ maximised on the ebb within three hours of high water. At the end of the ebb and during the flood, $\psi$ was very small or negative. During neap tides, $\psi$ at the head of the estuary was again small or negative at the end of the ebb and during the flood. However, at the most seaward cross-section of the survey, $\psi$, the velocity shear and stratification all maximised at low water rather than during the early ebb, a phenomenon ascribed to the ebb-flood asymmetry in the stratification and its effect on both intra-tidal and residual currents. Generally, vertical shear dispersion dominated transverse shear dispersion in the upper estuary.

Uncles and Stephens (1993) examined the fresh water-salt water interface in the upper estuary and concluded that its position was primarily controlled by the amount of freshwater run-off across the head of the estuary, and that spring-neap influences were slight. It is interesting to note that Uncles and Stephens adopt a three-term primary longitudinal momentum balance in their model, with the temporal acceleration being

balanced by the baroclinic pressure gradient and the vertical eddy viscosity (alternatively expressed as the vertical gradient in longitudinal turbulent stress).

A different contribution to estuarine mixing in the Tamar was examined by Sturley and Dyer (1992). Here, stratified flow over a topographic depression during a neap tide formed an internal wave along the pycnocline, in the manner described by Maxworthy (1979). The distortion of the pycnocline by the internal wave and the enhanced shear at the seaward end of the wave caused fresher water to be mixed from above the pycnocline down into it. Thus, the formation of internal waves is capable of radically altering the local stratification through enhanced vertical mixing.

Parsons (1987) also identified the significant influence of breaking internal waves, along with shear and buoyancy effects, on transverse diffusion and vertical shear dispersion in the region of the estuary just south of the Tamar-Lynher confluence. His work examined, in particular, cross-sectional mixing mechanisms at various stages during the tidal cycle, from which it was found that transverse diffusion was considerably less during the flood tide than the ebb tide.

From this summary of work previously conducted in the Tamar Estuary, it is apparent that the lower reaches of the estuary, where the survey area for this project is located, have been less extensively studied than the upper reaches. Where observations in the lower reaches have been made, vertical shear dispersion is found to dominate transverse shear dispersion although the latter process becomes increasingly significant as the estuary widens towards the sea. Additionally, gravitational circulation and tidal trapping make important contributions to the residual flow.

Many of these observations are based on tidally-averaged values of salinity and velocity, whereas this project investigates shorter time-scale variations in these properties over the course of an ebb tide. Thus, it is hoped that this investigation will provide some insight into aspects of the dynamic regime of the Tamar Estuary which have previously received comparatively little attention.

## 1.4 THE EQUATIONS OF MOTION

Considering that the major part of the analysis conducted in this project involves the application of the longitudinal and lateral equations of motion to our data set, this section presents a summary of previous studies which have also used the equations of

motion to assess the dynamics of various estuaries. The equations themselves are derived from Newton's second law of motion, and state that;

*acceleration = (pressure + gravity + frictional + tidal) forces / unit mass*

They are presented mathematically in chapter 5.1.

McAlister *et al.* (1959) conducted their study in a typical Alaskan fjord and found the longitudinal momentum balance to be between the longitudinal and vertical advection terms ($\bar{u}.\partial\bar{u}/\partial x$ and $\bar{w}.\partial\bar{u}/\partial z$), the baroclinic pressure gradient and the vertical stress gradient. The horizontal fluxes of turbulent momentum were considered to be negligible. Pritchard (1956) found a similar longitudinal balance in the James River, but also included a tidal inertial term such that the balance was between three accelerations, a pressure term and the vertical stress gradient. Again, the horizontal eddy fluxes of momentum were assumed to be negligible, and the longitudinal component of the pressure force was balanced mainly by the vertical eddy friction term ($\partial\overline{(u'.w')}/\partial z$) with the various spatial accelerations being less significant. Bowden (1960) assumed a spatially uniform flow field in his study of the Mersey Narrows, such that the temporal acceleration only was produced by baroclinic and barotropic pressure gradients and the vertical stress gradient.

Uncles *et al.* (1992) solved the equations of longitudinal momentum and salt conservation in the Merbok Estuary, Malaysia. Solutions showed that as the salinity stratification was primarily caused by vertical shear in the currents and advection of the longitudinal salinity gradient, it was therefore necessary to specify the vertical profile of the longitudinal density gradient in the equation of motion. The temporal longitudinal acceleration was found to be the result of an imbalance between the horizontal pressure gradients and the vertical stress gradient.

The lateral dynamic balance in the Vellar Estuary has been examined (Dyer and Ramamoorthy, 1969, Dyer, 1973) and it was found that the three spatial accelerations were produced by the pressure term, the Coriolis acceleration and the vertical stress gradient. The baroclinic pressure force was larger than the barotropic component, and the lateral advection was the dominant spatial acceleration. A curvature term, estimating the centrifugal force produced by flow round a bend in the river was included in the balance but experimental errors in the observations meant that the whole equation was difficult to balance numerically. The lateral balance in fjords is much simpler with

the Coriolis acceleration being balanced by the baroclinic pressure force, and all other terms in the equation being negligible. Dyer's work in Southampton Water again highlights the difficulties in balancing the equation of motion using fieldwork results. The lateral balance here is between the three spatial accelerations, the pressure term, the Coriolis acceleration and the curvature term, but only in three instances did the accelerations and forces nearly balance. In the James River, Pritchard (1956) found that in the lateral balance, the Coriolis force resulting from the mean horizontal motion was mainly balanced by the lateral pressure force such that the net acceleration (temporal and spatial) was close to zero. However, no streamline curvature term was included in this analysis.

Further work by Dyer (1977) on the lateral dynamic balance addresses the fact that secondary circulation patterns caused by cross-channel topography, its associated frictional effects and meanders in the river, are an important factor in both the dynamic and salt balances. From studies in the Vellar estuary and Southampton Water, he found that the water slope, the internal density distribution and the centrifugal force are dominant terms in the equation, and that the Coriolis acceleration is of secondary importance. Significant differences were found in the lateral circulation effects between salt-wedge, partially-mixed and well-mixed estuaries, and generally the assumption of lateral homogeneity in this type of analysis was found to be invalid.

Doyle and Wilson (1978) confirm Dyer's conclusion that the contribution from the centripetal acceleration is usually greater than the contribution from the Coriolis acceleration in the lateral momentum balance from their work in the Lower New York Harbor. The residual flow structure in this part of the estuary showed a characteristic two layer estuarine flow pattern, with landward flow at depth and seaward flow at the surface. The major terms contributing to the lateral balance were the lateral pressure gradients, the Coriolis acceleration and the field accelerations which were approximated using the tidally-averaged centripetal acceleration normal to the streamlines of flow through the cross-section. The turbulent stresses were not found to contribute significantly to the balance.

Münchow and Garvine (1993) applied the depth-averaged lateral equation of motion to a buoyancy-driven coastal current and identified two dynamically distinct regions, one of which, the 'source' region, was characterised by the presence of fronts and large

lateral density gradients. In this region, over shoaling areas many terms contributed to the balance with the Coriolis acceleration being the single largest. In deeper channels, however, the balance was primarily between the sea surface slope, the baroclinic pressure gradient and the Coriolis acceleration and was therefore almost geostrophic. The non-linear inertial forces (i.e. the spatial accelerations) were found to be important in the dynamics of the source region by other analysis techniques. As these terms appeared to be small in the across-shelf (lateral) balance, the authors concluded that they may be important in the along-channel (longitudinal) balance. The increased significance of the Coriolis acceleration in this study compared with the findings of Dyer and Doyle and Wilson probably arises because Münchow and Garvine's study was conducted in a coastal area as a opposed to a topographically-constrained estuarine environment.

Hughes and Rattray (1980) found that both the centrifugal and Coriolis forces were balanced with the pressure gradient in the lateral equation of motion, in their study of the Columbia Estuary.

The co-dependence of both the longitudinal and lateral momentum balances has been investigated by several authors. Scott (1994) used numerical modelling on data from the Conwy Estuary, Wales to show that the lateral circulation could strongly affect the longitudinal momentum balance. In this model, the longitudinal salinity gradient was assumed to be locally linear and steady over a tidal cycle. On the flood tide, differential longitudinal advection produced a lateral density gradient which drove a surface-convergent twin cell lateral circulation structure (Smith, 1976, Nunes and Simpson, 1985). On the ebb tide, water in the central part of the channel was fresher such that the lateral cells circulate in the opposite sense to the flood cells. This lateral circulation was found to be strong enough to modify the longitudinal momentum balance, as water with a longitudinal momentum deficit was transported near the surface to the centre of the channel during the flood. Similarly, the ebb tidal lateral circulation also modified the longitudinal balance, such that a lateral density gradient may have an indirect effect on the longitudinal equation of motion.

The importance of both lateral and longitudinal salinity (density) gradients in the horizontal momentum balances is again highlighted by Jin and Raney (1991). They looked at a well-mixed estuary in Florida using a two-dimensional depth-averaged

model. The results from their equations of motion showed that although velocity results at any specific time were not changed appreciably by the inclusion of horizontal density gradients in the model, the velocity integrated over a tidal cycle i.e. the mass transport, was significantly altered. Hence, even in well-mixed estuaries, horizontal density gradients constitute an important forcing mechanism in the longitudinal and lateral dynamics.

## 1.5 STRATIFICATION AND MIXING PROCESSES

The competition between stratification and mixing plays a crucial role in determining the dynamics of any estuary, and is perhaps especially important in the case of partially-mixed estuaries. This section reviews some previous work, conducted in both the field and the laboratory, which addresses various aspects concerning estuarine stratification and mixing.

The competition between stratification and mixing is parameterised by the gradient Richardson number (equation 1.1), which expresses whether shear is sufficient to overcome the stability caused by stratification, to produce mixing. Various laboratory and field studies by, amongst others, Thorpe (1973), Linden (1979), Thompson (1980), McEwan (1983), West *et al.* (1985) and Dyer (1988) confirm that for $Ri < 0.25$, the shear is sufficient to overcome stability and produce mixing. However, this mixing arises through various different mechanisms, and perhaps the simplest way to describe these processes is to consider a stably stratified, two-layer flow in which each of the layers is either turbulent or a parallel stratified shear flow. If the layer is initially turbulent, then this turbulence is the result of friction along the bed or sidewall, or it may be caused by friction due to wind stress on the surface of the flow.

Considering first the situation in which neither layer is initially turbulent, the velocity shear between the two layers produces internal Kelvin-Helmholtz waves along the density interface. These waves then form vortices, which either collapse to produce a horizontal interleaving of the two layers which mix because of density instability, or intense local shear within the vortices causes turbulent mixing (Dyer, 1988). In either case, the result is a layer of homogeneous density bounded by stable density gradients above and below. Hence this type of mixing is produced by internal waves.

If there is turbulence in one of the layers, the velocity shear will again generate internal waves which then break and interact with the turbulence such that there is a preferential transfer of water from the less turbulent layer into the more turbulent layer. When the discrete wave-breaking events are averaged over space and time, they can be considered as a continuous mixing process called entrainment (Dyer, 1988).

If both layers are initially turbulent, mixing takes place via turbulent diffusion which is a two-way process in which equal volumes of water are exchanged between the two layers such that there is a net exchange of salt or heat, but no net exchange of water (Dyer, 1973).

Hence, turbulence itself is produced both by internal velocity shear and external friction effects, and mixing occurs as the result of internal waves, entrainment or diffusion. In a more general sense, all three types of mixing represent the conversion of kinetic energy (i.e. from internal wave motion or turbulent motion) into potential energy, whereby the centre of mass of the water column has been elevated by the vertical transport of salt or heat. This summarises the process of mixing, which is opposed by the stratifying influences of gravitational circulation and tidal straining (Nunes Vaz and Simpson, 1994). Some of these aspects will now be reviewed in more detail.

The structure of turbulence itself was originally examined using quadrant analysis by Lu and Willmarth (1972,1973). In this technique, random perturbations in velocity on two perpendicular directions (u' and w') are divided into four quadrants such that $u' > 0$, $w' > 0$ and $u' < 0$, $w' < 0$ are termed outward and inward interaction events respectively, and $u' < 0$, $w' > 0$ and $u' > 0$, $w' < 0$ are termed ejections (or bursts) and sweeps respectively. Experimental work by Lu and Willmarth (1973) found that the ejections are the largest contributors to the Reynold's stress, $\overline{u'w'}$, followed by the sweeps. Fieldwork conducted by Heathershaw (1974), West and Shiono (1985) and Kawanisi and Yokosi (1993) also confirms that positive contributions to the turbulent Reynold's stresses are provided by ejections and sweeps, and negative contributions by the outward and inward interactions.

The Reynold's stresses themselves represent fluxes of turbulent momentum and similarly the Reynold's fluxes represent turbulent fluxes of salt, such that the Reynold's stresses can be related to the mean velocity gradients and the Reynold's fluxes can be related to the mean salinity gradients, e.g.:

$$-(\overline{u'w'}) = N_z\left(\frac{\partial u}{\partial z}\right) \qquad (1.4) \qquad -(\overline{w'S'}) = K_z\left(\frac{\partial S}{\partial Z}\right) \qquad (1.5)$$

$N_Z$ and $K_Z$ are referred to as the vertical eddy viscosity and the vertical eddy diffusivity respectively, and they provide a useful means of parameterizing vertical turbulent mixing. For example, Schröder and Siedler (1989) conducted fieldwork in the Elbe Estuary and found that the vertical eddy viscosity was up to four times greater during the flood tide than during the ebb, indicating a greater degree of stratification during the ebb tide. This is because in the presence of a density gradient, the turbulence has to work against the gradient to promote mixing, therefore both $K_Z$ and $N_Z$ are reduced below their homogeneous values. The relationship between $K_Z$, $N_Z$ and, effectively, the degree of stratification is examined using the flux Richardson number, Rf:

$$Rf = \frac{K_z}{N_z} Ri \qquad (1.6)$$

The flux Richardson number represents the fraction of the available turbulent kinetic energy which is converted via mixing into potential energy by raising the centre of mass of the fluid. Linden (1980) performed a series of experiments in a stratified flow to determine the curve of Rf vs. Ri. He found that as Ri increased from zero, so did Rf until it reached a maximum value of 0.12 at Ri = 1.3. As Ri increased further, Rf decreased. Rf is proportional to the vertical density flux and Ri is proportional to the vertical density gradient. Hence, when Rf increases with Ri, regions of high density gradient have high vertical fluxes which transport mass away from the high gradient region to diminish the stratification. When Rf decreases with increasing Ri, regions of high density gradient support smaller vertical fluxes which transport mass towards the high gradient region, increasing stability. Therefore, the effect of mixing on stratification depends on which side of the Rf vs. Ri curve the system lies; at low values of Ri, more energy is extracted by the turbulence by working against the buoyancy forces whereas at larger values of Ri, the efficiency of mixing is actually reduced by the buoyancy forces.

In general, it has been found that between one sixth and one quarter of the available kinetic energy is converted into potential energy (Linden, 1979). Additionally, at high values of Ri, a significant fraction of the turbulent kinetic energy is used to generate internal waves which, provided they do not break, will not contribute to the mixing or increase the potential energy. However, if an internal wave does break, the fraction of

the wave's kinetic energy which is converted into potential energy is again found to be about one quarter (Thompson, 1980). It should be noted that internal waves can break to cause turbulent mixing at mean values of Ri which are considerably greater than 0.25. This is because the internal waves cause stretching of the interface such that velocity shear is enhanced at the wave troughs and crests causing a local reduction in Ri and local instabilities which leads to turbulent mixing (Dyer, 1988). The formation of internal waves, their subsequent behaviour and the mechanisms by which they cause turbulent mixing are all complex processes which are described in detail by Thorpe (1973, 1987), Lee and Beardsley (1974), Maxworthy (1979), Thompson (1980), McEwan (1983a, b) and Sturley and Dyer (1992).

As well as examining the flux Richardson number, several authors have also looked at the relationship between $K_z/N_z$ and Ri, amongst them Munk and Anderson (1948), Bowden and Gilligan (1971) and Odd and Roger (1978). All of them found that $K_z/N_z$ decreases from unity and tends towards zero with increasing Ri. This is because the exchange coefficients of mass and momentum ($K_Z$, $N_Z$) are equal in homogeneous flow. As Ri increases, velocity shear across the interface produces perturbations which will not necessarily break. These non-breaking perturbations will exchange momentum but not mass with the surrounding fluid, such that $K_Z$ is reduced by a greater amount than $N_Z$ (Odd and Roger, 1978, Dyer, 1988).

Having considered the various effects of velocity shear and how they work to decrease the stability of the flow and consequently its Richardson number, we should also consider processes which increase the stability and inhibit mixing. Nunes Vaz and Simpson (1994) identified the vertical gravitational circulation and tidal straining as the primary causes of stratification in estuaries. Tidal straining occurs when vertical velocity shear in the presence of a longitudinal density gradient advects less dense fluid over more dense fluid during the ebb tide (Shiono and West, 1987, West and Shiono, 1988, Nunes Vaz and Simpson, 1994). The velocity shear during the ebb tide arises because the baroclinic pressure gradient opposes the barotropic pressure gradient at depth (Jay, 1990). As the baroclinic and barotropic gradients act in the same direction during the flood, the internal velocity shear is reduced, as is the degree of stratification. Nunes Vaz and Simpson found that on semi-diurnal and diurnal timescales, stratification was

primarily caused by tidal straining, whereas at the spring-neap frequency, it was mainly the result of vertical gravitational circulation.

# CHAPTER 2
# FIELDWORK AND DATA PROCESSING

This section describes the fieldwork that was carried out for the project, the equipment used and the processing applied to the data collected.

## 2.1 RATIONALE

The fieldwork for this project was conducted in two stages. The preliminary stage comprised several surveys in the area of the Lynher-Tamar confluence (figure 2.1) and its primary objective was to field test the estuarine thermistor spar (ETS). These initial surveys also provided useful background data on the seasonal variability in temperature within the survey region, and allowed us to assess whether the Tamar-Lynher front was a consistent feature of every ebb tide or whether its formation might be dependent on factors such as the spring-neap tidal cycle, the amount of fresh water inflow or prevailing wind conditions. During these surveys, it was possible to identify the best equipment deployment configuration and the optimum sampling frequency capable of providing good resolution of the frontal interface whilst keeping the raw data files to a manageable length for post-processing and graphic presentation.

The second stage of fieldwork involved conducting a more detailed survey in the region of frontogenesis in order to record the temperature and velocity fields across the front quasi-synoptically. The main objective of these surveys was to collect velocity and temperature data (which were subsequently combined with salinity data to approximate density) in order to calculate terms in the equations of motion and continuity, thus allowing the hydrodynamics within the region to be evaluated. Additionally, both the velocity and temperature data from survey lines which crossed the surface convergence provided 'images' of the front in cross-section.

## 2.2 EQUIPMENT

The surveys were carried out either from the University owned catamaran "Catfish" or from Plymouth Marine Laboratory's flat-bottomed sea truck "Tamaris". During preliminary surveying, the main piece of equipment deployed was the ETS. This instrument was designed and built by Darrell Sturley at the Institute of Marine

*Figure 2.1 Map of Tamar Estuary showing survey area*

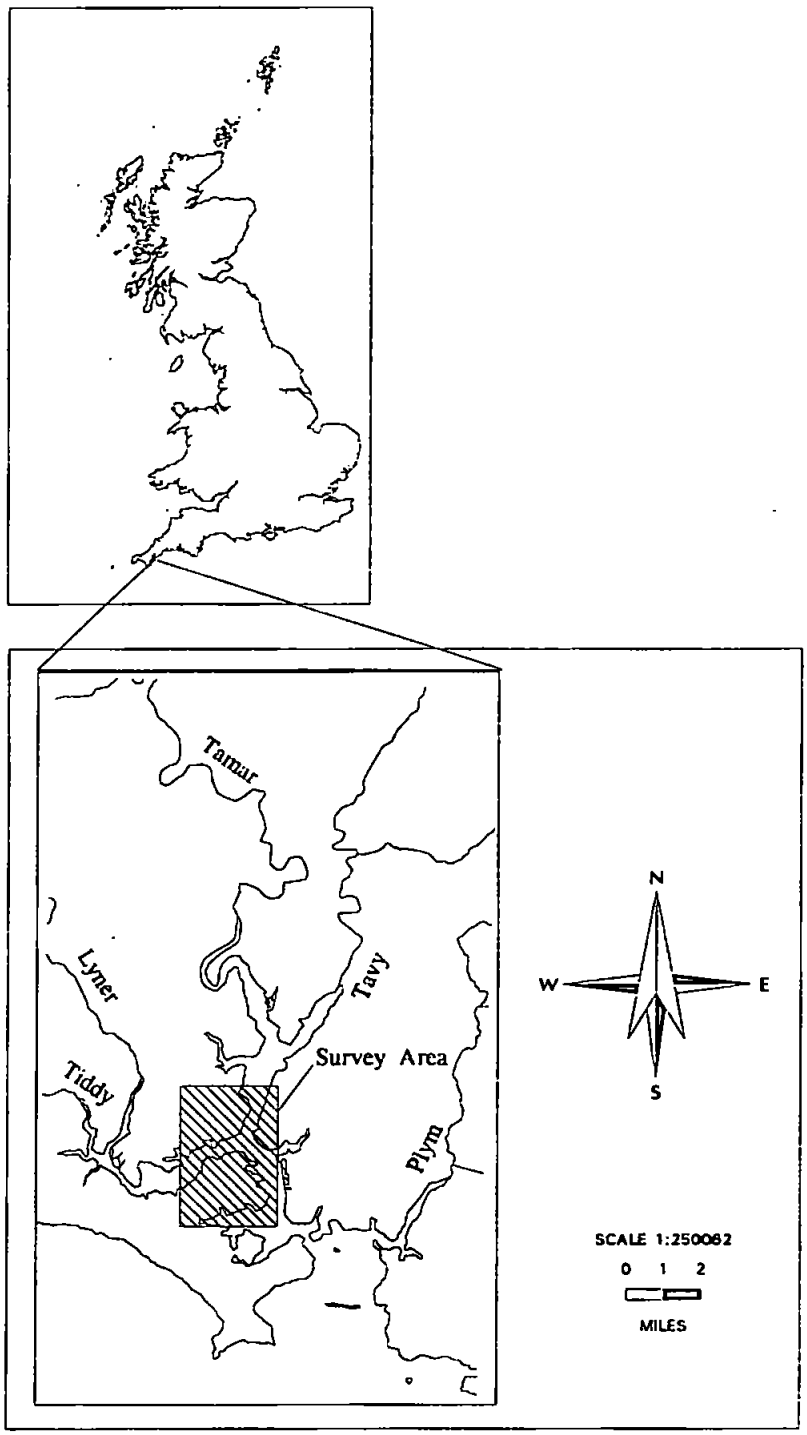

Studies, Plymouth University as part of his Ph.D. (Sturley, 1990). The ETS records continuous vertical profiles of temperature over the top 4 metres of the water column. It consists of a 6 metre length of alloy scaffold tube of diameter 5 cm, onto which 16 thermistors are attached at 0.25 m intervals over the lower 4 m of scaffolding (Sturley and Dyer, 1990). The time response of each thermistor is approximately 50 ms, allowing a realistic maximum sampling frequency of 20 Hz, and their resolution is 0.005°C. Theoretically, the output voltage from each thermistor should be linear with temperature such that 0.05 volts represents 1°C, however, this has not proved to be the case in practice, as will be discussed later.

On Catfish, the ETS was deployed vertically with the sensors pointing forwards, by attaching it to a horizontal scaffolding A-frame which was rigged across the bow of the boat. Guy ropes were fixed to the ETS to counteract the backwards force exerted on the lower part of the instrument as it moves through the water, thus holding it in a vertical position (see figure 2.2). On Tamaris, the ETS was fixed to a bracket on the side of the boat's hull. Again, guy ropes held the instrument vertical with the sensors pointing forwards (see figure 2.3). Both methods of deployment were devised to minimise the effect of the boat's wash on the sensors which, on Catfish, was achieved by mounting the ETS forward of the bow. Although on Tamaris, the ETS was mounted on the side of the boat, the design of the hull means that most of the wash goes under the boat with negligible wash generated along the sides. On both boats, the surveying speed was kept between 1 and 2 knots, again to minimise boat wash.

Other equipment used in the preliminary stage of surveying included an MC-5 temperature-salinity bridge (T-S bridge) used to take vertical profiles with measurements recorded at 1 m depth intervals over the top 5 m of the water column. These profiles were taken at the start and end of each transect in order to calibrate the ETS accurately. A 200 kHz echosounder was run continuously throughout each preliminary survey which allowed the front to be observed from the increased level of acoustic backscattering generated by suspended particles trapped there. Position fixes were obtained at the start and end of each transect and at approximately 1 minute intervals during the transect from a portable differential GPS system.

For the more detailed surveys, the ETS was used in conjunction with an Acoustic Doppler Current Profiler (ADCP) borrowed from Dr. Rocky Geyer at Wood's Hole

*Figure 2.2 Equipment deployment configuration on "Catfish"*

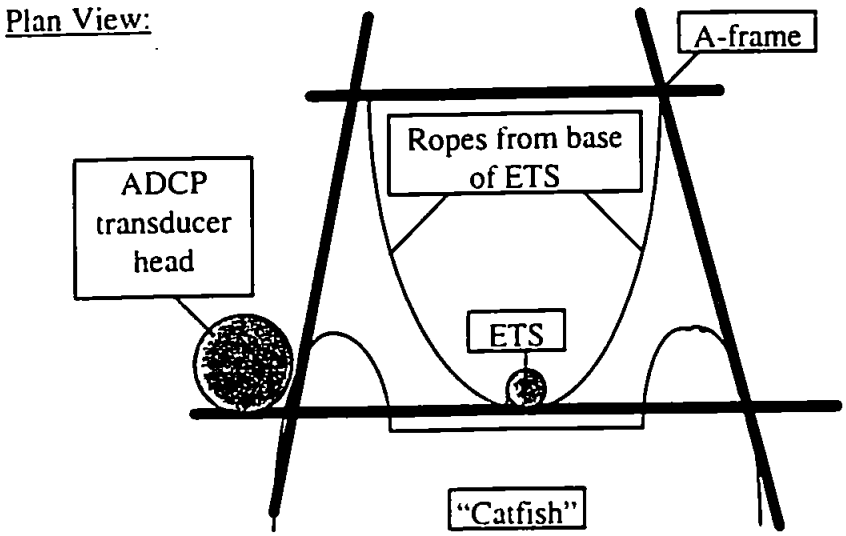


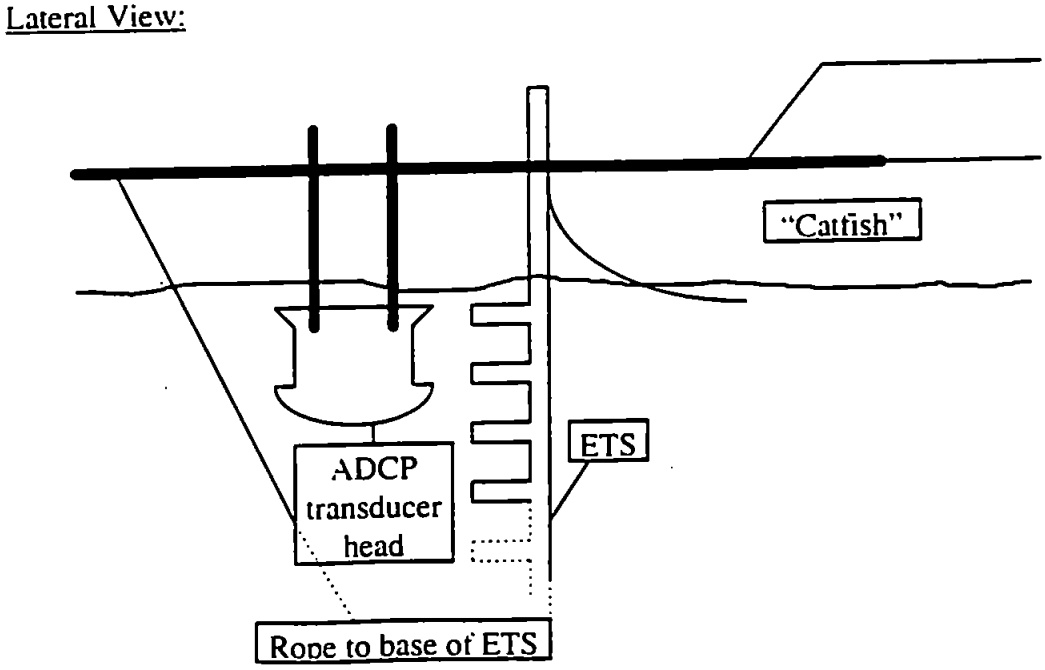

*Figure 2.3 Equipment deployment configuration on "Tamaris"*

Plan View:

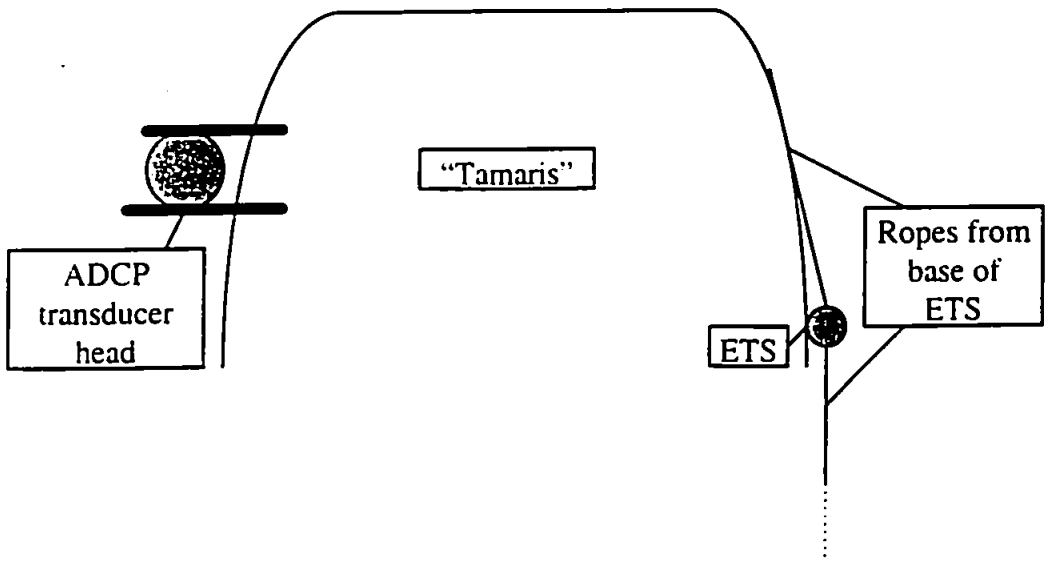


Lateral View:

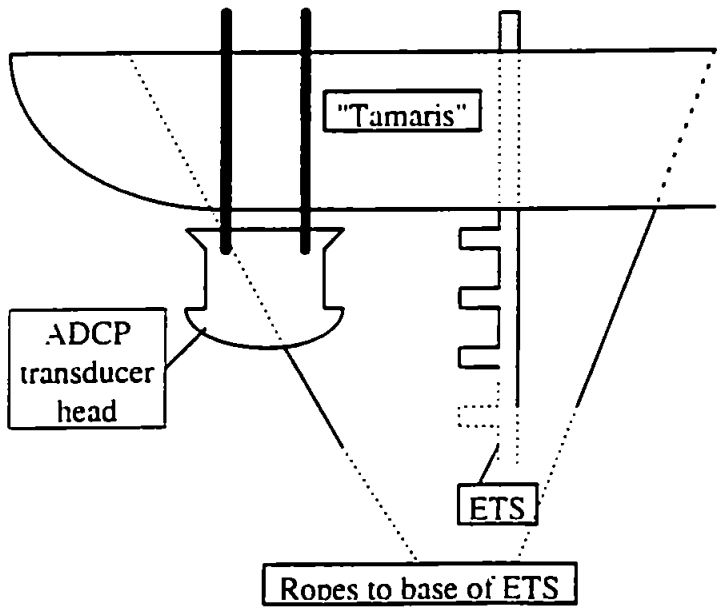

Oceanographic Institution, Massachusetts, USA. The ADCP transmits four orthogonally-oriented acoustic pulses down into the water column from the transducer head which is just below the surface. The acoustic energy is backscattered by sediment particles and plankton in the water, and the travel time of the returned pulse, as recorded by the transducers, allows the depth of backscattering to be determined. The Doppler shift of the backscattered signal is caused by the motion of the particles in the water, and by combining data from all four transducer faces, a continuous profile of velocity, resolved into east-west, north-south and vertical components, as a function of depth throughout the water column is obtained. The ADCP operates at a frequency of 1200 kHz and was deployed by attaching two short lengths of scaffolding to the transducer head, enabling the head itself to be held steadily with the transducers facing down at a level approximately 30 cm below the water surface, which was deemed sufficient to avoid the effect of wash over the instrument as it moved through the water. A circular bracket fitting round the cylindrical transducer head was made by Andy Prideaux in I.M.S., onto which the scaffolding poles were attached. An armoured cable ran from a watertight connection on the transducer head to the signal processing unit on the boat. During deployment, it was necessary to ensure that a minimum distance of approximately 2 m was maintained between the ADCP head and the ETS to avoid interference between them. To achieve this on Catfish, the ADCP was clamped to the outside of the A-frame whilst the ETS was secured in the centre (see figure 2.2). On Tamaris, the ADCP was deployed over the opposite side of the boat from the ETS, keeping it approximately 0.5 m away from the side so that the acoustic signals would not be backscattered by the hull (see figure 2.3). As the ADCP cannot resolve current velocity in the top 2 metres of the water column, any noise introduced by the boat's hull would occur in this null zone, leaving the remainder of the profile free from the effects of hull interference.

Although the ADCP head has its own heading sensor, it was only working intermittently during our survey, so additional heading data was recorded using a CETREK fluxgate compass fixed on the boat. The position of the ADCP head relative to the boat was constant, so the CETREK heading data could be used to correct any spurious headings recorded by the ADCP compass.

For the detailed survey, ETS data was sampled at a frequency of 5 Hz using a High Speed Data Collection package installed on P.C. The ADCP and heading data were logged on a separate P.C. using R.D. Instruments' TRANSECT package. The MC-5 temperature-salinity bridge was again used to take stationary vertical profiles, but the echosounder was not deployed for logistical reasons. The differential GPS system provided accurate position fixes.

## 2.3 SURVEYING METHOD

Preliminary surveys were conducted between January 1993 and January 1994 at approximately 3 monthly intervals on ebb tides ranging from springs to neaps. On each survey, sampling runs were conducted across the mouth of the Lynher River, from this region upstream to the Tamar Road Bridge, from the bridge downstream to Looking Glass Point, and back upstream from the Point to the Lynher mouth (see figure 2.1). Transects from the Lynher mouth west into the Lynher River were also carried out. On each occasion, surveying commenced at or around high water and continued to follow the sampling regime outlined above until a line of foam and debris at the surface indicated the position of the ebb tidal front in the mouth of the Lynher. Generally, this occurred approximately 4 to 5 hours after high water. As soon as the front had developed, a pattern of zig-zagging sampling runs across the front was carried out, in order to record measurements of the front with the ETS as often as possible, and at a range of sampling frequencies (2 Hz, 4 Hz, 5 Hz, 6 Hz, 8 Hz and 10 Hz). Stationary vertical temperature and salinity profiles were recorded to a depth of 4 or 5 m, with a 1 m sampling interval at the beginning and end of each transect. The front was continuously surveyed until its surface expression (i.e. the foam line) was no longer visible.

The dates and tidal conditions for the detailed survey are presented in table 2.1.

| *Date* | *High Water (B.S.T.)* | *Tidal Range (m)* | *Spring/Neap* |
|---|---|---|---|
| 20.04.94 | 1309 | 2.1 | Neap |
| 22.04.94 | 1554 | 3.3 | Neap + 2 days |
| 25.04.94 | 0600 | 5.0 | Spring - 1 day |

Table 2.1 Tidal conditions for detailed surveys

The weather conditions on all three survey days were good, with low winds and generally clear skies.

A 300 m by 600 m figure-of-eight shaped survey grid was used as a guideline in the mouth of the Lynher River (see figure 2.4). Transects were conducted along each 300 m side of the survey grid starting at or before high water on each day. The ADCP and ETS were recording simultaneously on each transect; the ADCP was set to emit an acoustic pulse every 0.1 seconds and then average the data from four pings (effectively, a sampling frequency of 2.5 Hz) and the ETS was sampling at a frequency of 5 Hz. Depending on whether the boat was moving with the current or against it, each transect took between 3 and 9 minutes, with an average time of 5 minutes. The figure-of-eight grid was followed as the ebb current increased and the front developed. As on previous surveys, stationary vertical profiles of temperature and salinity were recorded at the start and end of each transect, over the top 4 or 5 m of the water column at 1 m intervals using the T-S bridge. Position fixes were recorded approximately every two minutes from the GPS. In addition, a position fix was taken each time the front was crossed, as indicated by the surface foam line and the real-time display of ADCP data onboard.

## 2.4 DATA PROCESSING

In this section, the post-acquisition processing of both the ETS and the ADCP data from the detailed surveys will be described.

The output voltages from each thermistor on the ETS were recorded in a multiplexed format, so the first stage of processing was to demultiplex the data into sixteen channels, one for each thermistor. The lowermost thermistor on the ETS is known as the 'dummy' channel because instead of responding to temperature changes, this sensor is used to record internal electronic noise that may occur within the system. The signal from the dummy channel is then subtracted from the remaining fifteen channels.

Laboratory calibration tests were conducted both before and after fieldwork, in which each thermistor was individually immersed into ice (at approximately 0°C) and water of 9°C and 18°C. The calibration curves thus derived were applied to each channel's output voltages, and although the thermistor manufacturer's quoted voltage response to changes in temperature was 1 volt equivalent to 20°C, this was found to be inaccurate for most thermistors.

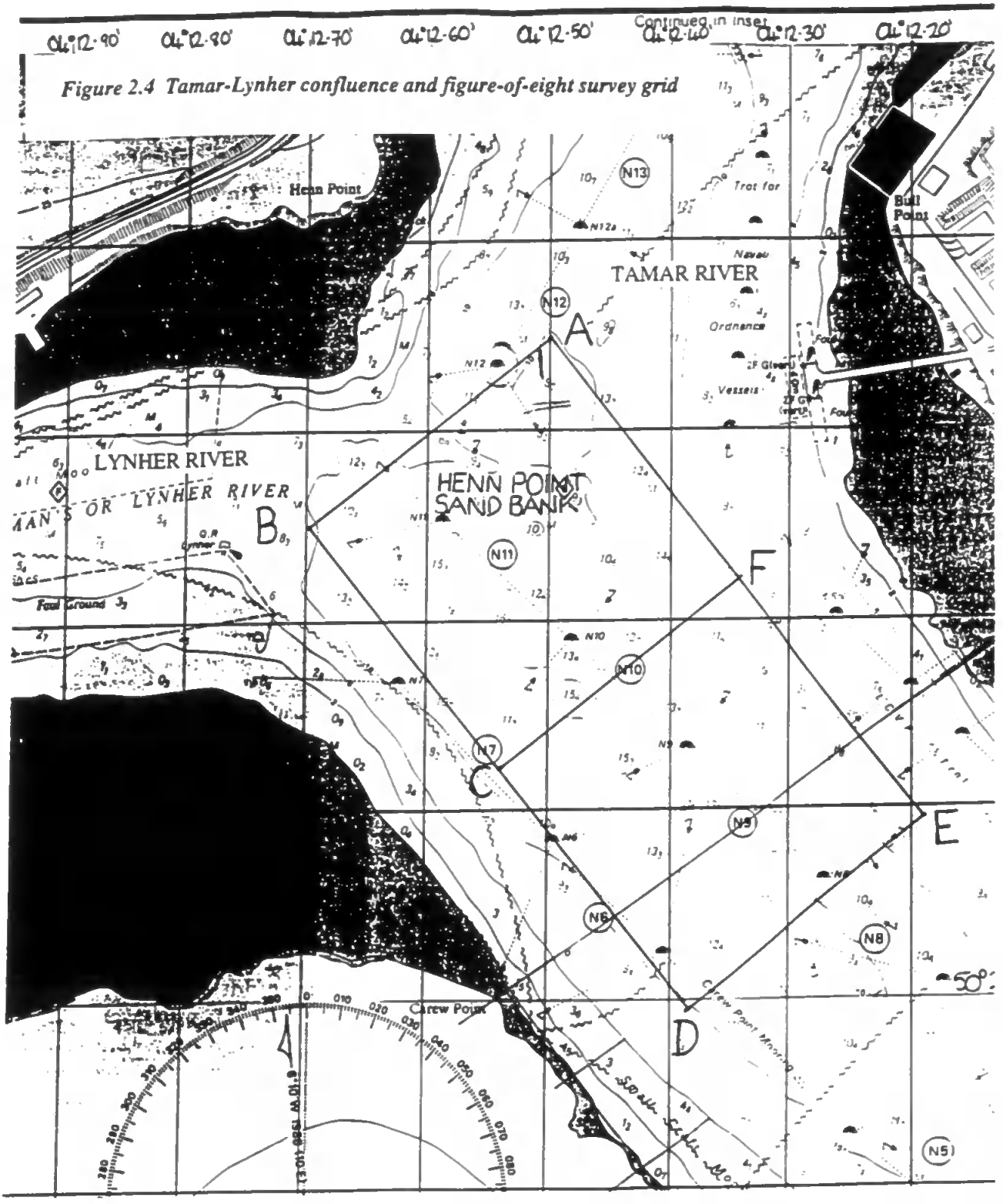


*Figure 2.4 Tamar-Lynher confluence and figure-of-eight survey grid*

At this stage, it became apparent that of the fifteen channels, only five were functioning properly; the remaining ten produced voltage traces which were either completely flat or excessively noisy with voltage fluctuations which, when calibrated, represented unrealistic variations in temperature of up to 10°C. The output from these channels was discarded from the data set.

It was then assumed that over the small ranges of temperature and salinity encountered during each of the second stage, more detailed surveys (as shown by the T-S bridge results discussed in chapter 3) it was reasonable to infer a linear relationship between both the output voltage and temperature, and the output voltage and salinity. Hence, each channel's output voltage at the start and end of each transect was compared to the salinity and temperature values recorded at the appropriate depth by the T-S bridge. The conversion coefficients derived in this way were generally found to be slightly different at the start and end of the transect, so it was assumed that they varied linearly over the duration of the transect, such that effectively, interpolated coefficients were applied to the output voltages to convert then into salinity and temperature values.

In order to obtain regularly spaced matrices of salinity and temperature values in which each value from the functioning channels was in the correct spatial position, weighted averaging was used to interpolate values for the missing channels from the available data. In this way, a matrix of temperature values and a matrix of salinity values were derived for each transect, which were re-formatted to be compatible with MATLAB software, for further analysis. It is obvious that the temperature and salinity values derived in this manner are of questionable accuracy. However, it was felt that the method of post-processing used was probably the best approach, given the poor quality of the initial data set.

The ADCP data also required some post-processing because the internal heading sensor located in the transducer head was giving spurious readings. The TRANSECT software package used to collect the data produced two output files containing the east-west velocities and the north-south velocities. However, these velocity directions were referenced to the incorrect ADCP headings, so initially the two matrices were combined to give a matrix of resultant velocities. The correct heading for each ensemble (an ensemble comprising the average velocity for four consecutive acoustic pings) was extracted from the output files from the CETREK fluxgate compass. The difference

between the incorrect ADCP heading and the correct CETREK heading was calculated for each ensemble. The resultant velocity vector for each ensemble was then rotated through the appropriate angle and resolved onto two orthogonal axes to give two new matrices of east-west and north-south velocities. Effectively, this procedure assumes that the initial resultant velocity vectors are correct but the orientation of the east-west and north-south axes is not, such that these orthogonal axes are then rotated into the correct orientation, according to the CETREK compass. Finally, the matrices of corrected east-west and north-south velocities were re-formatted for MATLAB. Had the ADCP been fully operational, the greater part of this post-processing would have been unnecessary. However, it is felt that as the processing described above was applied with care, the overall quality of the ADCP data was not substantially degraded as a result.

## 2.5 DATA ACCURACY

Factors to consider when assessing the accuracy of the ETS data, are the time response and resolution of the thermistors, and the resolution of the T-S bridge data which was used to calibrate the ETS results, as described in section 2.4. With each thermistor having a time response of 50 milliseconds, the sampling frequency of 5 Hz gives a sampling interval of considerably more than the response time. The quoted resolution of the thermistors is 0.005°C, however, as the ETS data had to be re-calibrated using T-S bridge data, a more realistic resolution is 0.05°C, which is the accuracy to within which the temperature can be determined from the T-S bridge. Similarly, salinity can be determined to an accuracy of 0.05 $^{o}/_{oo}$ using the T-S bridge which sets the limit of resolution for salinities derived from ETS results.

The technical manual for the ADCP gives an accuracy of 0.005 to 0.01 $ms^{-1}$ for the velocity data. Allowing for possible errors introduced by having to correct the ADCP heading data (see section 2.4) gives a resolution of 0.02 $ms^{-1}$, which is thought to be more realistic.

# CHAPTER 3
# DESCRIPTION OF INITIAL RESULTS

The purpose of describing the initial results is to assess how well temperature and salinity are correlated within the study area, for the subsequent calculation of density, and also to describe how the front is identified from each type of data.
During the preliminary surveys, the ADCP was unavailable and the ETS data were too noisy to be of any use, so only the vertical profiles of temperature and salinity collected with the T-S bridge can be discussed for this stage of the fieldwork (see section 3.1). From these earlier surveys, it seems that the front itself is a consistent feature of every ebb tide. Data collected during the detailed surveys on the 20, 22 and 25.04.94, will be discussed in section 3.2 (ETS results) and section 3.3 (ADCP results).

## 3.1 T-S BRIDGE RESULTS

In this section, the T-S bridge results for all surveys (both preliminary and detailed) have been collated, and table 3.1 shows tidal information for each of the ten surveys conducted between April 1993 and April 1994.

| *Date of Survey* | *State of Tide* | *Tidal Range (m)* | *Springs/Neaps* |
|---|---|---|---|
| 22.04.93 | Ebb | 4.4 | Spring |
| 23.04.93 | Ebb | 4.2 | Spring + 1 day |
| 28.07.93 | Ebb | 2.6 | Neap - 1 day |
| 25.08.93 | Ebb | 2.7 | Neap - 2 days |
| 26.08.93 | Ebb | 2.4 | Neap - 1 day |
| 18.01.94 | Ebb | 3.4 | Neap - 3 days |
| 19.01.94 | Ebb | 2.9 | Neap - 2 days |
| 20.04.94 | Ebb | 2.1 | Neap |
| 22.04.94 | Ebb | 3.3 | Neap + 2 days |
| 25.04.94 | Ebb | 5.0 | Spring - 1 day |

Table 3.1 Tidal conditions during surveying.

All surveys were conducted in the region of the Tamar-Lynher confluence, with the survey area extending north to the Tamar Road Bridge and south to Looking Glass Point. All temperature and salinity readings collected during this series of ebb-tidal

surveys are presented in figure 3.1 in the form of a T-S graph. The measurements were taken at various depths between the surface and 5 m depth. The T-S graph clearly demonstrates the seasonal temperature variability within the estuary, with temperatures as low as 6.9°C in January and up to 17.6°C in August. The range of temperatures encountered during one survey is usually no more than 1°C. For all surveys, the recorded salinity was between 9.3‰ which was observed in January and 34 ‰ observed in August. The range of salinities measured within the duration of one survey varied markedly. Salinity during the 19.01.94 survey ranged from 9.3 ‰ to 31.2 ‰, whereas during the 26.08.93 survey it only varied from 31.6 ‰ to 34 ‰. The salinity range encountered in each survey indicates the homogeneity of the water with both depth and in a lateral sense over the survey region. Where the salinity range was small and the temperature and salinity data plot to form a cluster on the T-S graph, the water was homogeneous i.e. it was comparatively well-mixed. A larger spread of data points indicates conditions which are either more stratified with respect to depth, or laterally inhomogeneous, or it may be that water of a different salinity was advected into the study area during the survey. Closer examination of the data collected during the 18 and 19.01.94 surveys, which display the largest salinity range, suggests that the water was depth-stratified, thus we can assume that a large salinity range indicates a more stratified water column. The degree of stratification inferred from the T-S graphs increased in the winter months and decreased during the summer months. This observation is consistent with the decreased amount of fresh water run-off from the rivers Tamar, Tavy and Lynher into the estuary over the summer months. The reduction in fresh water input effectively reduces the buoyancy of the water column which generally leads to better mixed, less stratified conditions during summer. However, this is not always the case; the T-S graph in figure 3.1 shows that conditions during the 28.07.93 survey appear to be anomalously well-stratified in comparison to other surveys conducted during the summer (i.e. the surveys on 25.08.93 and 26.08.93). The National Rivers Authority river flow data for both the Tamar and the Lynher, covering the entire year during which preliminary surveys were conducted were obtained from the N.R.A., Hydrometric Services, Exeter. Inspection of the Tamar flow data, measured upstream of the salinity intrusion, reveals

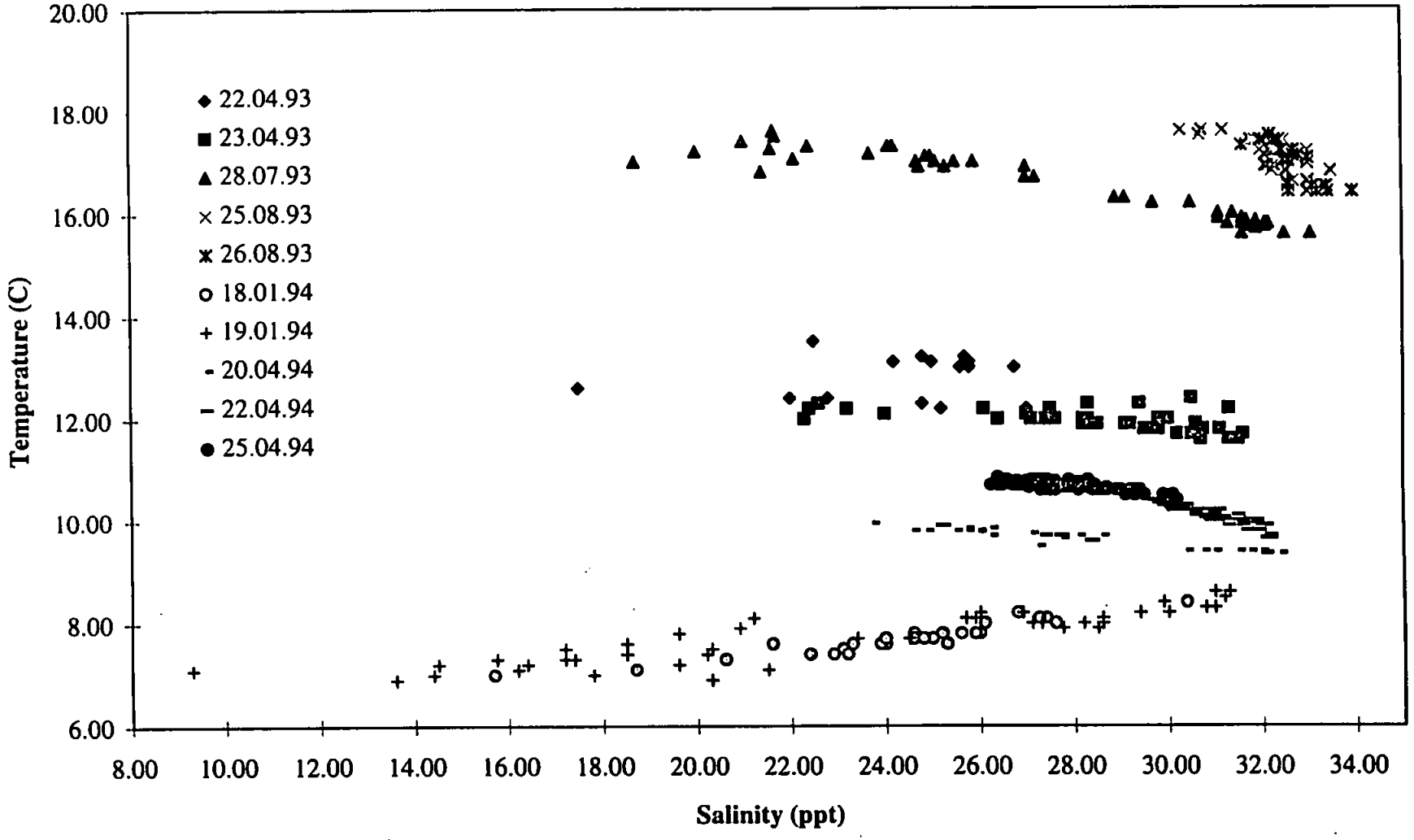


*Figure 3.1 Temperature and salinity data for all surveys*

that the 28.07.93 survey was carried out in the middle of a week-long period of higher than average fresh water run-off. On the day preceding the survey, the river flow reached its highest value since the 13.06.93, five weeks earlier. The peak in flow on the 27.07.93 had a value of 39.45 $m^3 s^{-1}$ on average throughout the day, compared with a mean daily averaged flow rate of 10.25 $m^3 s^{-1}$ for this particular month. After this period of high run-off, the flow rate decreased steadily over the next four weeks so that when the 25.08.93 and 26.08.93 surveys were conducted, the daily-averaged flow rate was only about 2 $m^3 s^{-1}$. Similarly, flow data from the Lynher river shows a large peak in run-off with a daily-averaged value of 3.46 $m^3 s^{-1}$ on the day before the 28.07.93 survey in comparison to the run-off values for the preceding four weeks. Again, the flow rate then decreased steadily after the 28.07.93 so that it was only about 1.5 $m^3 s^{-1}$(daily average) during the next two surveys.

Hence, it is likely that the high degree of stratification suggested by the temperature and salinity data taken during the 27.07.93 survey can be attributed to an increase in fresh water run-off and an associated increase in buoyancy over the week during which this survey was carried out.

The temperature and salinity values from the three detailed surveys on the 20, 22 and 25.04.94 show that on the 22 and 25.04.94, conditions were comparatively well-mixed, as in both cases, the measured salinity range is no more than 4 $^{o}/_{oo}$. During the 20.04.94, the salinity range was greater (approximately 9 $^{o}/_{oo}$) suggesting more stratified conditions. This survey was conducted on a neap tide when a decrease in tidal range and tidal current would allow a greater degree of stratification to develop during the ebb tide. Additionally, N.R.A. flow data for the Tamar and Lynher rivers shows that the amount of fresh water run-off for both rivers was generally decreasing throughout the month of April, such that a slightly higher degree of stratification would be expected during the earliest of the three detailed surveys, as appears to be the case.

The varying depth stratification over the three surveys is highlighted in figures 3.2 to 3.4 in which the temperature and salinity values recorded near the surface, and at about 5 m depth are both plotted for each day. As well as being slightly more stratified, the water column on the 20.04.94 had a slightly lower temperature than that observed during the following two surveys. The average temperature on the 20.04.94 was approximately

*Figure 3.2 T-S data at 1 m and 4m depths, 20.04.94 survey* FROM H.W. + 2 HRS TO H.W. + 3·5 HRS

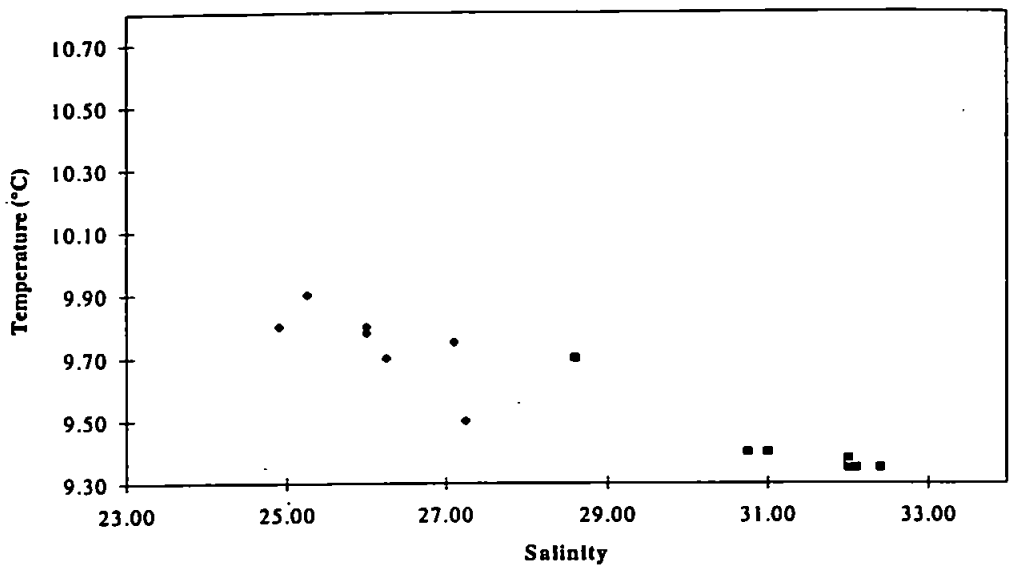


*Figure 3.3 T-S data at 1 m and 5 m depths, 22.04.94 survey* FROM H.W. - 0·5 HRS TO H.W. + 2·5 HRS

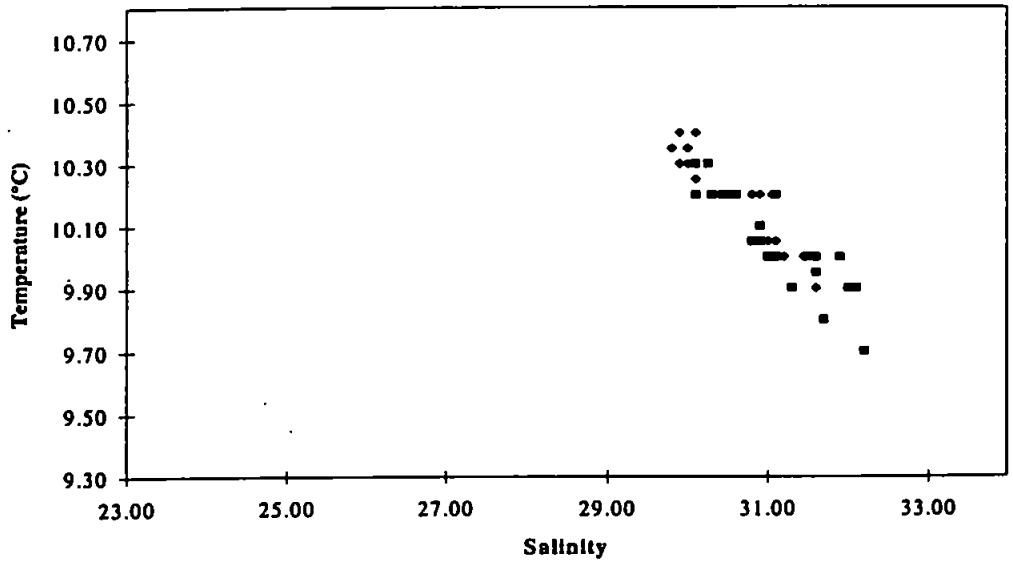


*Figure 3.4 T-S data at 1 m and 5 m depths, 25.04.94 survey* FROM H.W. + 3·5 HRS TO H.W. + 5·5 HRS

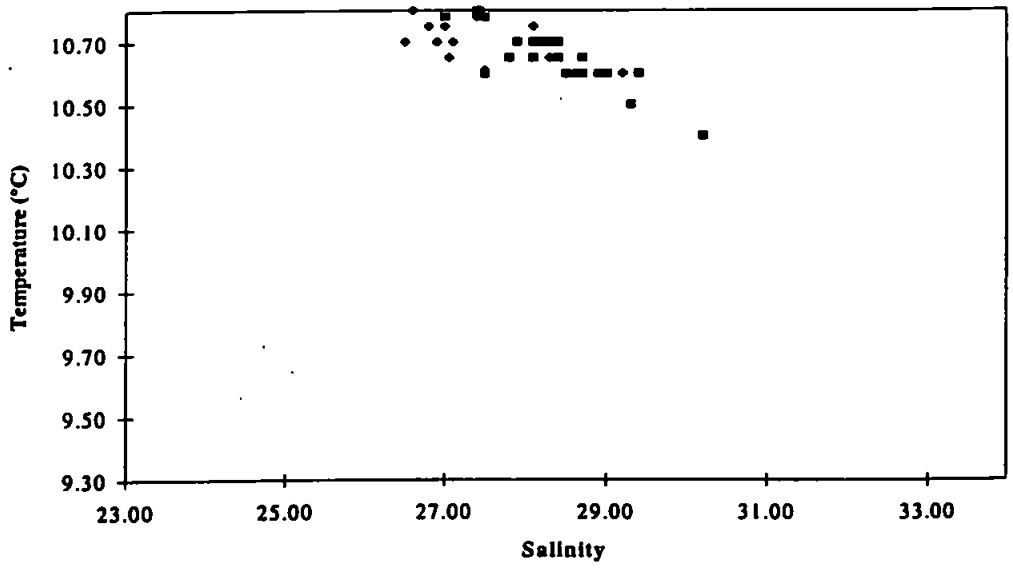

*Figure 3.5 3-D temperature surface plot of transect* AB2

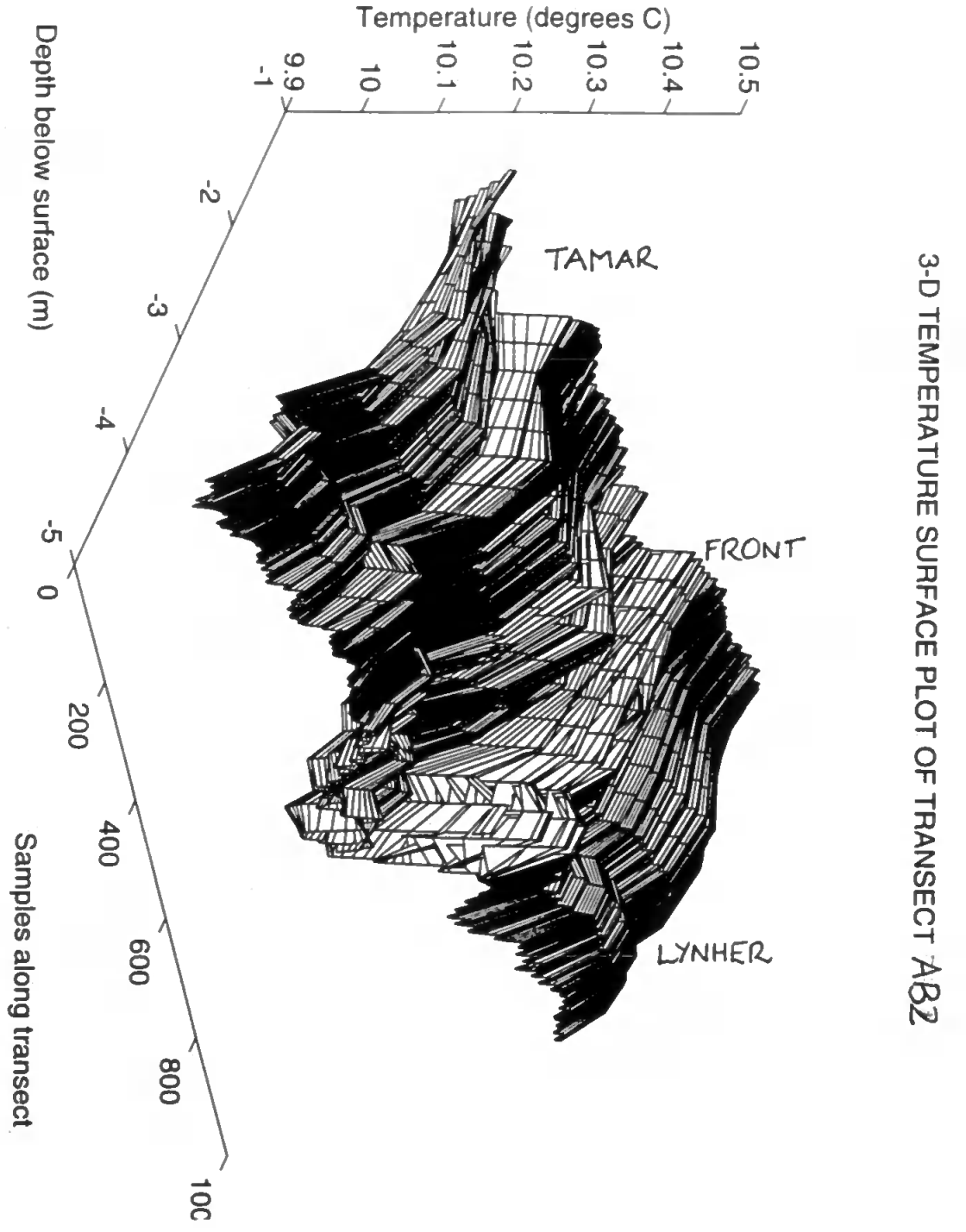

*Figure 3.6 3-D temperature surface plot of transect* AB3

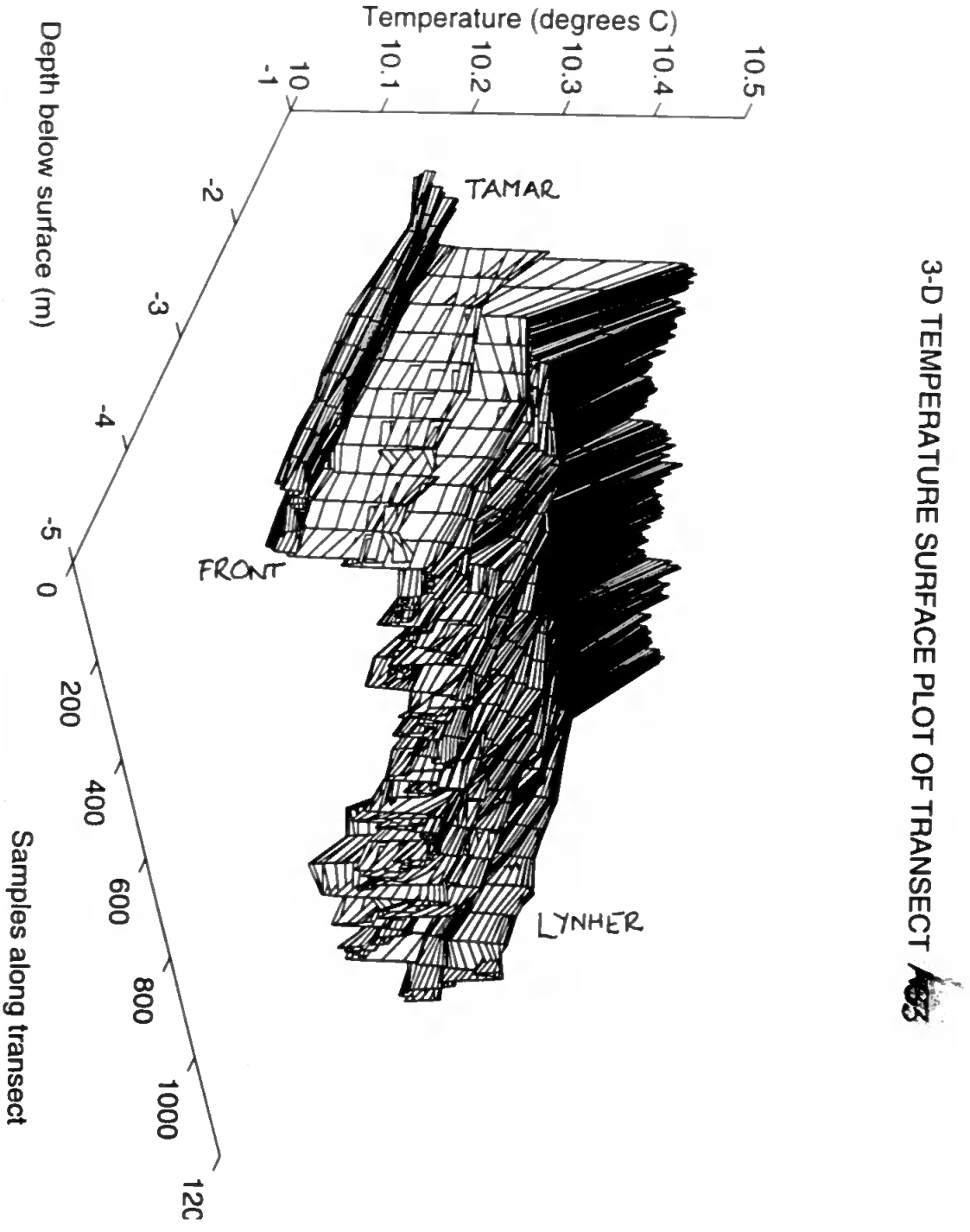

*Figure 3.7 3-D temperature surface plot of transect CB2*

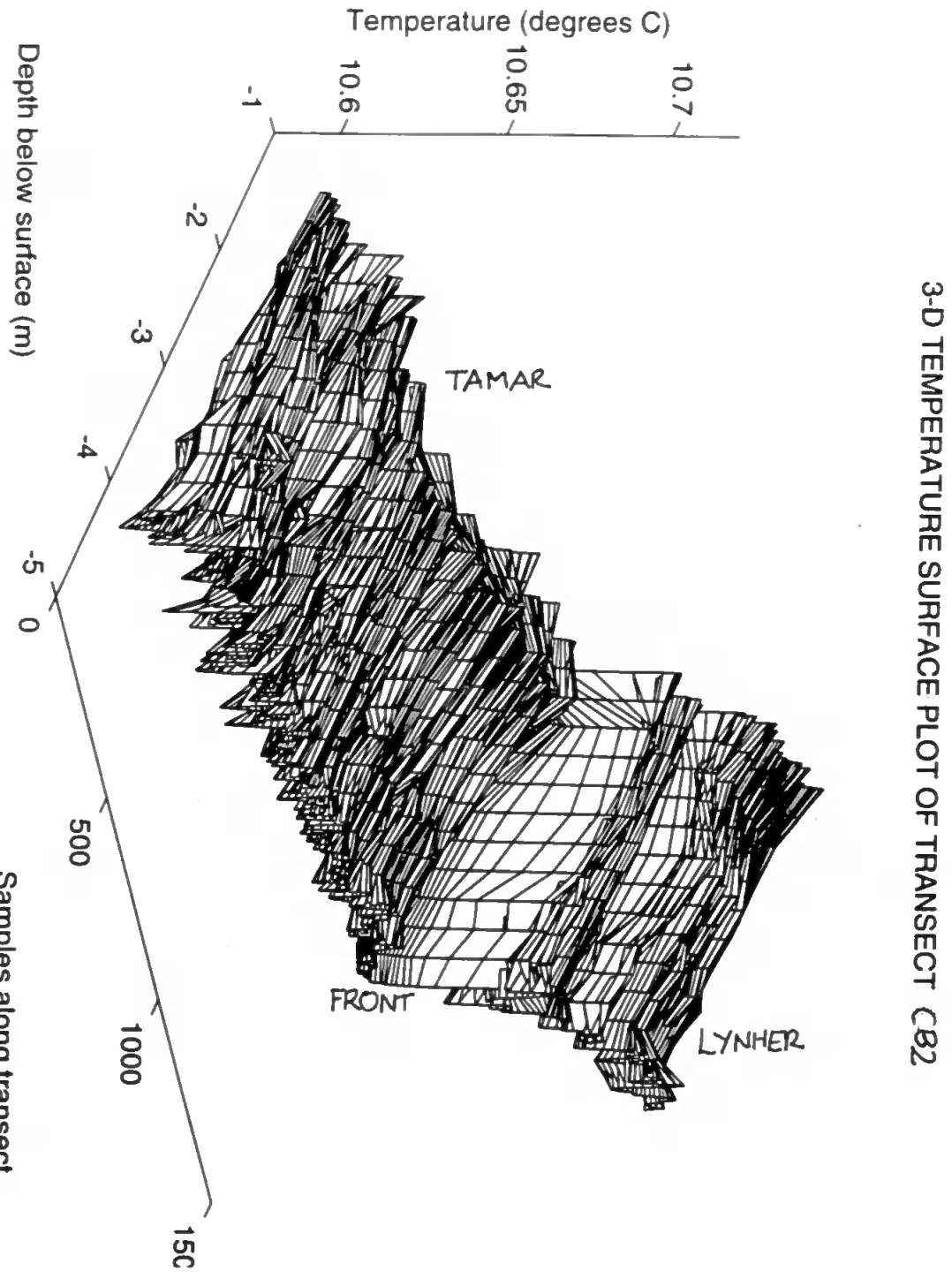

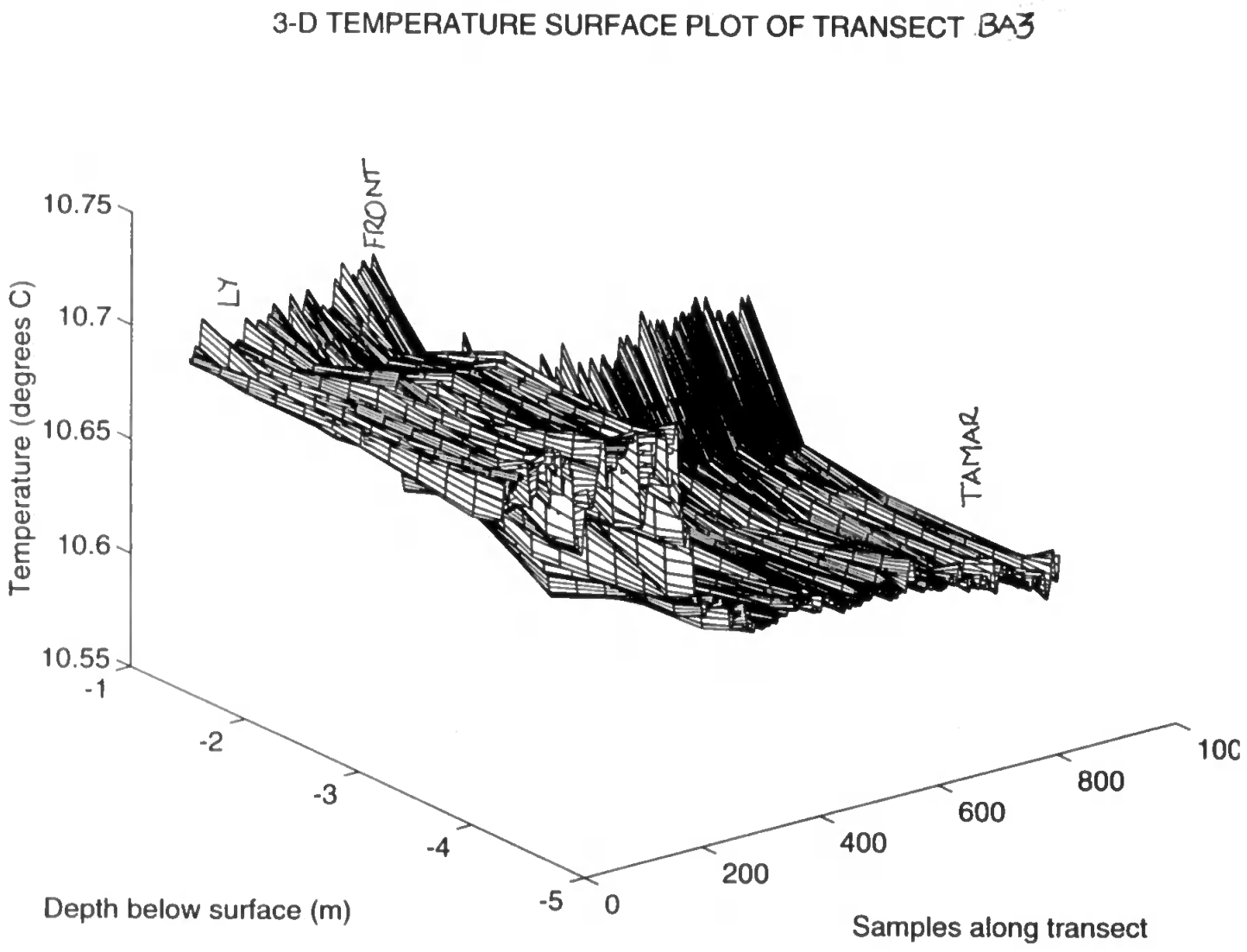


*Figure 3.8 3-D temperature surface plot of transect BA3*

around 1 hour 38 minutes after high water, on 22.04.94. A slight 'step' in the temperature surface can be seen between 600 and 700 samples along track. As we were traversing from the Tamar into the Lynher, then it appears that the Tamar water was at a cooler temperature than the Lynher water.

Transect AB3 (figure 3.6) also ran from A to B on the 22.04.94 survey, but this was recorded 2 hours 19 minutes after high water. The temperature step is again visible with cooler Tamar water at the start of the transect and warmer Lynher water at the end. By this stage in the tide, the temperature step has become more distinct than it was earlier in the tide, and the Lynher water seems to now show a small degree of stratification with a warmer layer extending upwards to the surface from approximately 2.5 m depth.

Transect CB2 (figure 3.7) was recorded during the 25.04.94 survey at 4 hours 14 minutes after high water, along side C to B. At this stage in the tide, it seems that the temperature step was now well developed and clearly defined the interface between cooler Tamar water and warmer Lynher water. Finally, figure 3.8 shows transect BA3, recorded 8 minutes later than transect CB2, along side B to A of the survey grid. Again, the temperature step was well defined between the Tamar and Lynher water. In terms of the temperature difference between these two water masses, it appears to be about 0.1°C on both the 22 and 25.04.94 surveys, well within the quoted resolution capability of the ETS which is 0.005°C. The question now arises as to whether this observed temperature step can be definitely associated with the front: as the temperature step occurred as the instrument went through the surface foam line, it is believed to represent the frontal interface between the Lynher and Tamar waters. However, for all transects which crossed the front, the five functioning thermistors recorded a temperature step at exactly the same point along the transect, such that the frontal interface appears to be linear and vertical. This apparently vertical orientation is partly the result of having to average between 'good' channels to fill in for missing channels, but probably also caused by electronic cross-talk between the thermistor channels. ADCP data, which will be presented in the next section, indicates that the frontal interface is in some cases inclined, and given the unreliability of the ETS data, an inclined interface is thought to be more likely.

Before discussing the ADCP results, salinity data from two transects are presented in the form of MATLAB colour plots in figures 3.9 and 3.10. Both transects were conducted

*Figure 3.9 Colour plot of salinity for transect* AB3

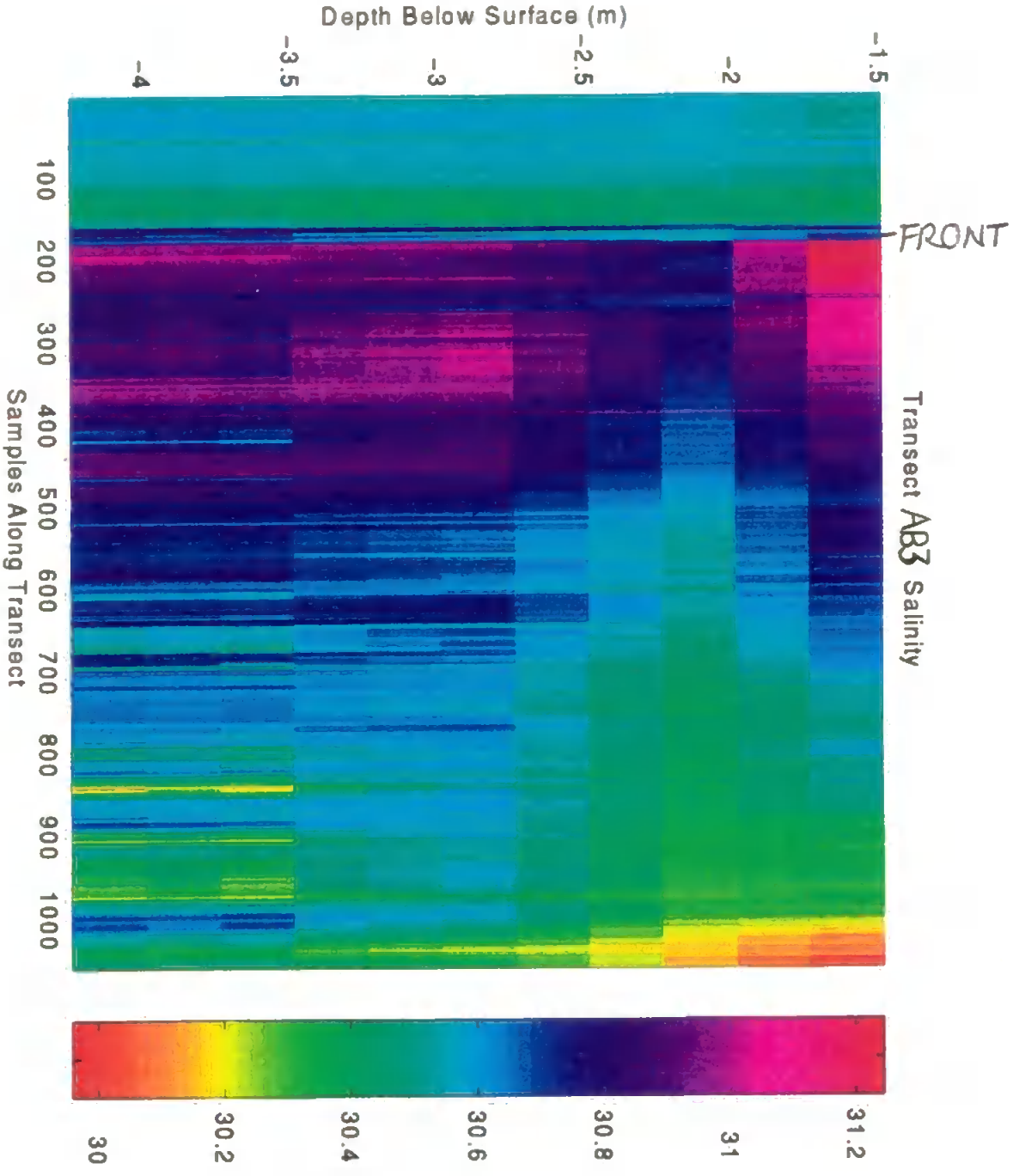

*Figure 3.10 Colour plot of salinity for transect* AB4

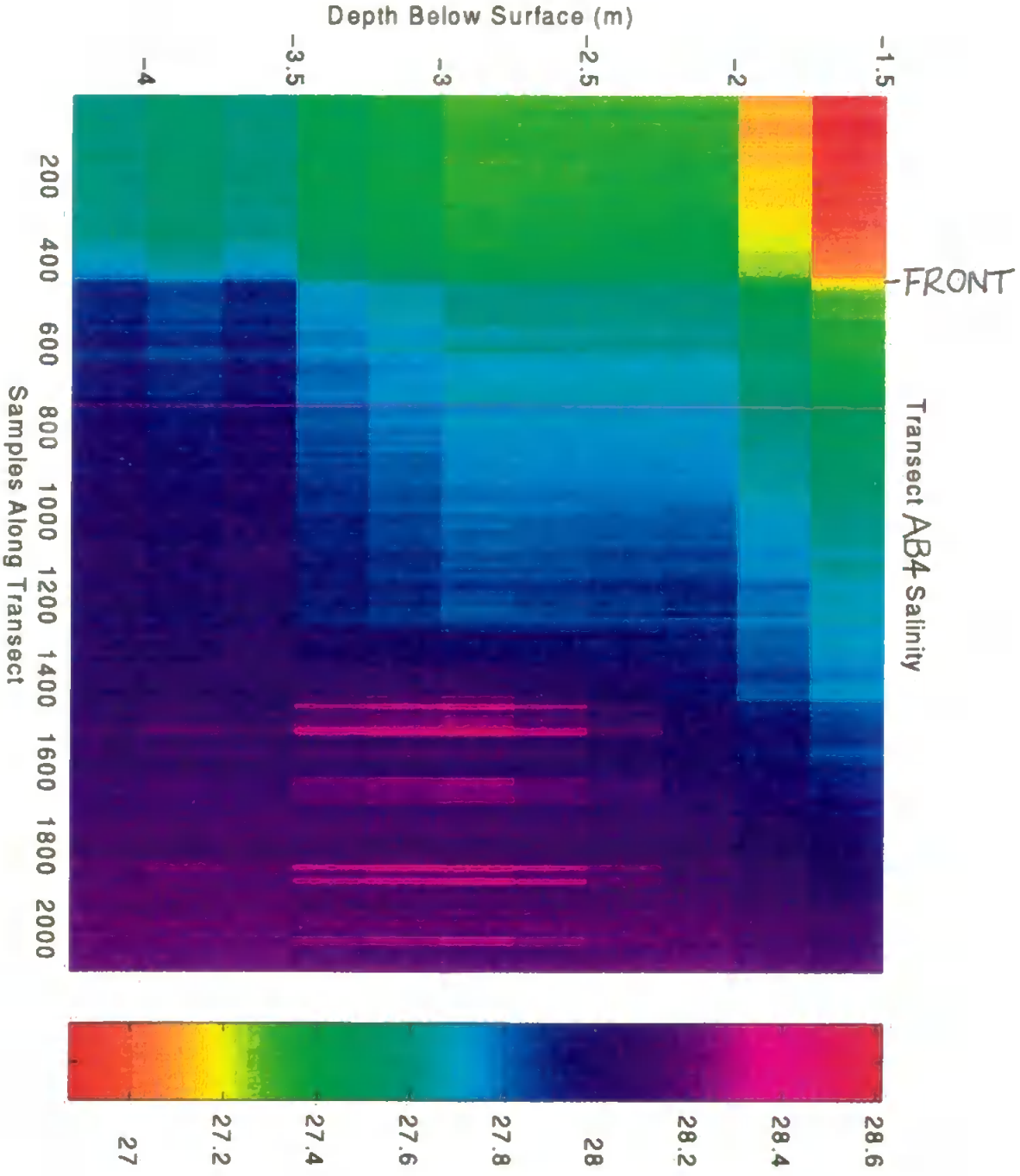

along side A to B of the survey grid, and figure 3.9 shows transect AB3, recorded on the 22.04.94 at 2 hours 19 minutes after high water. The front is located at 160 samples along the transect and again appears to be vertical, which is almost certainly not the case for reasons discussed above. The Tamar water is to the left of the frontal interface with a salinity of about 30.6 $^{o}/_{oo}$. Over the depth measured by the ETS, the Tamar water column appears relatively well-mixed whereas the Lynher water to the right of the frontal interface has a salinity range of 31 $^{o}/_{oo}$ grading to 30 $^{o}/_{oo}$ at distance from the front, and shows vertical structure. In transect AB4, shown in figure 3.10, the front is located at around 400 samples along track and both the Tamar water to the left and the Lynher water to the right seem to be stratified to some extent. The salinity range of the Tamar water is 27 $^{o}/_{oo}$ to 27.5 $^{o}/_{oo}$, whilst salinity in the Lynher ranges from 27.5 $^{o}/_{oo}$ to 28.5 $^{o}/_{oo}$. This transect was recorded on 25.04.94 at 4 hours 29 minutes after high water, thus it seems that a combination of a reduction in salinity at this later stage of the ebb tide, plus the effects of different tidal ranges and variations in fresh water run-off over the period from the 22 to the 25.04.94 is responsible for the changes in salinity structure between the two transects presented.

The ETS data from all three detailed surveys shows that Lynher water was warmer, slightly saltier and more stratified than Tamar water. The higher degree of stratification suggests that within the survey area, the Lynher water was more susceptible to the influence of freshwater input and its associated buoyancy effects, than the Tamar water.

### 3.3 ADCP RESULTS

In this section, MATLAB colour plots will be presented showing the east-west and north-south velocities for two transects which crossed the front. Transect AB3, surveyed on 22.04.94 at 2 hours 19 minutes after high water along side A to B of the survey grid is shown in figures 3.11a and b. On the east-west velocity plot (figure 3.11a), the frontal interface is believed to coincide with the boundary between westwards flowing water on the left and eastwards flowing water to the right. The westwards flowing water has a velocity of between 0 and 0.3 m $s^{-1}$ and is Tamar water. To the right of the interface is Lynher water flowing eastwards at between 0.1 and 0.6 m $s^{-1}$. The interface itself is inclined below the horizontal at an angle of approximately 6°

*Figure 3.11a Colour plot of east-west velocity (cm $s^{-1}$) for transect AB3 (east +, west -)*

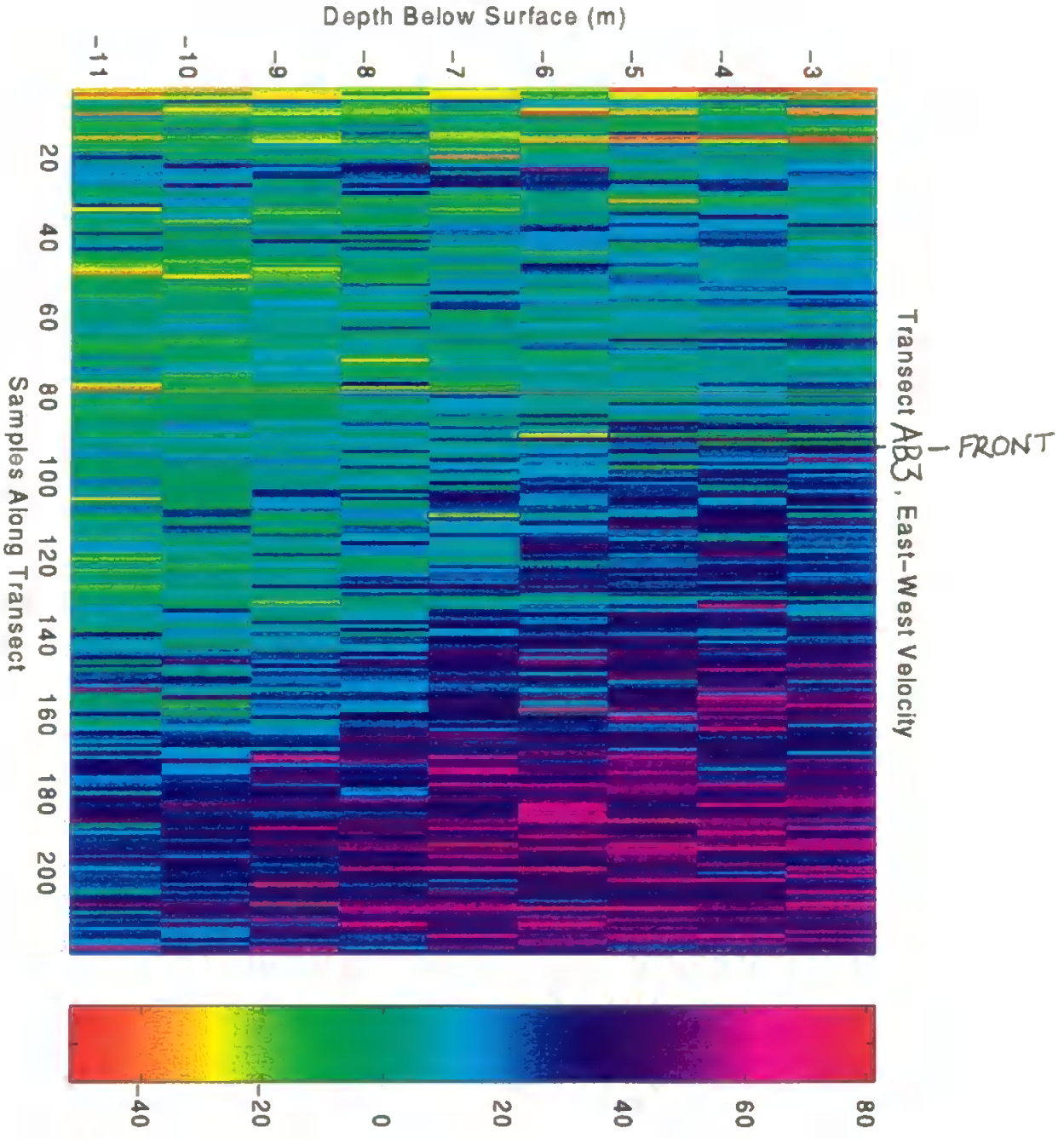

*Figure 3.11b Colour plot of north-south velocity ($cm\ s^{-1}$) for transect AB3 (north +, south -)*

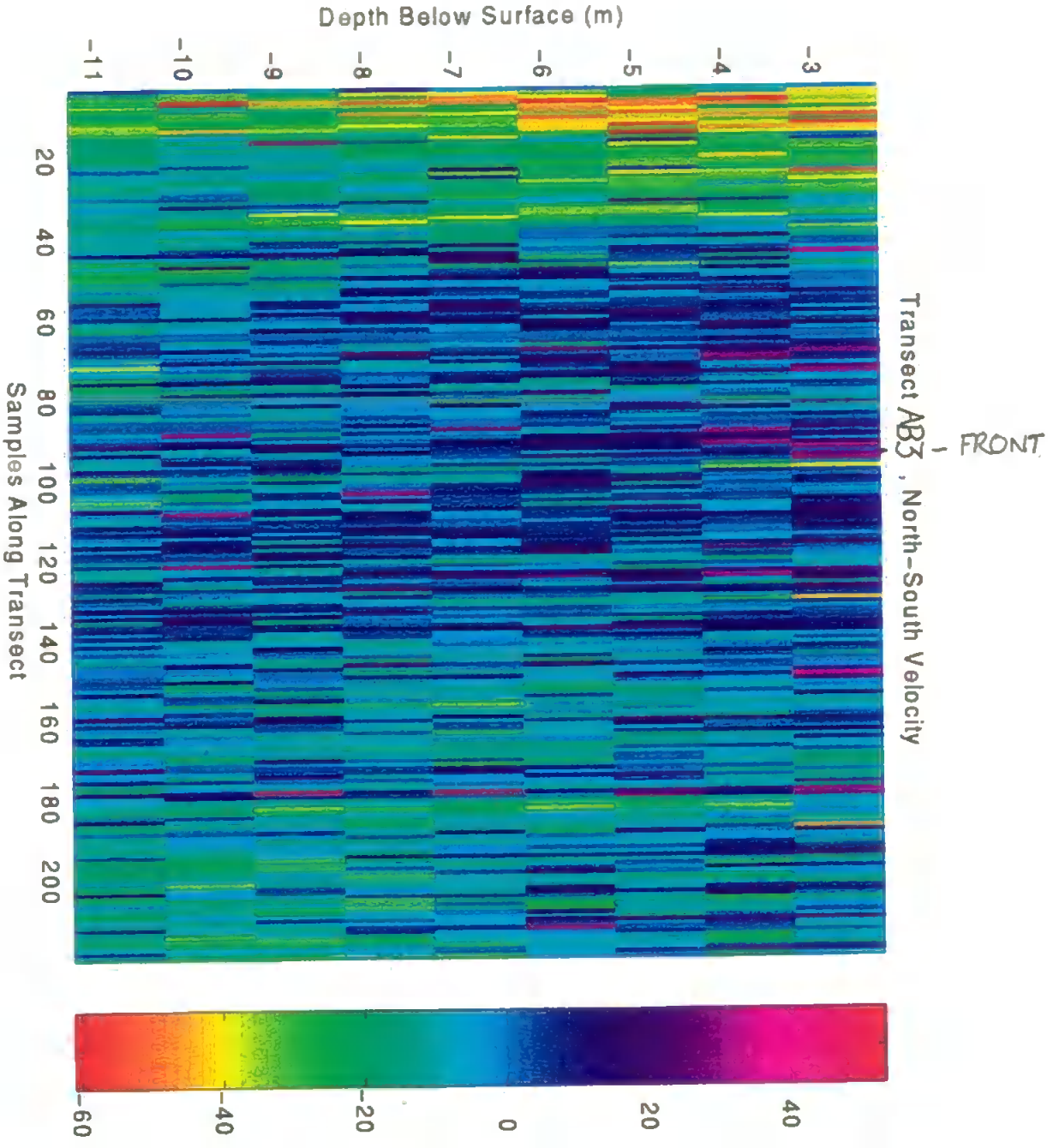

(bearing in mind the exaggeration in the vertical scale in the velocity plots) such that the interface is much closer to being horizontal than vertical. It should also be remembered that this is an apparent angle of inclination which depends on the angle at which the transect crossed the front. However, variations in the orientation of the transect with respect to the front will not alter the angle of inclination significantly.

The interface does not show up as well on the north-south velocity plot in figure 3.11b. There appears to be an indistinct boundary at about 50 samples along track, between an average flow of 0.2 m $s^{-1}$ southwards to the left of the interface, and a flow which varies from 0.2 m $s^{-1}$ southwards to 0.2 m $s^{-1}$ northwards, to the right. However, this boundary is not thought to represent the front because its surface position did not coincide with the foam line observed during surveying, whereas the boundary on the east-west velocity plot reached the surface at approximately the same position as the surface foam line.

Transect BA3 was surveyed on 25.04.94 at 4 hours 22 minutes after high water, along side B to A of the survey grid. Figure 3.12a shows the east-west velocity plot in which the frontal interface shows up clearly at about 75 samples along track. To the left of this boundary, Lynher water flows east at between 0.3 and 0.6 m s-1, and to the right Tamar water flows west at between 0 and 0.4 m s-1. It is interesting to note that in this transect, the frontal interface is approximately vertical, such that its orientation appears to change from being almost horizontal to almost vertical as the ebb tide progresses. Alternatively, the variation in orientation may also be linked to changes in general conditions within this part of the estuary in the three days between surveying transects AB3 and BA3.

The frontal interface does not show up at all in the north-south velocity plot for transect BA3, presented in figure 3.12b.

From this qualitative description of the results, it is apparent that the front can be clearly identified in the temperature, salinity and velocity data. In the next two chapters, the quantitative analysis applied to these results will be described, the outcome of which is discussed in chapter 6.

*Figure 3.12a Colour plot of east-west velocity ($cm\ s^{-1}$) for transect BA3 (east +, west -)*

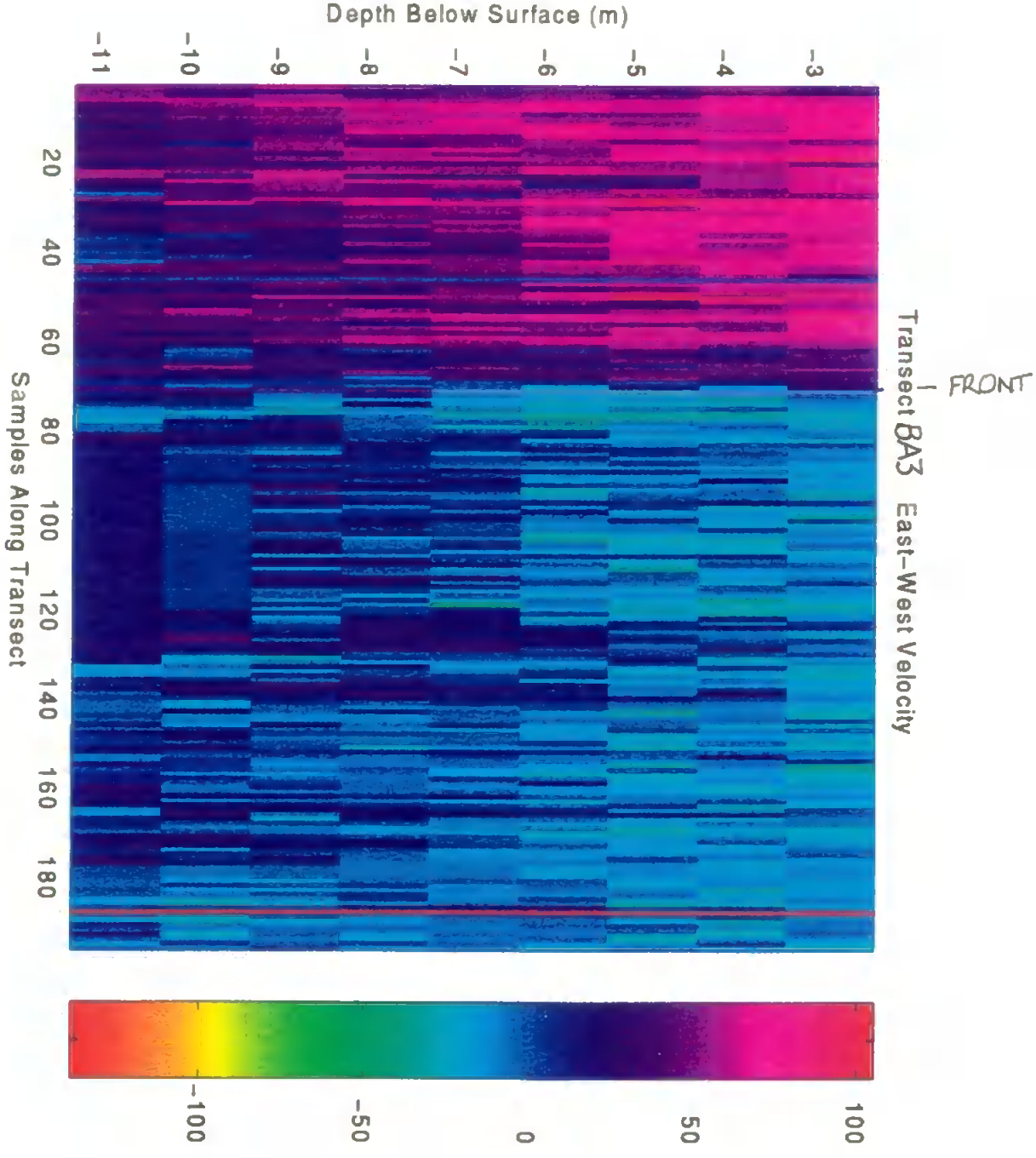

*Figure 3.12b Colour plot of north-south velocity ($cm\,s^{-1}$) for transect BA3 (north +, south -)*

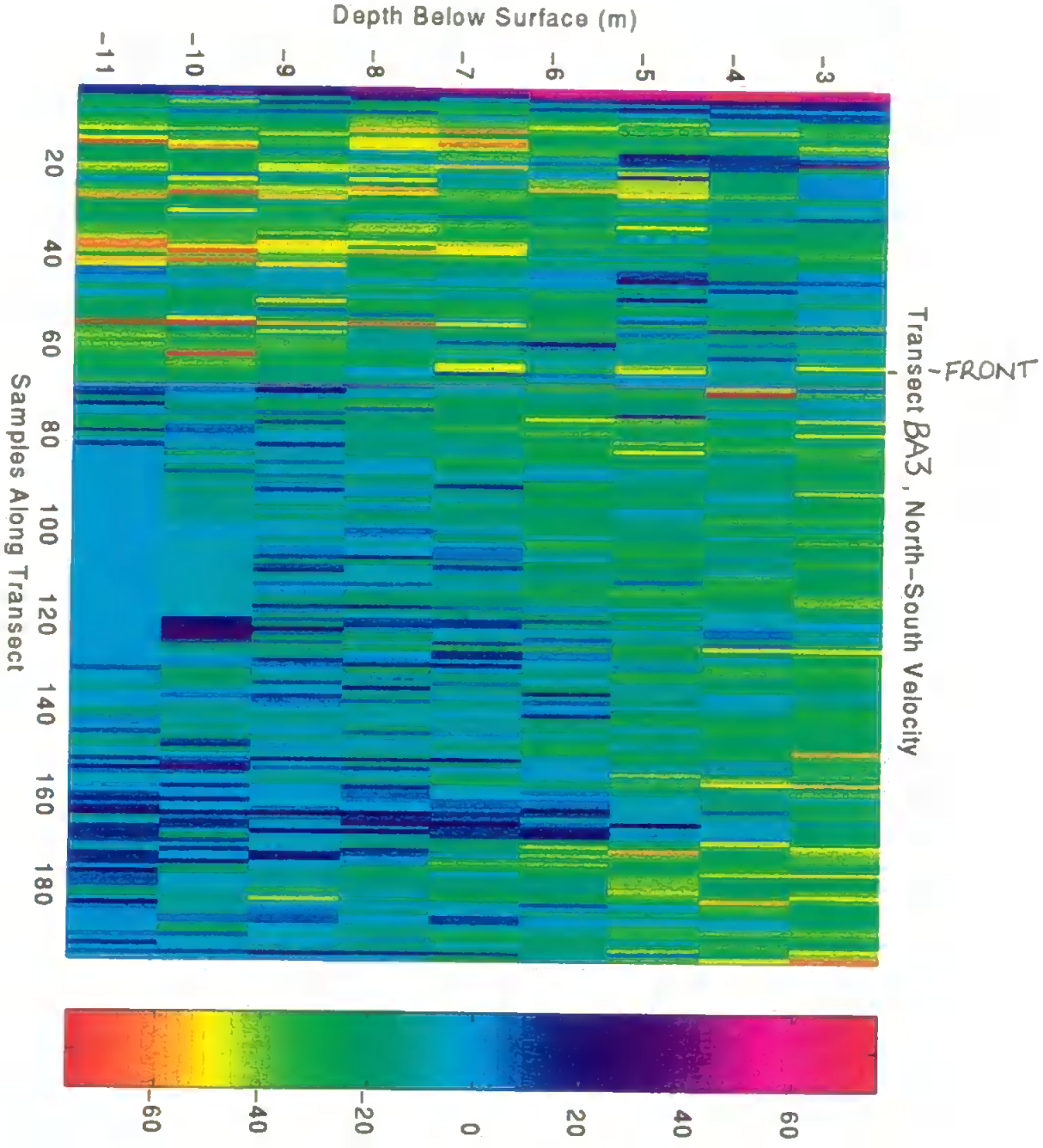

# CHAPTER 4

# THE APPLICATION OF THE EQUATION OF CONTINUITY

The ADCP and ETS results from the three days of surveying have been examined and interpreted qualitatively in the preceding chapter. In this chapter, a quantitative analysis and interpretation of the results will be undertaken by applying the equation of continuity. The objectives of using this equation are to provide estimates of average vertical velocity over the survey area and the cross-frontal transport of water at different stages of the ebb tide.

## 4.1. DERIVATION OF THE EQUATION OF VOLUME CONTINUITY

The equation of continuity can be applied to various water properties such as volume, mass and salinity, providing that each of them can be considered a conservative property, otherwise source and sink terms have to be defined. In order to estimate average vertical velocities over the survey area, the equation of continuity of volume was used which is derived following Pond and Pickard, 1983.

***Figure 4.1 Volume element with velocity and density***

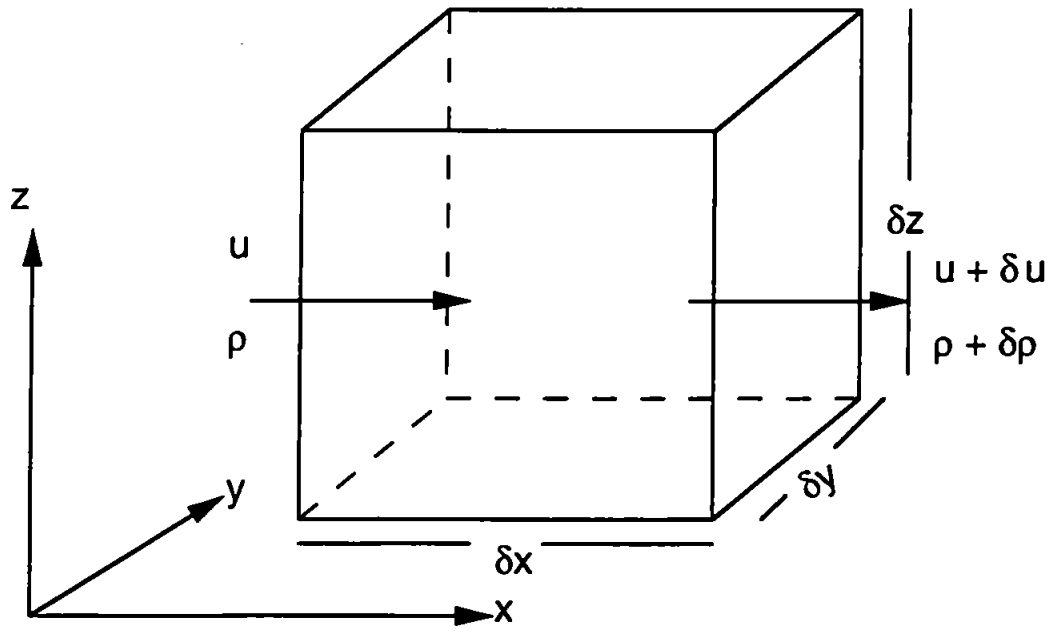

Referring to figure 4.1, at the left face of the rectangular volume depicted (with sides of lengths $\delta x$, $\delta y$ and $\delta z$), the velocity is u and the density is $\rho$. At the right face, the velocity and density are $u+\delta u$ and $\rho+\delta\rho$ respectively. These terms can be expressed as $u+(\partial u/\partial x)\delta x$ and $\rho+(\partial\rho/\partial x)\delta x$ via a Taylor expansion neglecting terms in $(\delta x)^2$ and higher, which vanish as $\delta x$ tends to zero. The mass flow into the volume is then:

$$\rho\, u\, \delta y\, \delta z \tag{4.1}$$

and the mass flow out of the volume is;

$$\left(\rho+\frac{\partial\rho}{\partial x}\delta x\right)\left(u+\frac{\partial u}{\partial x}\delta x\right)\delta y.\delta z \tag{4.2}$$

The net flow out of the volume in the x-direction is then equal to the difference between equations 4.2 and 4.1. When the brackets are multiplied out in equation 4.2 and terms are combined using the product derivative rule, we can write that the net flow out of the volume in the x-direction is;

$$\left[\frac{\partial(\rho u)}{\partial x}+0(\delta x)\right]\delta x\delta y\delta z$$

where $0(\delta x)$ indicates that this term is of the order $\delta x$ times some finite number and if $\delta x$ is sufficiently small, the term can be neglected. So the total flow out of the volume in all three component directions (neglecting terms which vanish as $\delta x$, $\delta y$ or $\delta z$ tend to zero) is now;

$$\left[\frac{\partial(\rho u)}{\partial x}+\frac{\partial(\rho v)}{\partial y}+\frac{\partial(\rho w)}{\partial z}\right]\delta x\delta y\delta z \tag{4.3}$$

where v and w are velocity components in the y and z-directions respectively. Within the volume $\delta x\ \delta y\ \delta z$, the mass which has not flowed out of the volume element changes by $(\partial\rho/\partial t)\ \delta x\ \delta y\ \delta z$ per unit time, and the sum of this term plus those in equation 4.3 must be zero if mass is conserved. Hence;

$$\frac{\partial\rho}{\partial t}+\frac{\partial(\rho u)}{\partial x}+\frac{\partial(\rho v)}{\partial y}+\frac{\partial(\rho w)}{\partial z}=0 \tag{4.4}$$

The total rate of change of density with the moving fluid will incorporate both the time and spatial derivatives such that;

$$\frac{d\rho}{dt}=\frac{\partial\rho}{\partial t}+u\frac{\partial\rho}{\partial x}+v\frac{\partial\rho}{\partial y}+w\frac{\partial\rho}{\partial z} \tag{4.5}$$

Equations 4.4 and 4.5 combine to give;

$$\frac{1}{\rho}\frac{d\rho}{dt}+\left[\frac{\partial u}{\partial x}+\frac{\partial v}{\partial y}+\frac{\partial w}{\partial z}\right]=0$$

which is the equation of continuity of volume.

If the fluid is considered to be incompressible, which is a valid assumption in the water depths (of no more than 11 metres) over our survey area, then $(1/\rho)(d\rho/dt) = 0$ and the equation of continuity becomes;

$$\frac{\partial u}{\partial x}+\frac{\partial v}{\partial y}+\frac{\partial w}{\partial z}=0$$

This equation is derived by considering the rate of change of mass in a fixed volume. If, however, the volume of the element itself is considered to be changing with time, then the rate of change of that volume can be written as;

$$\frac{\partial(\delta V)}{\partial t}=\delta V\left(\frac{\partial u}{\partial x}+\frac{\partial v}{\partial y}+\frac{\partial w}{\partial z}\right) \qquad (4.6)$$

where $\delta V=\delta x\ \delta y\ \delta z$.

It is this form of the equation of continuity of volume which is applied to our data set in the following section.

## 4.2. APPLICATION OF THE EQUATION OF VOLUME CONTINUITY

The equation of volume continuity is initially applied to the Tamar-Lynher data set to calculate values for the average vertical velocity over the survey area. The figure-of-8 shaped survey grid followed during the three days of surveying (described previously in section 3.2.) is treated as two adjacent boxes with sides of 300 metres length in order to apply the equation of continuity of volume. During the fieldwork, the northernmost box was surveyed seven times and the southernmost box was surveyed three times, at different stages of the tide. The ADCP transects along the sides of each box extend to a depth of 11.3 metres depending on the stage of the tide and the river bed topography over which the transect was recorded. Each of the survey boxes can therefore be considered as a stack of 1 metre thick depth slices, as the schematic in figure 4.2 demonstrates;

*Figure 4.2 Schematic of depth slices in survey grid*

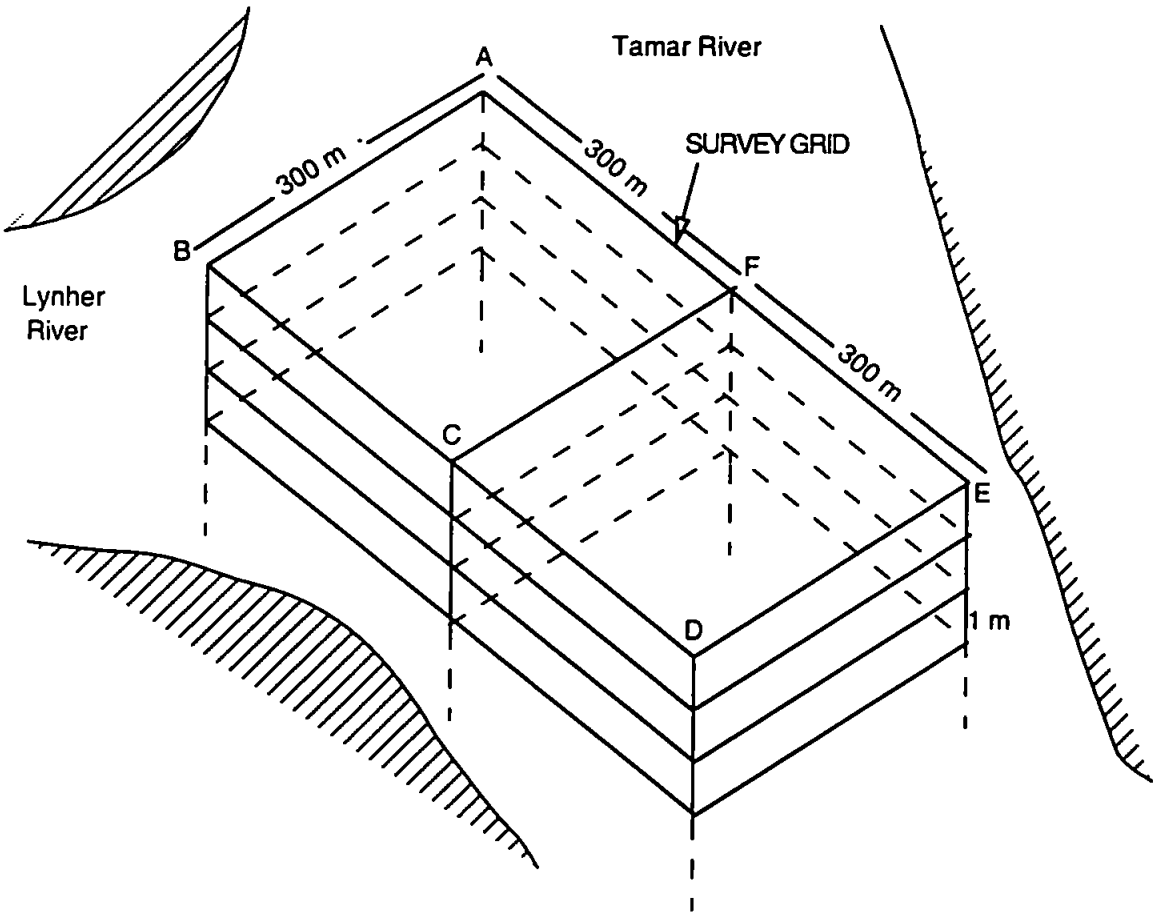


The thickness of 1 metre for each depth slice has been used because the ADCP automatically averages the east-west and north-south velocities from each transect into 1 metre depth bins. The shallowest depth bin is centred at a depth of either 2.2 metres on the 20.04.94 survey or 2.3 metres on the other two surveys. The discrepancy arises from the ADCP transducer head being positioned at slightly different depths during the three surveys. The ADCP cannot measure velocities at depths shallower than 2.2 metres because there is a time delay between the end of the transmitted pulse and the earliest backscattered signal that can be recorded. However, to apply volume continuity, the stack of depth slices which comprise each survey box must extend up to the water surface, so an additional depth slice of thickness 1.7 metres on the 20.04.94 survey, or 1.8 metres for the two consecutive surveys has been included. The velocities for this top

slice are assumed to be the same as those recorded by the ADCP for the underlying depth slice.

If we now consider each slice, the total volume of water flowing into or out of the slice is equal to the sum of the volume flowing horizontally into or out of the slice through each of its four sides, plus the volumes of water flowing into or out of the slice vertically through its base and top areas. In the case of the top slice, the top surface area is coincident with the water surface, so there can be no vertical flow through this area. This is an intuitive expression of the equation of volume continuity (equation 4.6) with the simplifying assumption that each of the flow components through the sides of each slice has been measured synoptically, so the overall flow is essentially non-accelerating. In other words, what flows into the slice must flow out, as long as the water is incompressible.

Assuming, momentarily, that there is no change of volume of the depth slice with time, equation 4.6 becomes;

$$\delta V\left(\frac{\partial u}{\partial x}+\frac{\partial v}{\partial y}+\frac{\partial w}{\partial z}\right)=0 \qquad (4.7)$$

A depth slice is shown in relation to a set of x, y, z axes in figure 4.3.

***Figure 4.3 Depth slice with respect to x y z axes***

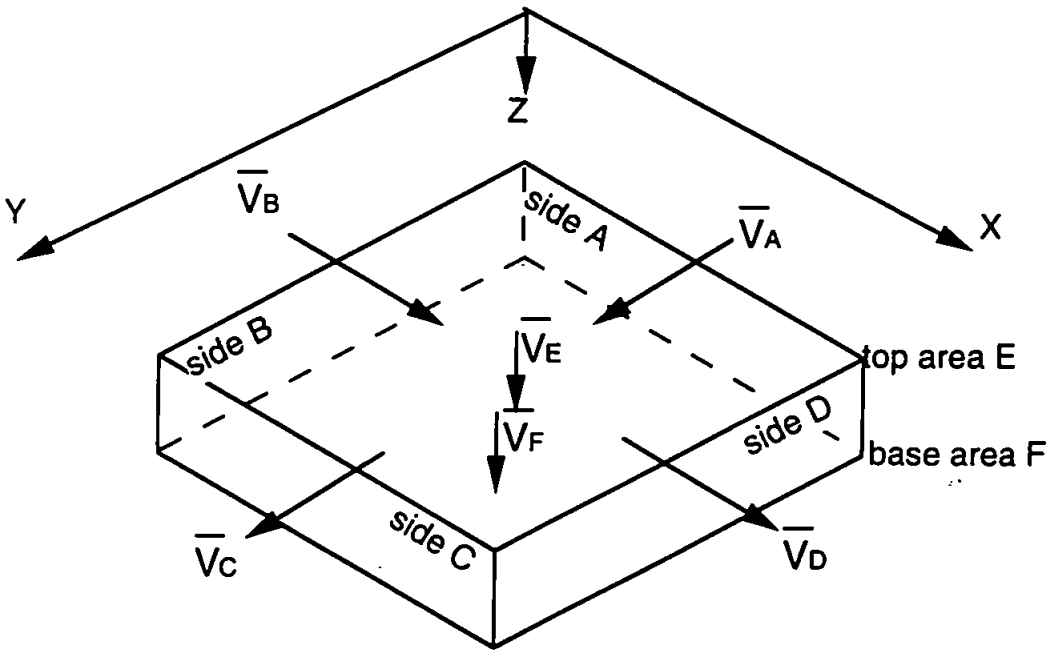

$\delta V = \delta x\ \delta y\ \delta z$ in equation 4.7 so for each of the depth slices apart from the top slice, $\delta V = 300m \times 300m \times 1m = 90000\ m^3$. Equation 4.7 becomes;

$$90000m^3 \times \left[ \frac{\left(\overline{V}_B - \overline{V}_D\right)}{300m} + \frac{\left(\overline{V}_A - \overline{V}_C\right)}{300m} + \frac{\left(\overline{V}_E - \overline{V}_F\right)}{1m} \right] = 0 \qquad (4.8)$$

In the case of the top slice, $\overline{V}_E$ will be zero, and the thickness of the slice (1 m in equation 4.8) is either 1.7 m or 1.8 m depending on the survey day.

In order to find $\overline{V}_A$, $\overline{V}_B$, $\overline{V}_C$ and $\overline{V}_D$ in figure 4.3, the component of velocity normal to the relevant side of the depth slice, and therefore the transect which was recorded along that side of the survey box, must be calculated. For each transect, the matrices of east-west and north-south velocities measured by the ADCP are combined into a matrix of resultant velocity vectors. Each resultant vector is then resolved onto a new set of perpendicular axes, one of which is parallel to the transect whilst the other is normal to the transect. The approximate heading of each transect is determined from plotting GPS position fixes taken during surveying to estimate the average transect orientation by eye. This produces two new matrices of velocity components, the "transect-normal" and the "transect-parallel" components which are averaged to find the mean velocity in each of these directions. Where a transect crosses the Tamar-Lynher front, the ADCP ensemble number at which the front was crossed is noted and mean velocities before and after the front are calculated. These mean velocities are then recombined to give overall mean transect-normal and transect-parallel velocities for the transect, using weighted averaging based on the ADCP ensemble number at which the front was crossed, f, and the total number of ensembles in the transect, t, i.e.;

[(pre-front mean velocity × f) + (post-front mean velocity × (t-f))] ÷ t =

Average mean velocity for whole transect

Until now, the term expressing the change in volume of the depth slice with time, i.e. $d(\delta V)/dt$ in equation 4.6 has been assumed to be zero in our analysis. This term can be thought of as the volume of water, $\delta V$, flowing into or out of each depth slice of each survey box due to the accelerating or decelerating ebb-tidal flow. Had each transect comprising the four sides of a survey box been conducted simultaneously, or had the mean tidal current been non-accelerating, there would be no need to estimate a value for

this term as it would be zero. However, in reality it took between 28 and 53 minutes to complete each survey box, during which time the mean tidal velocity had either accelerated or decelerated depending on the stage of the ebb tide. This change in mean tidal velocity, and the associated increase or decrease in the volume of the water flowing into the depth slice over the time taken to survey each box, must be accounted for in our analysis to avoid over or under-estimating the average vertical velocities. Hence, an estimate of the change in the mean tidal velocity over the time taken to complete the surveying, on each of the three days, is required. To find this value ($\partial\overline{V}_T/\partial t$ where $\overline{V}_T$ is the mean tidal velocity), the matrix of resultant velocities for each transect (produced by combining the east-west and north-south velocities) are averaged over the entire length and depth of the transect. The average direction of these resultant velocity vectors is 134°, which agrees closely with the qualitative observation made from ADCP data that the dominant flow direction over the survey area is south-east, as would be expected on the ebb tide in this part of the estuary. The magnitudes of the resultant velocity vectors are then plotted against the time after high water at which each vector was recorded, for each of the three survey days (see figure 1a, b and c, appendix). Resultant vectors from transects which crossed the front are omitted from this part of the analysis, to avoid the complicating influence of the convergent front in the estimation of tidal acceleration. Each of the three graphs in figure 1 (appendix) has a linear trend-line fitted, the equation of which gives an approximation of the change in $\overline{V}_T$ with time. Considering one survey box, then $t_1$ is the time after high water at which the survey started and $t_2$ is the time after high water the survey stopped. As already mentioned, $t_2$-$t_1$ can be as much as 53 minutes. So, $\overline{V}_T$ at $t_2$ minus $\overline{V}_T$ at $t_1$ represents an increase or decrease in velocity due to the tidal acceleration. This change in velocity multiplied by the area of the side of a depth slice is interpreted as the excess or deficit in the volume of the water in the depth slice due to the horizontal tidal acceleration or deceleration. By subtracting this volume from the total volume flowing horizontally into or out of each depth slice through the four sides, we are allowing for the time taken to complete the survey box and are essentially saying that all four transects were recorded simultaneously. The average vertical velocities are then assumed to be representative of those which would have been found if all four sides had been surveyed at the start-time of each survey box. In other words, the Eulerian component of the change in

volume, $\partial(\delta V)/\partial t$, has been removed from equation 4.7, so we are considering the advective components only.

The calculated average vertical velocities through the base area of each depth slice are plotted as depth profiles for each survey box, in figures 2a to 2j, appendix.

## 4.3. DERIVATION OF EQUATION OF SALT CONTINUITY

Mixing processes can be quantified by considering the budget of salt within an estuary. If salt is considered to be a conservative property, it can be treated with a continuity equation similar to that described in section 4.1. The continuity equation states that the mass of salt carried into a particular volume equals the mass of salt carried out and the change of salinity within the volume (Dyer, 1973). Following Dyer (1973), a small volume of estuary with sides of length $\delta x$, $\delta y$ and $\delta z$ is considered in figure 4.4.

***Figure 4.4 Volume element with velocity and salinity***

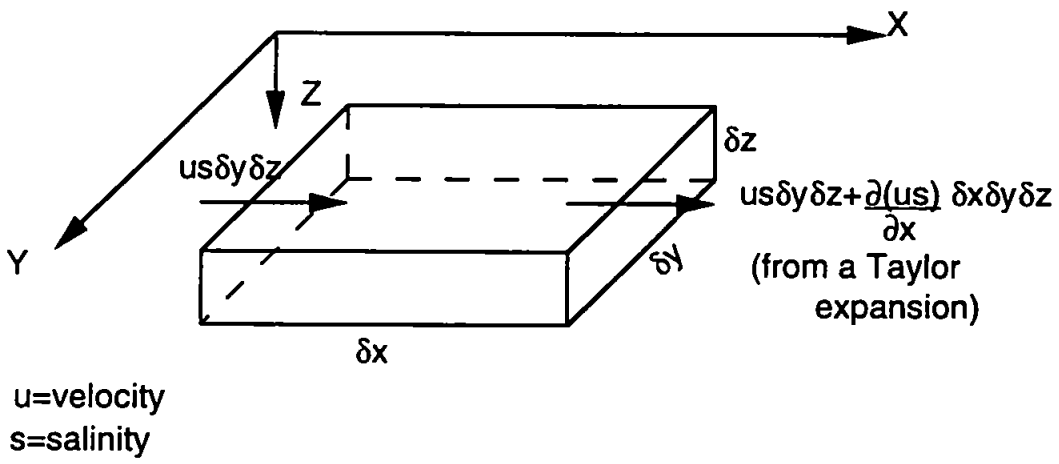


The advective flows of salt through sides 1 and 2 are shown in figure 4.4, and the net inflow of salt in the x-direction in a given time, $\delta t$ is;

$$-\frac{\partial(us)}{\partial x}\delta x.\delta y.\delta z.\delta t$$

Similarly, in the y and z directions, the inflow of salt is;

$$-\frac{\partial(vs)}{\partial y}\delta y.\delta z.\delta x.\delta t \text{ and } -\frac{\partial(ws)}{\partial z}\delta z.\delta x.\delta y.\delta t \text{ respectively.}$$

The molecular diffusion of salt through side 1 is; $-\varepsilon\frac{\partial s}{\partial x}\delta y.\delta z.\delta t$ and through side 2 is;

$$-\varepsilon\frac{\partial s}{\partial x}\delta y.\delta z.\delta t - \frac{\partial}{\partial x}\left(\varepsilon\frac{\partial s}{\partial x}\right)\delta x.\delta y.\delta z.\delta t$$

where $\varepsilon$ is the coefficient of molecular diffusion. The net diffusion in the x-direction is therefore;

$$+\varepsilon\frac{\partial^2 s}{\partial x^2}\delta x.\delta y.\delta z.\delta t$$

And in the y and z-directions is

$$+\varepsilon\frac{\partial^2 s}{\partial y^2}\delta y.\delta z.\delta x.\delta t \text{ and } +\varepsilon\frac{\partial^2 s}{\partial z^2}\delta z.\delta x.\delta y.\delta t \text{ respectively.}$$

Using a Taylor expansion again, the net increase in the amount of salt present in the volume over time $\delta t$ is;

$$\frac{\partial s}{\partial t}\delta x.\delta y.\delta z.\delta t$$

The increase or decrease in the amount of salt in the volume is equal to the amount of salt advected into or out of the volume and the amount of salt diffused into or out of the volume i.e.

$$\frac{\partial s}{\partial t} = -\frac{\partial(us)}{\partial x} - \frac{\partial(vs)}{\partial y} - \frac{\partial(ws)}{\partial z} + \varepsilon\left(\frac{\partial^2 s}{\partial x^2} + \frac{\partial^2 s}{\partial y^2} + \frac{\partial^2 s}{\partial z^2}\right) \qquad (4.9)$$

This is the equation of salt for instantaneous values of salinity and velocity. These instantaneous salinities and velocities can be separated into a tidal mean, a fluctuating tidal component and a short period turbulent fluctuation, such that;

$S = \bar{s} + s + s'$, $U = \bar{u} + u + u'$, $V = \bar{v} + v + v'$, $W = \bar{w} + w + w'$

where the overbar denotes the tidal mean, and a prime denotes the turbulent fluctuation (the remaining component being the fluctuating tidal component). During the Tamar-Lynher surveys, the duration of each transect was too short to allow the tidal mean component of the observed salinities and velocities to be determined. Therefore the salinity and velocity data are separated into two components;

$S = \bar{s} + s'$, $U = \bar{u} + u'$, $V = \bar{v} + v'$, $W = \bar{w} + w'$

where, this time, the overbar denotes a combination of the tidal mean and fluctuating tidal components and the prime still denotes the turbulent fluctuation. Multiplying out the first term on the right hand side of equation 4.9 gives the following;

$$-\frac{\partial}{\partial x}\left(\bar{u}.\bar{s}+\bar{s}.u'+\bar{u}.s'+u'.s'\right)$$

Using the Reynold's averaging criteria, in which it is assumed to be unlikely that the salinity fluctuations are correlated with the mean velocity, or that the velocity fluctuations are correlated with the mean salinity, the $\bar{s}.u'$ and $\bar{u}.s'$ terms are neglected, as they will be zero. Considering the left hand side of equation 4.9, it becomes

$$\frac{\partial \bar{s}}{\partial t}+\frac{\partial s'}{\partial t}$$

The average of the salinity fluctuations, $\partial s'/\partial t$ will be zero so equation 4.9 becomes

$$\frac{\partial \bar{s}}{\partial t}=-\frac{\partial\left(\bar{u}.\bar{s}\right)}{\partial x}-\frac{\partial\left(\bar{v}.\bar{s}\right)}{\partial y}-\frac{\partial\left(\bar{w}.\bar{s}\right)}{\partial z}-\frac{\partial\left(\overline{u'.s'}\right)}{\partial x}-\frac{\partial\left(\overline{v'.s'}\right)}{\partial y}-\frac{\partial\left(\overline{w'.s'}\right)}{\partial z} \qquad (4.10)$$

given that $-\left(\overline{u'.s'}\right)=\varepsilon\,\partial s/\partial x$ and likewise for v and w.

An adaptation of equation 4.10 will be used in the following analysis.

## 4.4. APPLICATION OF THE EQUATION OF SALT CONTINUITY

The equation of salt continuity is applied to the salinity and velocity data from the Tamar-Lynher surveys in a similar way to the equation of volume continuity. The figure-of-8 survey grid is again treated as two adjacent boxes, each of which is divided into depth slices of 1 metre thickness (except for the top slice) as shown in figure 4.2. The east-west and north-south velocity matrices are combined into resultant velocity vectors and resolved onto new axes orientated parallel and normal to the transect direction. The salinity data for each transect is also in the form of a matrix of values, with each salinity in its spatially correct position along-transect and with depth. However the salinity data was collected at a higher sampling frequency than the velocity data, both along-transect and with depth. In order to calculate the values of $\left(\overline{u'.s'}\right),\left(\overline{v'.s'}\right)$ and $\left(\overline{w'.s'}\right)$ in equation 4.10, the salinity data needs to be re-sampled into a new matrix which has the same spatial along-transect and depth resolution as the velocity matrices. This ensures that the velocity and salinity fluctuations are effectively

measured at the same point in space and time, and allows the diffusive flux terms to be calculated.

Initially, the velocity and salinity matrices were edited so that they represent the same cross-sectional area of the estuary. The ETS only measures down to depths of 3.75 metres on the 20.04.94 survey, or 4.75 metres on the two consecutive surveys, because of different equipment deployment configurations on the two survey vessels used. Therefore, only the uppermost 2 or 3 depth bins of velocity from each ADCP transect are required in this analysis. Likewise, because the ADCP cannot record velocities from the shallowest 2 metres of the water column, only the lowermost 5 or 9 channels of salinity data are used, depending on the survey day. Having reduced both the salinity and velocity matrices so that they are spatially coincident, the higher frequency salinity data must be re-sampled. In the along-transect direction, the number of salinity samples is divided by the number of velocity samples in the transect, which gives the number of salinity samples which must be averaged together to give one new value in the re-sampled matrix. The same procedure is applied over the depth so that either five or nine channels of salinity are averaged into two or three depth bins which match those in the velocity matrix (see figure 4.5).

***Figure 4.5 Diagram of re-sampling strategy***

| Original salinity matrix | Velocity matrix | Re-sampled salinity matrix | Original salinity matrix | Velocity matrix | Re-sampled salinity matrix |
|---|---|---|---|---|---|
| $S_1$<br>$S_2$ | $V_1$ | $[S_1+S_2+(S_3/2)]/2.5$ | $S_1$<br>$S_2$<br>$S_3$ | $V_1$ | $[S_1+S_2+S_3]/3$ |
| $S_3$<br>$S_4$<br>$S_5$ | $V_2$ | $[(S_3/2)+S_4+S_5]/2.5$ | $S_4$<br>$S_5$<br>$S_6$ | $V_2$ | $[S_4+S_5+S_6]/3$ |
| 20.04.94 SURVEY | | | $S_7$<br>$S_8$<br>$S_9$ | $V_3$ | $[S_7+S_8+S_9]/3$ |
| | | | 22.04.94 AND 25.04.94 SURVEYS | | |

The differing numbers of salinity channels and velocity depth bins on the different surveys arises because of the deployment configuration of the equipment on the two survey boats used.

Having manipulated the data in this way, we can now apply an adaptation of the equation of salt continuity to the two adjacent survey boxes described earlier. Unlike volume continuity, salt continuity can only be applied to a survey box comprising a

stack of either 2 or 3 depth slices depending on the survey day, owing to the limited salinity data set.

The total salt flux through each side of each depth slice is calculated by finding the sum of the advective and diffusive salt flux terms in equation 4.10. The advective component is found by multiplying the average transect-normal velocity with the average salinity for each side of the depth slice. Where a transect crosses the front, pre- and post-front average salinities and velocities are calculated and combined into one value by weighted averaging. The average velocity and salinity values are subtracted from the matrices of observed transect-normal velocity and salinity respectively, to leave two matrices containing the turbulent fluctuations of these two quantities. Again, in the case of a transect which crosses the front, the pre-front salinity or velocity average is subtracted from all pre-front salinities or velocities respectively, and likewise for post-front values. The two matrices are then multiplied together and averaged to give the diffusive salt flux term for that side of the depth slice. As with volume continuity, salt fluxes directed into the slice are assigned a positive value and those directed out of the slice are negative. The total (advective plus diffusive) salt flux terms of all four sides are added together and multiplied by the area of the side of the depth slice to give a value for the volume flux of salt, in a similar manner to the method used for volume continuity. An additional, slightly thicker depth slice is placed on top of the existing slices so that its top surface area is coincident with the water surface. Salinities and velocities for the top slice are assumed to be the same as those measured for the underlying slice. Hence, we know the total volume flux of salt which must be flowing through the base of each slice and dividing this value by the base area gives a vertical flux term in units of $^{o}/_{oo}$ m $s^{-1}$, which can be calculated at various depths for each survey box in the same way that average vertical velocities are derived. For the same reasons described in section 4.2, the change in the volume flux of salt due to the change in the mean tidal velocity and salinity over the time taken to survey the box must be accounted for in order to find vertical flux estimates which are effectively at a fixed point in time. The average resultant velocity vector multiplied by the average salinity for each transect is plotted against time after high water (see figure 3a, b and c, appendix). A linear trend-line is fitted to each graph (one for every survey day) and the change in $\overline{V}_T.\overline{S}$, where $\overline{V}_T$ is the mean tidal velocity and $\overline{S}$ is the average salinity, is calculated for each

survey box. The change in $\overline{V}_T.\overline{S}$ is multiplied by the area of the side of a depth slice and subtracted from the total volume flux of salt horizontally into the slice.

This approach is the same as applying a version of equation 4.10 in which all the terms have been multiplied by the volume of the depth slice. A value for $\partial\bar{s}/\partial t$ in equation cannot be calculated because we have to assume that the box is surveyed instantaneously and that this term is therefore zero. in order to solve the equation for the vertical flux term. The vertical flux terms for each box are presented as depth profiles in figures 4a to 4j, appendix.

## 4.5. CROSS-FRONTAL TRANSPORT

The cross-frontal transport of water can be estimated using modified versions of the equation of volume continuity. Of the ten survey boxes completed in the three days of fieldwork, one front is present in three of the boxes and two fronts are present in one of the boxes, as illustrated in figure 4.6.

***Figure 4.6 Plan view of survey boxes containing front***

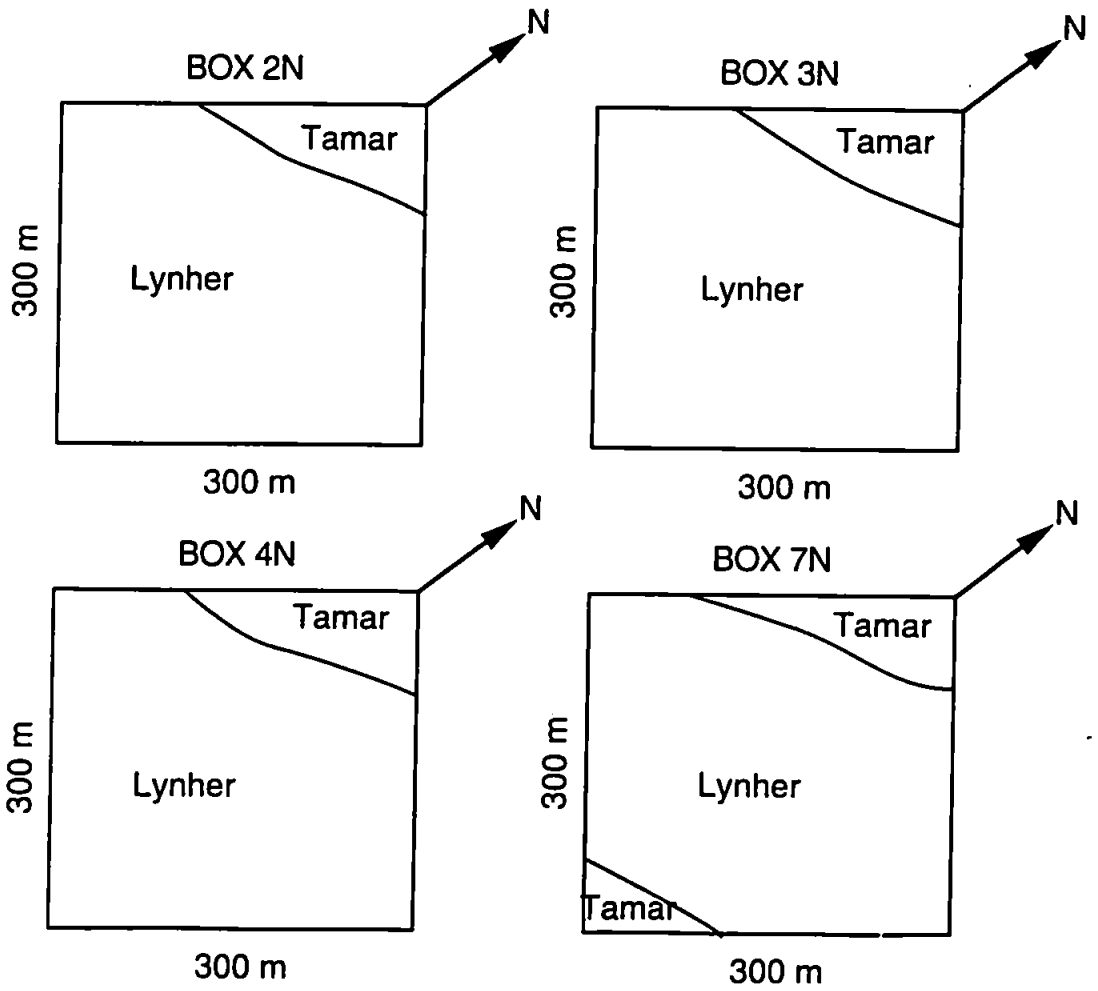

All four boxes represent the northern half of the survey grid. The box numbers are henceforth post-fixed with either 'N' to denote the northern half of the grid, or 'S' to denote the southern half.

The two fronts present in box 7N are actually part of the same front, which has curved back on itself at this stage in the tide and is becoming a plume. The identification of Lynher or Tamar water on either side of the front is made from a qualitative examination of temperature and velocity data, as described previously in chapter 3.

Each survey box illustrated is the northernmost half of the figure-of-eight survey grid. Whilst the surface expression, defined by a line of foam and debris was not observed to be exactly linear during surveying, the fronts are assumed to be linear within each box for the purpose of this analysis. Each box is again considered to be comprised of a stack of 1 metre thick depth slices, with the exception of the slightly thicker top slice, as shown in figure 4.2. The presence of the front, in the case of boxes 2N, 3N and 4N, is then considered to divide the top slice into two separate volumes, volume A and volume B (see figure 4.7). The volume of water flowing horizontally into each of the two new volumes is calculated, using the pre-front or post-front average velocities where appropriate. The vertical velocities recorded along the transects, or portions of transects, which define the sides of each of the two volumes are averaged to give an estimate of the vertical velocity on either side of the front. These average vertical velocities are then multiplied by the relevant fraction of the total base area of the depth slice, and the resultant volume fluxes are included in the summation, for each of the two new volumes. The change in volume due to the tidal acceleration or deceleration is also accounted for in each new volume. Theoretically, it should then be the case that if there is no flow across the front, the total volume of water flowing into and out of volume A is zero, as is the total volume flowing into and out of volume B. Similarly, the analysis is set up so that if there is a flow across the frontal interface, then the excess water volume in volume A equals the deficit water volume in volume B, and vice versa, thus satisfying continuity. A mathematical expression of this analysis, which is applied to the underlying depth slices as well as the top slice, follows figure 4.7.

*Figure 4.7 Depth slice with front for boxes 2N, 3N and 4N*

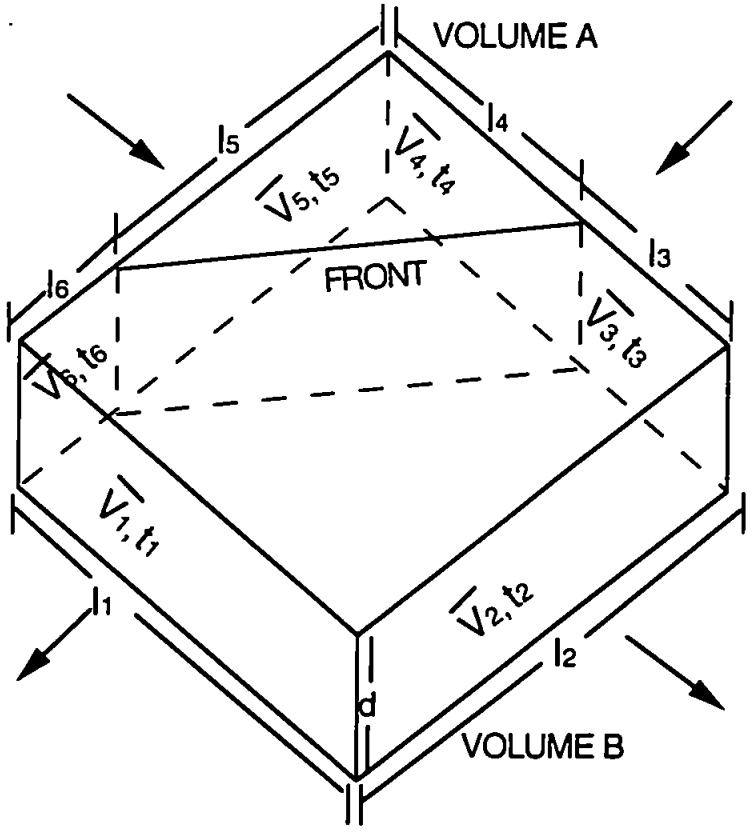


$\overline{V}_1$ to $\overline{V}_6$ = Average transect-normal velocity through transect/portion of transect (m $s^{-1}$). Velocities directed into the slice are positive, those out of the slice are negative.

$\overline{V}_{A\,top}$, $\overline{V}_{B\,top}$ = Average vertical velocity through top area of volumes A and B respectively (m $s^{-1}$)

$\overline{V}_{A\,base}$, $\overline{V}_{B\,base}$ = Average vertical velocity through base area of volumes A and B respectively (m $s^{-1}$)

$l_1$ to $l_6$ = Length of transect/portion of transect (m)

$t_1$ to $t_6$ = Time taken to complete transect/portion of transect (s)

A,B = Base areas of Volumes A and B respectively ($m^2$).

d = Thickness of depth slice (m).

Additionally, $d\overline{V}_T/dt$ is the change in mean tidal velocity with time.

Then, the volume of water in Volume A, $X_A$ is;

$$\left[\left(\frac{\overline{V}_4 l_4}{(l_3+l_4)}+\frac{\overline{V}_5 l_5}{(l_5+l_6)}\right)+\frac{d\overline{V}_T}{dt}(t_4+t_5)\right]\times 300m\times d+\left(\overline{V}_{A\,top}-\overline{V}_{A\,base}\right)\times A=X_A \tag{4.11}$$

And the volume of water in Volume B, $X_B$ is;

$$\left[\left(-\overline{V}_1-\overline{V}_2+\frac{\overline{V}_3 l_3}{(l_3+l_4)}+\frac{\overline{V}_6 l_6}{(l_5+l_6)}\right)+\frac{d\overline{V}_T}{dt}(t_1+t_2+t_3+t_6)\right]\times 300m\times d$$
$$+\left(\overline{V}_{B\,top}-\overline{V}_{B\,base}\right)\times B=X_B \tag{4.12}$$

And theoretically, $X_A = -X_B$.

In the case of the top slice, $\overline{V}_{A\,top}$ and $\overline{V}_{B\,top}$ are both zero.

Average cross-frontal velocity is then given by either $X_A$ or $X_B$, assuming they are equal in magnitude, divided by the cross-sectional area of the frontal plane, which is $\sqrt{(l_5^2+l_4^2)}\times d$.

The depth slice model shown in figure 4.7 is modified slightly for box 7N, through which the front passes twice (see figure 4.8).

***Figure 4.8 Depth slice with two fronts for box 7N***

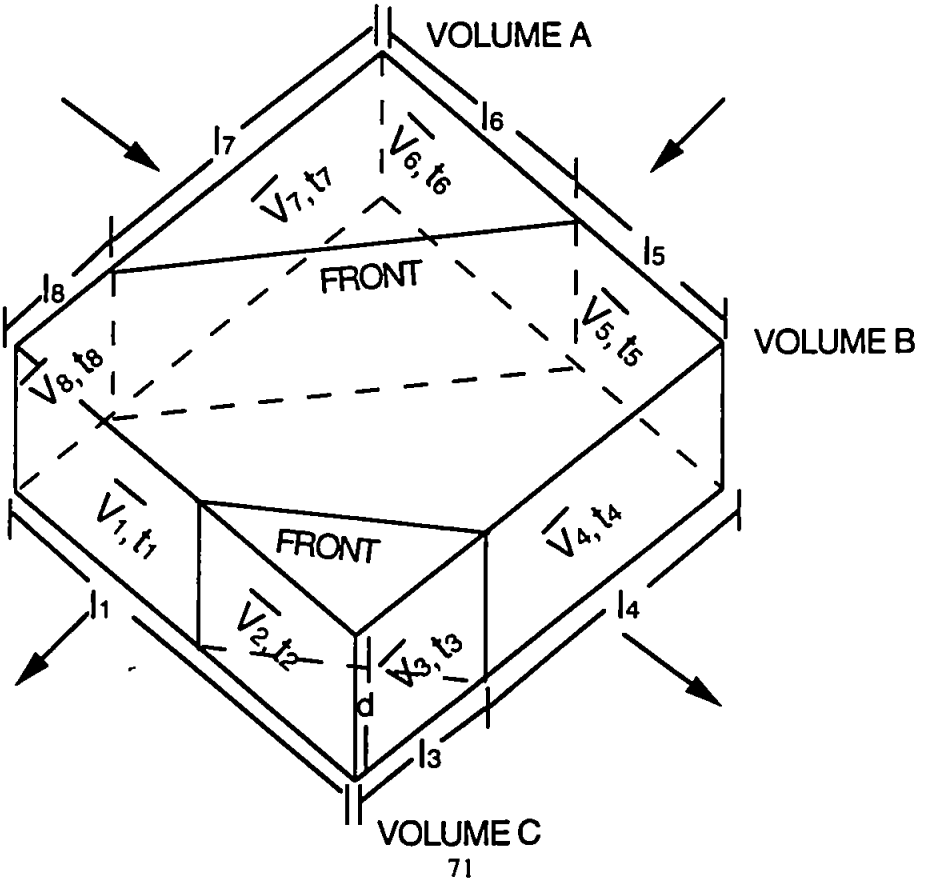

where;

$\overline{V}_1$ to $\overline{V}_8$ = Average transect-normal velocity through transect/portion of transect ($m\ s^{-1}$). Velocities directed into the slice are positive, those out of the slice are negative.

$\overline{V}_{A\ top}, \overline{V}_{B\ top}, \overline{V}_{C\ top}$ = Average vertical velocity through top area of volumes A, B and C respectively ($m\ s^{-1}$)

$\overline{V}_{A\ base}, \overline{V}_{B\ base}, \overline{V}_{C\ base}$ = Average vertical velocity through base area of volumes A, B and C respectively ($m\ s^{-1}$)

$l_1$ to $l_8$ = Length of transect/portion of transect (m)

$t_1$ to $t_8$ = Time taken to complete transect/portion of transect (s)

A,B, C = Base areas of Volumes A, B and C respectively ($m^2$).

d = Thickness of depth slice (m).

A similar approach as before is used, in that the volume of water through sides 6 and 7 into Volume A, plus the volume flowing in through the top area, less the volume flowing out through the base area is found, so that the excess or deficit in total water volume in Volume A is accounted for by cross-frontal transport between Volumes A and B. In Volume C, the total water volume is similarly calculated, allowing the cross-frontal transport between Volumes C and B to be estimated. Considering Volume B, the average velocity and hence the volume of water flowing through each side is now known and the total water volume here must, in theory, equal zero to satisfy continuity. Once again, the change in mean tidal velocity is accounted for.

The volume of water in Volume A, $X_A$ is;

$$\left[\left(\frac{\overline{V}_6 l_6}{(l_5+l_6)}+\frac{\overline{V}_7 l_7}{(l_7+l_8)}\right)+\frac{d\overline{V}_T}{dt}(t_6+t_7)\right]\times 300m\times d+\left(\overline{V}_{A\ top}-\overline{V}_{A\ base}\right)\times A=X_A \qquad (4.13)$$

The volume of water in Volume C, $X_C$ is;

$$\left[\left(-\frac{\overline{V}_2 l_2}{(l_1+l_2)}-\frac{\overline{V}_3 l_3}{(l_3+l_4)}\right)+\frac{d\overline{V}_T}{dt}(t_2+t_3)\right]\times 300m\times d+\left(\overline{V}_{C\ top}-\overline{V}_{C\ base}\right)\times C=X_C \qquad (4.14)$$

And the water volume in Volume B, $X_B$ is;

$$\left[\left(\frac{\overline{V}_8 l_8}{(l_7+l_8)}-\frac{\overline{V}_1 l_1}{(l_1+l_2)}-\frac{\overline{V}_4 l_4}{(l_3+l_4)}+\frac{\overline{V}_5 l_5}{(l_5+l_6)}\right)+\frac{d\overline{V}_T}{dt}(t_8+t_1+t_4+t_5)\right]$$

$$\times 300\text{m}\times d+\left(\overline{V}_{B\,top}-\overline{V}_{B\,base}\right)\times B+X_A+X_C=X_B=0 \qquad (4.15)$$

The cross-frontal velocity between Volumes A and B, $\overline{V}_{AB}$ is then given by;

$\overline{V}_{AB}=X_A\Big/\sqrt{\left(l_6^{\,2}+l_7^{\,2}\right)}\times d$ and the cross-frontal velocity between Volumes C and B, $\overline{V}_{CB}$ is $X_C\Big/\sqrt{\left(l_2^{\,2}+l_3^{\,2}\right)}\times d$.

The excess or deficit water volumes calculated for volumes A and B, in boxes 2N, 3N and 4N, and for volumes A, B and C in box 7N are presented in table 1, page vii, appendix. These results are discussed in sections 6.1.2 and 6.1.3.

# CHAPTER 5

# THE APPLICATION OF THE EQUATIONS OF MOTION

The equations of motion in two horizontal directions are applied to the Tamar-Lynher data set in order to assess the relative importance of different dynamic processes in maintaining the momentum balance in the longitudinal and lateral directions. Values of eddy diffusivity and eddy viscosity are derived and interpreted in terms of the competition between mixing and stratification within the study area in the Tamar Estuary.

## 5.1 DERIVATION OF THE EQUATION OF MOTION

The equation of motion is derived from Newton's Second Law which states that force equals mass times acceleration. Re-arranging this, we can write that:

*Temporal Acceleration + Advective Acceleration + Coriolis Acceleration = Pressure force per unit mass + frictional force per unit mass* (5.1)

which is the general form of the equation of motion.

Considering the right-hand side of this equation in one dimension acting on an element with sides δx, δy and δz (see figure 5.1), we need to find the pressure force and frictional force acting on the element (Dyer, 1973).

***Figure 5.1 Volume element with pressure***

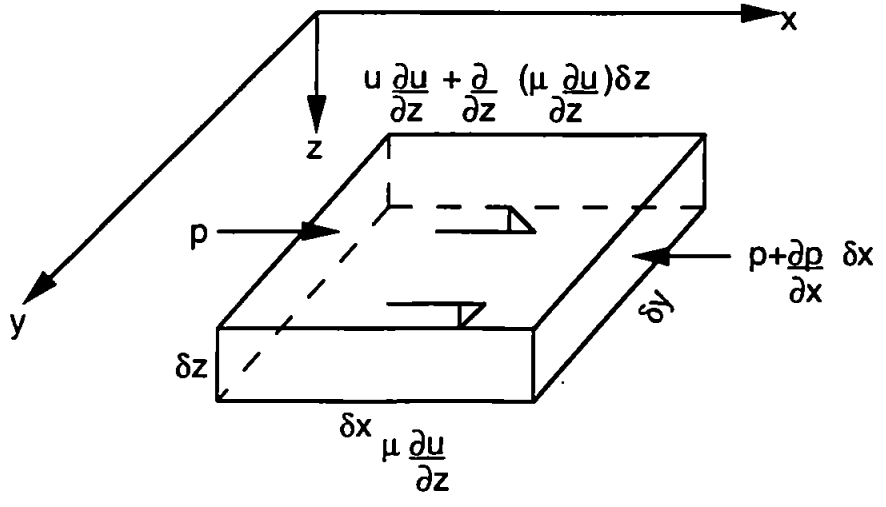

The frictional force on the bottom surface of the element is;

$$\mu \frac{\partial u}{\partial z} \delta x . \delta y \qquad (5.2)$$

where $\mu$ is the coefficient of molecular viscosity.

From a Taylor expansion, the frictional force on the top of the element is;

$$\mu \frac{\partial u}{\partial z} \delta x . \delta y + \frac{\partial}{\partial z}\left( \mu \frac{\partial u}{\partial z} \right) \delta z . \delta x . \delta y \qquad (5.3)$$

So this component of the total frictional force is equation 5.3 - equation 5.2 which gives;

$$\mu \frac{\partial^2 u}{\partial z^2} \delta z . \delta x . \delta y$$

Similarly, the component of total frictional force on the sides of the element is;

$$\mu \frac{\partial^2 u}{\partial y^2} \delta y . \delta x . \delta z$$

and on the ends of the element is;

$$\mu \frac{\partial^2 u}{\partial x^2} \delta x . \delta y . \delta z$$

The net pressure force on the element in the x-direction is $-(\partial P/\partial x)\delta x\, \delta y\, \delta z$. The temporal and advective accelerations on the left-hand side of equation 5.1 are;

$$\frac{\partial u}{\partial t} + u \frac{\partial u}{\partial x} + v \frac{\partial u}{\partial y} + w \frac{\partial u}{\partial z}$$

so that the longitudinal equation of motion is now;

$$\frac{\partial u}{\partial t} + u \frac{\partial u}{\partial x} + v \frac{\partial u}{\partial y} + w \frac{\partial u}{\partial z} = -\frac{1}{\rho} \frac{\partial P}{\partial x} - g \frac{\partial \zeta}{\partial x} + f_1 v + \frac{\mu}{\rho}\left( \frac{\partial^2 u}{\partial x^2} + \frac{\partial^2 u}{\partial y^2} + \frac{\partial^2 u}{\partial z^2} \right) \qquad (5.4)$$

The terms on the left-hand side of equation 5.4 have been divided through by density, $\rho$ to give force/mass, and the total pressure term has been split into two components comprising the contribution to the total longitudinal pressure gradient from the density distribution in the water column, and the contribution from the slope of the free surface, $\partial\zeta/\partial x$. The Coriolis parameter is $f_1$, such that;

$f_1 = 2\, \omega \sin \phi . v$ where $\omega$ is the angular speed of rotation of the earth, $\phi$ is the latitude and v is the velocity in the y direction.

In our analysis, the observed velocity in each of the x, y and z directions can be split into two components representing the combined tidal mean and fluctuating tidal component, and the turbulent fluctuation e.g.

$u = \bar{u} + u'$ (x direction)

$v = \bar{v} + v'$ (y direction)

$w = \bar{w} + w'$ (z direction)

where u, v and w are the observed velocities, $\bar{u}$, $\bar{v}$ and $\bar{w}$ are the combined tidal mean and fluctuating tidal components, and u', v' and w' are the turbulent fluctuations. Substituting this into equation 5.4 gives;

$$\frac{\partial \bar{u}}{\partial t} + \bar{u}\frac{\partial \bar{u}}{\partial x} + \bar{v}\frac{\partial \bar{u}}{\partial y} + \bar{w}\frac{\partial \bar{u}}{\partial z} = -\frac{1}{\rho}\frac{\partial P}{\partial x} - g\frac{\partial \zeta}{\partial x} + f_1\bar{v} - \frac{\partial}{\partial x}\left(\overline{u'.u'}\right) - \frac{\partial}{\partial y}\left(\overline{u'.v'}\right) - \frac{\partial}{\partial z}\left(\overline{u'.w'}\right) \quad (5.5)$$

Following exactly the same argument in the y direction gives;

$$\frac{\partial \bar{v}}{\partial t} + \bar{u}\frac{\partial \bar{v}}{\partial x} + \bar{v}\frac{\partial \bar{v}}{\partial y} + \bar{w}\frac{\partial \bar{v}}{\partial z} = -\frac{1}{\rho}\frac{\partial P}{\partial y} - g\frac{\partial \zeta}{\partial y} - f_2\bar{u} - \frac{\bar{u}^2}{R} - \frac{\partial}{\partial x}\left(\overline{v'.u'}\right) - \frac{\partial}{\partial y}\left(\overline{v'.v'}\right) - \frac{\partial}{\partial z}\left(\overline{v'.w'}\right) \quad (5.6)$$

and the additional $\bar{u}^2/R$ term on the right-hand side should be noted. This term is referred to as the curvature term and it is present in the lateral equation of motion because the curvature of the streamlines of the flow is likely to be significant in this direction (Dyer, 1973). The streamline curvature is produced by the meandering shape of the estuary, such that accelerations are produced in the lateral direction by a force acting normal to the predominantly longitudinal streamlines. As water flows round a bend, the surface elevation on the outside of the bend increases in comparison to the surface elevation on the inside of the bend, due to the centrifugal force. The resulting elevation gradient produces a pressure gradient which, in turn, generates a force acting normal to the streamlines and opposing the centrifugal force. The R in the term is the radius of curvature of the streamlines of the longitudinal flow in the y-direction. The radius of curvature of the streamlines is usually estimated using the radius of curvature of the estuarine topography. However, it should be remembered that the two are not necessarily the same, making the curvature term particularly difficult to calculate, as will be discussed later.

Equations 5.5 and 5.6 are applied to the data set in the following section.

## 5.2 APPLICATION OF THE EQUATION OF MOTION

The "figure-of-eight" survey grid is treated as two adjacent boxes, each comprising a stack of one metre thick depth slices with the exception of the top slice, as described and illustrated in section 4.2, figure 4.2. The east-west and north-south velocities measured by the ADCP for each transect are combined into resultant velocity vectors and resolved onto a set of right-handed orthogonal axes, x, y and z, such that u, v and w are the velocity components along each of those axes respectively. The orientation of the x and y axes are determined from the sides of the figure-of-eight survey grid shown in figure 4.2, section 4.2, with the x axes orientated longitudinally along the estuary, positive downstream at a bearing of 141°, and the y axis orientated laterally across the estuary, positive to the south-west at a bearing of 231°. Each transect now has three velocity matrices associated with it, containing the u, v and w components. Averaging each matrix gives values for $\bar{u}$, $\bar{v}$ and $\bar{w}$, and subtracting these mean velocities from the original u, v and w components generates three matrices containing the turbulent velocity fluctuations in the x, y and z directions. Where a transect crosses the front, the pre- and post-front mean velocities are combined by weighted averaging to find the mean value for the entire transect. The pre-front mean is subtracted from all observed pre-front velocities and the post-front mean is subtracted from all post-front velocities. The pre- and post-front turbulent fluctuations are then combined back into one matrix. Each side of each depth slice is now represented by three mean velocities and three matrices of turbulent fluctuations, as figure 5.2 demonstrates.

***Figure 5.2 Depth slice with average and fluctuating velocity components***

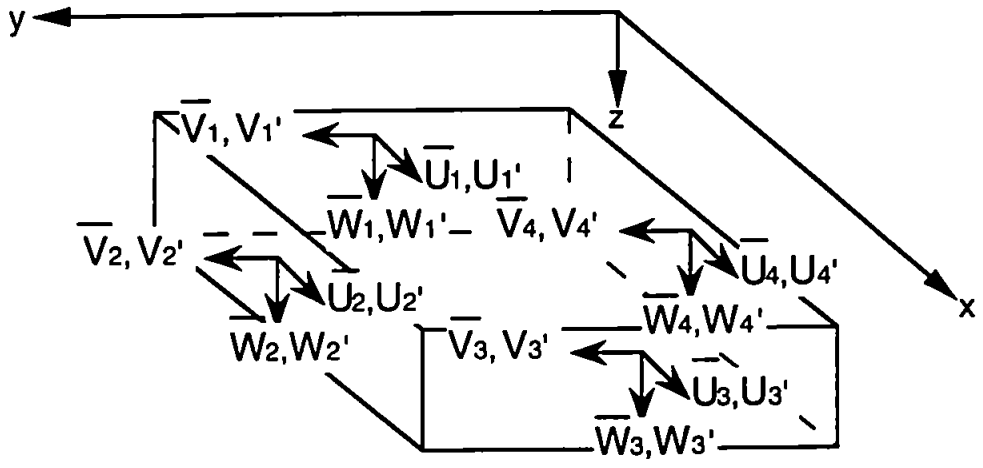


$\bar{U}, \bar{V}, \bar{W}$=mean velocities for each side
U',V',W'=matrices of turbulent fluctuations for each side

### *5.2.1. Temporal Accelerations*

The temporal acceleration terms are $\partial\bar{u}/\partial t$ and $\partial\bar{v}/\partial t$ in the longitudinal and lateral equations of motion respectively. To calculate these terms on each of the three survey days, $\bar{u}$ and $\bar{v}$ for the whole depth of each transect are plotted against the time after high water at which the transect was recorded. Graphs of the two mean velocity components against time, with a linear regression applied, are presented in figures 5a, b, 6a, b and 7a, b (appendix) for each survey day. On the 20.04.94 and the 25.04.94, the 'goodness of fit' of the regression lines, as indicated by the $R^2$ values, is poor for the u and v components because of the sparsity of data points. On the 22.04.94, the $R^2$ value of the $\bar{u}$ *vs.* time regression line is acceptable, whereas the data points on the $\bar{v}$ *vs.* time plot are scattered. The $\bar{v}$ velocities are significantly less than the $\bar{u}$ velocities, so the flow direction is predominantly longitudinal with small deviations in direction to either side of the x-axis.

For each of the ten survey boxes described in section 4.2, the time after High Water at which surveying of the box commenced is $t_1$, and the time it ended is $t_2$. Values of u and v are then calculated at $t_1$ and $t_2$, using the equation from the appropriate regression line. The temporal accelerations in the x and y directions can then be calculated.

The two accelerations are determined for the entire depth of each box and are therefore the same for each depth slice within a survey box. These accelerations and all other terms in the longitudinal and lateral equations of motion are presented in tables 2 and 3 in the appendix.

### *5.2.2. Advective Accelerations*

The advective or spatial acceleration terms in the two equations of motion are;

Longitudinal: $\bar{u}\left(\partial\bar{u}/\partial x\right),\ \bar{v}\left(\partial\bar{u}/\partial y\right),\ \bar{w}\left(\partial\bar{u}/\partial z\right)$

Lateral: $\bar{u}\left(\partial\bar{v}/\partial x\right),\ \bar{v}\left(\partial\bar{v}/\partial y\right),\ \bar{w}\left(\partial\bar{v}/\partial z\right)$

Of these six terms, four can be derived directly from our data set. Referring to figure 5.2, section 5.2, we can say that;

$$\overline{u}\left(\partial\overline{u}/\partial x\right)=\overline{u}_1.\frac{(\overline{u}_3-\overline{u}_1)}{300m}$$

$$\overline{v}\left(\partial\overline{u}/\partial y\right)=\overline{v}_4.\frac{(\overline{u}_2-\overline{u}_4)}{300m}$$

$$\overline{u}\left(\partial\overline{v}/\partial x\right)=\overline{u}_1.\frac{(\overline{v}_3-\overline{v}_1)}{300m}$$

$$\overline{v}\left(\partial\overline{v}/\partial y\right)=\overline{v}_4.\frac{(\overline{v}_2-\overline{v}_4)}{300m}$$

The remaining two terms are accelerations in the z direction, $\overline{w}\left(\partial\overline{u}/\partial z\right)$ and $\overline{w}\left(\partial\overline{v}/\partial z\right)$.

Here, $\overline{w}$ represents the average vertical velocity through the top and base of each depth slice. As an example, these top and base vertical velocities are annotated with the subscripts 5 and 6 respectively in figure 5.3.

***Figure 5.3 Depth slice with average vertical velocities***

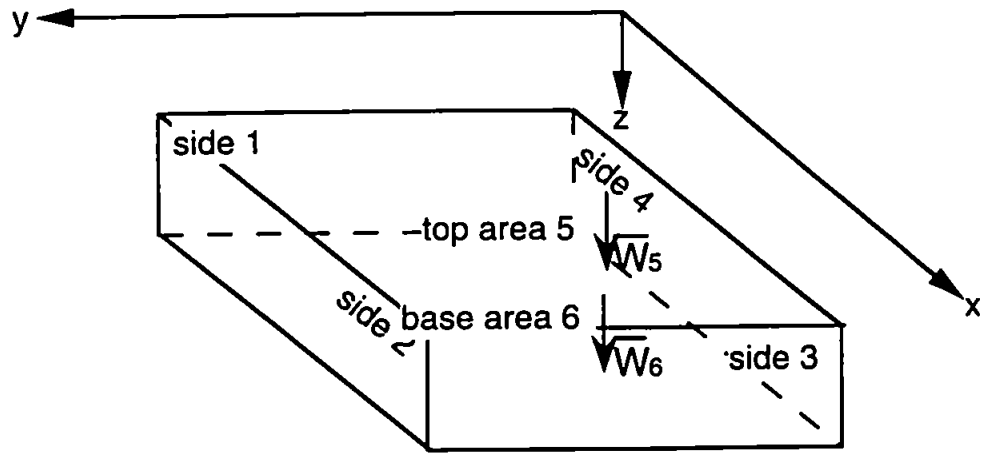


We know the values for $\overline{w}_5$ and $\overline{w}_6$ from the equation of volume continuity, section 4.2, so that in the two acceleration terms, $\overline{w}\left(\partial\overline{u}/\partial z\right)$ and $\overline{w}\left(\partial\overline{v}/\partial z\right)$, the $\overline{w}$ value is given by $\overline{w}_5$ in figure 5.3. To find $\partial\overline{u}/\partial z$, the mean longitudinal velocities for each of the four sides of the depth slice are averaged to give an estimate of $\overline{u}$ for the entire depth

slice. The mean lateral velocities for each side are also averaged to find $\bar{v}$ for the whole depth slice. These "slice-averaged" $\bar{u}$ and $\bar{v}$ values are plotted against the mid-depth of each slice which is also the mid-depth of the ADCP's depth bins. The data points in the slice-averaged $\bar{u}$ and $\bar{v}$ depth profiles for each box then have a linear, second-order or third-order polynomial fitted to them, and this stage of the analysis is shown in figures 8a, b to 17a, b, appendix. We now need to find mean longitudinal and lateral velocities for the top and base areas of each slice, so the equations in figures 8a, b to 17a, b are used to interpolate $\bar{u}$ and $\bar{v}$ values at depths 0.5 metres above and 0.5 metres below the mid-depth of each slice, allowing the last two acceleration terms to be estimated as;

$$\overline{w}\left(\partial\bar{u}/\partial z\right) = \overline{w_5}.\frac{(\overline{u_{6i}} - \overline{u_{5i}})}{d} \qquad \text{and} \qquad \overline{w}\left(\partial\bar{v}/\partial z\right) = \overline{w_5}.\frac{(\overline{v_{6i}} - \overline{v_{5i}})}{d}$$

where the subscript i indicates an interpolated value.

### *5.2.3. Pressure Terms*

The pressure terms in the two equations of motion are as follows;

Longitudinal: $-\frac{1}{\rho}\frac{\partial P}{\partial x} - g\frac{\partial \zeta}{\partial x}$

Lateral: $-\frac{1}{\rho}\frac{\partial P}{\partial y} - g\frac{\partial \zeta}{\partial y}$

where $\rho$ is density, P is pressure, g is gravitational acceleration and $\zeta$ is the water surface elevation. In the longitudinal and lateral equations, $-\frac{1}{\rho}\frac{\partial P}{\partial x}$ and $-\frac{1}{\rho}\frac{\partial P}{\partial y}$ are the horizontal pressure forces created by differences in the water density, and $-g\frac{\partial \zeta}{\partial x}$ and $-g\frac{\partial \zeta}{\partial y}$ are the horizontal pressure forces resulting from differences in the elevation of the water surface across the survey area (Dyer, 1977).

From the temperature and salinity data collected by the ETS, we can use an equation of state of seawater to find the density and therefore pressure values, allowing $-\frac{1}{\rho}\frac{\partial P}{\partial x}$ and $-\frac{1}{\rho}\frac{\partial P}{\partial y}$ to be calculated. The International Equation of State of Seawater, 1980 (IES 80) presented by Millero and Poisson, 1981, is used to convert salinities and temperatures into densities, and is written in full in the appendix. The Tamar-Lynher

data set has salinities and temperatures recorded for only two or three depth slices (below the extrapolated top slice) depending on the survey day. Therefore, estimates of density and pressure for the whole depth of the survey box must be inferred from the available data. Initially, densities for each side of the top two or three depth slices are calculated using IES 80 for each box. The densities are then converted to a pressure for each side of the slice, assuming hydrostatic equilibrium i.e.

$dP = -\rho g\, dz$ where dP is the pressure for one side of the depth slice, $\rho$ is the density and dz is the thickness of the slice.

For a survey box with three depth slices with measured salinities and temperatures, a slightly thicker top slice is added to the stack, as before, to make the top area of the stack coincident with the water surface. The top slice is assigned the same temperature and salinity values on each side as the slice below it, hence a total of four dP values have been found for each side of the box, as shown in figure 5.4.

***Figure 5.4 Hydrostatic pressure for a stack of depth slices***

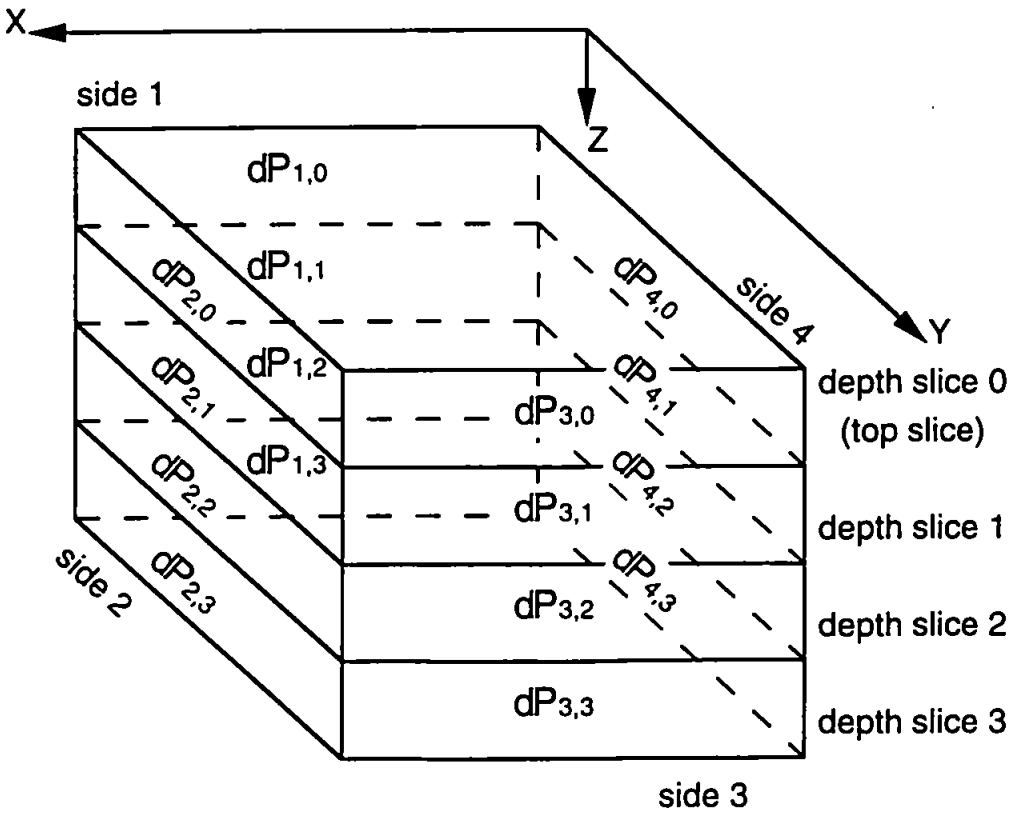

The total pressure at side 1, depth slice 0 ($P_{1,0}$) is;

$dP_{1,0} + P_a$ where $P_a$ is atmospheric pressure at the water surface. The total pressure of side 1, depth slice 1 ($P_{1,1}$) is;

$dP_{1,1} + dP_{1,0} + P_a$

Similarly, $P_{1,2}$ is;

$dP_{1,2} + dP_{1,1} + dP_{1,0} + P_a$

and $P_{1,3}$ is;

$dP_{1,3} + dP_{1,2} + dP_{1,1} + dP_{1,0} + P_a$

This summation is repeated for sides 2, 3 and 4 so that dP has been integrated over depth for each side to give the total baroclinic pressure in each depth slice. The pressure gradients in the x and y direction can now be found, i.e. for depth slice 0;

$$\frac{\partial P}{\partial x} = \frac{(P_{3,0} - P_{1,0})}{300m} \qquad \text{and} \qquad \frac{\partial P}{\partial y} = \frac{(P_{2,0} - P_{4,0})}{300m}$$

Pressure gradients for the lower three slices are derived in the same way.

In the absence of a more complete data set, the $\partial P/\partial x$ and $\partial P/\partial y$ values for the top three or four slices are plotted against the depth and linearly extrapolated to provide at least estimates of the $\partial P/\partial x$ and $\partial P/\partial y$ values in depth slices below those which have temperature and salinity data, for each of the survey boxes. The horizontal pressure gradients are now multiplied by the reciprocal of density to generate the pressure terms in the longitudinal and lateral equations. The density value is derived by finding the density of each side of the top three or four depth slices from temperature and salinity data. The average density for each slice is then found and linearly extrapolated over depth to give estimates of density in the remaining slices in the survey box. These densities have effectively been averaged over the survey box area and also averaged over depth, such that the horizontal pressure gradients for depth slice 4 are multiplied by the reciprocal of the average of the densities for slices 0,1 ,2 ,3 and 4. In other words, this density represents a value for the entire volume of water above and including the depth slice for which the pressure terms are being calculated.

The components of the horizontal pressure force resulting from changes in water surface elevation, $-g\frac{\partial \zeta}{\partial x}$ and $-g\frac{\partial \zeta}{\partial y}$ in the longitudinal and lateral equations, are unknown

because no attempt to measure water surface elevation was made during surveying. These surface elevation gradients are obviously the same for each depth slice in a survey box, and an approache for estimating the values of these terms will be discussed fully in section 5.3.

### *5.2.4. Coriolis Accelerations*

The Coriolis accelerations are included because the equations of motion are applied in a rotating frame of reference, i.e. the x, y and z axes are themselves subject to accelerations due to the Earth's rotation, and are not fixed in space. For each depth slice in a box, the horizontal Coriolis accelerations are;

$+ 2\,\omega \sin\phi .\, v$ [longitudinal]

$- 2\,\omega \sin\phi .\, u$ [lateral]

where $\omega$ is the angular speed of rotation of the Earth ($7.29 \times 10^{-5}$ radians $s^{-1}$), $\phi$ is the latitude of the survey area, $\theta$ is the angle between the positive x axis and east and u and v are the slice-averaged velocities in the x and y directions. In the case of the longitudinal and lateral equations, the components of Coriolis acceleration due to the vertical velocity have been omitted because they are negligibly small.

### *5.2.5. Frictional Forces (Reynold's Stress Terms)*

The Reynold's stresses represent the stress in the flow caused by turbulent fluctuations in velocity, and in the equations of motion they are used to find the flux of momentum due to turbulence, i.e. "chunks" of fluid moving back and forth exchanging momentum with the surrounding fluid. In three spatial dimensions, there are a total of nine Reynold's stresses, i.e. $\rho(\overline{u'.u'})$, $\rho(\overline{u'.v'})$ and $\rho(\overline{u'.w'})$ where $\rho$ is the density and u', v' and w' are turbulent fluctuations in velocity. In the equations of motion, the Reynold's stresses are differentiated to represent the frictional forces due to turbulence in the following way;

$$\frac{\partial(\overline{u'.u'})}{\partial x}, \frac{\partial(\overline{u'.v'})}{\partial y}, \frac{\partial(\overline{u'.w'})}{\partial z}$$ (Frictional forces in longitudinal equation)

$$\frac{\partial(\overline{v'.u'})}{\partial x}, \frac{\partial(\overline{v'.v'})}{\partial y}, \frac{\partial(\overline{v'.w'})}{\partial z}$$ (Frictional forces in the lateral equation)

Referring to figure 5.2, section 5.2, four of these terms can be determined directly from our data set, such that;

$$\frac{\partial(\overline{u'.u'})}{\partial x} = \frac{(\overline{u_3'.u_3'}) - (\overline{u_1'.u_1'})}{300m}$$

$$\frac{\partial(\overline{u'.v'})}{\partial y} = \frac{(\overline{u_2'.v_2'}) - (\overline{u_4'.v_4'})}{300m}$$

$$\frac{\partial(\overline{v'.u'})}{\partial x} = \frac{(\overline{v_3'.u_3'}) - (\overline{v_1'.u_1'})}{300m}$$

$$\frac{\partial(\overline{v'.v'})}{\partial y} = \frac{(\overline{v_2'.v_2'}) - (\overline{v_4'.v_4'})}{300m}$$

The remaining Reynold's stress terms, $\frac{\partial(\overline{u'.w'})}{\partial z}$ and $\frac{\partial(\overline{v'.w'})}{\partial z}$, are unknowns in the longitudinal and lateral equations respectively.

As mentioned before, the values of the terms that can be calculated in the equations are presented in tables 2 and 3, appendix.

## 5.3 SOLVING THE EQUATIONS OF MOTION

Having calculated as many terms as possible from the available data in the horizontal equations of motion, each equation must now be solved for the unknown terms. In the longitudinal equation, there are two unknowns, $g\frac{\partial \zeta}{\partial x}$, the barotropic pressure component and $\frac{\partial(\overline{u'.w'})}{\partial z}$, representing an exchange of turbulent longitudinal momentum equivalent to a frictional force on the x-y plane. In the lateral equation, the situation is more complex with three unknowns to solve for: the barotropic term, $g\frac{\partial \zeta}{\partial y}$, the frictional force on the x-y plane arising from the exchange of turbulent lateral momentum, $\frac{\partial(\overline{v'.w'})}{\partial z}$, and the curvature term, $\frac{\overline{u}^2}{R}$. In both the longitudinal and lateral directions, each depth slice within a survey box has an equation associated with it, however, the unknowns in these equations cannot be computed by solving the equations simultaneously because there will always n+1 unknowns (in the longitudinal case) or n+2 unknowns (in the lateral case) in n equations. Hence, a different approach is required and so the equation of the top slice of each survey box is initially considered independently. The top surface

area of this extrapolated top slice is coincident with the water surface, through which there can be no vertical flow of water. Therefore, both the $\overline{w}$ and w' components of velocity must be zero for this top area, which means that the values of $(\overline{u'.w'})$ and $(\overline{v'.w'})$ will also be zero. If we assume that both $(\overline{u'.w'})$ and $(\overline{v'.w'})$ increase slowly from zero over the depth of the top slice, effectively making the assumption that there is very little stress on the water surface caused by wind, and given the fact that the vertical velocity and the fluctuations thereof are small in comparison to u' and v', which indicates that $(\overline{u'.w'})$ and $(\overline{v'.w'})$ will be significantly less than the other Reynold's stresses $[(\overline{u'.u'}),(\overline{u'.v'}),(\overline{v'.v'})]$, then it seems reasonable to assume that the gradients of $(\overline{u'.w'})$ and $(\overline{v'.w'})$ are zero in the case of the top slice. The longitudinal and lateral equations for the top slice are then solved for $g\frac{\partial\zeta}{\partial x}$ and $g\frac{\partial\zeta}{\partial y}-\frac{\overline{u}^2}{R}$, by assuming that the unknown frictional force is zero. Considering the longitudinal equation, we now have a value for $g\frac{\partial\zeta}{\partial x}$, and as this term is constant with depth, its value is now included in the longitudinal equation for every remaining slice in the box, so that the equation can then be solved for the unknown Reynold's stress term, $\frac{\partial(\overline{u'.w'})}{\partial z}$. The $g\frac{\partial\zeta}{\partial x}$ terms calculated for each survey box in this manner change with time from being negative in the early ebb to positive in the later stages, which is thought to represent a realistic variation in surface water slope over the course of an ebb tide.

Similarly, in the lateral equation, zero is substituted for $\frac{\partial(\overline{v'.w'})}{\partial z}$ to find a value for $g\frac{\partial\zeta}{\partial y}-\frac{\overline{u}^2}{R}$ in the top slice. Both the barotropic and curvature terms are constant with depth and their combined value is substituted into each of the remaining equations for the underlying slices. This allows a value for the Reynold's stress term, $\frac{\partial(\overline{v'.w'})}{\partial z}$, to be determined in each slice. However, we are still left with one value for two unknowns, the barotropic and curvature terms. The curvature term is difficult to calculate

accurately, but an attempt has been made to find an estimate of its magnitude, so that it can be compared with the magnitude of barotropic term.

In order to estimate the curvature term, we have firstly assumed that the curvature of the longitudinal streamlines is the same as the curvature of the estuarine topography. Considering this topography in the area of the northern part of the survey grid, it has been assumed that there is a radius of curvature associated with the Lynher flow exiting the mouth of the Lynher river and rotating round as it joins the Tamar river. Similarly, there is likely to be a curvature of streamlines because of the bend in the Tamar river itself. These two radii of curvature will each promote a centrifugal force, and as the map of the area's topography in figure 2.1 shows, the two radii curve in the opposite sense such that the centrifugal forces and thus the resultant accelerations also oppose each other. Both radii have been orientated parallel to the y-axis and measured on a scale map of the area. The Lynher radius is approximately 2200 m and the Tamar radius is about 5300 m. Given that the Tamar radius will affect flow on the east side of the survey box more than flow on the west side, $\bar{u}$ values from the east of the box are used to find the curvature term. The converse situation applies in the case of the Lynher radius, such that $\bar{u}$ values from the west side of the box are used in the calculation. The difference between the two terms is then found for each of the slices in the northern boxes, and this value is assumed to be very approximately equivalent to the total laterally directed pressure force arising from the curvature of the two rivers' topography. This term, $\frac{\bar{u}^2}{R}$, is then compared to the value of the combined unknown, $g\frac{\partial \zeta}{\partial y} - \frac{\bar{u}^2}{R}$, in the lateral equation in order to assess which of the two component terms is likely to be the most important. It is found that the curvature term is, for nearly all of the depth slices in each of the northern survey boxes, one or two orders of magnitude smaller than the magnitude of the combined unknown, and these values are presented in table 4 of the appendix. Therefore, it is reasonable to treat the unknown in the lateral equation as being primarily composed of the barotropic pressure gradient, $g\frac{\partial \zeta}{\partial y}$. The topography of the Tamar river in the region of the southern box of the survey grid is essentially straight, thus the curvature term is assumed to be negligible here.

Having made this very approximate estimate of the curvature term, it is thought to be relatively unimportant in the lateral dynamic balance, and therefore the unknown term is henceforth referred to and interpreted as the lateral barotropic gradient.

# CHAPTER 6
# RESULTS AND DISCUSSION

Before discussing the results themselves, the errors associated with the terms calculated in the equations of continuity and motion (described in chapters 4 and 5) should be considered. The errors for these terms arise from a combination of measurement errors and those introduced by combining measured values to calculate terms.

Considering first measurement errors associated with ETS data, there are several factors which have considerably reduced the accuracy of the measurements. It had been noted in previous field tests that the thermistors themselves were prone to giving spurious readings and needed to be carefully calibrated in the laboratory both before and after fieldwork. This was probably because the ETS had not been used for three to four years prior to this period of fieldwork, and the thermistors may have been damaged in storage or transit. Additionally, there appeared to be some electronic 'cross-talk' between the thermistors so that each thermistor's data record did not represent a truly independent time series of temperatures recorded at a certain depth. Despite laboratory calibrations prior to surveying, most of the thermistors still recorded an unrealistic range of temperatures, such that the data had to be re-calibrated using measurements from the T-S bridge. When the temperature values were combined into a matrix to represent a transect along one side of the survey grid, values were interpolated to fill in the matrix wherever the recorded data from a thermistor had been discarded. All of these factors would have reduced the accuracy of the temperature data considerably.

In addition to these instrumental errors, there are also errors introduced during surveying, primarily due to deviations between the survey boat's course and the desired survey grid. Although the objective was to survey the grid shown in figure 2.4, strong tidal currents made this difficult, and the fact the subsequent analysis is based on the assumption that this survey grid was followed exactly causes further errors in the calculation of terms in the various equations.

Considering the instrumental errors associated with the ADCP, these should be smaller than those associated with the ETS. Although the ADCP's heading sensor did not work during surveying, the measurements of current speed would have been unaffected by

this and the process of rotating vectors round to their correct orientation should not have introduced any major errors. Obviously, the deviations from the desired survey grid would have affected the reliability of the ADCP data in the same way as the ETS data. In the case of both ETS and ADCP data, making a numerical assessment of the various errors is difficult. The accuracy of the measurements cannot be determined as no 'true' value for either current velocity or temperature was known. Similarly, the precision or reproducibility of the measurements cannot be assessed because of the time-varying nature of the velocity and temperature fields.

However, an estimation has been made of the errors associated with the terms calculated from the equations of continuity and motion. To do this, the absolute errors for velocity, salinity and temperature data, given in section 2.5 have been converted to percentage errors for typical values of each of these three parameters. Additionally, although the length of each side of the survey grid should have been 300 m, an absolute error of $\pm$ 50 m has been included in the calculations, to allow for deviations from the desired transect during surveying.

Values of average vertical velocity over the area of the survey box are found to have associated errors of approximately 60%, with the error increasing for smaller values of velocity and decreasing for larger values. The error is introduced primarily by possible deviations from the survey grid, rather than from inaccuracies in the velocity data. An error of similar magnitude has been found for the spatial acceleration terms in the equations of motion. Assuming that both latitude and the angular speed of rotation of the earth have negligibly small errors associated with them, the Coriolis acceleration can be calculated more accurately, with an error in the range 5% to 10%, introduced by the measurement error in the velocity. The errors for the Reynold's stress terms have been found to be between 40% and 60%. The errors associated with the baroclinic terms will be considerably larger because its calculation requires an estimate of density which is derived from temperature and salinity data. In the absence of a more complete data-set, salinity was inferred from temperature data, assuming a linear T-S relationship. As density was then calculated from the measured temperature and inferred salinity using a high order polynomial equation (the IES80), the errors associated with the density will be appreciably larger than those associated with the temperature. Thus, the baroclinic term is particularly inaccurate.

Considering the calculations of vertical eddy viscosity and vertical eddy diffusivity, the percentage errors associated with these values are higher and in many cases, greater than 100%. This is largely due to the fact that the vertical velocities have magnitudes which are similar to the absolute measurement error of $\pm$ 0.02 $ms^{-1}$, such that the percentage error are often in excess of 100% before any further calculations are done. This explains why the calculated eddy diffusivity, eddy viscosity and flux Richardson number results are largely found to be inaccurate, as will be discussed in section 6.3.

In general, the errors calculated for these terms are the smallest that could be expected with this data-set. It is very difficult to obtain a quantitative estimate of errors in this sort of exercise, but the orders of magnitude appear realistic.

## 6.1 QUALITATIVE INTERPRETATION OF RESULTS

The average vertical velocity profiles for each box (shown in figures 2a to 2j, appendix) and the ADCP data for each transect are now interpreted with the aim of determining the pattern of frontal evolution during an ebb tide. This will provide a framework within which the remainder of the results from the fieldwork and subsequent analysis can be interpreted.

The northernmost and southernmost survey boxes will be considered separately in the following two sections, and discussed in chronological order.

### *6.1.1 The Northernmost Survey Box*

Box 1N (in the northern half of the survey grid) shows a small downwards velocity at the surface which increases almost linearly with depth (see figure 2a, appendix). Box 1N was surveyed as the tide turned in this part of the estuary, which is clearly demonstrated by the north-south velocity matrices from the four component transects (figures 6.1b, 6.2b, 6.3b and 6.4b). Transect FA1, recorded 27 minutes before high water, shows an average northwards velocity of approximately 0.10 m $s^{-1}$. This decreases to an average of 0.05 m $s^{-1}$ in transect AB1 and only 0.02 m $s^{-1}$ in BC1, finally flowing southwards at approximately 0.01 m $s^{-1}$ in transect CF1, recorded 12 minutes after high water. The average vertical velocity is recorded at the start time of each survey box, which for box 1N is 27 minutes before high water. The downwards vertical velocity calculated at this time indicates that a larger volume of water is flowing horizontally into the box than is flowing out of it, therefore not only is the northwards velocity decreasing with time, it must also be decreasing in a northwards direction, such

*Figures 6.1a to 6.7b inclusive*

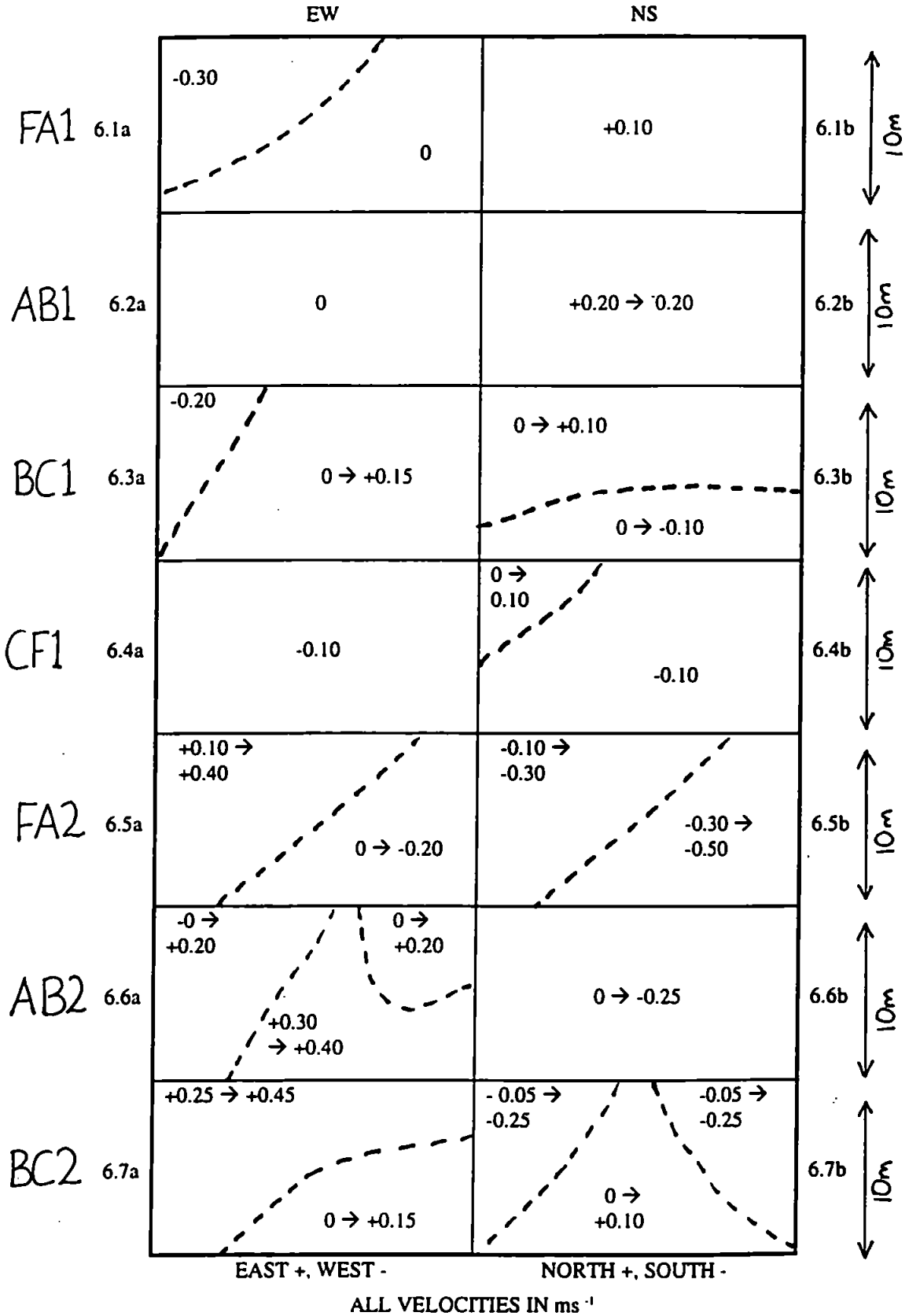

*Figures 6.8a to 6.14b inclusive*

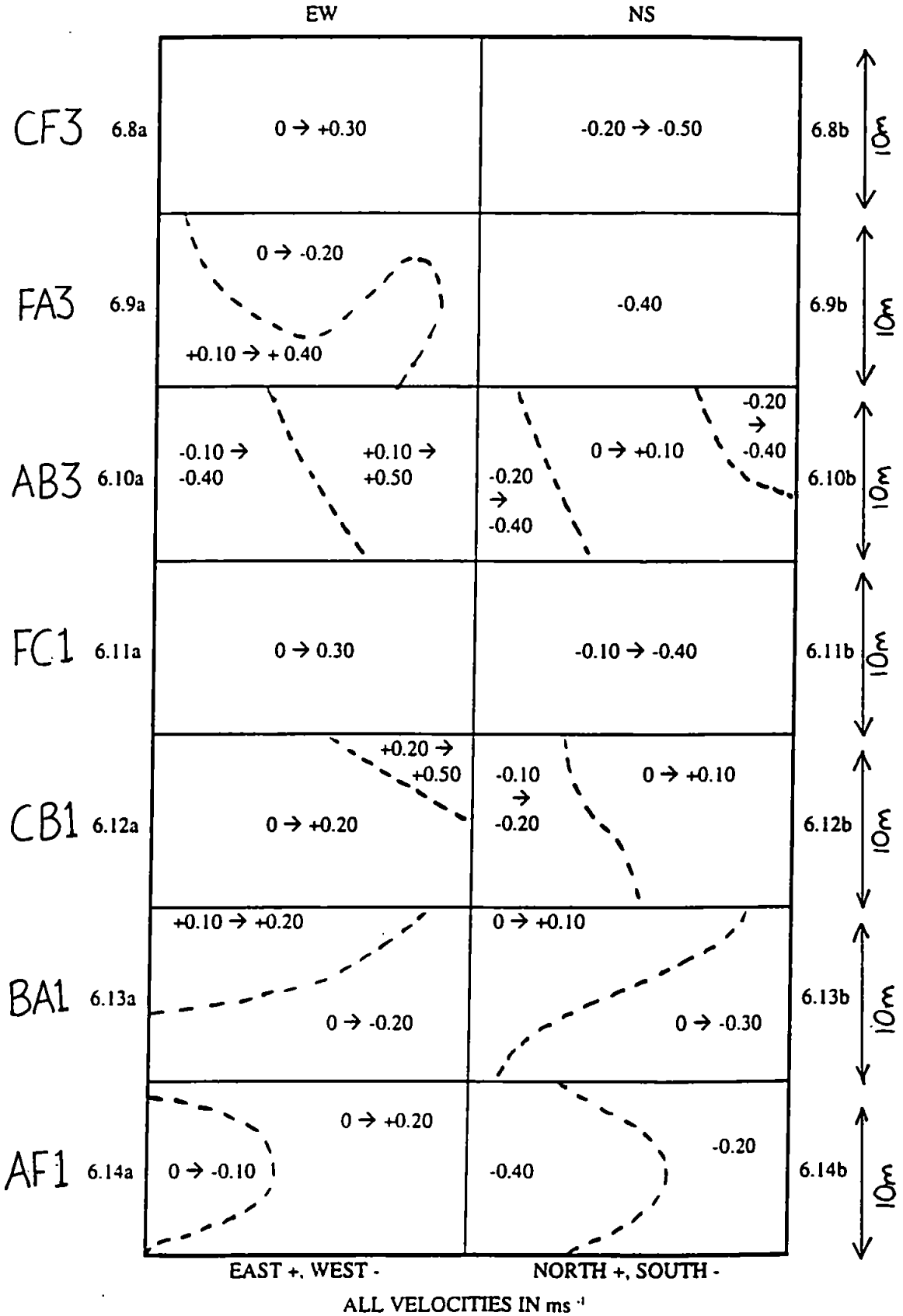

*Figures 6.15a to 6.21b inclusive*

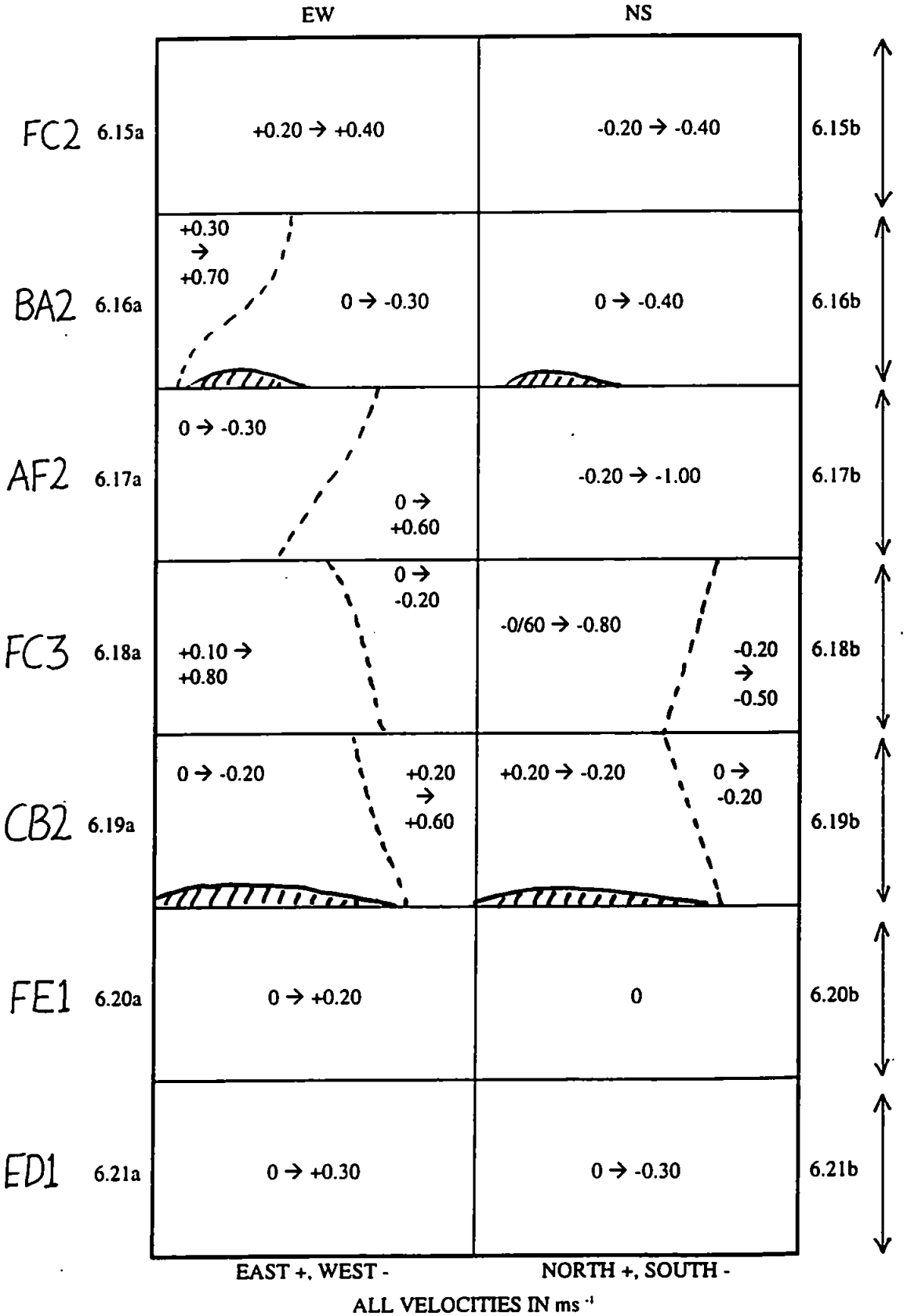

*Figures 6.22a to 6.27b inclusive*

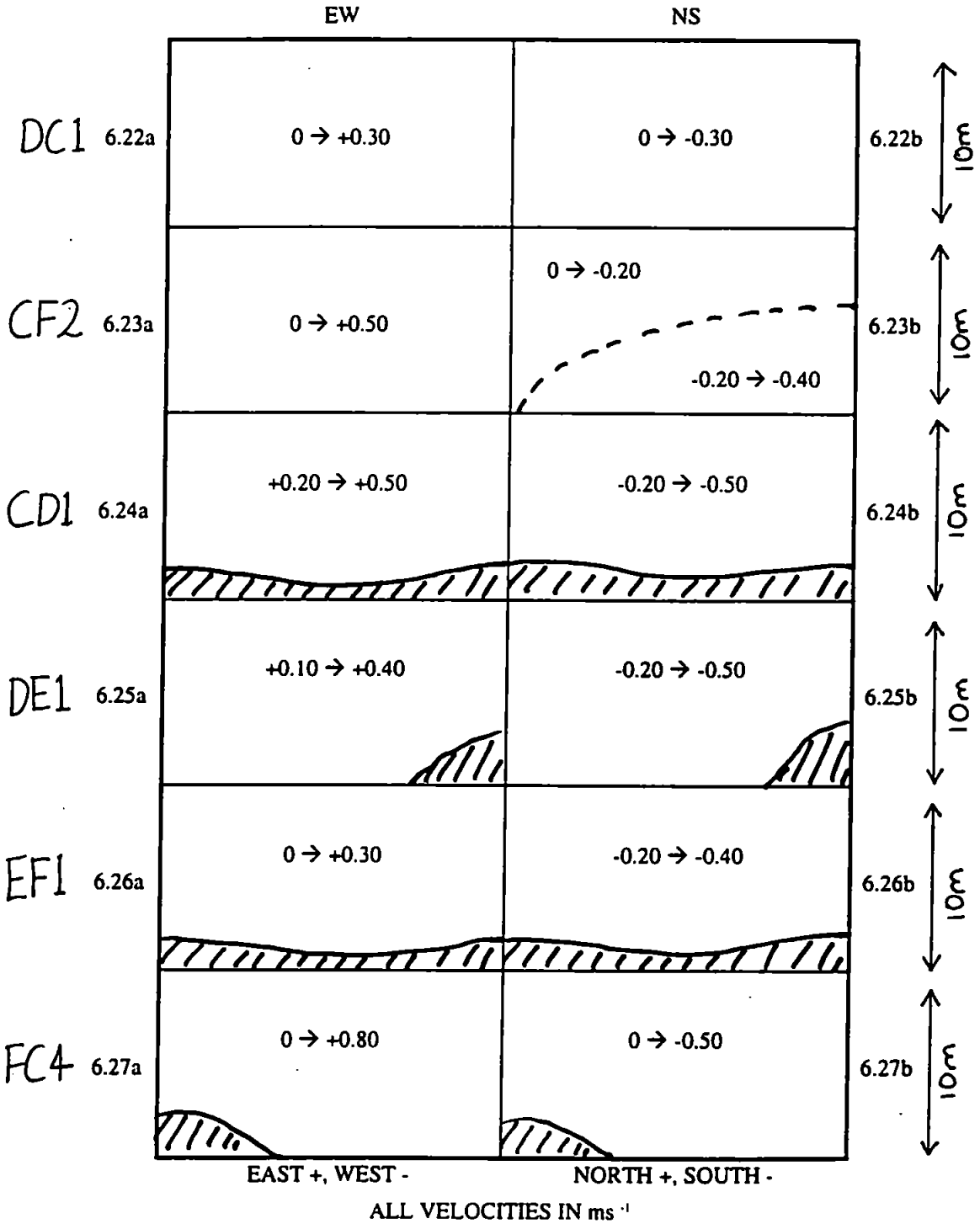

that more water flows into the south side of the survey box than flows out of the north side. The linear increase in average vertical velocity with depth suggests that this deceleration in northwards flow is uniform with depth, i.e. the whole depth of the measured water column undergoes the same reduction in velocity over the same distance. This is not to say that the whole depth of the transect will necessarily experience a change in flow direction at the same time. In fact, the north-south velocity plot for transect BC1 (figure 6.3b) suggests that this is not the case, with the shallower depths of the transect showing on average a northwards flow of 0.03 m $s^{-1}$, and the deeper part of the transect showing a southerly flow of about 0.03 m $s^{-1}$. This flow pattern is unusual in that it suggests that the deeper water has undergone a flow reversal, and has started to ebb before the shallower water. In estuaries, it is more usually the case that the surface layer starts to ebb before the deeper layer, causing tidal straining which increases the stratification. It may be that flow reversal, at or near high water, occurs at different times in the Lynher and Tamar rivers. Hence, if the Tamar river starts to ebb before the Lynher, and if Tamar water is denser than Lynher water (which appears to be the case from temperature and salinity data), this provides a possible explanation for the observed pattern of flow reversal in box 1N.

The next survey of the northernmost box (box 2N) was conducted between 1 hour and 26 minutes and 2 hours and 5 minutes after high water. The average vertical velocities calculated in this box are downwards and slightly larger than those calculated for box 1N (see figures 2a and 2b, appendix). The front was clearly observed in this survey box and the ADCP transects show that the Tamar water flowed south-westerly to the north of the front whilst the Lynher water flowed mostly south-easterly to the south of the front. The convergence along the axis of the front is believed to generate the increased downwards velocity in this survey box. The velocity again increased linearly with depth which suggests that the degree of convergence between the Lynher and Tamar waters was maintained throughout the depth of water measured with the ADCP. This is supported by the east-west and north-south velocity plots for transect FA2 (figures 6.5a and b), and by the east-west plot for AB2 (figure 6.6a), in which the frontal zone can be identified over the whole depth of the transects. However, it should be noted that the frontal zone illustrated by the east-west velocities of FA2 in particular is not vertically orientated, but inclined in such a way that the Lynher water appears to form a "wedge"

overlying the Tamar water. This observation is consistent with the ETS data which show that the Lynher water was slightly less dense than the Tamar water during the three days of surveying. However, Parsons (1987) concludes that the Lynher flow intrudes under the Tamar flow from his survey results, which suggests that the structure of the front may vary with mixing, tidal range and river in-flow. The north-south velocity plots show a southwards flow of as high as 0.50 m $s^{-1}$ for all four sides of the box, except for the central section of transect BC2 (figure 6.7b) which exhibits a northwards flow of up to 0.10 m $s^{-1}$.

Box 3N was surveyed between 1 hour and 38 minutes and 2 hours and 16 minutes after high water. It is comprised of transects AB2, BC2 and CF3 which are the same in box 2N, and additionally transect FA3. The exact location of the front is not clear from the ADCP data from transect FA3 alone (figure 6.9a and b), and was identified using a combination of surface observations and ETS data. The downwards vertical velocities for this box also suggest that a convergent front is present, given that the values calculated are the largest for all three survey days (see figures 2a to 2j, appendix). These values increase linearly with depth to approximately 5 m below the surface, where the gradient of the depth profile decreases slightly, indicating that convergence in the frontal zone may not be quite as strong in deeper water as it is near the surface.

In box 4N, surveyed from 1 hour 50 minutes to 2 hours 25 minutes after high water, the front is clearly visible in the east-west velocity matrix for transect AB3 (figure 6.10a). Again, it is seen to be sloping, with eastwards flowing, less dense Lynher water overlying westwards flowing, denser Tamar water in the form of a wedge. Transect AB3 runs from A to B on the survey grid (figure 2.4, section 2.3), and combining these data with transect FA2 which runs from F to A, we can visualize the front in the following way:

*Figure 6.28 Schematic of frontal wedge*

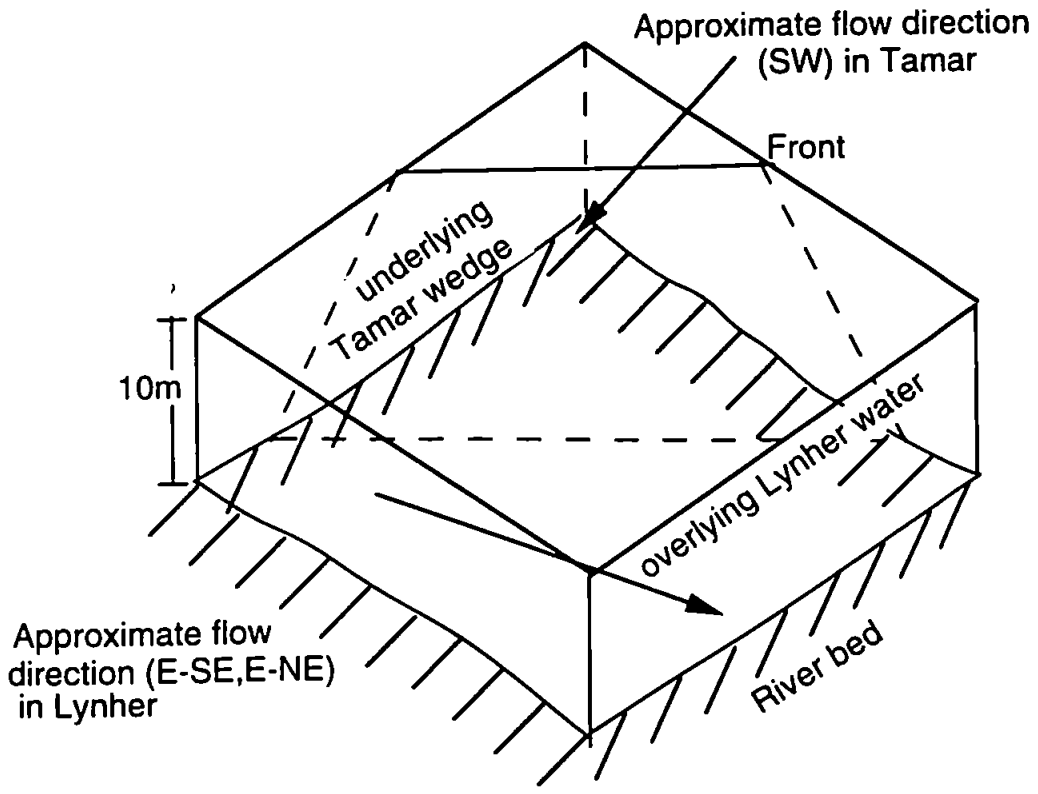


The north-south velocities from transect AB3 (figure 6.10b) show strong southward flow at each end of the transect, but indicate weak northwards flow in the region of the front. At this stage in the ebb tide, the northerly flow must be the result of water flowing strongly eastwards, with a small northwards component, out of the mouth of the Lynher river. The average vertical velocities for box 4N are directed downwards and are the second largest calculated over the three survey days (figures 2a to 2j, appendix). Similarly to box 3N, the velocities increase linearly to approximately 5 m depth, after which the degree of convergence in the frontal zone is assumed to decrease.

Boxes 5N and 6N, recorded between 2 hours 14 minutes and 3 hours 11 minutes after high water (but on a different survey day to boxes 1N, 2N, 3N and 4N) have both been analyzed assuming that the front is not present. No surface indication of the front was observed on any of the transects, and temperature data from the ETS show no significant

change which could be associated with the front. Referring to figure 2.4, section 2.3, the ADCP data from transects along sides F to C (FC1 in box 5N and FC2 in box 6N) and C to B (CB1 in both 5N and 6N) in both the boxes show fairly uniform eastwards flow as high as 0.40 m $s^{-1}$ (figures 6.11a, 6.12a and 6.15a). However, sides B to A (BA1, figure 6.13a and b) and sides A to F (AF1, figure 6.14a and b) suggest that the front may still be present in this northernmost corner of the survey box. In transect BA1, eastwards flowing Lynher water overlies westwards flowing Tamar water (figure 6.13a), as seen previously in boxes 2N, 3N and 4N. In transect AF1, there appears to be a "tongue" of westward flowing water at the northern end of the transect between 4 m and 9 m depth, which extends to just less than halfway along the transect (see figure 6.14a). Overlying this tongue of Tamar water is a layer of water flowing east at up to 0.15 m $s^{-1}$ and if this flow direction, measured at 2.2 m depth, can be extrapolated up to the surface, this would explain why no surface convergence was observed. Similarly in transect BA1, if the velocities recorded at 2.2 m depth are extrapolated upwards, then the surface flow is predominantly eastwards and no surface foam line was produced. The north-south velocity from the west corner of boxes 5N and 6N (i.e. point B in the survey grid) shows that the water flowing out of the Lynher river has a small northwards component of up to 0.10 m $s^{-1}$, as transects CB1 and BA1 demonstrate (figures 6.12b and 6.13b). This northward flow is also observed along side A to B of box 4N (figure 6.10b), and thus it would seem that as the ebb tide progresses, water from the Lynher flows strongly eastwards and slightly northwards across the northern part of the survey area, causing the front to be pushed back up the Tamar river. The ADCP data from boxes 5N and 6N also suggest that the retreating "tongue" of Tamar water is also covered by a layer of south-easterly flowing Lynher water, approximately 2 to 3 m thick, such that the relationship between Tamar and Lynher water at this stage of this tide can be summarised in figure 6.29:

*Figure 6.29 Schematic of retreating tongue of Tamar water*

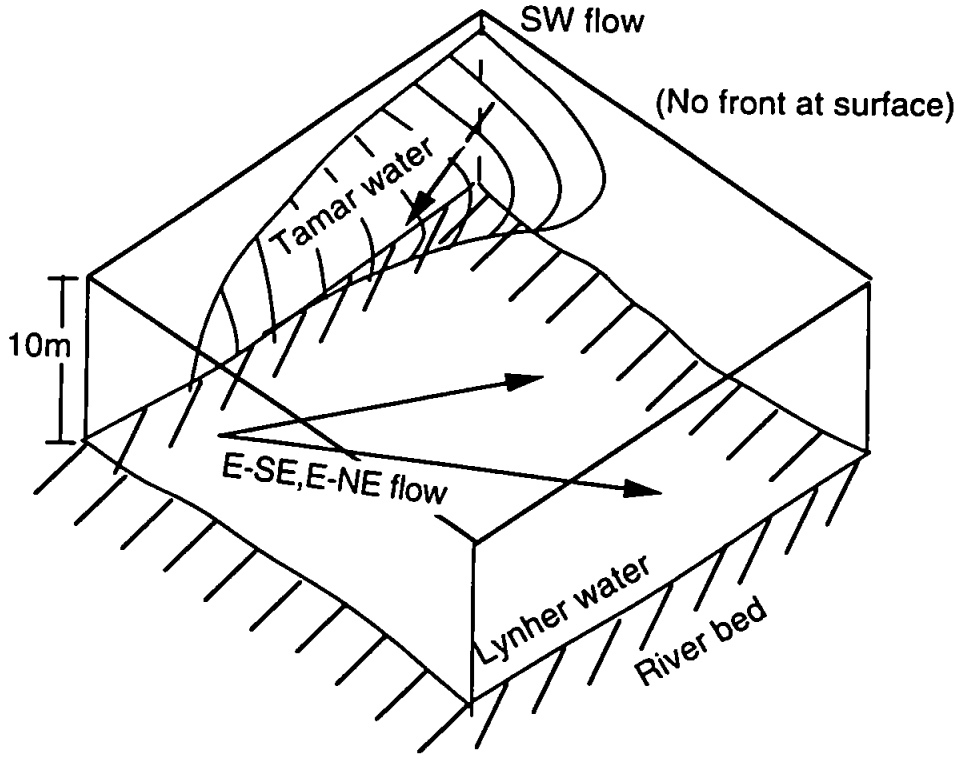


The front is still inclined in the same direction as in boxes 2N, 3N and 4N, but Tamar water occupies a smaller volume of the survey box with Lynher water in the remaining, much larger volume. The area of the frontal plane is also reduced in boxes 5N and 6N compared with 2N, 3N and 4N, and the average vertical velocities calculated show a corresponding decrease in magnitude, whilst still being directed downwards (figure2a to 2j, appendix). In both boxes 5N and 6N, these velocities are close to zero down to approximately 3 m depth, where they increase slightly and remain constant from 6 m to 9 m. These depth profiles of vertical velocity appear to be consistent with the supposition made earlier that both the volume of the Tamar water in the survey box and the front itself are submerged under a 2 to 3 m thick layer of Lynher water, so that the convergent frontal zone does not extend up to the surface.

Box 7N was surveyed from 3 hours 51 minutes to 4 hours 19 minutes after high water, and the front was again crossed on the northernmost two sides of the box. On each of the southernmost two sides, ADCP data identify a region of increased horizontal gradients in both the east-west and north-south velocities, which is interpreted as the boundary between Lynher and Tamar water (figures 6.18a, b and 6.19a, b). Figure 6.30 summarises the relationship between Lynher and Tamar water at this stage in the tide in box 7N:

*Figure 6.30 Schematic of Lynher jet*

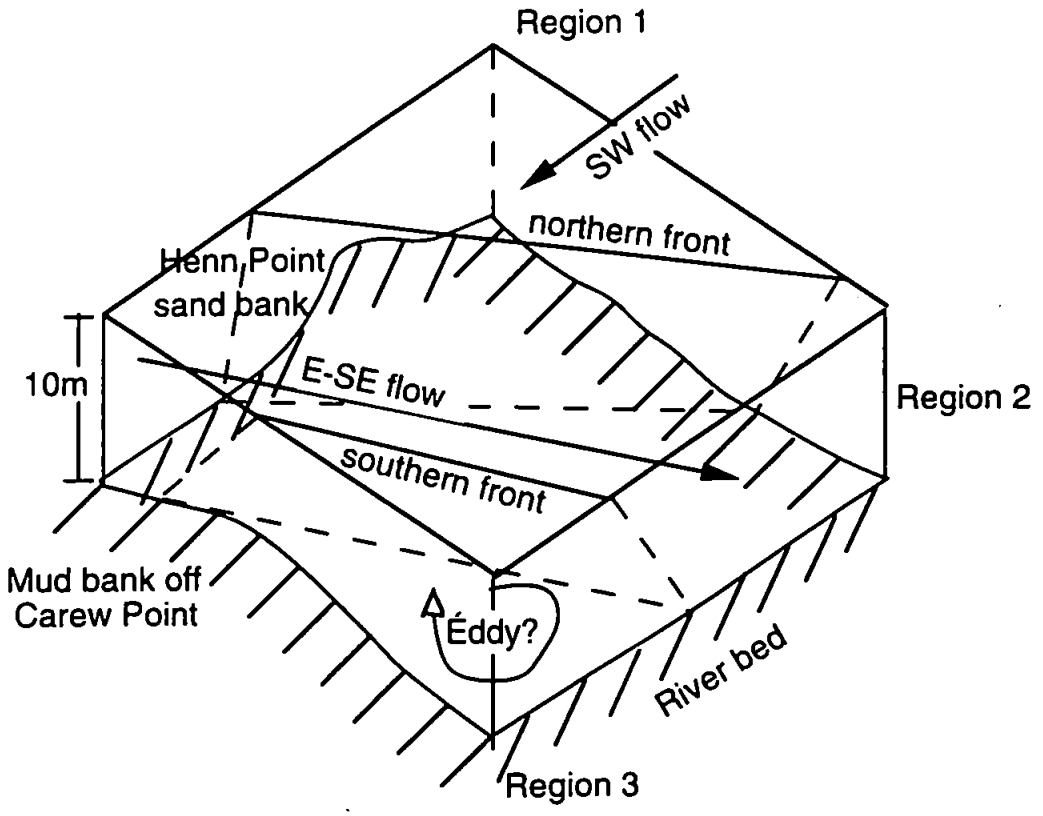


The Tamar water in region 1 is flowing in a south-westerly direction and the Lynher water in region 2 is flowing strongly eastwards (with velocities averaging 0.50 m $s^{-1}$) with a smaller southwards component (0.15 m $s^{-1}$) near the west corner of the box (figures 6.16a, b and 6.19a, b). On the east side of the box, the Lynher water is now flowing at approximately 0.35 m $s^{-1}$ east and 0.60 m $s^{-1}$ south (figures 6.17a, b and 6.18a, b), so the direction of the flow has swung round to a more southerly direction as

the water traverses the box. Region 3 presents a more complex situation. Temperature data from the ETS indicate that this is Tamar water, and along side B to C of box 7N, it has a velocity of about 0.09 m $s^{-1}$ west and 0.01 m $s^{-1}$ north (figure 6.19a, b). However, along side F to C, it has a velocity of 0.11 m $s^{-1}$ east and on average 0.44 m $s^{-1}$ south (figure 6.18a, b). The complexity of the flow pattern in region 3 can possibly be ascribed to its position over a mud bank near the river shore where friction would have some effect on the flow. Also, it can be seen from figure 6.30 that the Lynher water flows across the survey box in the form of a 'jet', as it exits the Lynher mouth. This jet of water may possibly introduce eddy effects as it extends into the Tamar flow, which may account for the irregular flow pattern indicated from the ADCP results.

Considering now the average vertical velocity, $\overline{w}$, calculated for the survey box, whilst this is still directed downwards over most of the depth profile, its magnitude is much smaller than in boxes 2N, 3N and 4N, and significantly smaller than in boxes 5N and 6N (figures 2a to 2j, appendix). In these preceding five boxes, there has been a small northwards component of flow exhibited by the Lynher flow over at least part of the survey box. The front in each of these boxes is orientated in an almost east-west direction. Therefore it is postulated that it is the north-south flow component which is most influential in generating the frontal convergence, in comparison to the east-west flow which contributes greatly to shear along the front but does not necessarily promote convergence and downwelling in the frontal zone. So, in the earlier stages of the ebb tide when the Lynher water had a northwards component as it flowed out of the Lynher mouth, a greater degree of convergence and downwelling would be expected than at this stage in the ebb tide, when water flows out of the Lynher mouth in an east to south-east direction. This explanation may account for at least part of the observed reduction in $\overline{w}$ values for box 7N. In addition to a change in direction of the Lynher flow as the ebb tide progresses, it is likely that the small $\overline{w}$ magnitudes are the result of an acceleration in the Lynher flow from the west to the east side of the box. The ADCP transects from the four sides indicate that this is the case (figures 6.16a, b to 6.19a, b). An acceleration in the Lynher flow calculated solely from these ADCP transects will include both spatial and temporal components. The admiralty chart of the survey area (figure 6.31) shows that the river bed slopes down from the mouth of the Lynher in a south-east direction

towards the centre of the Tamar by about 6 or 7 m within box 7N. It is suggested that water from the Lynher accelerates down this slope such that there is a spatial acceleration across the box from east to west in the surface layers. Hence, more water flows horizontally out of the box than flows into it, and in the absence of any frontal downwelling, this situation would cause the $\overline{w}$ values (representing the average vertical velocity over the whole box at the same point in time) to be directed upwards. In the case of box 7N, the proposed spatial acceleration, instead of producing upwards $\overline{w}$ values, works to reduce the downwards $\overline{w}$ values generated by frontal downwelling. Not only does the river bed topography affect the $\overline{w}$ values, it also appears to constrain the jet of Lynher water, such that the position of the frontal zones to the north and the south of the jet can be approximately described by the 10 m depth contour on the admiralty chart (figure 6.31). The northernmost front is just south of the Henn Point sand bank and the weaker southern front is located just off the mud bank at the river's edge off Carew Point.

### *6.1.2 The Southernmost Survey Box*

Considering now the southernmost part of the survey grid, and discussing the three survey boxes in this area chronologically, box 1S was recorded between 12 minutes and 1 hour 12 minutes after high water. Side C to F (transect CF1) was surveyed first, and the ADCP data indicate that the tide was turning, with some northward velocities being recorded in the shallower depths of the transect, whilst the flow is directed south in the underlying water (figure 6.4b). The east-west data show a small westwards flow over most of the transect (figure 6.4a), and it seems that the deeper water had undergone a flow reversal sooner than the shallower water. This was also observed in box 1N, and it is suggested that flow reverses sooner in the Tamar river than in the Lynher, with Tamar water forming the underlying layer in this survey box, as described previously in section 6.1.1. The remaining three transects in the box showed gradually increasing south-easterly flow (figures 6.20a, b to 6.22a, b), so it appears that the tide had turned slightly later here than in box 1N further north. Generally, flood currents in an estuary will reverse direction sooner at the upstream extent of the seawater intrusion than further downstream because of the increased influence of river flow and the shallower water depths leading to increased bed friction. The $\overline{w}$ values calculated for box 1S are

*Figure 6.31 Admiralty chart of survey area*

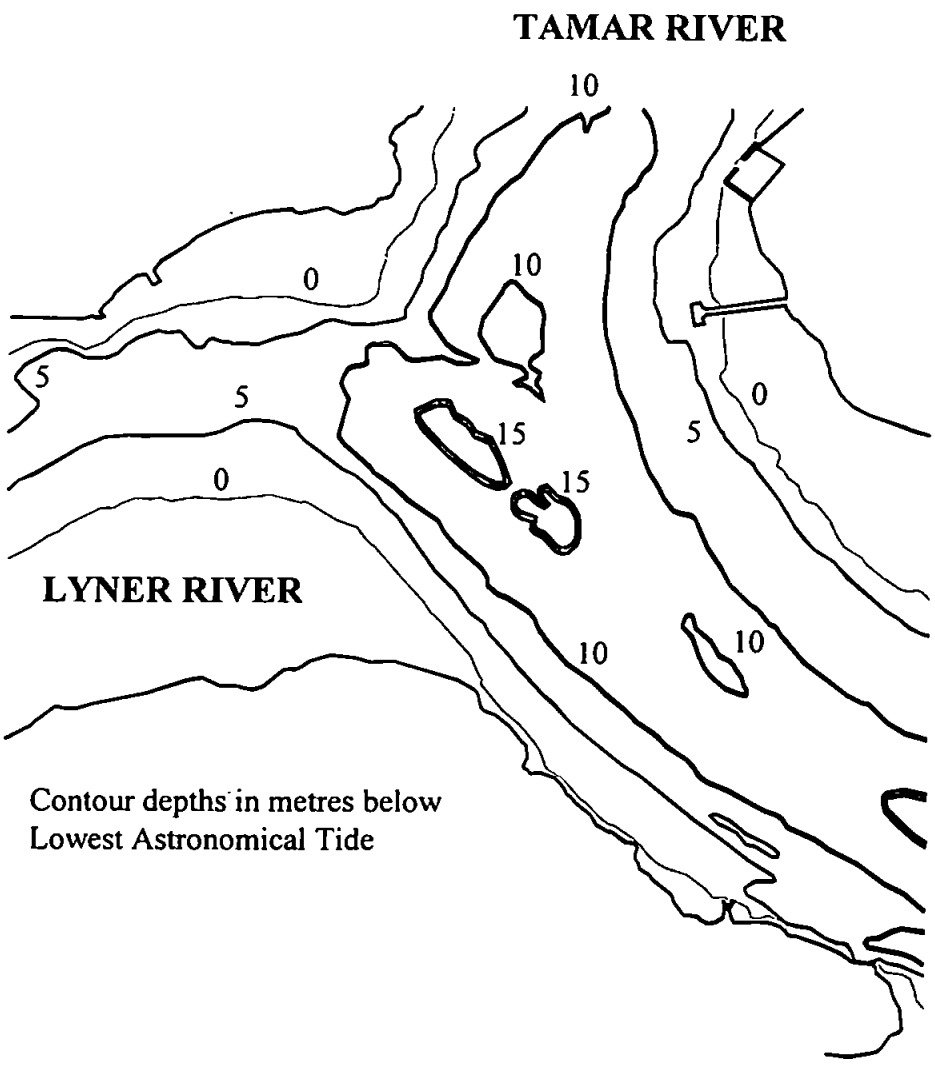

directed upwards and increase linearly with depth (figures 2a to 2j, appendix). Given that these values are effectively calculated at the start time of the survey box, their upward direction suggests that more water is flowing horizontally out of the survey box than is flowing into it. Hence, the approximately south-easterly flow is increasing in a south-eastwards direction i.e., it is increasing longitudinally as we move from side C to F to side D to E of box 1S. The linear increase in $\overline{w}$ with depth indicated that the increase in longitudinal velocity is uniform with depth.

Box 2S was surveyed slightly later than box 1S, from 41 minutes to 1 hour 22 minutes after high water. Calculated values of $\overline{w}$ for this box are again directed upwards but have a smaller magnitude than in box 1S, suggesting that the longitudinal velocity gradient had decreased. This assumption agrees with the north-south velocity data from transect EE09 (side C to F of box 2S) which show that the flow is now almost entirely southwards, with stronger flows of up to 0.40 m $s^{-1}$ in the deeper water, and flows of between 0 and 0.20 m $s^{-1}$ in the shallower water (figure 6.23b). The values of $\overline{w}$ for box 2S remain approximately constant with depth (figure 2i, appendix), so that the longitudinal gradient in south-eastwards velocity must be decreasing with depth. Comparison of the north-south velocities from transects CF2 and ED1 (figures 6.23b and 6.21b respectively) reveals this to be a reasonable interpretation because transect ED1 has velocities of up to 0.40 m $s^{-1}$ over the entire depth of the transect. Hence, by the time box 2S was surveyed, the reversal of flow associated with high water was almost complete in the southern half of the survey grid.

Box 3S was surveyed much later in the ebb, from 4 hours 47 minutes to 5 hours 25 minutes after high water. The flow was then directed approximately south-east over the whole survey box, and inspection of the east-west and north-south velocities for each of the four transects reveals that both the southwards and eastwards velocities for sides C to D and D to E (CD1 and DE1, figures 6.24a, b and 6.25a, b) were larger than the equivalent values for sides E to F and F to C (EF1 and FC4, figures 6.26a, b and 6.27a, b). This observed acceleration has both spatial and temporal components. Considering the plot of the mean tidal velocity ( $\overline{V}_T$ ) which was directed nearly south-east, for each transect against the time after high water at which it was recorded (figure 1c, appendix), the gradient of this graph is negative i.e. the flow is decelerating with time at this stage

of the tide. As sides E to F and F to C were surveyed later than sides C to D and D to E, the observed acceleration maybe wholly temporal. However, the $\overline{w}$ values for Box 3S are all directed upwards (figure 2h, appendix), suggesting that there is also a spatial acceleration across the box, from its north west corner to its south east corner. The $\overline{w}$ values increase to 4 m depth and then remain constant, suggesting that the magnitude of the spatial acceleration decreases with depth. The front was not present in box 3S, whereas it was observed on side F to C of box 7N earlier in the ebb. However, of the four transects in box 7N, the front was least distinct along side F to C. Therefore, in the time between surveying boxes 7N and 3S, it is suggested that the front along the southern side of the jet of Lynher water may have been weakened by cross-frontal mixing to the point where it was no longer visible along side F to C. Additionally, the curvature in the path of the Tamar river causes the Tamar water to change direction from south-west to south-east as it flows round the bend.

### *6.1.3 Summary of Frontal Evolution*

From the ADCP transects and average vertical velocity data described above, the behaviour of the Tamar and Lynher water in the region of the survey grid during the course of an ebb tide can be summarised as follows. Initially, at around the time of high water, the flow reversal in the northern part of the survey area occurs slightly before the flow reverses in the southern part. Additionally, the deeper water, below approximately 8 m depth undergoes a flow reversal sooner than the overlying water, over the whole survey grid, due to bed friction retarding the flow in the lower layer. After the tide has turned completely, the flow is directed south-easterly in the southern part of the area, and is accelerating in the downstream direction. In the northern part of the area, most of the water flowing out of the Lynher mouth is directed south-eastwards with a small volume of water curling round to have a northwards component as it exits the Lynher mouth. This Lynher water meets the south-westwards flowing Tamar water in the northernmost corner of the survey grid, to form a convergent front. The northwards component of the Lynher flow increases, an acceleration reflected in the increased level of convergence and downwelling in the frontal zone. The frontal zone itself slopes upwards in an upstream direction, such that the marginally denser Tamar water forms a wedge underlying the Lynher water. The continued increase in the velocity and volume of water flowing out of the Lynher then causes the frontal zone, which is orientated

approximately east-west at the surface, to be pushed northwards until it is just present in the northernmost corner of the survey grid. The lowering water level, as the ebb tide progresses, causes the river bed topography to then become influential in determining the path and acceleration of the Lynher water across the survey area, such that this water now forms a jet with a strong eastwards velocity component. This jet is constrained to the north by the inclined frontal zone described earlier which forms just south of the Henn Point sand bank. To the south, the jet is constrained by a weaker frontal zone orientated approximately north-west to south-east at the surface, which is located just upstream of the river-edge mud bank off Carew Point. The northern front has moved back southwards again by this time, as a result of increasing velocities in the Tamar river. Examination of the admiralty chart (figure 6.31) of the survey area suggests that the north and south boundaries of the Lynher jet are approximately described by the 10 m depth contour. The northwards component of the Lynher flow has at this stage disappeared, causing convergence and downwelling in the northern frontal zone to be reduced. The weaker southern front then diminishes to the extent that it is no longer detectable, possibly as a result of its position in comparatively shallow water (7 m depth) allowing turbulence generated by bed friction to reduce horizontal salinity and velocity gradients across the front. Finally, in the southern part of the survey grid, the flow is almost uniformly directed south-east and is accelerating in the downstream direction. The time-scale of the events described above is represented in figure 6.32.

*Figure 6.32 Time-scale of frontal evolution*

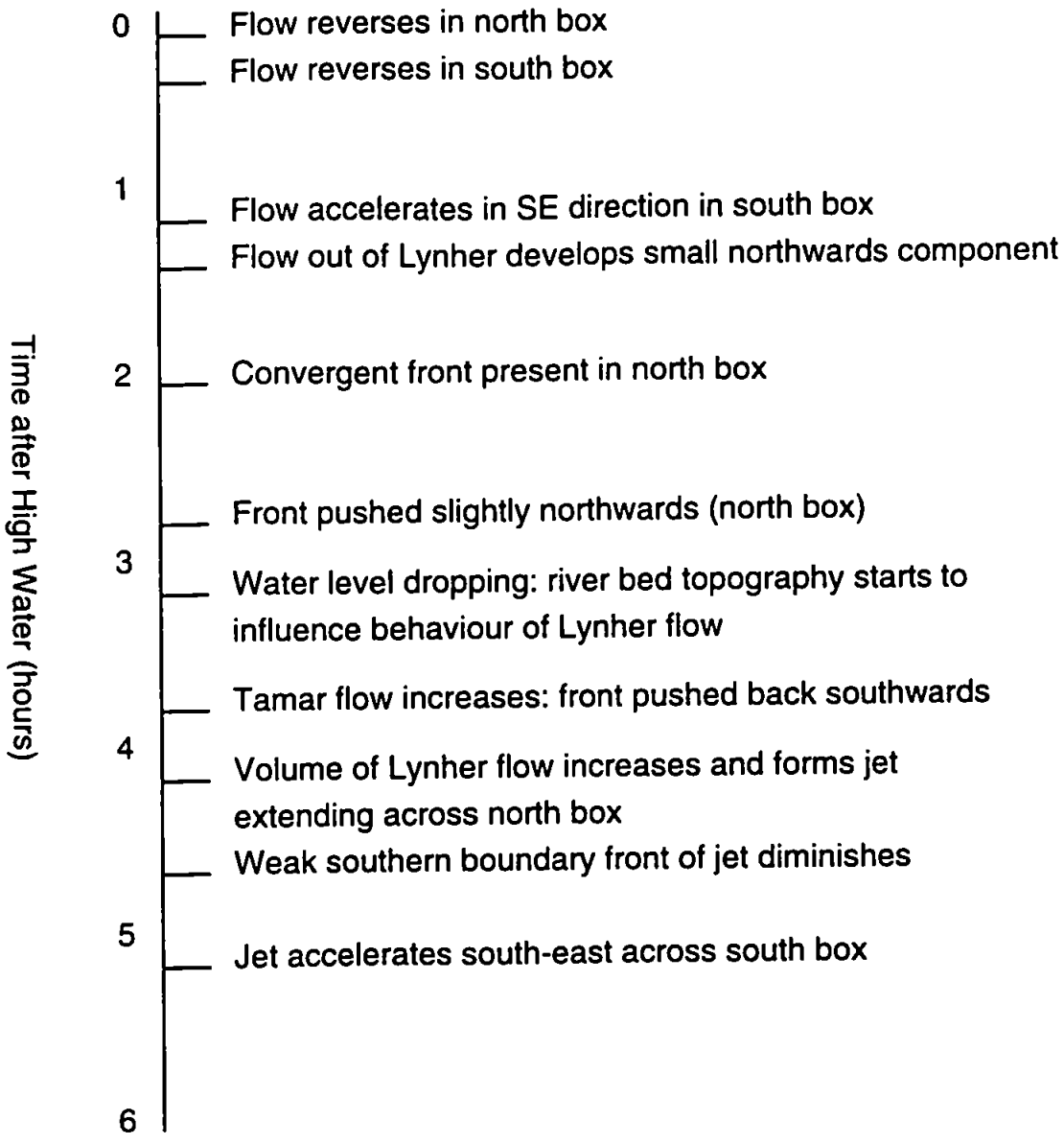


### *6.1.4 Cross-Frontal Transport*

An attempt to assess the cross-frontal transport of water has been made for boxes 2N, 3N, 4N and 7N using the principle of volume continuity, described in section 4.5. As explained in that section, in the case of boxes 2N, 3N and 4N, the excess or deficit water volume on one side of the front should equal the deficit or excess water volume respectively on the other side of the front. Similarly for box 7N, in theory there should

be a zero volume flux in volume 2 if the principle of continuity is observed. As the results of the analysis for all four boxes show (table 1, appendix), the principle of continuity is apparently not obeyed in any of the depth slices. The most likely source of error is the values of the average vertical velocity through the top and base of each slice. These average vertical velocities are determined from transects covering only a tiny fraction of the area over which they are assumed to be representative, in contrast to the average horizontal velocities used in the analysis, which can be determined much more accurately from the available data. Thus it seems that the vertical velocity varies considerably over the top and base areas of each slice, a factor which cannot be addressed satisfactorily with our data set in this analysis. The horizontal variability in the vertical velocity seems even more likely when the presence of the front itself is taken into account: given its convergent nature, increased downwelling and therefore larger vertical velocities would be expected in the frontal zone, in comparison to those recorded further away from the front.

Hence, there is no way of accurately quantifying the vertical velocity through the top and base area of each slice from our data set, and this shortcoming is manifested in the results. However, it may still be possible to determine at least the direction of transport of water across the frontal zone. In the case of boxes 2N, 3N and 4N, depth slices in which the calculated volume fluxes for volumes A and B are of opposite polarity are thought to be less erroneous than the results from other slices, since at least the polarity of the volume fluxes suggests transport of water in the same direction across the front. In these depth slices, it can be assumed that the calculated average vertical velocities are closer to the true values than in the other depth slices. The slices with opposite polarity volume fluxes suggest that the direction of transport of water across the front is from volume A to volume B in all three survey boxes, i.e. from the Tamar to the north of the front to the Lynher to the south.

A similar approach is used in the case of box 7N: here, the direction of transport across the two fronts in the box is probably indicated most reliably by depth slices in which the volume flux in volume 2 is closest to zero, which is the ideal solution. The three depth slices with the smallest volume fluxes for volume 2 show that the direction of transport across the northernmost front is from north to south, i.e. from the Tamar to the Lynher.

Across the southernmost front, the direction of transport again appears to be from the north, this time from the Lynher to the Tamar.

The analysis method followed also introduces a second complication to consider when examining the results. For both the northern and southern fronts, the frontal plane was assumed to extend vertically downwards from the observed surface line of convergence, to simplify the analysis. As the previous section describes, this is not the case in boxes 2N, 3N and 4N, where the frontal zone slopes down southwards from the surface foam line. In box 7N, the frontal plane appears to be less inclined and more vertically orientated, so the assumption made is more realistic in this case. However, in the previous three boxes, the cross-frontal transports have effectively been calculated over a vertical plane which is located within the wedge of south-west flowing Tamar water for most of the depth (see figure 6.28). The transports calculated through this plane would therefore be expected to indicate flow in an approximately southwards direction.

### *6.1.5 Mixing Across the Fronts*

In the case of the northern front, the Tamar water is thought to be transported across the front into the Lynher jet by entrainment. Turbulent diffusion may also be active across the front, but this process causes a transport of mass (or salt) but no net transport of water. Hence, the cross-frontal transport is the result of entrainment. The process of entrainment occurs because there is a strong element of shear between the overlying Lynher jet (flowing east-south east or even east-north east) and the underlying Tamar wedge, flowing south west. This shear may generate small, three-dimensional, internal waves on the interface between the two water masses, which then break and eject the slightly denser Tamar water upwards into the overlying Lynher water, such that the less turbulent Tamar water is entrained into the more turbulent Lynher jet. Whilst the breaking of each interfacial wave is a discrete process, it is one which occurs continuously over space and time so that, when averaged, it can be considered as a flow, i.e. a velocity of entrainment (Dyer, 1977). Very approximate estimates of this entrainment velocity have been calculated, as described in section 4.5, for those depth slices in which the volume fluxes on each side of the front indicate a cross-frontal transport of water in the same direction. The volume fluxes in each depth slice have been averaged, and in boxes 2N and 3N, the entrainment velocity appears to be in the region of 0.5 m $s^{-1}$. This figure increases to 0.7 m $s^{-1}$ in box 4N. In box 7N, the

entrainment velocity from volume 3 to 2 (see figure 4.8) is 0.4 m $s^{-1}$, and from volume 2 to 1 is 0.2 m $s^{-1}$. As these entrainment velocities have comparable magnitudes to the longitudinal velocities, they are thought to be unrealistically high. This is almost certainly the result of using inaccurate estimates of the average vertical velocity on each side of the front in calculating the entrainment velocities, as described in section 6.1.4. However, the interpretation of entrainment occurring across the front is consistent with the assumption that the Lynher water can be thought of as forming a turbulent, buoyant jet across the survey area at certain stages of the tide. Laboratory observations of a turbulent, buoyant jet (Crow and Champagne, 1971, Fischer et al., 1979) have shown that the shear layer between the jet (i.e. Lynher water) and the ambient fluid (i.e. Tamar water) comprises large, cylindrical waves that appear to entrain the ambient fluid and then break down to mix the two fluids. Whilst laboratory observations are not directly applicable to fieldwork observations, it seems that entrainment of the ambient Tamar water into the turbulent Lynher jet by breaking internal waves generated by shear along the interface between the two water masses, is likely to be occurring in the northern frontal zone.

In the weaker southern frontal zone, the calculated cross-frontal transport indicates the water from the Lynher jet is being transported across the frontal zone into the ambient Tamar water. In this case, the velocity of entrainment is directed out of the Lynher jet. A possible explanation for this is offered by laboratory observations of a turbulent, buoyant jet discharging into a cross-flow (Fischer et al., 1979). Again, any comparisons between laboratory and fieldwork observations should be treated with caution, however, the laboratory situation does seem reasonably analogous to the Lynher jet discharging into the flowing Tamar water. In the laboratory, a large, trailing eddy was observed to form along the side of the jet which was downstream in relation to the cross-flow. If an eddy forms similarly on the downstream edge of the Lynher jet, this may explain the calculated direction of entrainment, and also the complex flow pattern partially recorded in this region by the ADCP (see section 6.1) in box 7N.

### *6.1.6 Salt Fluxes*

An average vertical flux of salt has been calculated for the base area of each depth slice as described in section 4.4, and results are presented in the form of depth profiles for each box in figure (figures 4a to 4j, appendix). A comparison between the advective

and diffusive salt fluxes reveals that the advective fluxes are very much larger in magnitude than the diffusive fluxes, and therefore dominate the total salt flux values. Given that the salinity changes by only 1 or 2 $^{o}/_{oo}$ at most over the survey area, variations in advective salt flux (and therefore in the total salt flux) are primarily controlled by changes in velocity. Hence, it is not surprising to see that the vertical salt flux and the average vertical velocity vary in the same way, both with depth and time. It is also reasonable to assume that the cross-frontal transport of salt would be in the same direction as the cross-frontal transport of water and hence, the same arguments used to explain the velocity values in sections 6.1.2 and 6.1.3 are deemed applicable to the salt flux values.

## 6.2 PRIMARY MOMENTUM BALANCE

The primary momentum balance has been found for the longitudinal and lateral and equations of motion, for each slice of each survey box. This has been done by identifying the largest terms, such that each equation numerically balances, preferably to within $1 \times 10^{-5}$ in most cases, or to $2 \times 10^{-5}$ occasionally. For some slices, the desired balance is achieved using only the first two or three largest terms, whereas for other slices up to eight terms must be included to balance the equation to that level. The primary momentum balance for each slice is presented in table 5 (for the longitudinal equation) and table 6 (for the lateral equation) in the appendix. The terms have been ranked in order of magnitude, with the necessary number of terms included to balance the equation. This type of analysis allows us to identify the most important forces and accelerations present in each depth slice, and comment on the hydrodynamic processes occurring therein. However, whilst examining the two momentum balances in a depth slice, the geometry of the depth slice must be considered. In our analysis, the shape of the depth slice means the frictional force on the top and base of a slice is acting over a far larger area than the frictional forces on the sides and ends of the slice, and consequently appears larger than expected. If we divide each frictional force by the area over which it is acting (effectively reducing a depth slice to a cubic volume element of 1 $m^3$), it can be seen that the frictional force on the top and base of the cube is now two or three orders of magnitude less than the other frictional forces, as expected.

When assessing the terms in the equations of motion in order to understand the dynamics within each box, the Reynold's stress terms are the most difficult to interpret meaningfully. This is because they are both the cause and effect of the accelerations on the right-hand side of the equations at the same time. Velocity shear in the water column (effectively, a spatial acceleration) will produce turbulent momentum. This turbulent momentum is exchanged in such a way that the faster, more turbulent flow loses momentum to the slower, less turbulent flow. The Reynold's stress terms express this turbulent momentum exchange, which serves to reduce the velocity of the faster flow and increase the velocity of the slower flow, and it is for this reason that each of the terms is analogous to a frictional force. However, this frictional force works to reduce the velocity shear which initially gave rise to the turbulent momentum exchange. So the Reynold's stress terms are sometimes described as secondary forces, in that they

result from motion already present, rather than causing the motion in the first place. Effectively, having been initially generated by a spatial acceleration, they then 'damp out' that same acceleration, and therefore no simple relationship exists between the Reynold's stress terms and the accelerations.

In the following section, the primary momentum balances and their variation with depth will be considered for each box. In section 6.2.2, the boxes will be grouped together according to the day on which they were surveyed, and the temporal variation in their hydrodynamic regimes will be discussed in relation to the observations made in section 6.1. Finally, section 6.2.3 will attempt to describe and explain both the temporal and spatial variations in the hydrodynamics within the survey grid, over the course of a generalised ebb tide.

### *6.2.1 The primary longitudinal and lateral momentum balances for each box*

In this section, the primary momentum balances (tables 5 and 6, appendix) derived from the two horizontal equations of motion will be discussed for each of the ten survey boxes. As in section 6.1, the northernmost boxes will be considered first in chronological order, followed by the southernmost boxes of the survey grid. Figure 6.33 shows on which survey day and at what time after high water each of the ten boxes was recorded. Throughout the following discussion, the longitudinal dynamic pressure refers to $\partial\overline{(u'.u')}/\partial x$ in the longitudinal equation of motion. Likewise, lateral dynamic pressure is $\partial\overline{(v'.v')}/\partial y$ in the lateral equation. The remaining Reynold's stress terms in the two equations all represent gradients of turbulent shear stress and will be referred to in the following way: in the longitudinal equation, $\partial\overline{(u'.v')}/\partial y$ and $\partial\overline{(u'.w')}/\partial z$ are the lateral and vertical stress gradients respectively and in the lateral equation, $\partial\overline{(v'.u')}/\partial x$ and $\partial\overline{(v'.w')}/\partial z$ are the longitudinal and vertical stress gradients respectively.

***BOX 1N- recorded from high water (HW) - 0 hrs 27 mins to HW + 0 hrs 18 mins.***

The longitudinal momentum balance for box 1N is just between the accelerations and the all three Reynold's stress terms, in various combinations, throughout the whole depth of the box. Both the baroclinic and barotropic pressure gradients are comparatively small in magnitude, which suggests that the water surface elevation is virtually constant in the x-direction, and that the water in the box is longitudinally well-mixed. In a partially-mixed estuary such as the Tamar, bottom friction induced mixing during the

*Figure 6.33 Time and duration of survey boxes from all three days*

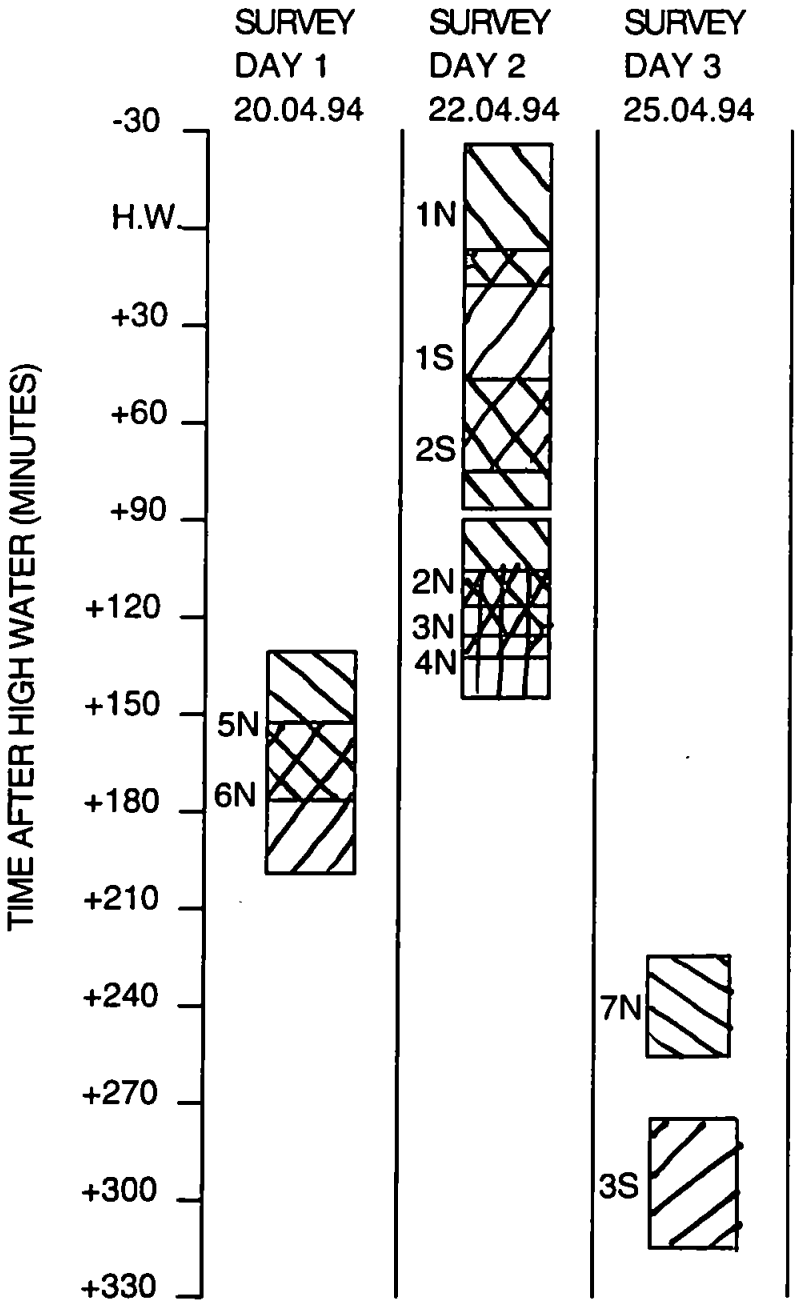

flood tide promotes the most longitudinally homogeneous density structure in the water column at high water, which appears to be the case in box 1N. However, the absence of any significant pressure gradients means that there is no primary forcing mechanism active in box 1N to produce the accelerations in the momentum balance. During the early ebb tide, tidal straining is often a notable feature of estuarine circulation and in this process, velocity shear in the presence of a longitudinal density gradient causes stratification. Whilst there is no significant longitudinal density gradient in box 1N, the presence of velocity shear would still produce turbulent stresses in the water column, which explains the predominance of the three turbulent stress gradients in the momentum balance. The Reynold's stress terms cannot initially generate a velocity, however they will serve to modify an existing velocity structure within the box. So it seems likely that the initial motion is produced by primary forces acting outside the area of box 1N, in another region of the estuary, and this momentum is then advected into the box. Closer examination of the accelerations within box 1N shows that down to approximately 9.3 m, the temporal acceleration which is positive downstream, is opposed by the non-linear term $\bar{u}.\partial\bar{u} / \partial x$ because there is northwards flow increasing in the -x direction. This apparent spatial acceleration may be present because the northerly side of the box was surveyed before the southerly side. Hence, the element of temporal variation in velocity introduced by the non-synchronous surveying method must be remembered when looking at all spatial acceleration terms, but its effect will be most pronounced in box 1N which was surveyed as the tide turned. Near the surface, only the lateral stress gradient is of significant magnitude and it indicates that there is an increased level of turbulent stress in the east of the box compared to the west. Turbulent momentum will therefore be transferred from east to west such that the magnitude of the associated frictional force increases in the -y direction, which is equivalent to an acceleration in the +y direction. Below 2.8 m, the presence of the longitudinal dynamic pressure in the balance suggests that the more turbulent flow is in the north of the survey box so that friction increases along the -x axis. Additionally, in the deepest layer of the box, turbulent stress increases with depth, as shown by the vertical stress gradient in the balance, and this is attributed to the proximity of the river bed and the consequent increase in friction. The spatial accelerations at this depth show that the flow is still directed north in the east side of the box but is south on the west side. Again, as the east

side was surveyed first, this is possibly more of a temporal acceleration than a genuine spatial one. If there is a degree of spatial acceleration present, then turbulent stress appears to be higher in the water which is still flowing northwards. The northwards (-$\bar{u}$) flow is decelerating with depth.

Considering the lateral balance, for most of the depth of box 1N there is little lateral acceleration because the two primary forces oppose each other, i.e. the water surface elevation increases in the +y direction, producing an acceleration in the -y direction, whereas the presence of denser water on the east side of the box generates an acceleration in the +y direction. The denser water also appears to be more turbulent, as indicated from the lateral dynamic pressure in the near surface momentum balance. With increasing depth, the vertical stress gradient shows that turbulent momentum and friction also increase, and in the lowest layer of the box, the $\bar{w}.\partial\bar{v}/\partial z$ term shows that the -$\bar{v}$ flow is accelerating with depth. Considering both the vertical advection of lateral momentum and the equivalent term, $\bar{w}.\partial\bar{u}/\partial z$ in the longitudinal equation, the overall direction of the flow at depth seems to be rotating round from north to east. This rotation may be due to the tide turning; alternatively it may be an artefact introduced by the element of time-averaging inherent in the calculation of vertical advection terms.

***BOX 2N- recorded from high water (HW) + 1 hrs 26 mins to HW + 2 hrs 05 mins.***

In the longitudinal balance, the two horizontal pressure gradients provide the primary forcing mechanism which generates longitudinal acceleration in box 2N. In the shallowest layer of the box, only the barotropic component is important and it shows that the water surface elevation increases in the -x direction i.e. the surface slopes downwards in the downstream direction. This causes the longitudinal flow to accelerate downstream producing a large $\bar{u}.\partial\bar{u}/\partial x$ term to add to the temporal acceleration. Below 1.8 m, the baroclinic pressure gradient indicates that denser water is present on the downstream side of box 2N, which produces an upstream directed force. Initially, the barotropic component still has a large enough magnitude to overcome the opposing baroclinic force and maintain the temporal and longitudinal accelerations. However, with increasing depth the baroclinic component increases in magnitude and the longitudinal acceleration reduces accordingly. This decrease in acceleration may also explain why the vertical stress gradient shows that turbulent longitudinal stress is also decreasing with depth.

In the lateral momentum balance, the situation is similar in that the slope of the water surface provides the primary forcing mechanism in the shallowest layer. The surface elevation increases in the +y direction such that the Lynher-side of the box has a higher surface elevation than the Tamar-side. Examination of the $\bar{v}.\partial\bar{v}/\partial y$ term shows that the acceleration is the result of the presence of $-\bar{v}$ flow on the Lynher side and $+\bar{v}$ flow on the Tamar side, such that there is a convergent front where the two water masses meet which is reflected by the line of foam and debris observed at the surface in box 2N. Hence, the barotropic pressure gradient will enhance the easterly flow of the Lynher water and reduce the westerly flow of the Tamar water. Below 1.8 m, denser water present on the Tamar side of the box produces a force acting in the +y direction to oppose the barotropic component and generate a $+\bar{v}$ flow. Additionally, the vertical stress gradient indicates that turbulent lateral stress is increasing with depth. The $\bar{u}.\partial\bar{v}/\partial x$ term shows that the flow has a $+\bar{v}$ component on the downstream side of the box and a larger $-\bar{v}$ component on the upstream side. Below 5 m, the $-\bar{v}$ flow decreases quite rapidly with depth, shown by $\bar{w}.\partial\bar{v}/\partial z$, and finally becomes a $+\bar{v}$ flow in the lowest level of the box, owing to the baroclinic pressure gradient increasing with depth. Given that the front is present in this box, we can postulate that the shallower, Lynher water is primarily accelerated by the barotropic pressure gradient, whereas the deeper, Tamar water is accelerated by the baroclinic pressure gradient. The shear produced between these two layers may result in the turbulent momentum exchanges expressed by the vertical stress gradients.

***BOX 3N- recorded from high water (HW) + 1 hrs 38 mins to HW + 2 hrs 16 mins***

Throughout the depth of box 3N, the two longitudinal pressure gradients are again of comparable magnitude but of opposite sign, to provide the primary forcing mechanism. The water surface slopes downwards downstream to accelerate the flow in the +x direction whilst the presence of denser water downstream accelerates the flow upstream. From the surface to 3.3 m, the longitudinal dynamic pressure is also significant indicating decreasing turbulent stress in the +x direction, such that turbulent momentum is transferred from the upstream to the downstream side of the box, so that the frictional force and the barotropic component overcome the opposing baroclinic force. Hence, the temporal acceleration is positive, and the $\bar{u}.\partial\bar{u}/\partial x$ shows that the downstream velocity

increases in the downstream direction. Below 3.3 m, the temporal acceleration is less important and the vertical stress gradient is now complementing the barotropic component. Turbulent longitudinal stress is therefore decreasing with depth. At around 5 m depth, the baroclinic component has increased in magnitude so that it now cancels the barotropic force, hence there is no primary forcing mechanism operating in this particular region of the flow. Whilst the spatial acceleration has decreased slightly in comparison to the near surface flow, it still has an appreciable magnitude and it is suggested the transfer of turbulent momentum down into this region from the shallower water is responsible for sustaining this acceleration which itself must have originated outside of the region. In the lowest layer of box 3N, below 6.8 m, the barotropic component and the vertical stress gradient once again outweigh the other pressure gradient to produce a downstream spatial acceleration. However, the $+\bar{u}$ component of velocity is also decreasing with depth as shown by the negative $\bar{w}.\partial\bar{u}/\partial z$ term.
The dynamics described by the lateral balance are similar to those in box 2N. Once again, the two pressure gradients oppose each other and show that the water surface slopes downwards from the mouth of the Lynher river out to the central region of the Tamar, whilst the presence of denser Tamar water on the east of the survey box opposes that acceleration. In the near surface Lynher flow, just the presence of the surface slope is sufficient to balance the $\bar{v}.\partial\bar{v}/\partial y$ term, as in box 2N. Again, inspection of $\bar{v}.\partial\bar{v}/\partial y$ shows that the flow has a $-\bar{v}$ component in the Lynher mouth but a $+\bar{v}$ component on the Tamar side of the box, generating a convergence. The barotropic component enhances the $-\bar{v}$ (eastwards) flow, and reduces the $+\bar{v}$ (westwards) flow which cannot have been initially generated by the barotropic gradient within the area of box 3N. Hence, the $+\bar{v}$ flow has been initiated elsewhere in the estuary and has subsequently been advected into box 3N. Below about 2.8 m, the baroclinic component becomes larger, although unlike in box 2N, it never becomes large enough to overcome the barotropic component and as a result, the $+\bar{v}$ flow on the Tamar side is decreasing with depth due to the influence of the stronger barotropic force. The substantial decrease in $+\bar{v}$ flow with depth is reflected by the comparatively large magnitude of the $\bar{w}.\partial\bar{v}/\partial z$ term in the deepest layer of the box. As in box 2N, the vertical stress gradient suggests that turbulent stress is increasing with depth in this layer.

***BOX 4N- recorded from high water (HW) + 1 hrs 50 mins to HW + 2 hrs 25 mins***

In the longitudinal balance of this box, the water surface is again more elevated upstream to generate a downstream directed force such that there is a spatial acceleration downstream in the $\bar{u}$ velocity component, and a positive temporal acceleration. The water downstream is denser and counteracts the barotropic pressure gradient, as seen previously in boxes 2N and 3N. The larger barotropic component successfully exceeds the baroclinic force from the surface to 6.3 m, when vertical advection and the longitudinal dynamic pressure additionally become important. The $\bar{w}.\partial\bar{u}/\partial z$ term shows that the average longitudinal velocity over the whole area of box 4N is decreasing with depth as a result of the baroclinic component increasing with depth. In addition, the longitudinal dynamic pressure indicates that the flow is more turbulent upstream. At around 7 to 8 m depth, the two pressure gradients cancel out, however, whereas in box 3N there was still a net acceleration when the pressure gradients cancelled, in this box the net acceleration now drops to zero at this depth. Below this level, the baroclinic force is solely responsible for the reduction in longitudinal velocity with depth.

Considering the lateral balance, the relationship between the opposing pressure gradients again controls the dynamics. In the shallower half of the box, the increased surface elevation of the Lynher water produces the lateral spatial acceleration, $\bar{v}.\partial\bar{v}/\partial y$, which again shows $-\bar{v}$ Lynher flow and $+\bar{v}$ Tamar flow. Also, the $\bar{u}.\partial\bar{v}/\partial x$ term has again become significant in this box, as it was in box 2N, and shows weak $+\bar{v}$ flow on the downstream side and strong $-\bar{v}$ flow on the upstream side. This flow convergence appears to be the result of the baroclinic pressure gradient producing a force in the +y direction. Below 6.8 m, $\bar{w}.\partial\bar{v}/\partial z$ replaces the longitudinal advection in the balance, and the fact that it shows a change in direction from $-\bar{v}$ to $+\bar{v}$ flow with depth is also ascribed to the increasing baroclinic component. Finally, at the base of the slice, the two pressure gradients cancel and hardly any acceleration is produced as a result.

***BOX 5N- recorded from high water (HW) + 2 hrs 14 mins to HW + 2 hrs 57 mins***

Throughout the depth of box 5N, the two spatial acceleration terms show that the longitudinal velocity is increasing downstream i.e. accelerating in the +x direction, and

also increasing eastwards i.e. accelerating in the -y direction. In the surface 4 m of the box, $\bar{u}.\partial\bar{u}/\partial x$ is larger than $\bar{v}.\partial\bar{u}/\partial y$, as a result of the barotropic component exceeding the baroclinic force. The water surface slopes downwards downstream, as it did in boxes 2N, 3N and 4N, to accelerate the flow in the +x direction. The baroclinic gradient arises from denser water present on the downstream side of the box, and the resultant upstream directed force equals the magnitude of the barotropic component at about 4.2 m depth. Below this level, $\bar{v}.\partial\bar{u}/\partial y$ has the larger magnitude of the two accelerations, and the baroclinic component now exceeds the barotropic component. Hence, a similar interpretation can be applied to this box as has been applied to the longitudinal balances of boxes 2N, 3N and 4N: where the flow is primarily accelerated by the barotropic pressure gradient, it is assumed to be Lynher water and where it is accelerated by the baroclinic pressure gradient, it is thought to be Tamar water.

The lateral momentum balance of box 5N presents an interesting situation, especially when compared to the lateral balances of boxes 2N, 3N and 4N. The $\bar{u}.\partial\bar{v}/\partial x$ term near the surface shows that the lateral flow is positive downstream and negative upstream, whilst $\bar{v}.\partial\bar{v}/\partial y$ shows negative lateral flow on the western side of the box changing to positive on the eastern side. The pressure gradients which balance these two accelerations indicate that the surface elevation decreases and density increases in the +y direction. Effectively, this means that the water surface slopes down from the Tamar side of the box towards the Lynher mouth, and that the water on the Lynher side is denser than water on the Tamar side. The polarity of both the lateral pressure gradients is reversed in box 5N compared to the preceding three boxes. This will be discussed later. Below this surface layer at about 3.3 m, the two pressure gradients cancel out so that the absence of a primary forcing mechanism at this depth renders the net acceleration close to zero. For the remainder of the box, the vertical stress gradient and the barotropic component combine, but are still unable to overcome the large baroclinic component which produces only a $\bar{v}.\partial\bar{v}/\partial y$ acceleration. Turbulent lateral momentum is decreasing with depth and this appears to be reflected in the decreasing lateral velocity with depth shown by the $\bar{w}.\partial\bar{v}/\partial z$ acceleration in the lowest layer of the box.

***BOX 6N- recorded from high water (HW) + 2 hrs 27 mins to HW + 3 hrs 11 mins***

In the longitudinal balance of box 6N, the only primary forcing mechanism is the barotropic pressure gradient produced by a downward slope of the water surface in the +x direction. In the surface layer of about 3 m thickness, the longitudinal dynamic pressure shows that turbulent stress is higher on the downstream side of the box and turbulent momentum is transferred from downstream to upstream such that the flow is accelerated in the -x direction. However, the longitudinal dynamic pressure has a smaller magnitude than the barotropic component so the resultant acceleration is in the +x direction, as shown by $\bar{u}.\partial\bar{u}/\partial x$. At around 3.2 m depth, the vertical stress gradient effectively replaces longitudinal dynamic pressure in the balance, with the transfer of turbulent momentum being from the deeper, more turbulent water upwards into the overlying, less turbulent water. The $\bar{v}.\partial\bar{u}/\partial y$ term at this depth shows that longitudinal velocity increases in the -y direction. This flow is advected into the box by a positive lateral velocity hence the acceleration is effectively negative.

The lateral momentum balance in box 6N is essentially the same as that in box 5N: near the surface the lateral flow is positive downstream and negative upstream such that $\bar{u}.\partial\bar{v}/\partial x$ represents a positive acceleration primarily generated by the barotropic pressure gradient. The $\bar{v}.\partial\bar{v}/\partial y$ deceleration arises because the lateral flow accelerates from negative to positive in the -y direction, and this change is caused principally by the baroclinic pressure gradient. In addition, the lateral dynamic pressure shows that turbulent momentum is being transferred from the Lynher side of the box to the Tamar side, thus effecting a negative acceleration in the +y direction. The two pressure gradients cancel each other out at 2.2 m depth, below which the increasing magnitude of the baroclinic component dominates the balance to generate a significant $\bar{v}.\partial\bar{v}/\partial y$ only. From 6.3 m, the vertical stress gradient suggests that turbulent lateral momentum decreases with depth, such that the downwards transfer of momentum is equivalent to a positive acceleration in the +z direction. The longitudinal stress gradient is also significant below this depth, indicating that turbulent stress decreases in the +x direction and the associated acceleration is therefore positive in the +x direction. As in box 5N,

the presence of the $\bar{w}.\partial\bar{v}/\partial z$ term in the lowest layer of the box is the result of a reduction in the lateral velocity with depth.

***BOX 7N- recorded from high water (HW) + 3 hrs 51 mins to HW + 4 hrs 19 mins***

The primary forcing mechanism in the longitudinal balance of box 7N is the barotropic component, which shows that the water surface elevation increases in the +x direction, such that the resultant force is directed upstream. This produces a large negative acceleration, $-\bar{v}.\partial\bar{u}/\partial y$, which shows that the longitudinal flow increases dramatically from the Lynher side to the Tamar side of the box, with an average flow of 0.06 m $s^{-1}$ accelerating to 0.52 m $s^{-1}$ over the lateral extent of the box. Because the longitudinal flow is advected into the area by a positive lateral flow, the acceleration is actually negative in that longitudinal velocity decreases in the +y direction. Additionally, the temporal acceleration $\partial\bar{u}/\partial t$ is also negative such that the magnitude of the longitudinal flow is decreasing as the end of the ebb tide is approached. In conjunction with the barotropic term, the longitudinal dynamic pressure also effects an upstream acceleration because turbulent stress increases downstream, therefore momentum is transferred from downstream to upstream. However, the combined magnitude of the $\partial\bar{u}/\partial t$ and $\bar{v}.\partial\bar{u}/\partial y$ accelerations is larger than the combined magnitude of the two upstream forces, so that the positive acceleration $\bar{u}.\partial\bar{u}/\partial x$ must be included to balance the equation. This longitudinal acceleration arises from an increase in the longitudinal velocity downstream such that its magnitude has more than doubled at the surface and tripled at the base of the box from the upstream side to the downstream side. Considering just this longitudinal acceleration, it cannot have been produced by the barotropic term present in box 7N, therefore we can only assume that the acceleration was generated outside the area of box 7N, further upstream. This downstream acceleration would then be reduced by the barotropic term in box 7N so that the original acceleration may have been even larger than that shown by the $\bar{u}.\partial\bar{u}/\partial x$ term. In general, the spatial variation in magnitude shown by $\bar{u}.\partial\bar{u}/\partial x$ and $\bar{v}.\partial\bar{u}/\partial y$ may represent a change in direction of the net flow as it passes through box 7N. Thus it seems that in this box, the barotropic pressure gradient does not cause a straightforward deceleration in the longitudinal flow, as might be expected, but instead effects the rotation of an already accelerating flow.

In the lateral balance, the lateral flow accelerates from being close to zero on the Lynher side to up to 0.44 m $s^{-1}$ on the Tamar side, to give the negative $\bar{v}.\partial\bar{v}/\partial y$ term. This acceleration is produced by the barotropic pressure gradient which shows that the Lynher side of the box has a higher surface elevation than the Tamar. The lateral dynamic pressure present in the near surface layer accelerates the flow in the opposite direction due to turbulent stress decreasing along the +y axis. In the lower layer of box 7N, the two remaining Reynold's stress terms feature in the balance, and turbulent momentum decreases in the +x direction and with depth.

***BOX 1S- recorded from high water (HW) + 0 hrs 12 mins to HW + 1 hrs 12 mins***

The absence of a significant baroclinic pressure gradient in the longitudinal balance of box 1S suggests a reasonably uniform density distribution in the x direction and leaves the barotropic component to provide the primary forcing mechanism. The water surface elevation decreases in the +x direction such that the resultant force generates a positive temporal acceleration in the surface layer of the box. From 4.3 m to 8.3 m depth, the $\bar{v}.\partial\bar{u}/\partial y$ and $\bar{w}.\partial\bar{u}/\partial z$ accelerations are additionally important and show that the positive longitudinal flow increases in the +y direction and decreases with depth. Whilst the decrease in velocity in the +z direction would normally produce a negative $\bar{w}.\partial\bar{u}/\partial z$ term, the $\bar{w}$ velocity is directed upwards in this box so that $\bar{w}.\partial\bar{u}/\partial z$ is positive at this depth. In the base of the box, however, $\bar{w}.\partial\bar{u}/\partial z$ becomes negative because the longitudinal flow increases slightly between 10.8 m and 11.8 m. This vertical advection is now balanced solely by the vertical stress gradient showing an increase in turbulent stress with depth, which effects a negative acceleration in the +z direction.

In the lateral balance of box 1S, there is little acceleration from the surface to about 4.8 m depth. The water on the east side of the box is denser than water on the west side, and from this density distribution arises the baroclinic component which accelerates the flow in the +y direction. In the surface layer, this acceleration is almost entirely cancelled out by the Coriolis force. At slightly greater depths of about 3 m, the Coriolis force is replaced in the balance by the vertical stress gradient, arising from the increase in turbulent stress with depth. From 4.8 m to 8.3 m, the vertical stress gradient exceeds the baroclinic component so that significant accelerations are produced. The lateral velocity on the west side of the box is negative to 6.8 m, after which it becomes smaller

and positive. The velocity on the east side of the box is larger and negative so that overall a deceleration in the +y direction is produced. The $\bar{w}.\partial\bar{v}/\partial z$ term shows that negative lateral flow averaged over the whole area is decreasing with depth. In the lowest layer of the box, there is again little net acceleration because the baroclinic component has increased to a similar magnitude as the vertical stress gradient, and the two cancel out. So in general, the force produced from the density gradients within the box is balanced with a varying degree of success by the acceleration produced by the vertical transfer of turbulent momentum.

***BOX 2S- recorded from high water (HW) + 0 hrs 41 mins to HW + 1 hrs 22 mins***

Throughout the whole depth of box 2S, the barotropic component has a sufficiently large magnitude to make it the primary forcing mechanism in the longitudinal balance, with the baroclinic component only becoming significant in the deepest 3 m. The water surface slopes down in the +x direction to produce the positive accelerations, $\partial\bar{u}/\partial t$ and $\bar{u}.\partial\bar{u}/\partial x$ near the surface. The longitudinal advection term results from a small increase in longitudinal velocity in the downstream direction in this surface layer. The lateral stress gradient represents an increase in turbulent momentum in the +y direction so that the resultant acceleration opposes that produced by the barotropic component. At around the mid-depth of the box, the longitudinal velocity is seen to decrease downstream, and $\bar{u}.\partial\bar{u}/\partial x$ becomes negative accordingly. The lateral acceleration, $\bar{v}.\partial\bar{u}/\partial y$, increases in magnitude from the surface to 7.3 m then decreases to the base of the box. It only plays a significant role in the balance at 6.3 m, when the increase in longitudinal velocity in the +y direction gives it a large enough magnitude. Below this depth, the temporal and longitudinal accelerations are again the most important but are now acting in opposite senses. The baroclinic pressure gradient generates a negative acceleration owing to the presence of denser water on the downstream side of the box. The two pressure gradients are supplemented by the vertical stress gradient which gives an acceleration in the -z direction and the lateral stress gradient giving an acceleration in the -y direction. These two Reynold's stress terms show that turbulent stress is higher on the west side of the box, and at depth.

In the surface 6 m of box 2S, the lateral balance shows that no net acceleration is produced. This is because various combinations of terms on the left-hand side of the equation are cancelling each other out. The barotropic and baroclinic components arise

from a higher surface elevation and water of a higher density being present on the east side of the box, respectively, to produce positive accelerations in the +y direction. However, these primary forces are opposed by the Coriolis acceleration and by the vertical stress gradient which shows an increase in turbulent stress with depth, and a corresponding negative acceleration. Below 6.3 m, the vertical stress gradient is now sufficiently large to outweigh the baroclinic gradient and there is now a negative $\bar{v}.\partial\bar{v}/\partial y$ term because the lateral flow is positive on the west of the box and negative on the east. In the lowest layer of the box, the vertical stress gradient continues to exceed the baroclinic component but now the dominant acceleration is $\bar{u}.\partial\bar{v}/\partial x$, which shows that the lateral flow is positive upstream and negative downstream.

***BOX 3S- recorded from high water (HW) + 4 hrs 47 mins to HW + 5 hrs 251 mins***

Considering the longitudinal balance, in the shallower part of box 3S, the acceleration in the -x direction produced by the water surface sloping down in the -x direction is reduced by the effect of the longitudinal dynamic pressure, representing an acceleration along the +x axis. The longitudinal dynamic pressure is sufficiently large to exceed the barotropic force such that the resulting longitudinal acceleration is positive and velocity increases downstream. At depth, the increase in water density downstream and the water surface slope both produce -x directed accelerations. However, the increase in turbulent stress in the shallower, upstream water produces +x directed accelerations. Whilst the temporal acceleration is negative as a result of the two pressure gradients, the remaining three spatial accelerations are positive. The highest longitudinal velocities are occurring in the southernmost corner of the survey box (corner D) near the surface. In the lateral direction, the decreasing surface elevation in the +y direction produces a positive acceleration, $\bar{u}.\partial\bar{v}/\partial x$, in which a small $+\bar{v}$ flow on the north side accelerates across the longitudinal extent of box 3S. The baroclinic gradient also produces an acceleration in this direction, but its magnitude is insignificant in the momentum balance. At about 4.8 m, the lateral flow on both sides becomes negative and also decreases with depth. The stress gradients show that turbulent stress is highest in the southernmost corner of the box for the whole of the measured depth, which reduces the effect of the barotropic component.

### *6.2.2 Temporal variations in the primary momentum balances*

In this section, the boxes will be grouped together according to their location and the day on which they were surveyed. The temporal variations in the momentum balances within each group will be assessed, and the reader is referred to the summary of frontal evolution during the ebb tide in section 6.1.1, which provides a basis for the following interpretations.

***Boxes 1N, 2N, 3N and 4N***

The variation in the longitudinal momentum balance between box 1N, surveyed as the tide turned, and box 2N, surveyed about 1 hour and 50 minutes later, can be summarised as follows: in box 1N, the net acceleration is balanced by all three Reynold's stress terms and the two primary forces are insignificant, whereas in box 2N, the two pressure gradients now drive the net acceleration. In box 1N, the longitudinal flow reverses and the velocity shear associated with this acceleration is responsible for the three dynamic pressure terms. It can be assumed that prior to high water, the upstream longitudinal flow was decelerating as a result of the barotropic and baroclinic pressure gradients prevailing at the time. The barotropic gradient would presumably have had the same polarity as that in box 1N, so that the water surface elevation was increasing upstream, whilst the baroclinic pressure gradient would be expected to have had a small magnitude reflecting the comparatively homogeneous density structure of the water column shortly before high water. The resultant deceleration is then enhanced by the turbulent stress gradients to the point where the flow reverses, as seen in box 1N. By the time box 2N was recorded, the longitudinal velocity was directed downstream everywhere in the box, and both pressure gradients had increased in magnitude such that they generated the longitudinal acceleration. The Reynold's stress terms are less significant than in box 1N. The change in the longitudinal momentum balance describes the tide turning at high water and then accelerating downstream as the ebb tide progresses.

In box 1N, the lateral momentum balance shows that the net acceleration is close to zero because the pressure gradients and the turbulent stress gradients all cancel out. By the time box 2N was surveyed, there is a small net deceleration which is the result of the barotropic component, the Coriolis acceleration and the vertical stress gradient outweighing the baroclinic term. This situation arises despite the fact that the baroclinic term has increased in magnitude from box 1N to box 2N, which suggests that the more

homogeneous density structure present at high water is now being reduced, possibly because water of differing densities is being advected into the survey box from the Lynher and Tamar rivers at this stage in the ebb tide. This assumption is supported by the lateral velocity structure, which shows a negative flow on the Lynher side and a positive flow on the Tamar side of the box. The Coriolis acceleration has also increased from box 1N to box 2N as a result of the temporal acceleration in the downstream flow between the two boxes. So, the temporal variation in the lateral dynamics arises because the tide is turning in box 1N and in box 2N, the onset of the ebb tide means that water of differing densities is now being advected into the area.

The momentum balances from boxes 2N, 3N and 4N are now discussed to give a summary of the flow's behaviour in the northern part of the survey grid over the period from 1 hour 26 minutes to 2 hours 25 minutes after high water. Firstly, making some general observations about the longitudinal balance, it can be seen that whilst the barotropic component increases from box 2N to box 4N, the baroclinic magnitude remains approximately the same. The two dominant acceleration terms ($\bar{u}.\partial\bar{u}/\partial x$ and $\overline{w}.\partial\bar{u}/\partial z$) also increase in magnitude whereas the most significant Reynold's stress terms decrease in magnitude from box 2N to box 4N.

Bearing in mind the flow pattern outlined in section 6.1.1, it appears that each box can be divided into two layers. The shallowest layer comprises Lynher river water, in which the flow accelerates in the +x direction as well as accelerating temporally. These accelerations are produced primarily by the pressure gradient arising from the slope of the water surface. In box 2N, the Reynold's stress terms show that turbulent longitudinal momentum decreases downstream and with depth in this upper layer. In box 3N, only the longitudinal dynamic pressure is significant, and by the time box 4N was recorded no turbulent momentum exchanges are included in the balance. Referring back to figure 6.28, section 6.1, the Reynold's stress terms indicate that the shallower Lynher water is more turbulent than the deeper Tamar water, and also that the turbulent stress is higher in the mouth of the Lynher river in comparison to further downstream. The lower layer in boxes 2N, 3N and 4N is interpreted as Tamar water, and in this layer, the vertical spatial deceleration gradually increases with time to first equal and then exceed the magnitude of $\bar{u}.\partial\bar{u}/\partial x$. This increase in $\overline{w}.\partial\bar{u}/\partial z$ corresponds to an increase in the magnitude of the baroclinic pressure gradient such that the longitudinal

density gradient is believed to be responsible for the observed vertical deceleration in the Tamar water. The baroclinic component shows that the denser and therefore more saline water is downstream, as would be expected in a partially-mixed estuary. Again, the vertical stress gradient suggests that turbulent stress decreases with depth and hence, the Lynher water is thought to be more turbulent. Finally, it is postulated that where the two opposing pressure gradients balance each other almost exactly, this may indicate the position of the frontal zone between the Lynher and the Tamar. If the frontal interface can be identified in this manner, then the increasing slope of the Lynher water surface with time causes the inclined frontal zone to be pushed back in the upstream direction, effectively increasing the depth of the Lynher water layer.

Considering now the lateral momentum balance, the two horizontal accelerations, $\bar{u}.\partial\bar{v}/\partial x$ and $\bar{v}.\partial\bar{v}/\partial y$, both increase in magnitude from box 2N to box 4N. The variation of the $\bar{w}.\partial\bar{v}/\partial z$ term is more complex in all three boxes. It is negative in the shallowest layer, and then becomes positive at greater depths. However, in box 3N it reverts to being negative again at the deepest level. The magnitudes of $\bar{w}.\partial\bar{v}/\partial z$ are generally smaller than the other two accelerations over most of the depth in all three boxes. Unlike the longitudinal case, the magnitude of the baroclinic component increases with time, whereas the barotropic component increases from box 2N to box 3N then decreases from box 3N to box 4N. The only Reynold's stress term of significance is the vertical stress gradient which decreases with time. Initially, in box 2N, the baroclinic component is larger than the barotropic component, but the converse is true for the remaining two boxes. The relationship between the two pressure gradients is consequently less straightforward than in the longitudinal balance. However, in boxes 2N and 3N, the surface layer, which is again interpreted to be Lynher water, undergoes a lateral acceleration produced by the water surface sloping down in the -y direction. As the depth increases, the opposing baroclinic component starts to generate other spatial accelerations; in box 2N, the $+\bar{v}$ flow is accelerated along the +x axis and this $+\bar{v}$ flow also increases with depth, such that the deeper downstream water flows in the +y direction and the shallower upstream water flows in the -y direction. However, in box 3N, the $\bar{w}.\partial\bar{v}/\partial z$ term in the lowest layer shows that the $+\bar{v}$ flow is now decreasing with depth. In both boxes, the turbulent lateral momentum increases

with depth, such that the deeper westwards flowing Tamar water is more turbulent than the Lynher water. In box 4N, the whole depth of water is accelerated by both pressure gradients, and neither force can be said to dominate the balance. This more complicated dynamic relationship highlights the fact that the distinction between the Tamar and Lynher water is less easy to make here than in the longitudinal balance. However, it still seems plausible that the Lynher flow is accelerated mainly by the barotropic component and the Tamar flow is more dependent on the baroclinic force. If we can assume that wherever the barotropic magnitude exceeds the baroclinic magnitude, Lynher water is present and in the converse situation, Tamar water is present, then it can be seen that in box 2N, the change from Lynher to Tamar water (i.e. the frontal interface) occurs at about 2.2 m. In box 3N, it occurs presumably deeper than the measured base of the box, as the baroclinic component is approaching the magnitude of the barotropic component as the depth increases. In box 4N, the frontal interface is at about 9.8 m. Admittedly, this analysis is crude, but it does suggest that the depth of the frontal interface is increasing over time which agrees, in principle, with observations made from the longitudinal balance.

***Boxes 5N and 6N***

Boxes 5N and 6N were surveyed on the first survey day, unlike the preceding 4 boxes which were surveyed on the second day. However, boxes 5N and 6N were surveyed at a slightly later stage in the ebb tide than the preceding boxes, and therefore it may be possible to infer how the dynamics have developed over this time period despite the lack of surveying continuity.

Considering the implications of the momentum balances in boxes 5N and 6N, the longitudinal dynamics here are reasonably similar to those of boxes 2N, 3N and 4N. The most notable difference is that the lateral advection $\bar{v}.\partial\bar{u}/\partial y$ has increased in magnitude and significance in boxes 5N and 6N. However, the two pressure gradients have the same polarity as in the preceding boxes and hence the primary forcing mechanism is unchanged. Following the same argument used in boxes 2N, 3N and 4N, where the barotropic magnitude exceeds the baroclinic magnitude , the presence of Lynher water is inferred and in the converse situation the presence of Tamar water is inferred. Thus, it seems that the frontal interface between Lynher and Tamar water is at approximately 4.2 m in box 5N, whilst the dominance of the barotropic term throughout

the whole depth of box 6N suggests that most, if not all of the box is Lynher water. The position of the frontal interface appears to have deepened from box 5N to box 6N which agrees with the interpretation offered for boxes 2N, 3N and 4N and is also concurrent with the flow behaviour described by figure 6.29, section 6.1.

The lateral momentum balances for boxes 5N and 6N are very different to the balances of the preceding boxes because of the reversed polarity of both the baroclinic and barotropic pressure gradients. In boxes 2N, 3N and 4N, the water surface sloped downwards from the Lynher to the Tamar side of the box, and the Tamar water had a higher a density than the Lynher water. In 5N and 6N, the water surface is sloping down from the Tamar side to the Lynher side, with the water on the Lynher side being denser than water on the Tamar side. This density gradient is the result of water from the Lynher being slightly more saline and cooler than the Tamar water, as shown by the T-S bridge profiles taken during surveying. The reversal in the polarity of the pressure gradients suggests the presence of a wholly different dynamic regime on the day boxes 5N and 6N were surveyed, compared to boxes 2N, 3N and 4N. An alternative explanation is that the reversal in polarity of both the lateral pressure gradients may be a typical temporal variation associated with the progressing ebb tide. If we assume that all survey boxes were recorded during the same ebb tide, then given that box 4N was recorded from 1 hour 50 minutes to 2 hours 25 minutes after high water, and box 5N was recorded from 2 hours 24 minutes to 2 hours 57 minutes after high water, the lateral water surface slope must have changed direction in this short time. Likewise, in the case of the baroclinic pressure gradient, either intense lateral mixing has re-distributed the density within box 5N compared to box 4N, or water of different density has been advected into the box in the short time between surveying 4N and 5N. It is thought that both of these scenarios are unlikely to be general features of a typical ebb tide. Therefore, it is postulated that the basic longitudinal dynamic regime is more constant over the survey days in question that the lateral dynamic regime. Differences in the lateral dynamics are probably the result of variations in tidal range, river inflow, surface wind stress and the amount of vertical mixing in both the Lynher and Tamar rivers between the two survey days.

*Box 7N*

Because box 7N was surveyed on the third survey day, the question again arises as to whether the dynamic regime in the box can be treated as a general feature of a typical ebb tide, or whether it is the result of specific conditions in this part of the estuary that were prevailing on this survey day. Whereas the water surface slopes in the same direction in box 7N as in boxes 2N, 3N and 4N in the lateral balance, the longitudinal barotropic gradient in box 7N has reversed polarity. This change from a negative elevation gradient directed downstream to a negative gradient directed upstream may be a feature of the ebb tide at this time after high water, such that the barotropic gradient now serves to reduce the positive longitudinal velocity as slack low water is approached. However, this scenario is considered to be unrealistic, and the calculated reversal in barotropic gradient is more likely the result of experimental errors. In both the longitudinal and lateral case, the baroclinic pressure gradients have diminished in magnitude to the extent that a more homogeneous density distribution is present in box 7N, in comparison to the preceding boxes. As with boxes 5N and 6N, this suggests that either mixing is reducing the density gradients in the box, or that the density of the water advected into the box has changed, if we assume that all boxes were surveyed during the same ebb tide. Considering now the Reynold's stress terms from both horizontal momentum balances, these show turbulent stress decreases with depth. This appears to agree with the interpretation offered in section 6.1 that the Lynher water forms a buoyant, turbulent jet in box 7N. Additionally, lateral turbulent momentum is higher on the northern side of the box and longitudinal turbulent momentum is higher on the southern side of the box. This may be connected with the observations made from ADCP data earlier that the Lynher water enters the box with a strong eastwards velocity and therefore a large lateral flow component, and exits the downstream side of the box with a strong southwards velocity and therefore a large longitudinal flow component. Hence the change in direction of the Lynher flow as it traverses box 7N may explain the distribution of turbulent momentum. It is postulated in section 6.1.3 that Tamar water is entrained into the Lynher jet, and this mixing may be at least partly the cause of the more uniform density distribution indicated by the baroclinic pressure gradients. Generally, the dynamic regime in box 7N can be adequately explained in terms of the

front evolving into a turbulent, buoyant jet as described earlier, but it may equally be attributed to a different set of conditions (i.e. tidal range, tidal current strength, freshwater inflow, surface wind stress, water temperature) prevailing on the day of the survey.

***Boxes 1S and 2S***

Boxes 1S and 2S were surveyed from 12 minutes to 1 hour 22 minutes after high water, so care must be taken when interpreting the spatial accelerations as these will inevitably include an element of temporal acceleration, as was the case in box 1N. Examination of the $\bar{u}.\partial\bar{u}/\partial x$ terms for both boxes reveals that the longitudinal velocity was approximately zero on the upstream side of box 1S, accelerating to about 0.24 m $s^{-1}$ on the downstream side. By the time box 2S was surveyed, the change in velocity between the two sides of the box is less pronounced, with the magnitudes both upstream and downstream being between 0.22 m $s^{-1}$ and 0.31 m $s^{-1}$. If the $\bar{u}.\partial\bar{u}/\partial x$ term is taken to be purely a spatial acceleration, then it appears that the tide turns earlier downstream than it does upstream. In reality, the upstream side of box 1S was surveyed before the downstream side, whereas the downstream side of box 2S was surveyed before the upstream side. Hence, in box 1S the observed acceleration is almost certainly temporal because the box was surveyed so shortly after high water. When box 2S was surveyed a little later, the acceleration is probably both temporal and spatial. The $\bar{v}.\partial\bar{u}/\partial y$ term reaches its largest magnitude in the mid-depths of each box and in both cases is larger than $\bar{u}.\partial\bar{u}/\partial x$. The primary forcing mechanism to generate these accelerations changes slightly from box 1S to box 2S. The barotropic component, representing a downwards surface slope downstream, is the dominant force in both boxes, so the longitudinal acceleration is effectively driven by the head of water further upstream, as would be expected at the start of the ebb tide. The smaller baroclinic component changes polarity from box 1S to box 2S, such that the denser water is present on the upstream side of box 1S, and on the downstream side of box 2S. The comparatively small magnitude of the baroclinic component suggests that this region is reasonably homogeneous longitudinally, and this again is expected close to the time of high water, although longitudinal density differences are becoming greater at depth especially in box 2S. The baroclinic component's change in polarity is possibly explained as follows; higher density water is advected into box 1S through the upstream side but by the time box 2S

was surveyed, it has been advected in the +x direction such that it is now present on the downstream side of the box. At the base of both boxes, turbulent stress increases with depth which is attributed to the frictional forces generated by the river bed. Turbulent stress is also higher on the west side of both boxes which may be because the water shallows on the west of the box, as the river bank is approached.

Considering the lateral balance, both the water surface elevation and the density decrease from the east of boxes 1S and 2S to the west. The lateral surface slope has increased from box 1S to box 2S and when considered in conjunction with the longitudinal barotropic gradient, it can be seen that the northernmost corner of the box (corner F) is elevated so that overall, the surface slopes down in the downstream direction. The baroclinic magnitude remains the same for both boxes. These two primary forces are cancelled out by the Coriolis force and the vertical dynamic pressure down to 4.8 m in box 1S and 6.8 m in box 2S, such that there is only a net acceleration below these depths. This suggests that the ebb tide commences sooner in deeper water. All spatial accelerations contain an element of temporal acceleration as described earlier, however looking at lateral velocity data from just one side of each box reveals a negative flow in the surface and a positive flow at depth. Given the orientation of the y-axis in relation to the topography of the estuary, it is reasonable to interpret a $-\bar{v}$ component as indicative of a flood current and a $+\bar{v}$ component as indicative of an ebb current. As the shallower and deeper velocities are obviously recorded synchronously, this supports the suggestion that frictional effects cause the deeper flow to reverse direction earlier than the shallower flow at around the time of high water. Furthermore, turbulent stress increases with depth in both boxes which is ascribed to the increasing proximity of the river bed. These observations are also concurrent with the interpretation made for box 1N which was also surveyed close to high water.

***Box 3S***

Considering box 3S in terms of the interpretation in section 6.1, both the $\bar{u}$ and $\bar{v}$ components of flow increase from the northern corner to the southern corner of the box and decrease with depth. This accelerating, shallower flow is thought to be Lynher water which was accelerated across the northern box of the survey grid in a turbulent, buoyant jet in box 7N and continues to accelerate across the southern box of the grid, i.e. box 3S. The change from a positive lateral flow at the surface to a negative one at

depth is possibly the result of the curvature in the Tamar river, and therefore the change in lateral flow is not necessarily indicative of a change from Lynher water to Tamar water, as was the case in boxes 2N, 3N and 4N. The two baroclinic pressure gradients in box 3S are smaller than those in boxes 2N, 3N, 4N, 5N and 6N but slightly larger than those in box 7N. It may be the case that both Tamar and Lynher water was present in the northern boxes up to box 6N, but that the bulk of box 7N comprised Lynher water, hence the reduction in density differences. Following this argument suggests that box 3S may contain both Tamar and Lynher water, and the baroclinic components show that the denser water is in the easternmost corner of the box. If the increased density indicates Tamar water, its presence in the east of the box seems reasonable given the position of the survey grid. The lateral and longitudinal barotropic gradients of box 3S show that the eastern corner of the box (corner E) now has the highest surface elevation. An explanation for the surface slope may be that the volume of water flowing out of the Lynher mouth has at this stage of the tide diminished, such that the surface of the Tamar water on the east side of the survey box is elevated in comparison.

### *6.2.3 Overview of the dynamics of a generalised ebb tide*

In this section, the variation in the hydrodynamic regime within the survey area in terms of the evolution of the Tamar-Lynher front from an initially convergent feature into a turbulent, buoyant jet during an ebb tide, will be discussed. To facilitate this, each term in the horizontal equations of motion has been depth-averaged for each survey box and plotted against the time after high water at which the box was surveyed. The results for the northern and southern boxes have been plotted separately, and these results are shown in figures 6.34a, b to 6.41a, b. Given that the boxes were surveyed on three separate days (see figure 6.33), any conclusions drawn concerning the development of the dynamics during the ebb tide will be of a generalised nature. However, an attempt will be made to discriminate between hydrodynamic variations which are likely to occur during every ebb tide, and those which appear to be more the result of changes in factors such as river inflow and tidal range over the three survey days. If we start by considering the primary forcing mechanism within the survey grid, this distinction is relatively easy to make for the barotropic pressure gradient. Figures 6.34a and b show that the surface elevation slope across both north and south boxes seems to vary predictably in the longitudinal direction during an ebb tide. At or close to high water, the surface elevation is approximately constant over the whole survey area. Over the

*Figure 6.34a Longitudinal and lateral barotropic pressure gradients vs. time (northern survey box)*

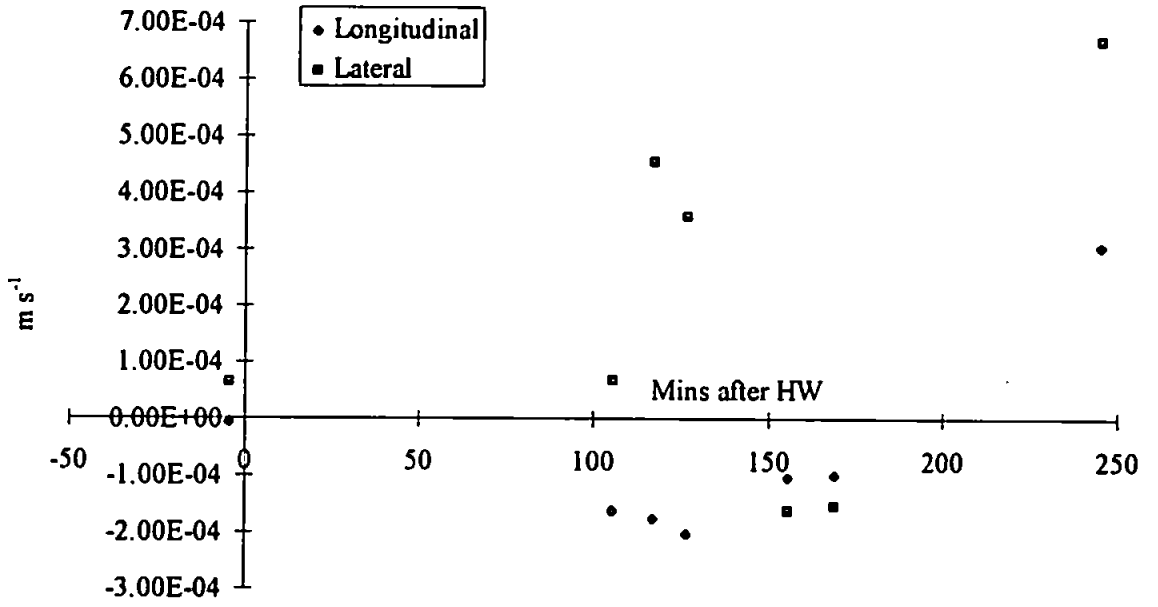


*Figure 6.34b Longitudinal and lateral barotropic pressure gradients vs. time (southern survey box)*

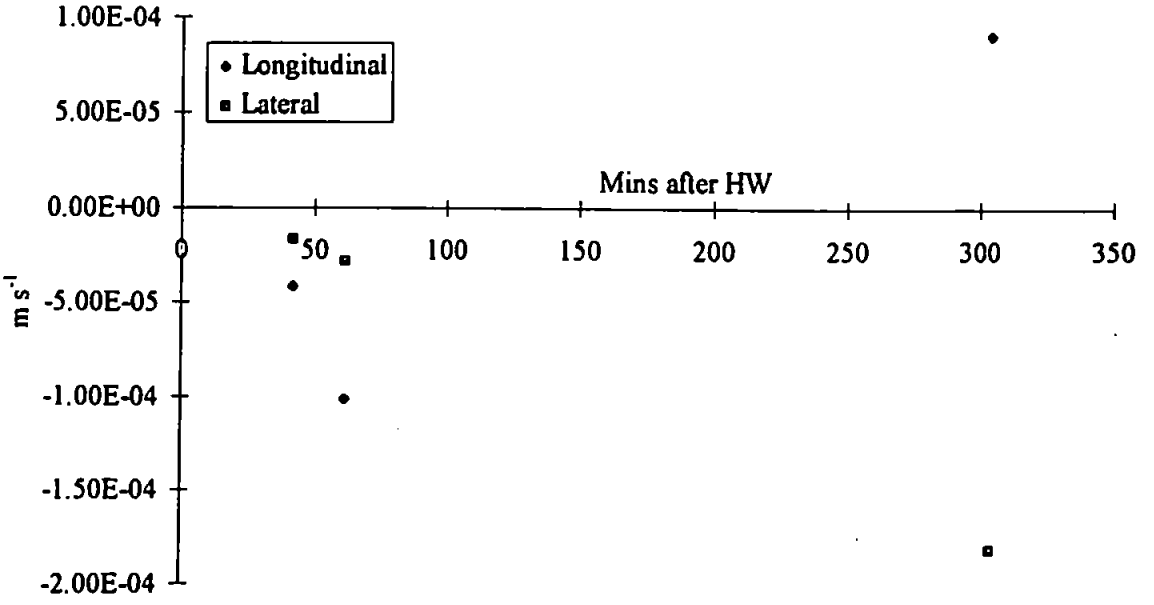

following two hours, the water surface upstream is becoming gradually more elevated in comparison to the water surface downstream. This trend then reverses so that the difference in the elevation from upstream to downstream is now decreasing. Between three and four and a half hours after high water, the surface elevation gradient again becomes zero. Its polarity then changes, such that the downstream water surface is elevated in comparison to the upstream surface. It is possible that in the early ebb, the seaward flow of water in the lower reaches of the estuary leaves a head of water upstream whereas in the later stages of the ebb, the change in surface slope may be related to variations in the relative surface slopes of the Tamar and Lynher rivers. If this is the case, then the increased surface elevation downstream from about four and a half hours after high water may be caused by an increased volume of water exiting the mouth of the Lynher river in the form of a jet. The jet flows across the southernmost part of the northern survey box, and across most of the southern box, such that a downstream increase in surface elevation associated with the jet is feasible.

The lateral barotropic gradient varies much less predictably after high water, when the water surface elevation is constant over the whole survey area. From about 1 hour 50 minutes after high water, the general trend in the north of the grid then appears to be an increase in the elevation of the Lynher side of the box in comparison to the Tamar side. However, boxes 5N and 6N show that the surface slopes in the opposite direction between 2 and 3 hours after high water. This reversal in surface slope is considered unlikely to be a feature of the generalised ebb tide, and more likely the result of specific conditions prevailing on the day on which 5N and 6N were surveyed.

Addressing just the positive lateral barotropic gradient, this may arise for similar reasons to the longitudinal gradient in the early ebb, i.e. the water downstream starts to flow seawards sooner than the water upstream to leave an up-river head of water. Given the orientation of the path of the Lynher river in relation to the survey grid, this provides an explanation for the positive lateral barotropic term in the early ebb, especially considering that the magnitude of both the longitudinal and lateral terms is comparable up to about 2 hours after high water. However, a different explanation is required to account for the sudden increase in the magnitude of the positive lateral gradient after high water plus 2 hours. After this time, it is postulated that the depth of water within the survey grid will have reduced to the point where the river bed topography may now

have an appreciable effect on the water surface elevation. The bathymetric chart presented in section 6.1, figure 6.31 shows the river bed sloping down from the Lynher mouth towards the centre of the Tamar by 6 or 7 metres within the survey grid. At 4 hours after high water, the average depth of water in the northern box is only about 7 metres, so perhaps the slope in topography is reflected in the slope of the water surface, which may explain the large magnitude of the positive lateral barotropic term in the later stages of the ebb tide. Additionally, the volume of flow exiting the Lynher mouth may have reached its maximum at this point in time which would also explain the barotropic term's magnitude.

The lateral barotropic term in the southern part of the survey grid is negative throughout the ebb tide. Shortly after high water, its magnitude is very small indicating a constant surface elevation at the start of the ebb. At 5 hours after high water, the surface is elevated on the Tamar side of the box in comparison to the Lynher side. From the bathymetric chart, it can be seen that the river bed topography in this region is reasonably uniform, therefore it is suggested that the volume of water ebbing out of the Lynher mouth and flowing down the western side of the Tamar river has diminished in comparison to the volume of water flowing down the eastern side of the Tamar, which explains the calculated surface slope.

Generally, it seems that the longitudinal barotropic gradient varies more predictably with the progression of the ebb tide than the lateral barotropic gradient, which is influenced by the river bed topography and the volume of water flowing out of the Lynher river. The effect of this latter factor may also explain why the lateral gradient appears to be more sensitive to variations in river inflow and tidal range over the combined survey period than the longitudinal term.

In the case of the other primary force in the equations of motion, it again seems that the longitudinal baroclinic pressure gradient varies in a more predictable manner over the course of the ebb tide than the lateral term (see figures 6.35a and b). For both boxes of the survey grid, the longitudinal gradient is close to zero from high water until about 1 hour later, after which it becomes positive with an average magnitude of $1 \times 10^{-4}$ m $s^{-1}$ until 5 hours after high water, which represents the end of the combined surveying period. Hence, at high water, the water within the survey grid has a longitudinally homogeneous density structure, which is interpreted to be the result of bottom friction

*Figure 6.35a Longitudinal and lateral baroclinic pressure gradients vs. time (northern survey box)*

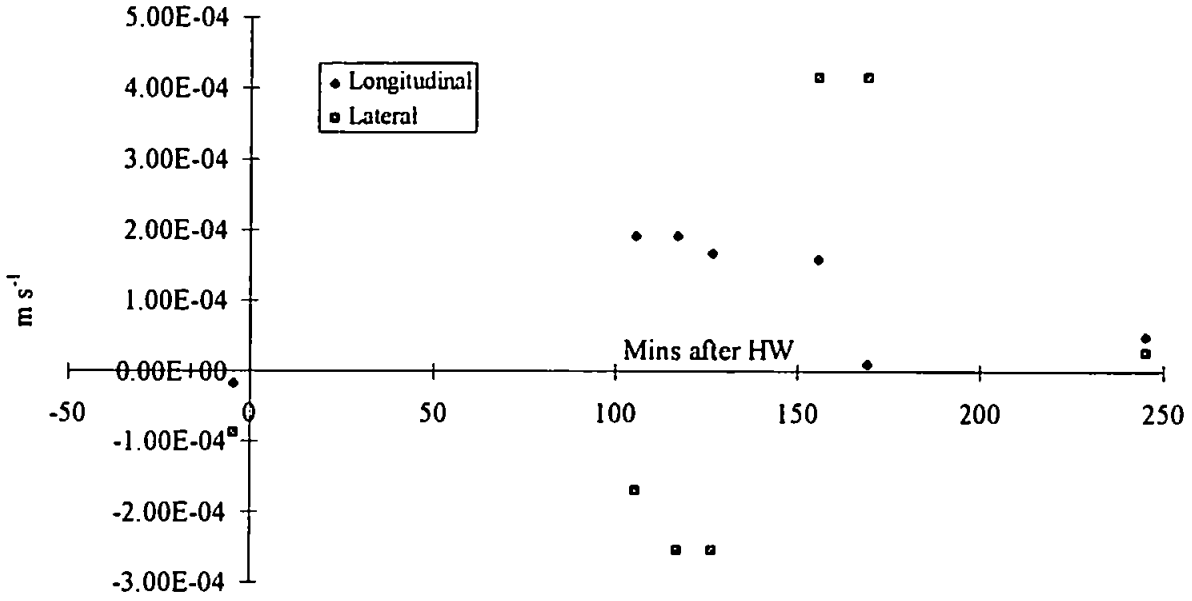


*Figure 6.35b Longitudinal and lateral baroclinic pressure gradients vs. time (southern survey box)*

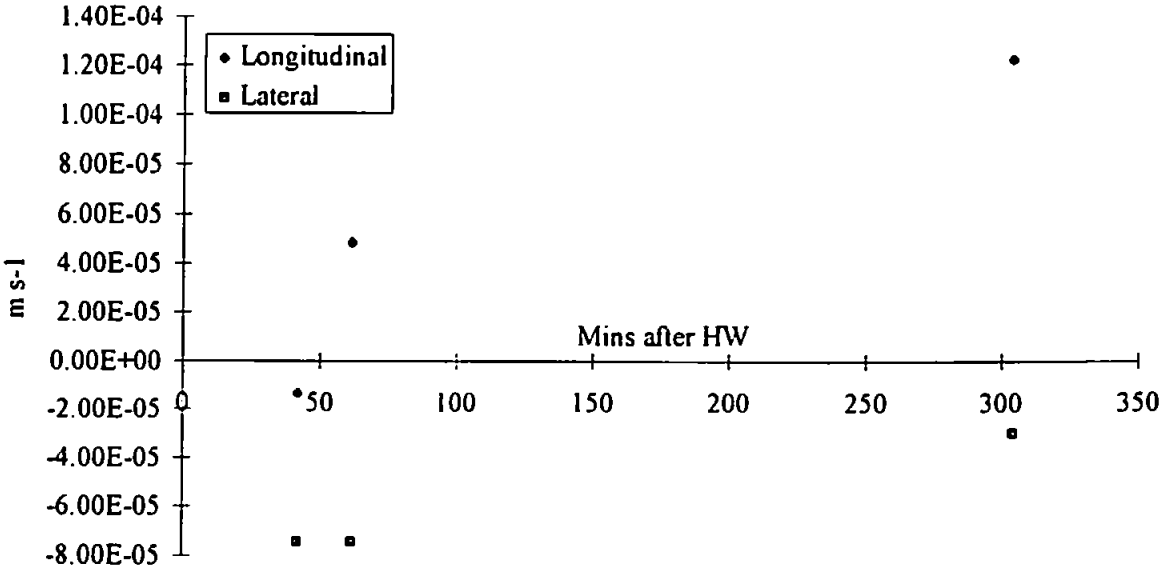

induced turbulent mixing during the flood tide. As the ebb tide progresses, a longitudinal density gradient develops such that the denser, more saline water is downstream, suggesting that the slower velocities during the ebb tide no longer have the necessary amount of kinetic energy required to maintain the degree of longitudinal homogeneity seen at high water.

The lateral baroclinic pressure gradient varies in a more complex manner over the ebb tide. Considering the northern part of the survey grid, the pressure gradient is negative for the first 2 hours 20 minutes of the ebb tide, and then becomes positive until 4 hours after high water at which point it reduces to almost zero. The negative gradient reveals that the water on the Lynher side of the box is less dense than the water on the Tamar side, which agrees with observations made from T-S bridge data, from which Lynher water was identified by its higher temperature and lower salinity in comparison to Tamar water. However, boxes 5N and 6N have a positive gradient such that water on the Lynher side of the box is now denser than water on the Tamar side. A possible explanation for this is the advection of different density water into the survey box from both the Lynher and Tamar rivers, which then alters the lateral density distribution within the box. Alternatively, it is suggested that the change in polarity of the baroclinic term is the result of a change in the general conditions in the estuary between survey days. This assumption is supported by preliminary observations made from T-S bridge data in chapter 3, in which it was noted that the water column in the region of the survey grid was cooler and more stratified on the first survey day, when 5N and 6N were recorded, than on the following two. The reduction in the magnitude of the baroclinic gradient by 4 hours after high water represents an increase in the lateral homogeneity of the density structure in the northern box. This is thought to arise because the Lynher water forms a jet which extends across most of the area and all of the depth of the survey box. Therefore, there is no longer a contrast between Lynher and Tamar water to produce a lateral density gradient. Additionally, mixing by entrainment is occurring at the boundaries of the jet, which also serves to reduce any density differences in the survey box.

In the southern part of the grid, the baroclinic gradient is again negative, albeit of a smaller magnitude than the gradient in the north. This is similarly interpreted to represent less dense Lynher water on the west of the box and denser Tamar water on the

east, such that a contrast between the two water masses is still detectable slightly downstream of the frontal region.

To summarise the primary forcing mechanism within the survey grid, longitudinally it is provided by the relationship between the negative barotropic term and the positive baroclinic term. The barotropic gradient has the largest magnitude so that throughout the ebb, the surface slope forces the water to accelerate downstream, overcoming the upstream directed force generated by the presence of denser water downstream, which agrees with the findings of Parsons (1987). Laterally, it is also the larger barotropic gradient that overall dominates the negative baroclinic term to accelerate the flow in the north of the grid. Here, the barotropic term is positive and competes with the baroclinic term, whereas in the south of the grid, the barotropic term is negative such that it is complemented by the other pressure gradient. Both the longitudinal and lateral barotropic and baroclinic pressure gradients are practically zero at high water and thus any accelerations seen at this time must have been initiated outside the survey area.

The Reynold's stress terms plotted against time after high water (figure 6.36a, b for the longitudinal equation and figure 6.37a, b for the lateral equation) provide an indication of how the distribution of turbulent stress varies throughout the ebb tide. Considering the terms in the longitudinal equation first, in the northern box the depth-averaged $\partial\overline{(u'.u')}/\partial x$ values are small and negative from high water to 2 hours 40 minutes later, after which they become positive and the magnitude increases dramatically. Hence, in the early ebb, longitudinal turbulent stress is slightly higher upstream but in the later stages of the ebb, it becomes much higher downstream. The same term in the southern box is close to zero in the early ebb and then becomes large and negative by 5 hours after high water, such that longitudinal turbulent stress is appreciably higher on the upstream side of the box.

Over the whole survey grid, the depth-averaged $\partial\overline{(u'.v')}/\partial y$ term is small, indicating a uniform lateral distribution of longitudinal turbulent stress. The depth-averaged $\partial\overline{(u'.w')}/\partial z$ term is initially positive at high water, in both the north and south boxes. In the north, it then fluctuates around zero before becoming large and negative in the later stages of the ebb. Similarly in the south, the term becomes negative towards the end of the ebb. The implications of the behaviour of all three terms seem to be that the

*Figure 6.36a Longitudinal Reynold's stress terms vs. time (northern survey box)*

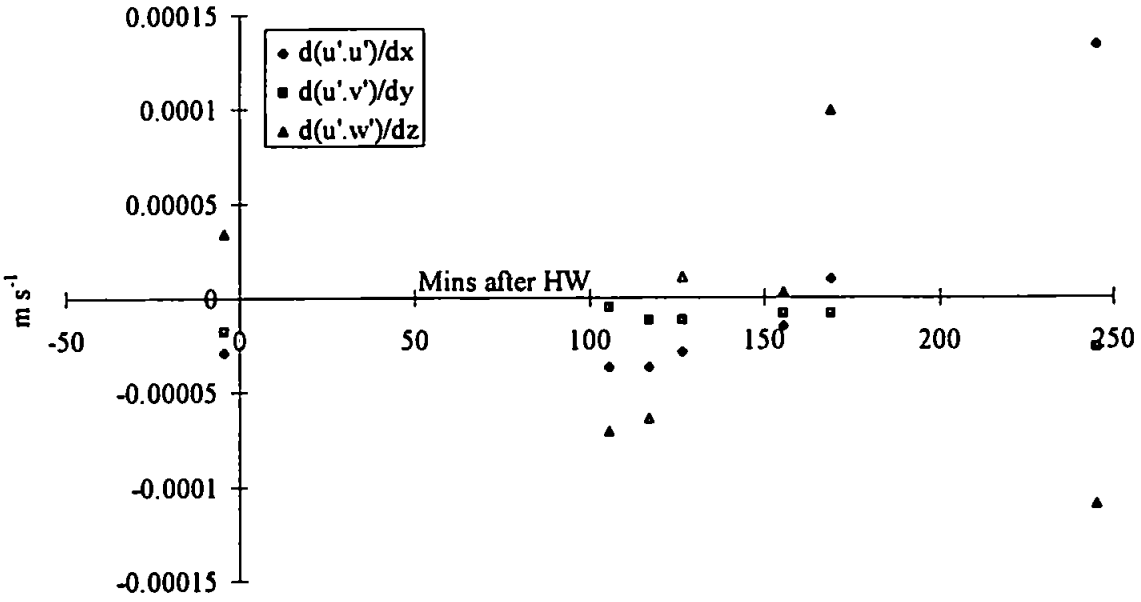


*Figure 6.36b Longitudinal Reynold's stress terms vs. time (southern survey box)*

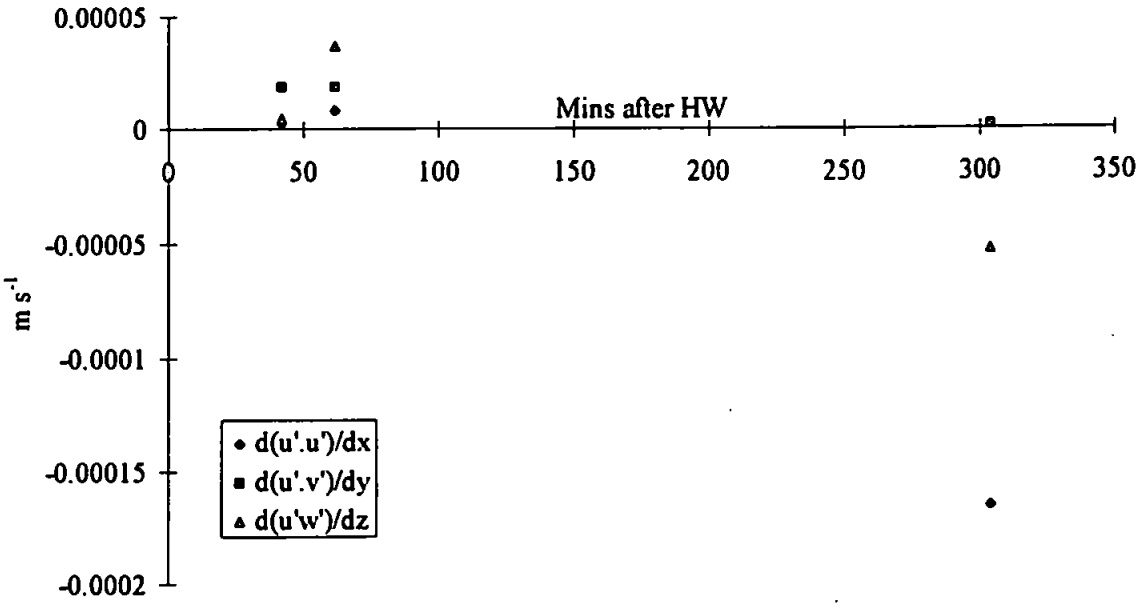

*Figure 6.37a Lateral Reynold's stress terms vs. time (northern survey box)*

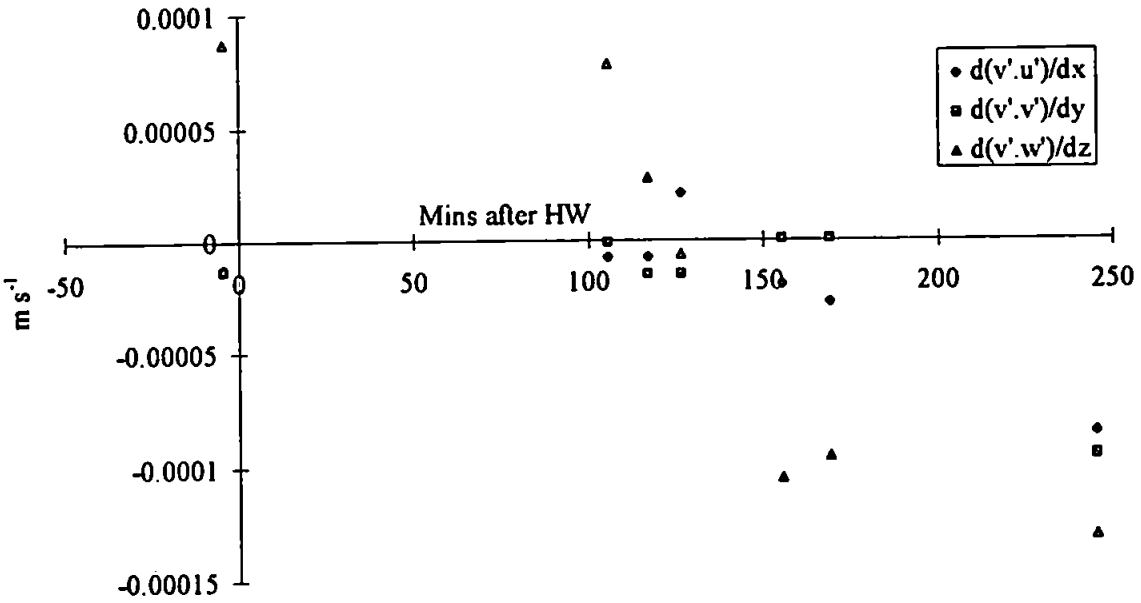


*Figure 6.37b Lateral Reynold's stress terms vs. time (southern survey box)*

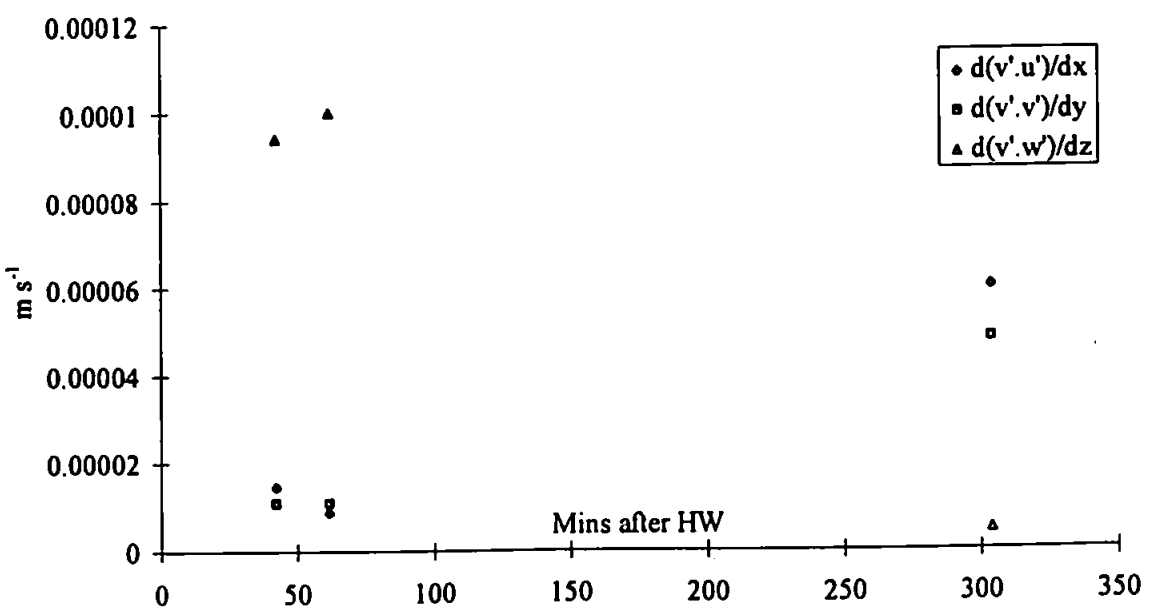

deeper water is more turbulent at or near high water, and this is associated with bottom friction inducing more turbulence at depth as the tide turned. Also, by the end of the ebb, the distribution of longitudinal turbulent stress strongly suggests the presence of a shallow, more turbulent layer extending across the middle of the whole survey grid, i.e. in the downstream part of the northern box and the upstream part of the southern box. This synopsis fits well with the idea of the formation of a turbulent, buoyant jet of Lynher water in the later stages of the ebb.

In the case of the lateral Reynold's stress terms, both the depth-averaged $\partial\overline{(v'.u')}/\partial x$ and $\partial\overline{(v'.v')}/\partial y$ terms are approximately zero until around 3 hours after high water, when they become negative and increase in magnitude in the northern box. In the southern box, both terms are initially close to zero and then become positive as the ebb tide progresses. This suggests that by the end of the ebb, lateral turbulent stress is highest in the most northerly and southerly corners of the survey grid (corners A and B respectively) with a lower level of turbulent stress in the central section of the grid. It is postulated that higher lateral turbulent stress is associated with the Tamar water into which the Lynher jet flows, with its higher longitudinal turbulent stress. In the northern box, the depth-averaged $\partial\overline{(v'.w')}/\partial z$ term is positive until about 2 hours after high water and then becomes negative. Similarly to the longitudinal case, this suggests that the deeper water is more turbulent in the early ebb as a result of bottom friction, whereas the presence of the Lynher jet has reversed this turbulence distribution by the end of the ebb. In the southern box, the $\partial\overline{(v'.w')}/\partial z$ term again shows turbulence increasing with depth at the start of the ebb, but it has decreased to zero 5 hours later, suggesting that the whole depth of the water column is now equally turbulent. This may be because the interface between the turbulent Lynher jet and the underlying Tamar water has deepened to the extent that the majority of the southern box is now filled with Lynher water with a reasonably uniform lateral turbulent stress distribution. The deepening of the Lynher-Tamar interface during the course of the ebb tide was suggested earlier in section 6.2.2. In both horizontal equations of motion, the Coriolis acceleration is the least important term and varies predictably over the ebb tide as the average longitudinal and lateral velocities increase (see figure 6.38a, b). Over the whole survey grid, the lateral Coriolis

*Figure 6.38a Longitudinal and lateral Coriolis accelerations vs. time (northern survey box)*

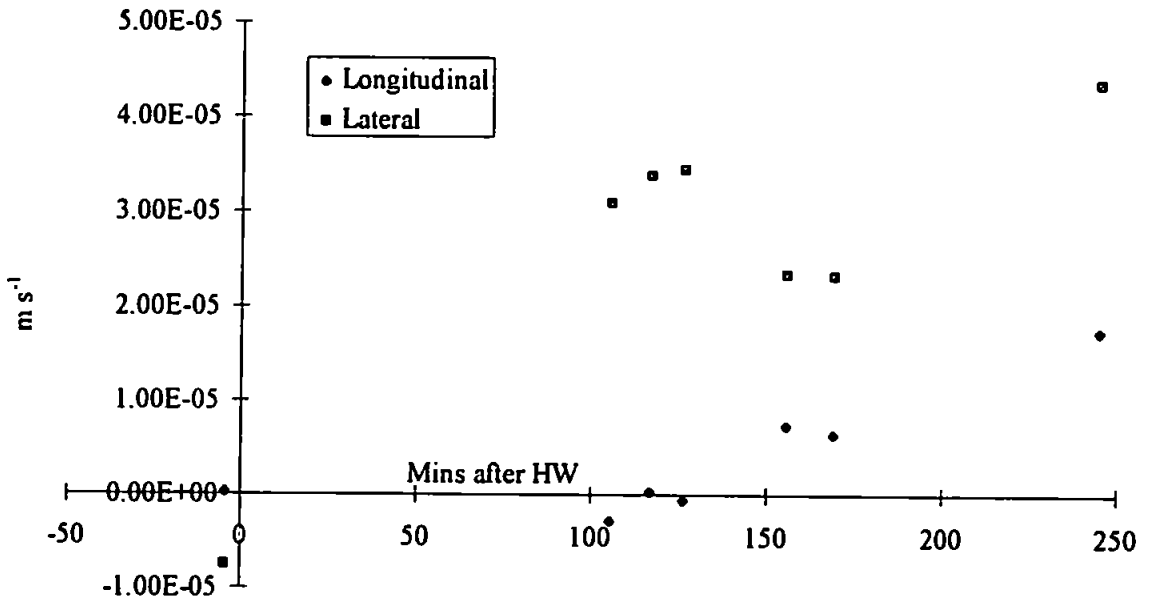


*Figure 6.38b Longitudinal and lateral Coriolis accelerations vs. time (southern survey box)*

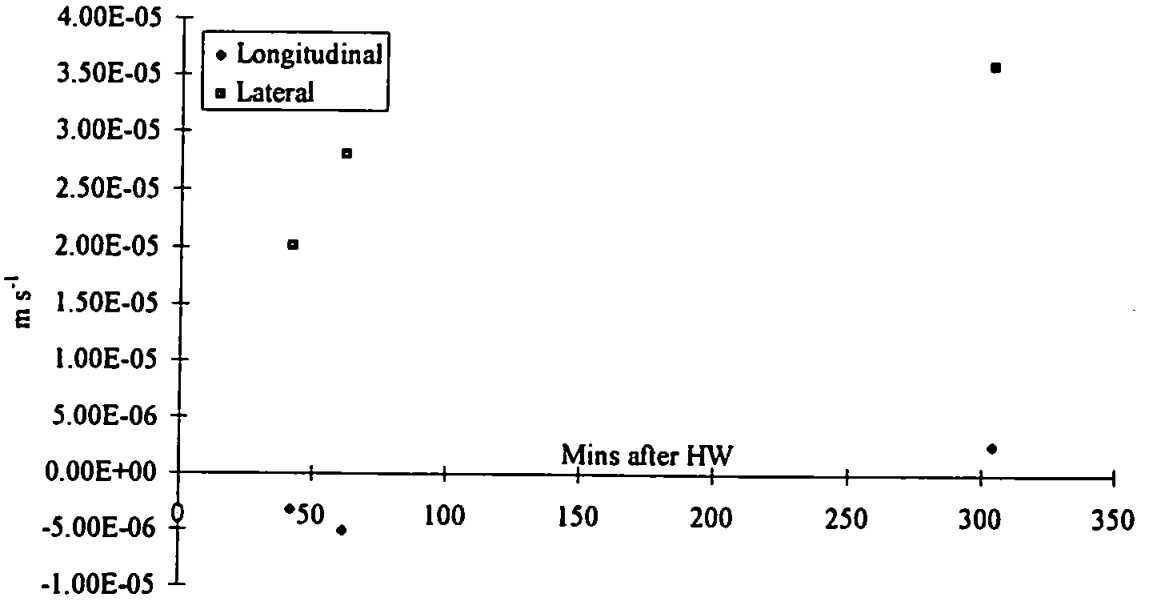

acceleration increases steadily from high water, and the lateral Coriolis acceleration is initially negative near high water, becoming positive 2 hours later.

The depth-averaged total temporal and spatial acceleration in both the longitudinal and lateral directions is plotted against time after high water in figure 6.39a, b. Again, the longitudinal term shows a smoother and more predictable variation over the course of the ebb tide than the lateral term. In the northern box, the longitudinal acceleration is small and positive at high water, and reaches a maximum positive value 2 hours later. It then reduces to zero approximately 40 minutes later, after which it becomes very large and negative. Inspection of the component temporal acceleration and the three spatial accelerations in the longitudinal equation, which are plotted in figure 6.40a, b, reveals that the longitudinal flow is still accelerating in the downstream direction in the later stages of the ebb, but it is the combination of a temporal deceleration and, in particular, the large negative $\bar{v}.\partial\bar{u}/\partial y$ term which causes the total acceleration to change polarity 2 hours 40 minutes after high water. This $\bar{v}.\partial\bar{u}/\partial y$ term arises because of the strong acceleration in the longitudinal flow across the box from the Lynher side to the Tamar side. In other words, it is the spatial acceleration of the Lynher jet which dominates the total longitudinal acceleration in latter stages of the ebb tide. A similar development is seen in the depth-averaged total lateral acceleration (figure 6.39a) in the northern box. The total acceleration is small and negative until 2 hours after high water, after which its negative magnitude increases suddenly. The cause of the increase is attributed to the $\bar{v}.\partial\bar{v}/\partial y$ term (see figure 6.41a) which shows that the $-\bar{v}$ flow on the Lynher side of the box is decreasing and the $+\bar{v}$ flow on the Tamar side is increasing as the tide progresses. Considered in conjunction with the $\bar{v}.\partial\bar{u}/\partial y$ term, this effectively represents a change in direction of the net flow as it crosses the northern box, and the net flow rotation is associated with the increasing strength of the Lynher jet in the northern box during the ebb.

In both the longitudinal and lateral momentum balances, the longitudinal advection terms $\bar{u}.\partial\bar{u}/\partial x$ and $\bar{u}.\partial\bar{v}/\partial x$ respectively, remain positive throughout the ebb, increasing slightly in the latter stages as the jet of Lynher water accelerates down the river bed slope. Both vertical advection terms, $\bar{w}.\partial\bar{u}/\partial z$ and $\bar{w}.\partial\bar{v}/\partial z$, are zero at the start and end of the combined surveying period. From about 1 hour 40 minutes to 2

*Figure 6.39a Longitudinal and lateral depth-averaged total accelerations vs. time (northern survey box)*

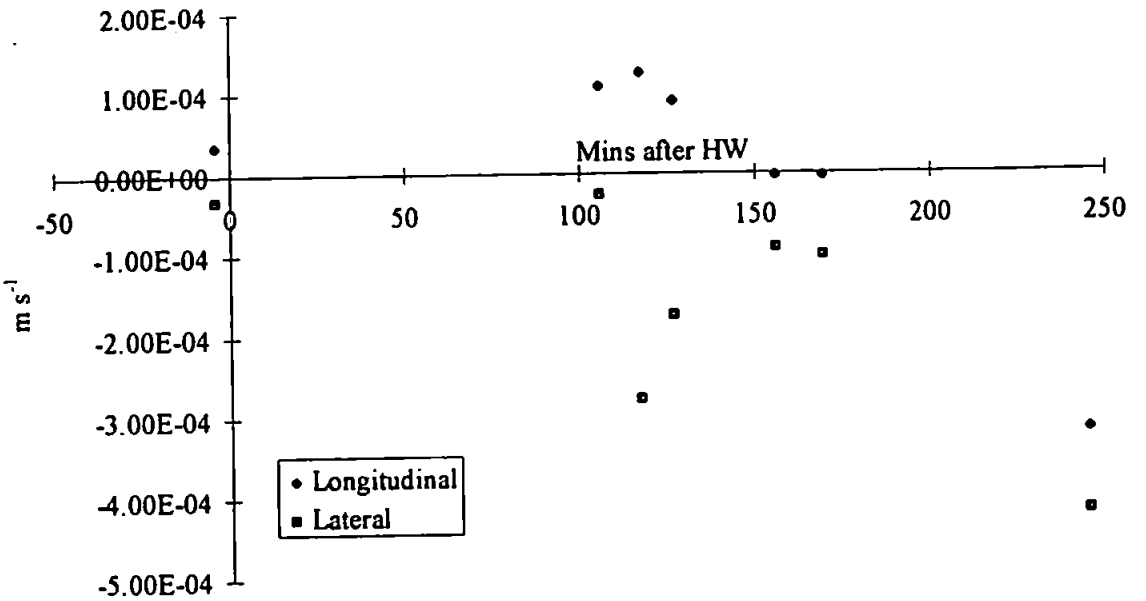


*Figure 6.39b Longitudinal and lateral depth-averaged total accelerations vs. time (southern survey box)*

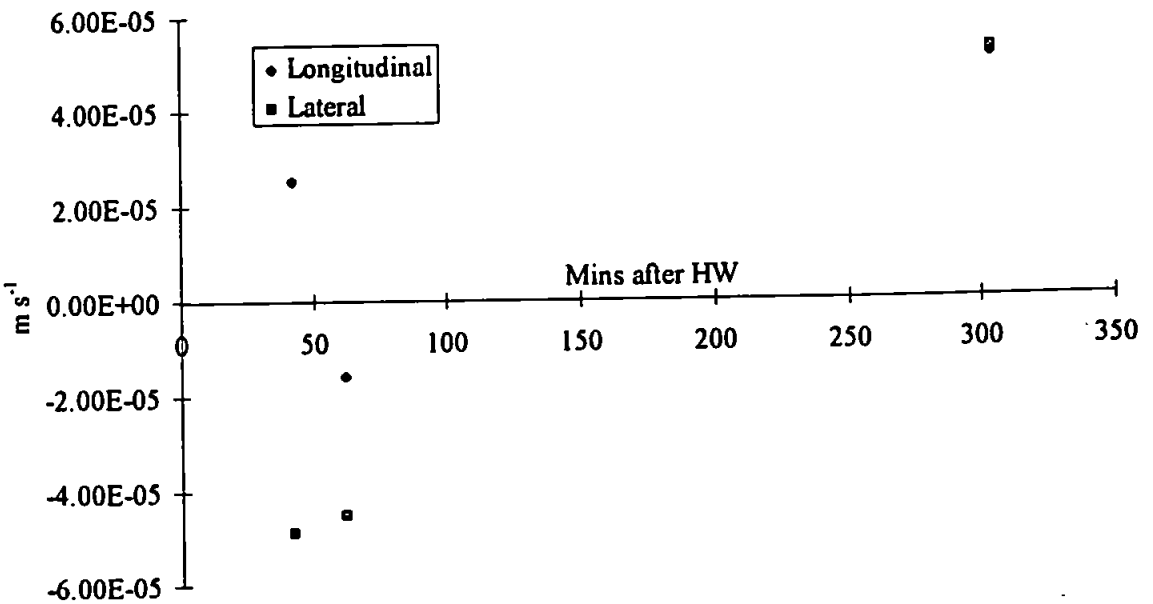

*Figure 6.40a Longitudinal spatial acceleration terms vs. time (northern survey box)*

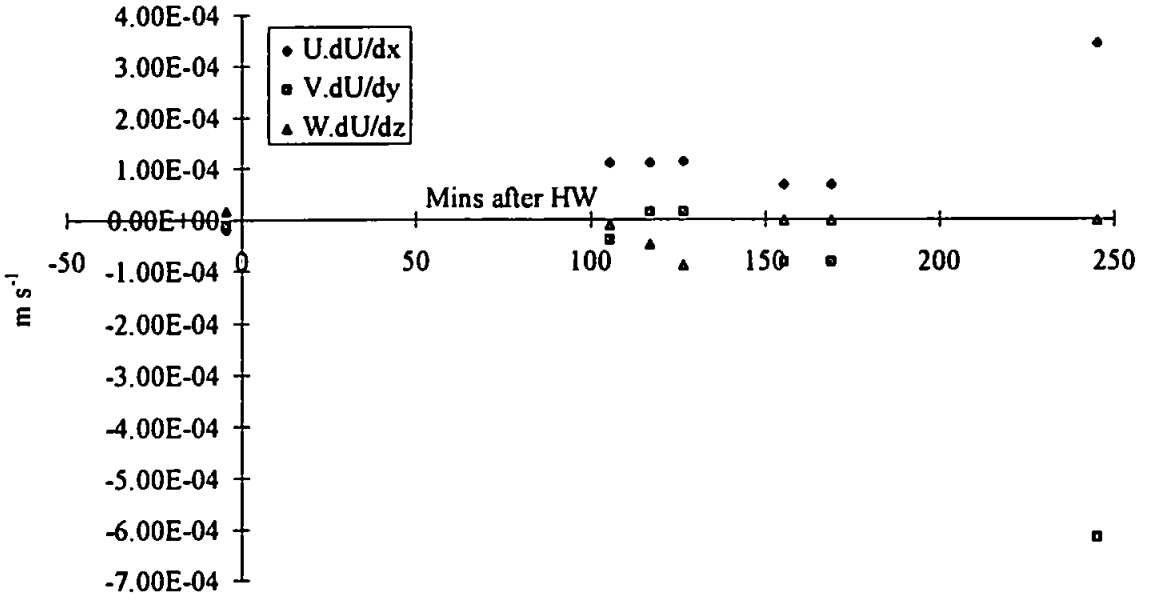


*Figure 6.40b Longitudinal spatial acceleration terms vs. time (southern survey box)*

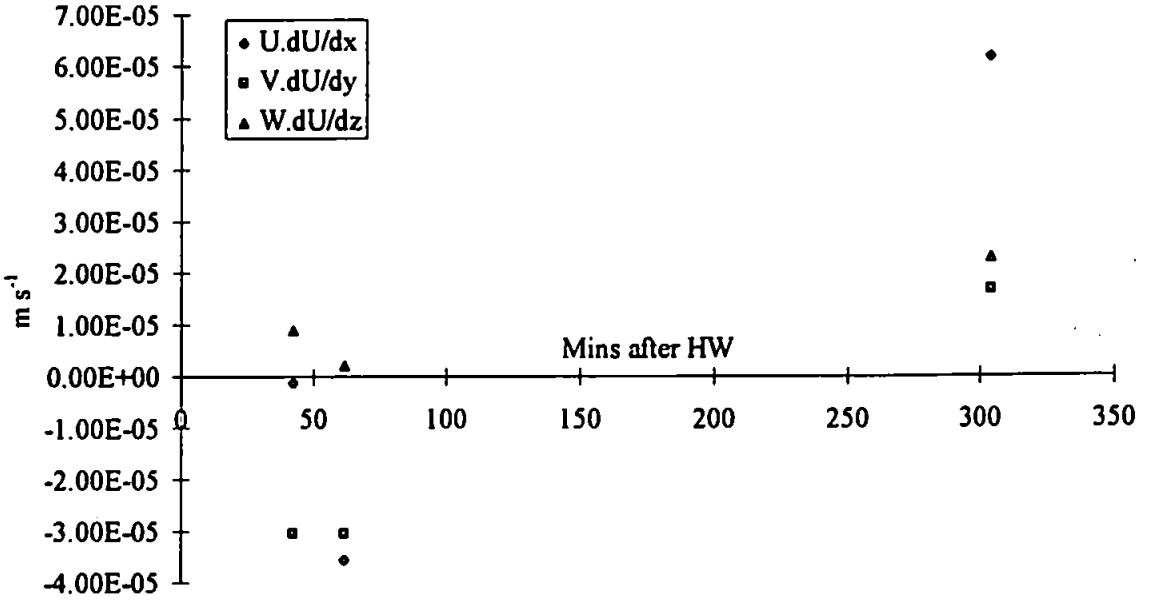

*Figure 6.41a Lateral spatial acceleration terms vs. time (northern survey box)*

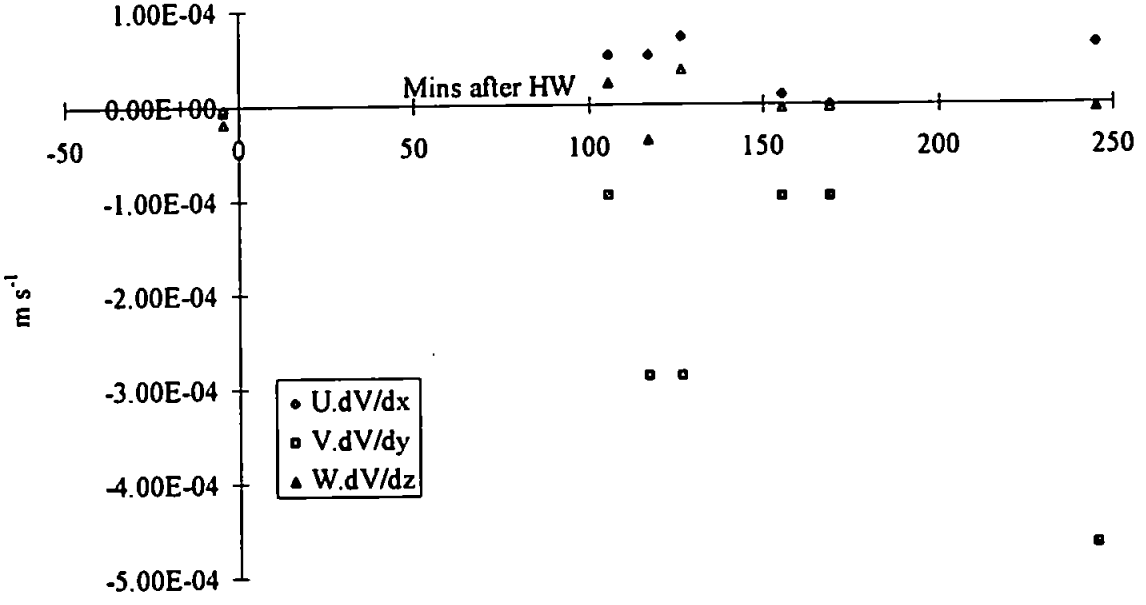


*Figure 6.41b Lateral spatial acceleration terms vs. time (southern survey box)*

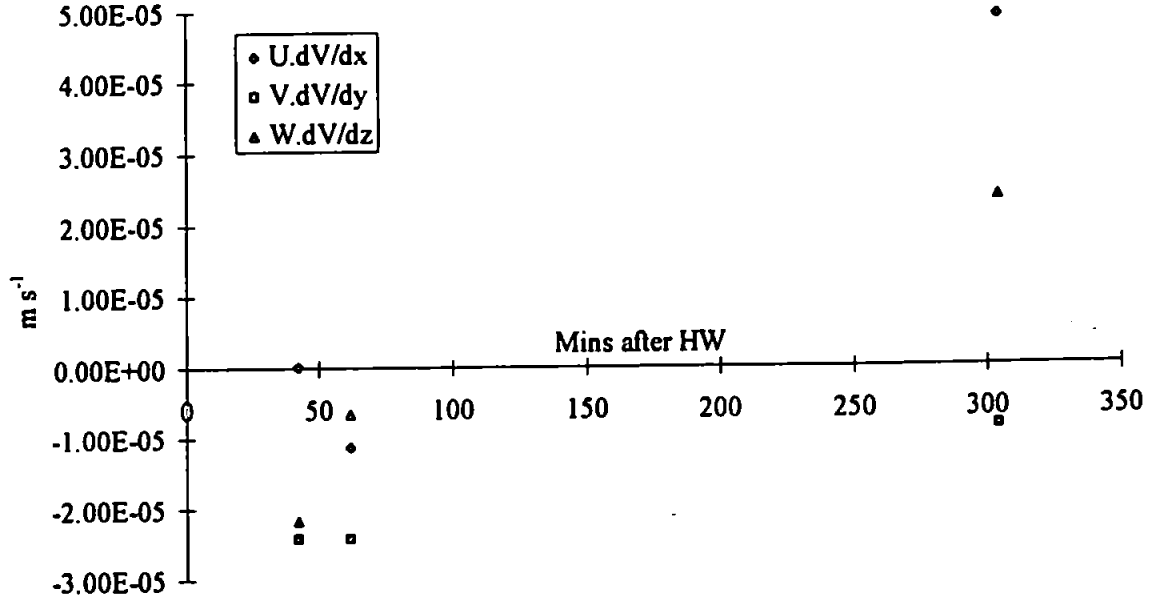

hours 10 minutes after high water, their magnitudes increase. In the longitudinal balance, the term becomes negative and in the lateral balance, the equivalent term varies from negative to positive and then back to positive in this mid-ebb period. The increase of both these terms in the middle of the surveying period represents an increased degree of horizontal velocity shear in the vertical direction, which coincides with the development of a two-layer flow system in the northern box as the Tamar-Lynher front evolves, prior to the onset of the Lynher jet.

The depth-averaged total accelerations in the southern box (see figure 6.39b) are significantly smaller in both horizontal directions than those in the northern box. Examination of the three spatial acceleration terms in each equation (figures 6.40b and 6.40b) reveals that both longitudinal advection terms, $\bar{u}.\partial\bar{u}/\partial x$ and $\bar{u}.\partial\bar{v}/\partial x$, are initially zero shortly after high water. They then have a small negative magnitude which has developed into a larger positive magnitude by 5 hours after high water. Hence, at this later stage both the longitudinal and lateral flow is accelerating downstream such that these two terms are now the largest spatial accelerations in their respective momentum balances. The lateral advection terms, $\bar{v}.\partial\bar{u}/\partial y$ and $\bar{v}.\partial\bar{v}/\partial y$, are both small and negative shortly after high water. The negative magnitude of $\bar{v}.\partial\bar{v}/\partial y$ has reduced by 5 hours later, whilst $\bar{v}.\partial\bar{u}/\partial y$ has become positive because the longitudinal flow is accelerating from the Tamar side to the Lynher side of the box, which is the reverse of the situation seen in the northern box at around this time. Finally, the $\bar{w}.\partial\bar{u}/\partial z$ is small and positive whilst the $\bar{w}.\partial\bar{v}/\partial z$ term is small and negative just after high water. Both terms have a larger positive magnitude by 5 hours later, such that the net horizontal velocity is decreasing with depth.

For a generalised ebb tide, we can draw the following conclusions from examining the acceleration terms. Firstly, there is little spatial acceleration over the whole survey grid at and shortly after high water. Approximately 2 hours after high water, the increase in vertical shear indicated by $\bar{w}.\partial\bar{u}/\partial z$ and $\bar{w}.\partial\bar{v}/\partial z$ marks the development of the Tamar-Lynher front in the north of the area, and its associated two-layer flow structure. At the end of the ebb, the onset of the Lynher jet is indicated by a large increase in the lateral advection of both longitudinal and lateral momentum, i.e. $\bar{v}.\partial\bar{u}/\partial y$ and $\bar{v}.\partial\bar{v}/\partial y$. Considered together, these two terms represent a rotation in the net flow, and

this rotation is thought to continue across the boundary between the northern and southern boxes so that in the south of the survey grid, the dominant spatial accelerations are now $\bar{u}.\partial\bar{u}/\partial x$ and $\bar{u}.\partial\bar{v}/\partial x$.

## 6.3 RICHARDSON NUMBER, VERTICAL MIXING COEFFICIENT AND FLUX RICHARDSON NUMBER ANALYSIS

In this section, the overall Richardson number, the vertical mixing coefficient and the flux Richardson number will be discussed for each box, and their variation during the ebb tide assessed.

### *6.3.1 The Overall Richardson Number, Ri and Vertical Mixing Coefficient, $\mathcal{E}_v$*

The overall Richardson number has been calculated for each slice of every survey box. A total mean velocity was determined for each slice from the slice-averaged values of $\bar{u}$ and $\bar{v}$, allowing the change in mean velocity with depth to be found. The slice-averaged density values for the top two or three slices, calculated from temperature and salinity measurements, were extrapolated linearly to approximate the change in density with depth.. These two depth gradients were then used to find Ri, such that:

$$Ri = \frac{g\left(\frac{\partial \rho}{\partial z}\right)}{\rho\left(\frac{\partial V_T}{\partial z}\right)^2} \qquad (6.1)$$

where $\rho$ is slice-averaged density, g is gravitational acceleration and $V_T$ is the total mean velocity. The minus sign usually present on the right-hand side of equation 1 is omitted to account for the z-axis in our analysis being positive downwards.

It should be noted that in some slices, the calculated values of Ri are very large because the change in $V_T$ over the thickness of the slice is very small. These values are discarded to allow the use of a reasonable scale when presenting the results graphically. All Ri values are presented as depth profiles for each box in figures 6.42a to 6.42j. Given the linear nature of the extrapolated density gradients, the variation in Ri within each box is primarily attributed to changes in velocity shear and the associated turbulence, rather than changes in the degree of density stratification in the water column. This is an inevitable consequence of the calculation method and the Richardson number results are interpreted with this in mind.

The depth profiles for the northern survey boxes develop in the following way; in box 1N (figure 6.42a), in which the tide is turning, Ri is approximately constant with depth, with the exception of a maximum peak at 4.3 m depth. This increase in stability is the result of a more uniform localised flow in the upper part of the water column, such that

*Figure 6.42a Ri vs. depth, box 1N*

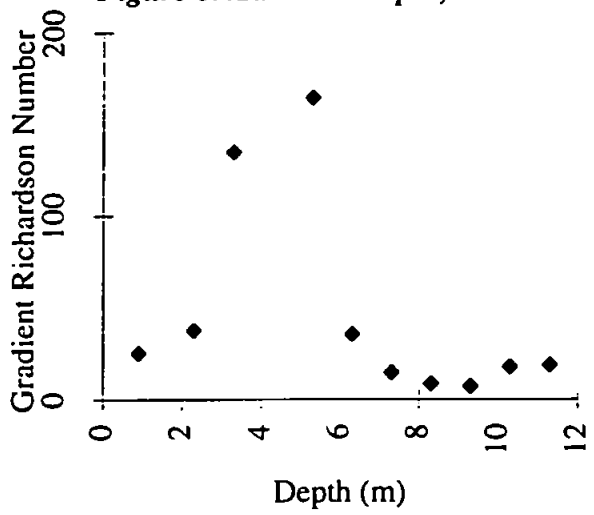


*Figure 6.42b Ri vs. depth, box 2N*

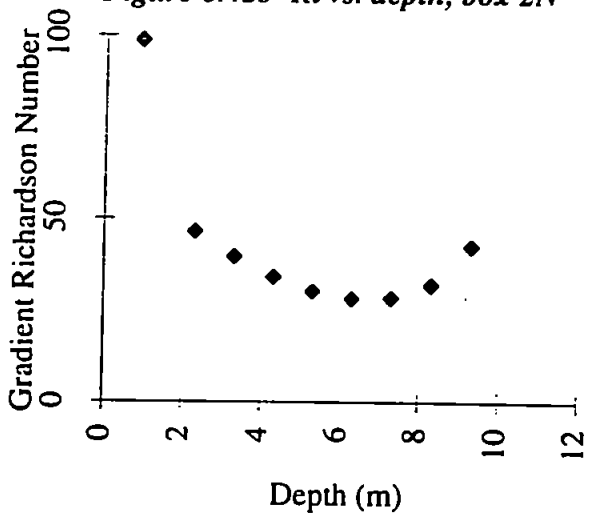


*Figure 6.42c Ri vs. depth, box 3N*

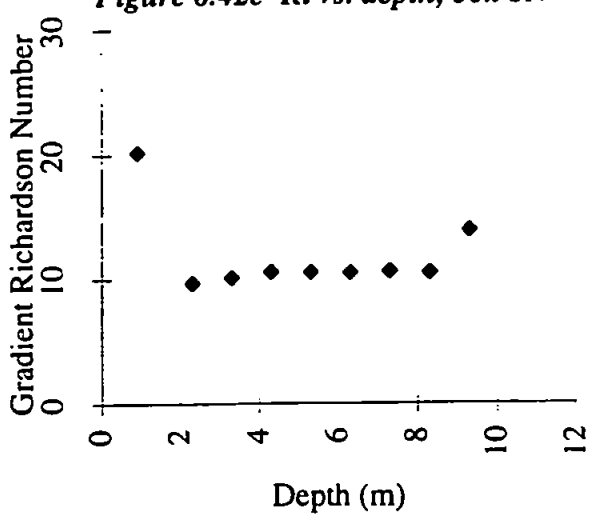


*Figure 6.42d Ri vs. depth, box 4N*

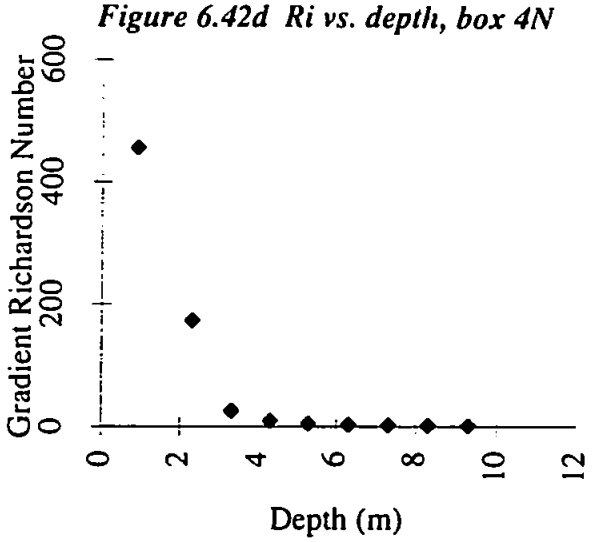


*Figure 6.42e Ri vs. depth, box 5N*

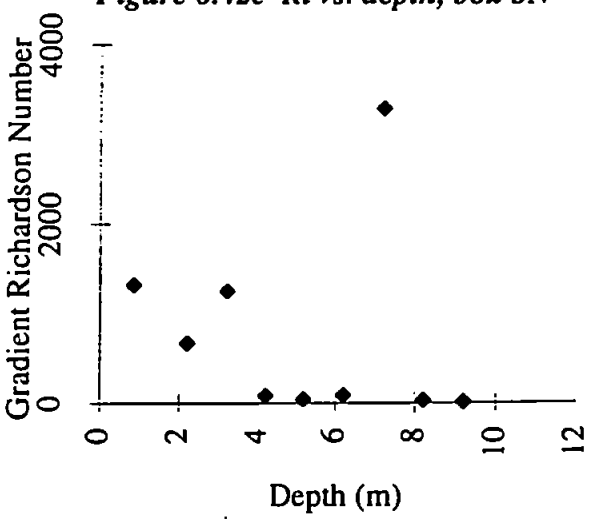

the flow reversal and its associated increase in velocity shear occurs below the peak in Ri, from around 6.3 m depth and below. The depth profiles for boxes 2N, 3N and 4N (figures 6.42b, 6.42c and 6.42d) all show high Ri values at the surface, which decrease from the surface to about 3.3 m and are then constant with depth. This generalised profile shape indicates that the near surface flow has a reasonably uniform velocity throughout its depth, whereas the deeper flow exhibits a higher degree of shear, which is interpreted to be the result of the formation of the frontal interface. If this is the case, then the frontal interface does not appear at a discrete depth from the Ri profiles; rather its presence is inferred from the increased velocity shear and turbulence over the depth range 3.3 m to 9.3 m. Profiles for boxes 5N and 6N (figures 6.42e and 6.42f) show very much higher Ri values over the whole depth than in the preceding boxes. This is interpreted as indicating a higher degree of ambient stratification on the day on which 5N and 6N were surveyed, in comparison to the other two survey days. The profile for box 7N (figure 6.42g) has a similar depth variation to those of boxes 2N, 3N and 4N, such that a uniform flow in the surface layer overlies a more turbulent flow with higher velocity shear at depth. The transition between the two types of flow occurs at approximately 2 m depth.

Considering the depth profiles for the southern boxes, 1S and 2S (figures 6.42h and 6.42i) both have two distinct maxima in Ri values at about 2 m and 9 m depth for 1N, and slightly deeper at 3 m and 10 m for 2N. The profile for 3S (figure 6.42j) also has a maximum at approximately 2 m depth, below which Ri remains constant with depth. It is postulated that the profiles for 1S and 2S represent a two layer flow with Ri values being highest in the more uniform flow in each of the two layers, and lowest in the more turbulent environment between the two layers. Considering the early stage of the ebb tide at which these two boxes were recorded, the two layer flow structure is likely to be associated with the flow reversing earlier in the deeper layer than in the shallower layer. The interface between the two layers appears to be centred at approximately 6.3 m depth in both boxes. In box 3S, the transition from uniform to more turbulent flow occurs between 3 m and 4 m depth.

Having examined the Ri values for each box, a parameter describing the amount of vertical mixing can be determined following the analysis of Munk and Anderson (1948). Their work determined empirically the following relationship;

*Figure 6.42f Ri vs. depth, box 6N*

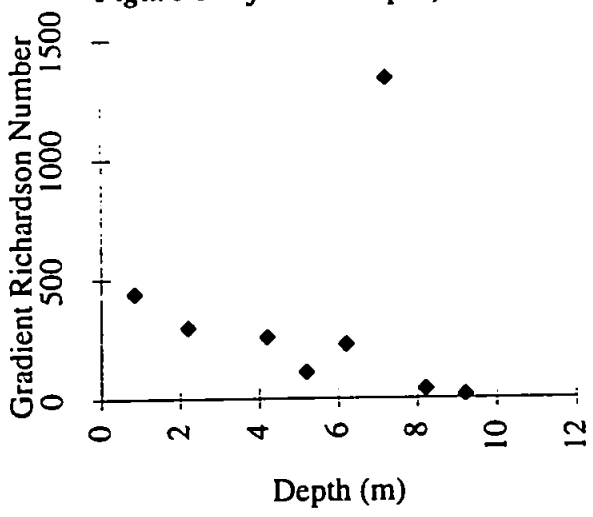


*Figure 6.42g Ri vs. depth, box 7N*

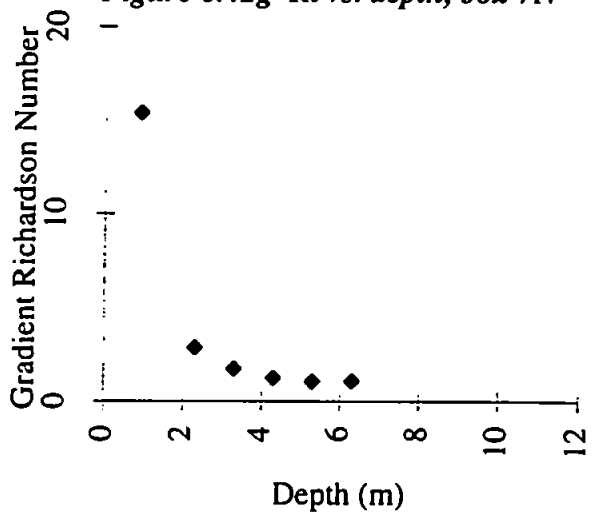


*Figure 6.42h Ri vs. depth, box 1S*

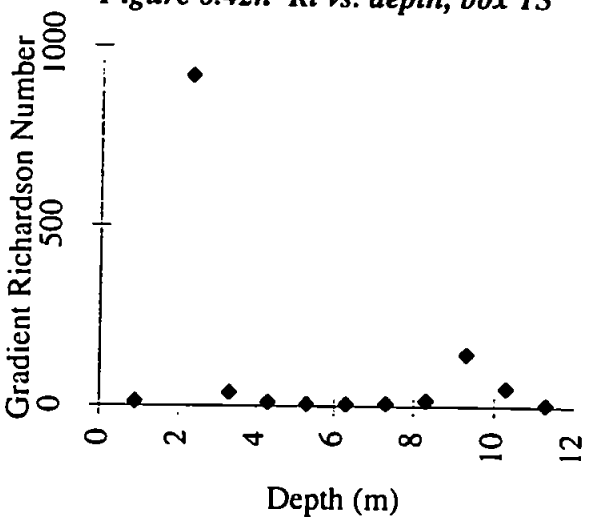


*Figure 6.42i Ri vs. depth, box 2S*

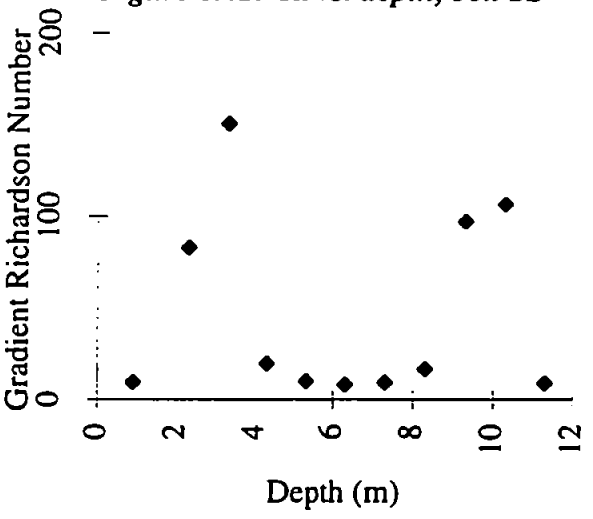


*Figure 6.42j Ri vs. depth, box 3S*

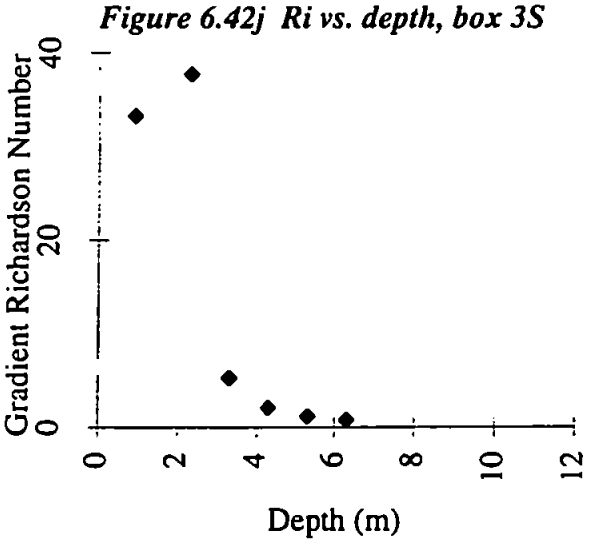

$$\varepsilon_v = \varepsilon_0 (1 + 3.33\ Ri)^{-3/2} \qquad (6.2)$$

where $\varepsilon_v$ is the vertical mixing coefficient, and $\varepsilon_0$ is the value of $\varepsilon_v$ for a flow with neutral stability. From equation 6.2, the parameter $\varepsilon_v/\varepsilon_0$ can be found for each depth slice, and the results are presented as depth profiles for each box in figures 6.43a to 6.43j. As expected, these profiles are closely and inversely related to the Ri depth profiles (figures 6.42a to 6.42j). Thus, in 1N (figure 6.43a) the highest level of vertical mixing occurs at 9.3 m, near the base of the water column and is probably caused by the proximity of the river bed and the resulting friction-induced turbulence. In boxes 2N and 3N (figures 6.43b and 6.43c) $\varepsilon_v/\varepsilon_0$ is small at the top and the base of the water column with a maximum in between, which is associated with the formation of the Tamar-Lynher front. Peak vertical mixing occurs at between 6 m and 7 m, which provides a good indication of the average depth of the frontal interface at this point in the ebb. In boxes 4N and 7N (figures 6.43d and 6.43g), $\varepsilon_v/\varepsilon_0$ has increased by, on average, an order of magnitude in comparison to 3N. The general shape of the profiles has also changed such that $\varepsilon_v/\varepsilon_0$ starts to increase from 4 m depth in 4N and 1 m depth in 7N. It seems that from 1N to 7N, the water column is becoming gradually more turbulent, such that in 7N the majority of the water depth has a high vertical mixing coefficient. This is consistent with the onset of the turbulent jet of Lynher water, which has been previously discussed and which dominates the hydrodynamics in box 7N. Boxes 5N and 6N (figures 6.43e and 6.43f) have thus far been omitted from this discussion. This is because the values of $\varepsilon_v/\varepsilon_0$ are very small in both boxes over the whole of the water depth, and whilst this may indicate a genuine reduction in the vertical mixing coefficient, the observed change in the ambient stratification on this survey day will alter the value of $\varepsilon_0$, such that no conclusions can be drawn about vertical mixing in these two boxes.

In the southern part of the area, values of $\varepsilon_v/\varepsilon_0$ are small in 1S and 2S (figures 6.43h and 6.43i) increasing dramatically in 3S (figure 6.43j), such that the effect of the Lynher jet extends over the entire survey grid in the late ebb.

*Figure 6.43a Ev/E0 vs. depth, box 1N*

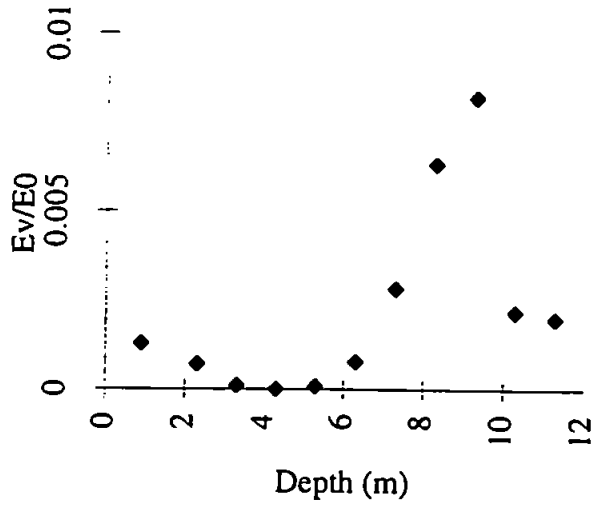


*Figure 6.43b Ev/E0 vs. depth, box 2N*

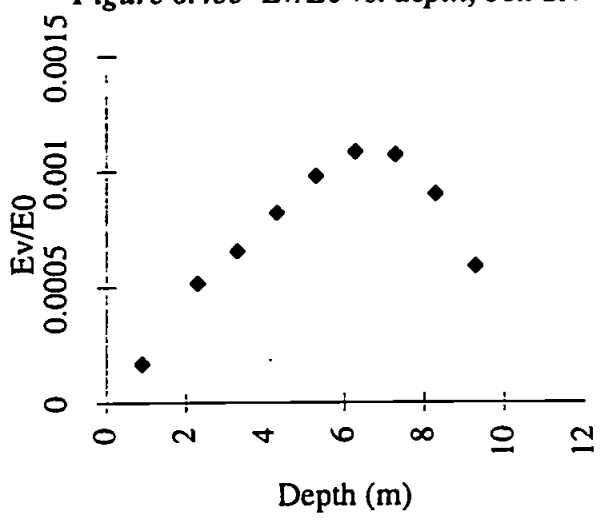


*Figure 6.43c Ev/E0 vs. depth, box 3N*

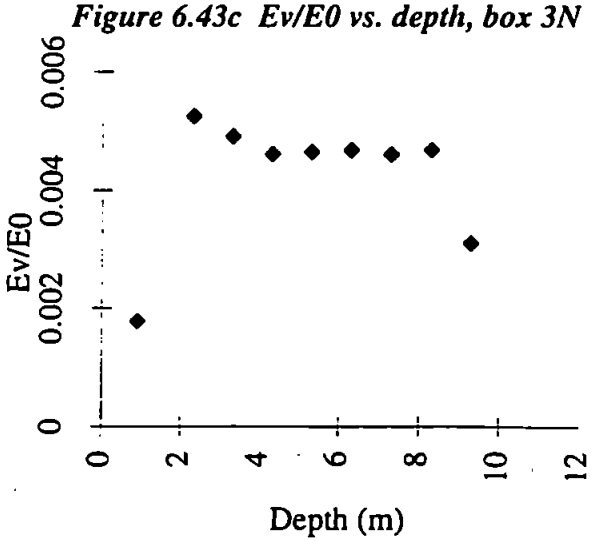


*Figure 6.43d Ev/E0 vs. depth, box 4N*

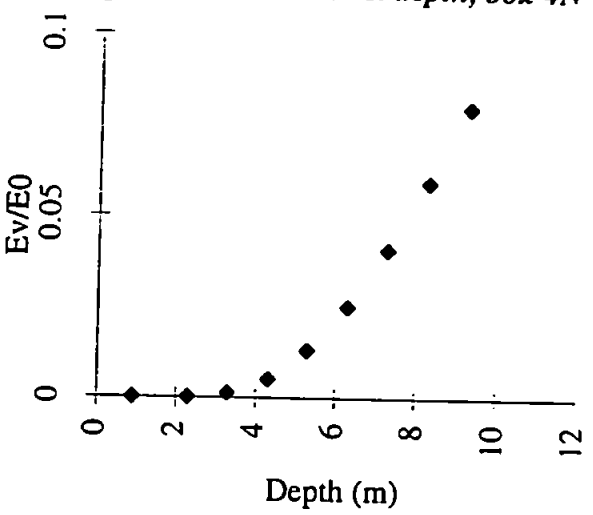


*Figure 6.43e Ev/E0 vs. depth, box 5N*

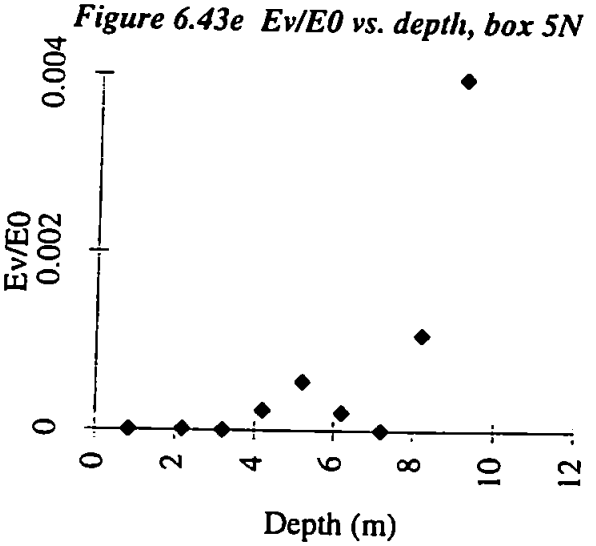

*Figure 6.43f Ev/E0 vs. depth, box 6N*

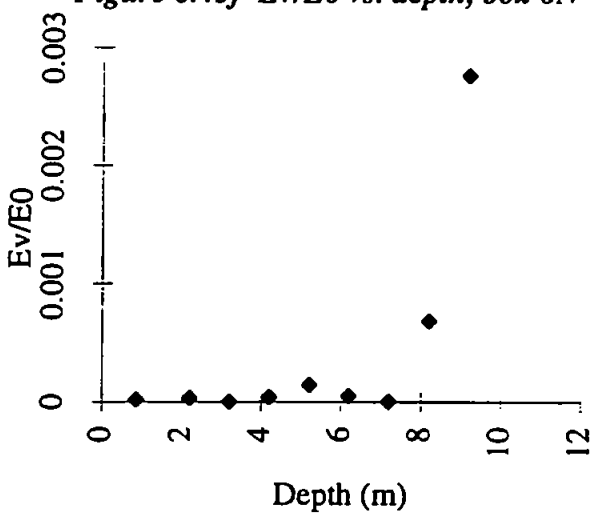


*Figure 6.43g Ev/E0 vs. depth, box 7N*

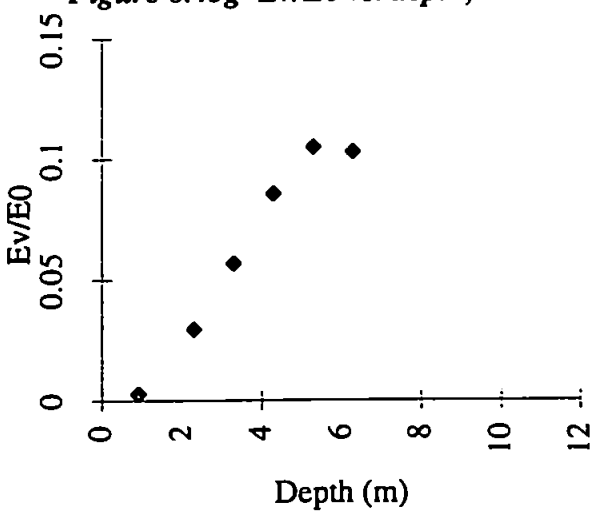


*Figure 6.43h Ev/E0 vs. depth, box 1S*

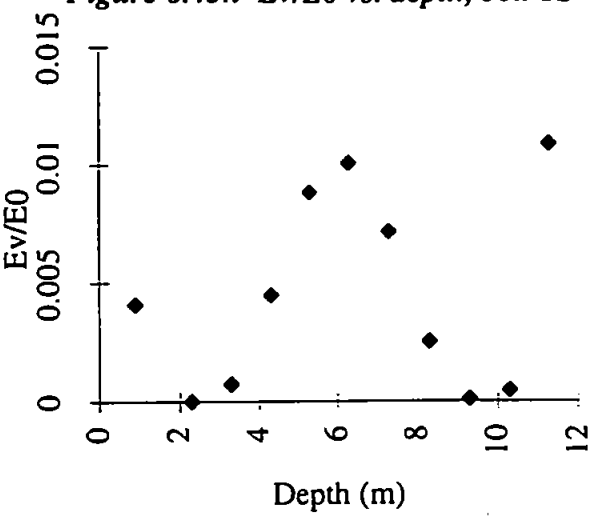


*Figure 6.43i Ev/E0 vs. depth, box 2S*

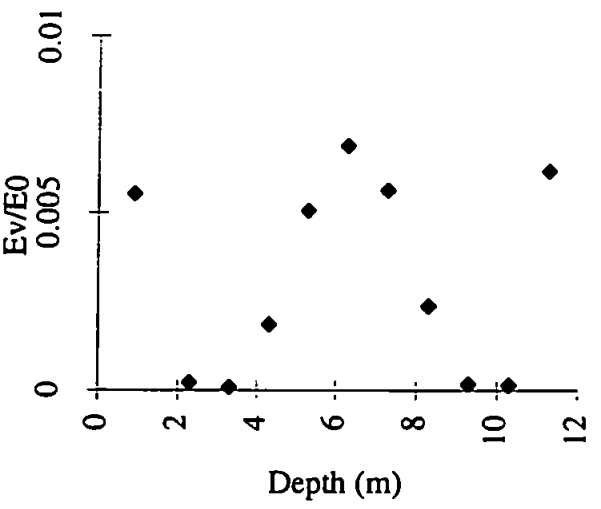


*Figure 6.43j Ev/E0 vs. depth, box 3S*

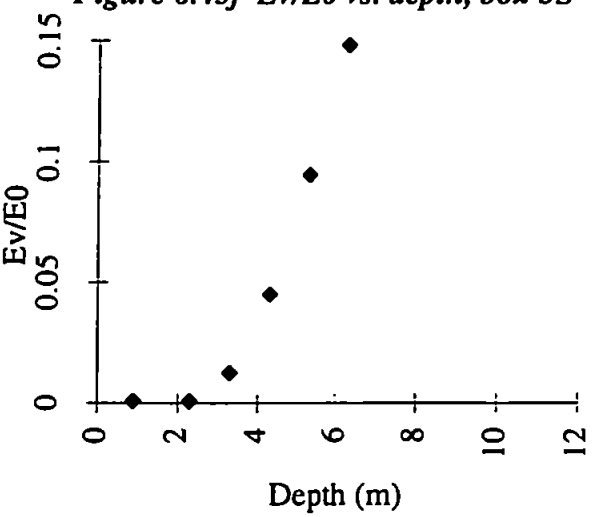

Considering both the Richardson number and the vertical mixing parameter together, it appears that the development of the flow within the survey area occurs in several distinct stages over the ebb tide. Initially, as the tide turns, a uniform flow overlies a more turbulent flow, and the turbulence is interpreted to be the result of both bed-induced friction, and a non-synchronous flow reversal throughout the depth of the water column. Then, in the early stages of the ebb, the low tidal velocities allow the formation of two separate, uniformly-flowing layers which are separated by a layer of more turbulent flow. The upper layer of uniform flow is interpreted to be Lynher water, the lower layer is Tamar water and the turbulent, intermediate layer is thought be the frontal interface. From one hour forty minutes after high water onwards, the evolution of the intermediate turbulent layer dominates the dynamic regime. Initially, the turbulence appears to erode the underlying region of more uniform flow, and this process may be assisted by the increasing tidal flows generating more turbulence at the base of the water column, near the river bed. By two hours after high water, the more uniform layer of Tamar water has been eroded away completely so that the water column now comprises an upper, uniform layer of flow, below which the region of high turbulence and increased vertical mixing extends right to the base of the water column. By the late ebb, the turbulence has now eroded the upper uniform layer, so that the majority of the water depth now has a low Ri value and a high $\varepsilon_v/\varepsilon_0$ value. Only the uppermost metre of the water column still has a very slightly more uniform flow structure.

Examination of the vertical density gradients for each box over the whole survey grid shows a gradual decrease in $\partial\rho/\partial z$ from high water to about 3 hours later, where it reaches a minimum value before increasing slightly as low water is approached. Thus it seems that there is a higher degree of stratification at the start of the ebb which is then mixed away as the ebb progresses. This is the converse of the generalised situation in estuaries, where a mixed water column at high water gradually becomes more stratified during the ebb. Therefore, it seems that the turbulence caused initially by velocity shear at the frontal interface and sustained in the form of the Lynher jet, serves to reduce the stratification during the ebb tide, effectively suppressing the more usual development of estuarine stratification as the tide ebbs. However, the expected increase in stratification is seen right at the end of the combined survey period from 5 hours after high water onwards.

### *6.3.2 Flux Richardson number Analysis*

For each of the four sides of every depth slice, two flux Richardson numbers have been calculated, one using longitudinal velocity data and the other using lateral velocity data. In order to calculate flux Richardson numbers, the vertical eddy diffusivity and viscosity must first be found. Considering first the eddy viscosity, this parameter describes the relationship between the Reynold's stress and the mean velocity gradient. With velocity data divided into three orthogonal components, there are nine different Reynold's stresses which can be calculated, however, we are primarily interested in the exchange of momentum by turbulent stress in the vertical direction. Hence, for each side of a depth slice, the following two equations were applied to find two values of eddy viscosity, $N_{zu}$ and $N_{zv}$:

$$-\overline{(u'.w')} = N_{zu}\left(\partial\bar{u}/\partial z\right) \qquad (6.3)$$

$$-\overline{(v'.w')} = N_{zv}\left(\partial\bar{v}/\partial z\right) \qquad (6.4)$$

The Reynold's stresses are calculated from the turbulent fluctuations of longitudinal and vertical velocity in equation 6.3, and from the turbulent fluctuations in lateral and vertical velocity in equation 6.4. For each of the four sides of a survey box, depth profiles of the mean longitudinal and lateral velocities were plotted from the $\bar{u}$ and $\bar{v}$ values for each slice. The profiles were interpolated to give new values for $\bar{u}$ and $\bar{v}$ at the top and base of each slice, allowing $\partial\bar{u}/\partial z$ and $\partial\bar{v}/\partial z$ to be found for each slice.

The eddy diffusivity coefficient, $K_z$ relates the Reynold's flux to the vertical gradient of salinity and this coefficient can only be found in the top two or three slices of the survey box where salinity data is available. The following equation was applied to each side of the top two or three slices;

$$-\overline{(w'.S')} = K_z\left(\partial\bar{S}/\partial z\right) \qquad (6.5)$$

The Reynold's flux on the left-hand side is calculated from the turbulent fluctuations in vertical velocity and salinity, and the depth profile of mean salinity was used to find the mean salinity gradient across the 1m thickness of each slice.

Having found two eddy viscosities and an eddy diffusivity for each side of the top two or three depth slices, two flux Richardson numbers are calculated as follows;

$$Rfu = \left(K_z / N_{zu}\right) Ri_u \quad (6.6)$$

$$Rfv = \left(K_z / N_{zv}\right) Ri_v \quad (6.7)$$

$Ri_u$ and $Ri_v$ denote Richardson numbers calculated for each depth slice using slice-averaged values of $\bar{u}$ and $\bar{v}$ respectively instead of the total mean velocity $V_T$ used previously in section 6.3.1. Thus, the two flux Richardson numbers are effectively expressing the fraction of the available kinetic energy from either the longitudinal or lateral flow which is used to mix the fluid, and thus becomes potential energy associated with the change in stratification. Values of $Ri_u$, $Ri_v$, $N_{zu}$, $N_{zv}$, $K_z$, Rfu and Rfv for each side of each depth slice are presented in table 7 of the appendix.

Both the eddy viscosities and the eddy diffusivity should have positive values to be meaningful in terms of the physical processes they represent. This is because at any point in the flow, the Reynold's stresses and the Reynold's flux will, on average, have the opposite polarity to the mean gradients of either velocity or salinity respectively. Hence, all calculated values of $N_{zu}$, $N_{zv}$ and $K_z$ should be positive. As the results in table 7 (appendix) clearly show, this is not found to be the case in our analysis. Only 45% of the $K_z$ values, 41% of $N_{zu}$ values and 69% of $N_{zv}$ values are positive.

Initially, it was hoped that these results could be used to perform a similar analysis to that undertaken by Linden (1980) in which the flux Richardson numbers are plotted against the overall Richardson numbers, for laboratory observations. However, not only are the eddy diffusivity and viscosity results disappointing, but it is obvious from the definition of the flux Richardson number that this parameter cannot be greater than one. For our results, it was found that only 25% of Rfu values and 23% of Rfv values are less than one. In both the longitudinal and lateral directions, only about 10% of the total number of depth slices had meaningful values of the flux Richardson number, eddy diffusivity and viscosity, and thus it was considered to be statistically invalid to apply Linden's Rf versus Ri analysis to this data-set.

Despite finding that the flux Richardson numbers in our analysis are, for the most part, erroneous, an attempt has been made to find the critical flux Richardson number, Rfc, for the longitudinal and lateral data sets. Following the work of, originally, Ellison (1957) and more recently Odd and Rodger (1978), $K_z/N_{zu}$ and $K_z/N_{zv}$ are plotted against $Ri_u$ and

$Ri_v$ respectively. Ellison stated that as Ri increases, Rf increases to a maximum value, Rfc, and $K_z/N_z$ decreases from unity and tends towards zero. The parameter Rfc expresses the maximum fraction of the turbulent energy generated by internal shearing which is available for increasing the potential energy of the flow. In our analysis, for both horizontal directions, only those depth slices with positive values of Kz and $N_{zu}$ or $N_{zv}$, and with Richardson numbers ($Ri_u$ or $Ri_v$) of less than 1000 were including, substantially reducing the size of the data sets. The graph of $K_z/N_{zu}$ vs. $Ri_u$ is presented in figure 6.44 and $K_z/N_{zv}$ vs. $Ri_v$ is in figure 6.46.

Figure 6.44

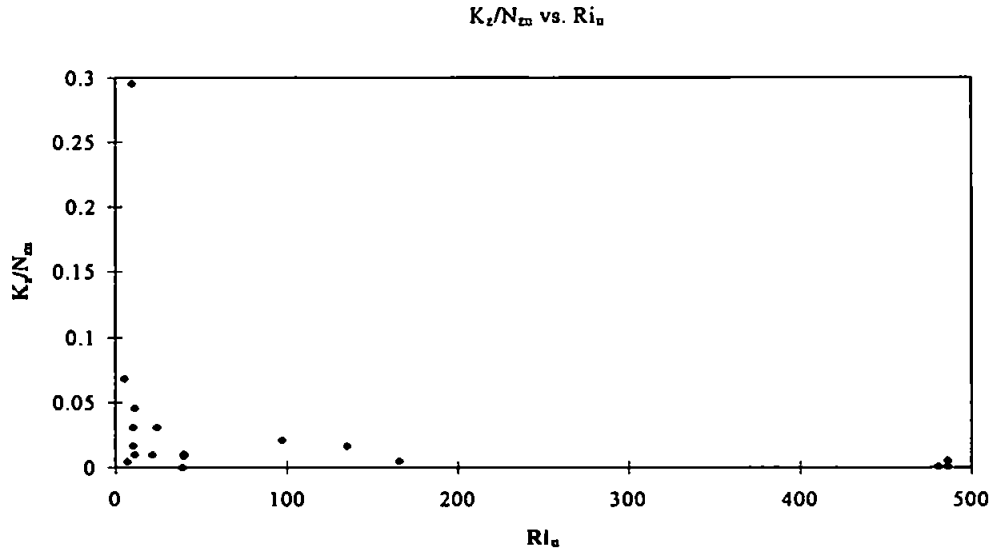


Considering first the longitudinal results, the data points on the graph lie along a curve which has a similar shape to those plotted by Ellison for varying values of Rfc and shown in figure 6.45.

*Figure 6.45 Ellison's curve of $K_z/N_z$ vs. Ri*

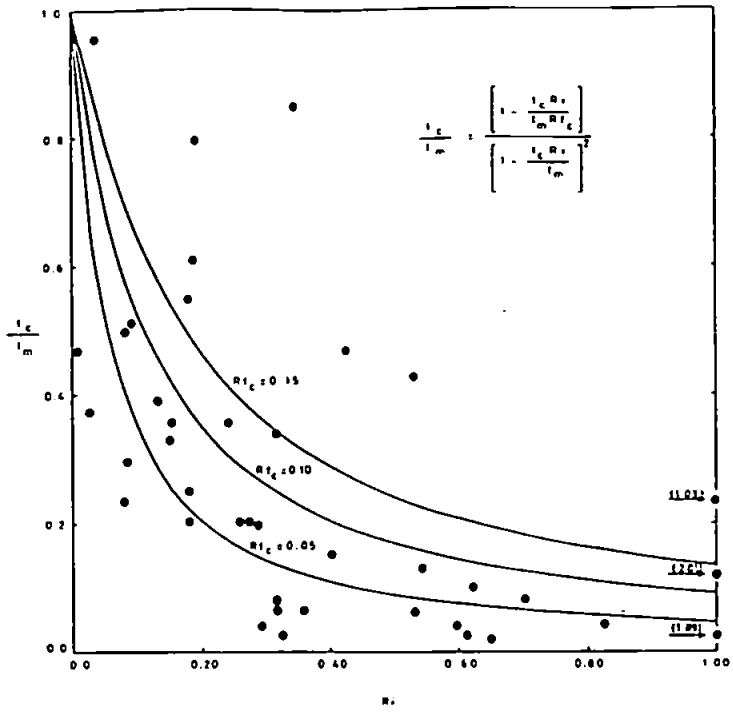

(from Odd and Rodger, 1978)

However, the values of $K_z/N_{zu}$ decrease from 0.3 in our data, as opposed to 1 in Ellison's work, and no $Ri_u$ values of less than 1 were found in our analysis, so that a direct comparison between the two sets of results is impossible. It can be seen that $K_z/N_{zu}$ does appear to tend towards zero though, as predicted. Whilst the limited number of data points on the $K_z/N_{zu}$ vs. $Ri_u$ graph prevents a direct comparison, the general shape of the graph and the magnitudes of the values plotted are similar to results obtained by Parsons (1987) from data collected during his survey in this part of the estuary during the ebb tide. The graph of $K_z/N_{zv}$ vs. $Ri_v$ in figure 6.45 has no relationship to the work of Ellison whatsoever.

Figure 6.46

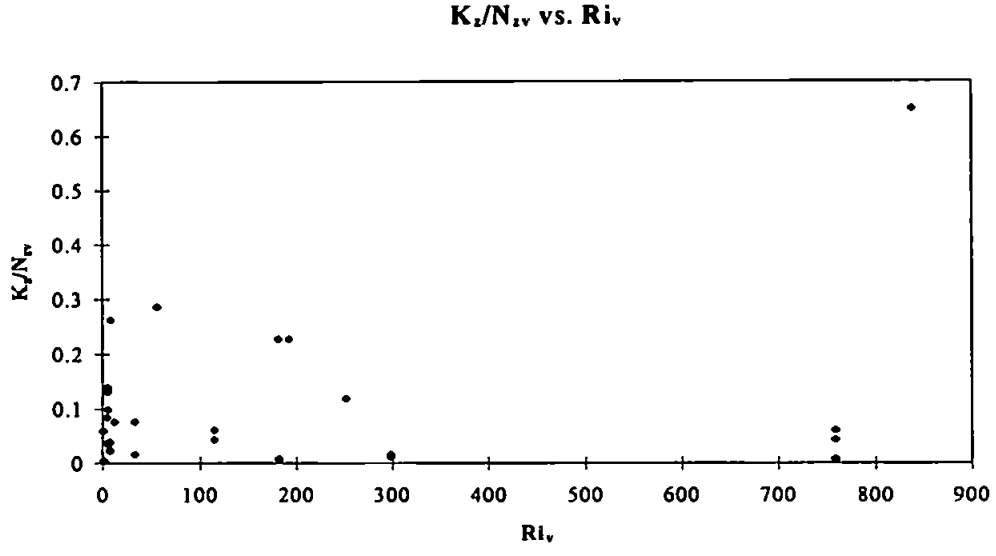


It is possible that the dynamics in the lateral direction are more varied and complex than this analytical approach allows for.

From his results, Ellison derived the following relationship;

$$K_z = N_z \frac{1-\left(\frac{K_z}{N_z}\right)\left(\frac{Ri}{Rfc}\right)}{\left[1-\left(\frac{K_z}{N_z}\right)Ri\right]^2} \qquad (6.8)$$

It should be noted that in his work, Ellison actually used the momentum and solute mixing lengths instead of the eddy viscosity and diffusivity. However, as the ratio of the solute mixing length to the momentum mixing length is equal to the ratio of eddy diffusivity to eddy viscosity, Ellison's original equation is equivalent to equation (8). This has been used to determine a value of Rfc in both horizontal directions, for the sake of completeness, from each of the data points plotted in figures 6.44 and 6.45. The average value of Rfc in the longitudinal direction is 0.36 and in the lateral direction is 0.41. These values are considerably higher than Ellison's, who found Rfc to be 0.15, and very much higher than Odd and Rodger's value of Rfc which is 0.08. Our results, which are obviously inconclusive, appear to suggest that a larger fraction of turbulent kinetic energy can be used to increase the potential energy of the flow than previously thought,

and that the energy transfer in our particular dynamic system is apparently more efficient than that found by previous authors. If this is indeed the case, then it implies that less kinetic energy than expected is being used to produce internal waves which are eventually dissipated by viscous effects, and thus more energy is available to mix the fluid. Internal waves require a sharp density interface along which to propagate, and it may be that the density interface within our survey area is not sufficiently well-defined. Although in terms of the flow direction, there are two layers certainly in the early stages of front formation, the density contrast between these two layers may not be large enough to allow internal wave generation. Also, turbulence appears to mix away what little contrast there is fairly rapidly in the early to middle stages of the ebb tide, and hence if internal waves cannot form, more turbulent kinetic energy becomes available to mix the fluid, which is a possible explanation for the high Rfc values. Alternatively, because both of the layers identified in our survey appear to become increasingly turbulent as the ebb tide progresses, this may explain the high Rfc values. In Ellison's work, only one layer was turbulent and it seems reasonable that the mixing efficiency would be increased in the presence of two turbulent layers in comparison to the efficiency determined for only one turbulent layer.

# CHAPTER 7
# CONCLUSIONS AND FUTURE WORK

Before drawing any conclusions from the work conducted during this project, it should be noted that several equipment and logistical problems have reduced the overall reliability of the results. The accuracy of the ETS results are particularly questionable owing to the fact that so many of the thermistors were faulty, and data from those thermistors which were functioning were considerably degraded by electronic noise. The ADCP results are generally more reliable, although having to use navigation data from a separate heading sensor may have introduced errors into the data set. During the period of detailed surveying, it was not possible to conduct a complete and continuous survey of one whole ebb tide, for various logistical reasons. Given that the aim of the project was to examine frontal evolution during an ebb tide, the fact that the fieldwork was interrupted produced a data set which was far from ideal. However, as the major part of the fieldwork was conducted on three separate days, some conclusions can be drawn about the extent to which variable background conditions affecting the survey region of the estuary appear to influence the evolution of the front and its dynamics. Bearing this in mind, most of the conclusions that have been reached can only be considered as an approximate indication of what may be happening during the course of a generalised ebb tide, based on the available data.

## 7.1 BACKGROUND CONDITIONS WITHIN THE SURVEY AREA

*i.* There is a seasonal variation in temperature in the region of the Tamar-Lynher confluence of over 10°C, with the coldest temperatures in January and the warmest in August. Salinity is generally higher during the summer months than during the winter.

*ii.* The degree of stratification in this region of the estuary also varies seasonally, with high run-off during the winter increasing the stratification in comparison to more homogeneous conditions during summer. On a shorter time-scale, periods of anomalously high run-off are seen to stratify the water column to a greater extent than expected from a consideration of just the seasonal variability in stratification.

*iii.* During the three detailed surveys, temperature and salinity differences across the Tamar-Lynher front were slight, with the Lynher water being warmer by 0.05°C to

0.1°C and more saline by up to 1‰ than the Tamar water. The Lynher water column was also marginally more stratified than the Tamar water column.

## 7.2 EVOLUTION OF THE FRONT AND ITS CHARACTERISTICS

*i.* The evolution of the front in the region of the Tamar-Lynher confluence appears to occur in two stages, the first being the formation of a convergent interface between south-westwards flowing Tamar water and south-eastwards flowing Lynher water. This phase commences approximately 1 hour 30 minutes after high water and continues until about 3 hours after high water. In the second stage, from 3 hours after high water onwards, the convergent front is pushed south-eastwards, further out into the Tamar river and evolves into a jet which extends across most of the detailed survey area. The initial convergent front then forms the northernmost boundary of the jet with a second, less distinct front delineating the southernmost boundary.

*ii.* During the first stage of frontal evolution, the interface between the two water masses is almost horizontal, being inclined by only about 6°. The marginally denser Tamar water forms a wedge underlying the Lynher water.

*iii.* During the second stage, the fronts on both the northern and southern boundaries of the jet have an orientation which is now closer to vertical than horizontal such that the Lynher water now extends from the surface down to the river bed, within the jet. As the tide ebbs and the depth of the water column is reduced, the jet becomes increasingly constrained by the river-bed topography, with the position of both boundary fronts being approximately described by the 10 m depth contour. Flow within the jet itself is accelerating south-eastwards down a slope in the river-bed topography.

*iv.* The vertical velocity averaged over the area of the survey grid and calculated from a consideration of continuity, is directed downwards in the northern half of the grid which is consistent with the down-welling expected at the convergent front formed in the early part of the ebb tide. The average vertical velocity increases initially as the convergent front becomes better established, but then decreases as the front evolves into a jet and down-welling is reduced. In the southern half of the grid, the average vertical velocity is smaller and directed upwards throughout the ebb tide. It is possible that the influx of water into this part of the survey grid from the south-easterly flowing jet generates a slight up-welling in this region.

*v.* The cross-frontal transport of both water and salt across the northern boundary front is directed from the Tamar into the Lynher jet, via entrainment by interfacial waves. From the few estimates of entrainment velocity that have been obtained, it seems that the cross-frontal transport increases as the initial convergent front develops into a jet. Across the weaker, southern boundary front, the transport of water and salt appears to be less compared with the northern boundary, and here the transport is directed out of the Lynher jet back into the surrounding Tamar water. It is postulated that this transport may be explained by the presence of eddies along the southern boundary of the jet, a phenomenon which has been observed in laboratory studies of jets discharging into a cross-flow.

## 7.3 THE MOMENTUM BALANCE

*i.* During the three detailed surveys, the longitudinal dynamics within the area vary in a more predictable manner throughout the ebb tide than the lateral dynamics, which are thought to be more susceptible to the influence of temporal changes in tidal range and river inflow.

*ii.* At high water, there are no primary forces acting either longitudinally or laterally, such that the initial velocities seen at this time must have originated outside the survey area. Longitudinally, the flow is accelerated downstream primarily by the pressure gradient arising from the slope of the water surface, and it is resisted by the upstream-directed force arising from the density distribution. Hence, the longitudinal dynamics are characterised by the competition between the barotropic and baroclinic terms. Laterally, the situation is more complex, but again the flow is primarily accelerated by the barotropic term. It should be noted that the complexity in the variation of the lateral dynamic balance is possibly due to an inadequate assessment of the curvature term in the equation of motion.

*iii.* In the early stages of the ebb tide, turbulent stress increases with depth owing to friction effects at the river bed. Longitudinally, there is a reasonably homogeneous density distribution within the survey area, as evidenced by the small baroclinic gradient. Laterally, the advection of less dense Lynher water and denser Tamar water into the two sides of the survey area promotes a comparatively larger lateral baroclinic gradient.

*iv.* Approximately 2 hours after high water, there is a marked increase in the vertical shear in horizontal velocity associated with the development of the near-horizontal frontal interface between Tamar and Lynher waters.

*v.* A two-layer flow structure has now developed in which the Lynher water overlies the Tamar water. In both the longitudinal and lateral directions, the Lynher flow is primarily accelerated barotropically, whereas the Tamar flow is mainly accelerated by the baroclinic force. The barotropic and baroclinic pressure gradients produce forces which oppose each other, and the depth at which these two forces cancel each other out, such that there is no net primary forcing mechanism, is interpreted to be the depth of the frontal interface.

*vi.* From 2 to 3 hours after high water, a comparison of the magnitudes of the barotropic and baroclinic pressure gradients suggests that the depth of the frontal interface is increasing with time. Turbulent stress is now decreasing with depth, such that the overlying Lynher water is more turbulent than the underlying Tamar water.

*vii.* At approximately 3 hours after high water, the two-layer flow structure has now been replaced by a turbulent, buoyant jet of Lynher water across the area. Lynher water now extends from the surface to the river bed throughout most of the survey grid, and turbulent stress is highest near the surface within the jet.

*viii.* Generally, the level of turbulent stress in the water column (which is now predominantly Lynher water within the survey area) has increased considerably from high water. Mixing by entrainment at the boundaries of the jet is occurring such that lateral differences in density between Lynher and Tamer waters are now reduced, and there is a corresponding decrease in the magnitude of the lateral baroclinic term.

*ix.* Towards the end of the ebb tide, the formation of the Lynher jet results in large spatial accelerations in both the longitudinal and lateral directions which represent a rotation in the net flow of the jet, from having a large eastwards velocity component as it enters the survey area in the north, to having a dominantly southwards component as it exits the survey area in the south.

*x.* Classically, river flow is forced barotropically, the flow in coastal seas is forced baroclinically and estuarine flow is forced by both barotropic and baroclinic pressure gradients. Thus, perhaps it can be said that the dynamics of the Lynher flow are more 'riverine' in nature than those of the Tamar flow. If this is the case, then we would

expect the Lynher flow to be particularly influenced by variations in fresh water run-off. Given the orientation of the survey grid with respect to the topography of the Lynher river, it seems feasible that the lateral dynamics in the survey area are strongly affected by the behaviour of the Lynher flow. As this flow appears to be more sensitive to variations in run-off than the Tamar flow, this provides a possible explanation for the inconsistent behaviour of the lateral dynamics in comparison to the longitudinal dynamics, during the three days of detailed surveying. Additionally, variations in other factors such as tidal range and wind stress may also be responsible, all of which will affect the formation and behaviour of the front. From his work in the region of the Tamar-Lynher confluence, Parsons (1987) also postulates that mixing, river discharge and tidal range may strongly influence the structure and dynamics of the front.

## 7.4 MIXING

*i.* From Richardson number and vertical mixing coefficient profiles, the flow structure and mixing regime within the survey area can be seen to develop in several distinct stages during the course of an ebb tide.

*ii.* As the tide turns, a uniform flow overlies a more turbulent flow, where the turbulence is believed to be the result of bed-induced friction, and internal velocity shear associated with a non-synchronous flow reversal throughout the depth of the water column.

*iii.* In the early stages of the ebb, a two-layer flow structure evolves in which the upper layer is interpreted to be Lynher water and the lower layer is interpreted as Tamar water. These two uniformly-flowing layers are separated by a region of more turbulent flow thought to represent the frontal interface.

*iv.* From 1 hour 40 minutes after high water, the intermediate turbulent region expands such that initially, the turbulence erodes the underlying layer of uniform flow, assisted by increasing tidal currents generating more turbulence at the base of the water column, due to bed friction. By 2 hours after high water, the more uniform layer of Tamar water has been eroded away completely.

*v.* By the late ebb, the turbulence has now eroded the upper uniform layer, such that the majority of the water depth now has a low Richardson number and a high

vertical mixing coefficient. This stage of the flow development represents the establishment of the Lynher jet.

*vi.* Consideration of the vertical density gradients shows that there is a higher degree of stratification at the start of the ebb which is then mixed away as the ebb progresses. The classical situation in estuaries is that a mixed water column at high water gradually becomes more stratified during the ebb, thus it seems that turbulence induced by velocity shear at the frontal interface and sustained by the Lynher jet suppresses the expected development of stratification as the ebb tide progresses.

*vii.* Results from the flux Richardson number analysis are inconclusive. However, the estimate of the critical flux Richardson number is higher than expected from previous work by various authors. Possible explanations are that there is an insufficient density contrast in the water column to allow the formation of internal waves, hence more kinetic energy is available for mixing. Alternatively, it may be that previous experimental work was conducted with one uniform layer and one turbulent layer, whereas in our case, both layers rapidly become turbulent, which may account for the discrepancy between values of the critical flux Richardson number.

In terms of the classification of estuarine fronts reviewed in chapter 1, the Tamar-Lynher front cannot be easily categorised. The first stage of the front's development is perhaps best described as a plume front (section 1.2.1) in which the less dense Lynher water spreads out and flows over the denser Tamar water. The dynamics of a plume front are observed by Bowman (1988) to be controlled by surface pressure gradients, interfacial friction and entrainment. Given that the Lynher flow is accelerated barotropically, and turbulent stress is highest at the frontal interface, describing the first stage of the front as a plume front seems reasonable. The second stage in the front's development is perhaps better described as a turbulent jet rather than a front; however the boundary of the jet does have some similarities to a tidal mixing front (section 1.2.2) in that it separates the more turbulent Lynher water with its increased vertical mixing, from the less turbulent Tamar water.

## 7.5 RECOMMENDATIONS FOR FUTURE WORK

This thesis has attempted to describe and quantify the structure and dynamics of the Tamar-Lynher front throughout its development during an ebb tide. Recommendations to improve the work conducted for this project will be described, followed by a summary of suggestions for future work arising from the conclusions of this thesis.

*i.* Perhaps the most obvious improvement would be to obtain a more complete and reliable set of temperature results from the ETS. The front should also be surveyed continuously from high water to low water in order to make a more comprehensive assessment of its evolution and behaviour.

*ii.* Given that the density within an estuary is predominantly controlled by the salinity, measurements of both the fluctuating and time-averaged components of salinity over the area of each side of the survey grid would allow the equations of continuity and motion to be calculated more accurately.

*iii.* Wherever possible, the time taken for one box to be surveyed (usually between thirty and forty minutes) has been accounted for in the analysis and interpretation of results. Ideally, a more truly synoptic approach to surveying would permit a better resolution of the dynamics operating at various stages throughout the ebb tide. As such, using two or more research vessels to complete each box of the survey grid would significantly reduce the surveying time and improve accuracy.

*iv.* The ambient temperature and salinity characteristics within the survey region could be better defined using continuously recording instruments mounted on fixed moorings at each corner of the survey grid.

*v.* Drogue-tracking or dye-release experiments in the survey region would provide information on the pattern of surface convergence at the front. Additionally, the stream-lines determined from, for example, a drogue-tracking experiment would allow a far more accurate assessment of the curvature term in the lateral dynamic balance to be made.

As mentioned earlier, whilst the surveying strategy in this project was not ideal, it has indicated that the evolution and dynamics of the Tamar-Lynher front may vary from day to day, depending on factors such as river inflow, tidal range, ambient temperature, salinity and stratification and wind surface stress. The lateral dynamics in particular seem

to be influenced by variations in these factors, whereas indications are that the longitudinal dynamics are more 'robust' and less variable. Hence an experiment designed to concentrate more exclusively on determining the lateral dynamic regime across the front for a range of tidal and run-off conditions, would lead to a better understanding of the relationship between the general conditions in the estuary and the formation of the front.

# REFERENCES


Bowden, K.F., 1960. Circulation and mixing in the Mersey Estuary. I.A.S.H. Commission of Surface Waters, No. 51: 352-360.

Bowden, K.F. and Gilligan, R.M., 1971. Characteristic features of estuarine circulation as represented in the Mersey Estuary. *Limnology and Oceanography,* 16: 490-502.

Bowman, M.J., 1988. Estuarine fronts. In: "Hydrodynamics of Estuaries" (ed., Kjerfve, B.), vol. 1, CRC Press, 85-132.

Bowman, M.J. and Esaias, W.E., 1981. Fronts, stratification and mixing in Long Island and Block Island Sounds. *Journal of Geophysical Research,* 86: 4260-4264.

Bowman, M.J. and Iverson, R.L., 1977. Estuarine and plume fronts. In: "Oceanic Fronts in Coastal Processes" (eds., Bowman, M.J. and Esaias, W.E.), Springer-Verlag, 87-104.

Cameron, W.M. and Pritchard, D.W., 1963. Estuaries. In: "The Sea" (ed., Hill, M.N.), vol. 2, John Wiley and Sons, New York, 306-324.

Chereskin, T.K., 1983. Generation of internal waves in Massachusetts Bay. *Journal of Geophysical Research,* 88(C4): 2649-2661.

Crow, S.C. and Champagne, F.H., 1971. Orderly structure in jet turbulence. *Journal of Fluid Mechanics,* 48: 547-596.

Dyer, K.R., 1973. "Estuaries: A Physical Introduction", John Wiley and Sons, London.

Dyer, K.R., 1977. Lateral circulation effects in estuaries. In: "Estuaries, Geophysics and the Environment", National Research Council, Geophysics of Estuaries Panel, Washington, D.C.: 22-29.

Dyer, K.R., 1982. Localised mixing of low salinity patches in a partially mixed estuary (Southampton Water, England). In: "Estuarine Comparisons", Academic Press, Inc., 21-36.

Dyer, K.R., 1988. Tidally generated estuarine mixing processes. In: "Hydrodynamics of Estuaries" (ed., Kjerfve, B.), vol. 1, CRC Press, 41-57.

Dyer, K.R. and Ramamoorthy, K., 1969. Salinity and water circulation in the Vellar Estuary. *Limnology and Oceanography,* 14: 4-15.

Doyle, B.E. and Wilson, R.E., 1978. Lateral dynamic balance in the Sandy Hook to Rockaway Point transect. *Estuarine and Coastal Marine Science,* 6: 165-174.

Ellison, T.H., 1957. Turbulent transport of heat and momentum from an infinite rough plane. *Journal of Fluid Mechanics,* 2: 456-466.

Farmer, D.M. and Smith, J.D., 1977. Nonlinear internal waves in a fjord. In: "Hydrodynamics of Estuaries and Fjords" (ed., Nihoul, J.C.J.), Elsevier Oceanography Series 23, Elsevier, Amsterdam, 465-493.

Farmer, D.M. and Smith, J.D., 1980. Tidal interaction of stratified flow with a sill in Knight Inlet. *Deep-Sea Research,* 27A: 239-254.

Fearnhead, P.G., 1975. On the formation of fronts by tidal mixing around the British Isles. *Deep-Sea Research,* 22: 311-321.

Fischer, H.B., List, E.J., Koh, R.C.Y., Imberger, J. and Brooks, N.H., 1979. "Mixing in Inland and Coastal Waters". Academic Press, Inc. (London) Ltd.

Gargett, A.E., 1976. Generation of internal waves in the Strait of Georgia, British Columbia. *Deep-Sea Research,* 23: 17-32.

Garvine, R.W., 1974. Dynamics of small-scale oceanic fronts. *Journal of Physical Oceanography,* 4: 557-569.

Garvine, R.W. and Monk, J.D., 1974. Frontal structure of a river plume. *Journal of Geophysical Research,* 79(15): 2251-2259.

George, K.J., 1975. The tides and tidal streams of the Tamar estuary. Ph.D. Thesis, University of London.

Haury, L.R., Briscoe, M.G. and Orr, M.H., 1979. Tidally generated internal wave packets in Massachusetts Bay. *Nature,* 278: 312-317.

Heathershaw, A.D., 1974. "Bursting" phenomena in the sea. *Nature,* 248: 394-395.

Hughes, F.W. and Rattray Jr., M., 1980. Salt flux and mixing in the Columbia River Estuary. *Estuarine and Coastal Marine Science,* 10: 479-493.

Huzzey, L.M., 1982. The dynamics of a bathymetrically arrested estuarine front. *Estuarine, Coastal and Shelf Science,* 15: 537-552.

Huzzey, L.M., 1988. The lateral density distribution in a partially mixed estuary *Estuarine, Coastal and Shelf Science,* 9: 351-358.

Huzzey, L.M. and Brubaker, J.M., 1988. The formation of longitudinal fronts in a coastal plain estuary. *Journal of Geophysical Research,* 93(C2): 1329-1334.

Jay, D.A., 1990. Residual circulation in shallow estuaries: shear, stratification and transport processes. In: "Residual Curents and Long-term Transport" (ed. Cheng, R.T.), Springer-Verlag, New York, Inc.

Jin, K.-R. and Raney, D.C., 1991. Horizontal salinity gradient effects in Apalachicola Bay. *Journal of Waterway, Port, Coastal and Ocean Engineering,* 117(5): 451-470.

Kawanisi, K. and Yokosi, S., 1993. Measurements of turbulence and suspended sediment in tidal river. *Journal of Hydraulic Engineering,* 119(6): 704-724.

Klemas, V. And Polis, D.F., 1977a. A study of density fronts and their effects on coastal pollutants. *Remote Sensing of Environment,* 6: 95-126.

Klemas, V. And Polis, D.F., 1977b. Remote sensing of estuarine fronts and their effects on pollutants. *Photogrammetric Engineering and Remote Sensing,* 43(5):599-612.

Largier, J.L., 1993. Estuarine fronts: How important are they? *Estuaries,* 16(1): 1-11.

Lee, C.-Y. and Beardsley, R.C., 1974. The generation of long nonlinear internal waves in weakly stratified shear flow. *Journal of Geophysical Research,* 79(3): 453-462.

Linden, P.F., 1979. Mixing in stratified fluids. *Geophysical and Astrophysical Fluid Dynamics,* 13: 3-23.

Linden, P.F., 1980. Mixing across a density interface produced by grid turbulence. *Journal of Fluid Mechanics,* 100(4): 691-703.

Lu, S.S. and Willmarth, W.W., 1972. The structure of the Reynold's stress in a turbulent boundary layer. O.R.A. report, 021490-2-T, Department of Aerospace Engineering, University of Michigan.

Lu, S.S. and Willmarth, W.W., 1973. Measurements of the structure of the Reynold's stress in a turbulent boundary layer. *Journal of Fluid Mechanics,* 60(3): 481-511.

Maxworthy, T., 1979. A note on the internal solitary waves produced by tidal flow over a three-dimensional ridge. *Journal of Geophysical Research,* 84(C1): 338-346.

McAlister, W.B., Rattray Jr., M. and Barnes, C.A., 1959. The dynamics of a fjord estuary: Silver Bay, Alaska. Department of Oceanography Technical Report, No. 62, University of Washington, Seattle, Washington.

McEwan, A.D., 1983(a). The kinematics of stratified mixing through internal wavebreaking. *Journal of Fluid Mechanics,* 128: 47-57.

McEwan, A.D., 1983(b). Internal mixing in stratified fluids. *Journal of Fluid Mechanics,* 128: 59-80.

Münchow, A. and Garvine, R.W., 1993. Dynamical properties of a buoyancy-driven coastal current. *Journal of Geophysical Research,* 98(C11): 20063-20077.

Munk, W.H. and Anderson, E.R., 1948. Notes on a theory of the thermocline. *Journal of Marine Research,* 7: 276-295.

New, A.L., Dyer, K.R. and Lewis, R.E., 1986. Predictions of the generation and propagation of internal waves and mixing in a partially stratified estuary. *Estuarine, Coastal and Shelf Science,* 22: 199-214.

New, A.L. and Dyer, K.R., 1987. On the generation of lateral internal waves by a surface seiche in a partially mixed estuary. *Estuarine, Coastal and Shelf Science,* 24: 557-566.

New, A.L., Dyer, K.R. and Lewis, R.E., 1987. Internal waves and intense mixing periods in a partially stratified estuary. *Estuarine, Coastal and Shelf Science,* 24: 15-33.

Nunes, R.A. and Simpson, J.H., 1985. Axial convergence in a well-mixed estuary. *Estuarine, Coastal and Shelf Science,* 20: 637-649.

Nunes Vaz, R.A. and Simpson, J.H., 1994. Turbulence closure modeling of estuarine stratification. *Journal of Geophysical Research,* 99(C8): 16143-16160.

Odd, N.V.M. and Rodger, J.G., 1978. Vertical mixing in stratified tidal flows. *Journal of the Hydraulics Division, Proceedings of the Americal Society of Civil Engineers,* 104(HY3): 337-351.

O'Donnell, J., 1993. Surface fronts in estuaries: A review. *Estuaries,* 16(1): 12-39.

Parsons, A.P., 1987. Circulation and mixing of solutes in the Lower Tamar Estuary. Ph.D. Thesis, University of Birmingham.

Pinckney, J. And Dustan, P., 1990. Ebb-tidal fronts in Charleston Harbor, South Carolina: Physical and biological characteristics. *Estuaries,* 13(1): 1-7.

Pingree, R.D., Bowman, M.J. and Esaias, W.E., 1977. Headland fronts. In: "Oceanic Fronts in Coastal Processes" (eds., Bowman, M.J. and Esaias, W.E.), Springer-Verlag, 78-86.

Pond, S. and Pickard, G.L., 1983. "Introductory Dynamical Oceanography", 2nd edition. Pergamon Press Ltd.

Pritchard, D.W., 1956. The dynamic structure of a coastal plain estuary. *Journal of Marine Research,* 15(1): 33-42.

Rattray Jr., M. and Dworski, J.G., 1980. Comparison of methods for analysis of the transverse and vertical circulation contributions to the longitudinal advective salt flux in estuaries. *Estuarine and Coastal Marine Science,* 11: 515-536.

Sarabun Jr., C.C., 1993. Observations of a Chesapeake Bay tidal front. *Estuaries,* 16(1): 68-73.

Schröder, M. and Siedler, G., 1989. Turbulent momentum and salt transport in the mixing zone of the Elbe Estuary. *Estuarine, Coastal and Shelf Science,* 28: 615-638.

Scott, C.F., 1994. A numerical study of the interaction of tidal oscillations and non-linearities in an estuary. *Estuarine, Coastal and Shelf Science,* 39: 477-496.

Sharples, J. and Simpson, J.H., 1993. Periodic frontogenesis in a region of freshwater influence. *Estuaries,* 16(1): 74-82.

Shiono, K. and West, J.R., 1987. Turbulent perturbations of velocity in the Conwy Estuary. *Estuarine, Coastal and Shelf Science,* 25: 533-553.

Simpson, J.E. and Linden, P.F., 1989. Frontogenesis in a fluid with horizontal density gradients. *Journal of Fluid Mechanics,* 202: 1-16.

Simpson, J.H. and Hunter, J.R., 1974. Fronts in the Irish Sea. *Nature,* 250: 404-406.

Simpson, J.H. and James, I.D., 1986. Coastal and estuarine fronts. In: "Baroclinic Processes on Continental Shelves" (ed., Mooers, C.N.K.), American Geophysical Union, Washington, D.C., 63-93.

Simpson, J.H. and Nunes, R.A., 1981. The tidal intrusion front: An estuarine convergence zone. *Estuarine, Coastal and Shelf Science,* 13: 257-266.

Simpson, J.H. and Turrell, W.R., 1986. Convergent fronts in the circulation of tidal fronts. In: "Estuarine Variability" (ed., Wolfe, D.A.), Academic Press, Orlando, Florida, 139-152.

Sturley, D.R.M., 1990. Topographically induced internal waves and enhanced vertical mixing in an estuary. Ph.D. Thesis, Polytechnic South West.

Sturley, D.R.M and Dyer, K.R., 1990. The estuarine thermistor spar: An instrument for making thermal profiles in shallow water. *The Hydrographic Journal,* 55: 13-21.

Sturley, D.R.M and Dyer, K.R., 1992. A topographically induced internal wave and mixing in the Tamar Estuary. In: "Dynamics and Exchanges in Estuaries and the Coastal Zone" (ed., Prandle, D.), American Geophysical Union, Washington, D.C., 57-74.

Thompson, R.O.R.Y., 1980. Efficiency of conversion of kinetic energy to potential energy by a breaking internal gravity wave. *Journal of Geophysical Research,* 85(C11): 6631-6635.

Thorpe, S.A., 1973. Turbulence in stably stratified fluids: a review of laboratory experiments. *Boundary-Layer Meteorology,* 5: 95-119.

Thorpe, S.A., 1987. Transitional phenomena and the development of turbulence in stratified fluids: a review. *Journal of Geophysical Research,* 92(C5): 5231-5248.

Turrell, W.R.,1989. Axial fronts and transverse flows in well-mixed estuaries. Ph.D. Thesis, University College of North Wales.

Uncles, R.J. and Jordan, M.B., 1980. A one-dimensional representation of residual currents in the Severn Estuary and associated observations. *Estuarine, Coastal and Marine Science,* 10: 39-60.

Uncles, R.J. and Stephens, J.A., 1990. Salinity stratification and vertical shear transport in an estuary. In: "Residual Currents and Long-term Transport" (ed. Cheng, R.T.), Springer-Verlag, New York, Inc.

Uncles, R.J. and Stephens, J.A., 1993. The freshwater-saltwater interface and its relationship to the turbidity maximum in the Tamar Estuary, United Kingdom. *Estuaries,* 16(1): 126-141.

Uncles, R.J., Elliott, R.C.A. and Weston, S.A., 1985(a). Observed fluxes of water, slt and suspended sediment in a partly mixed estuary. *Estuarine, Coastal and Shelf Science,* 20: 147-167.

Uncles, R.J., Elliott, R.C.A. and Weston, S.A., 1985(b). Dispersion of salt and suspended sediment in a partly mixed estuary. *Estuaries,* 8(3): 256-269.

Uncles, R.J., Elliott, R.C.A. and Weston, S.A., 1986. Observed and computed lateral circulation patterns in a partly mixed estuary.. *Estuarine, Coastal and Shelf Science,* 22: 439-457.

Uncles, R.J., Gong, W.-K. and Ong, J.-E., 1992. Intratidal fluctuations in stratification within a mangrove estuary. *Hydrobiologia,* 247: 163-171.

Uncles, R.J., Bale, A.J., Howland, J.M., Morris, A.W. and Elliott, R.C.A., 1983. Salinity of surface water in a partially-mixed estuary and its dispersion at low run-off. *Oceanologica Acta,* 6(3): 289-296.

West, J.R. and Shiono, K., 1985. A note on turbulent perturbations of salinity in a partially mixed estuary. *Estuarine, Coastal and Shelf Science,* 20: 55-78.

West, J.R. and Shiono, K., 1988. Vertical turbulent mixing processes on ebb tides in partially mixed estuaries. *Estuarine, Coastal and Shelf Science,* 26: 51-66.

West, J.R., Knight, D.W. and Shiono, K., 1985. A note on the determination of vertical turbulent transport coefficients in a partially mixed estuary. *Proceedings of the Institution of Civil Engineers,* 79(2): 235-246.

Wilson, R.E., 1988. Dynamics of partially mixed estuaries. In: "Hydrodynamics of Estuaries" (ed., Kjerfve, B.), vol. 1, CRC Press, 1-15.

Yanagi, T. and Tamaru, H., 1990. Temporal and spatial variations in a tidal front. *Continental Shelf Research,* 10(7): 615-627.

# APPENDIX

## LIST OF CONTENTS


| Contents | | Page Number |
|---|---|---|
| Figure 1a | Resultant velocity ( $\overline{V}_T$ ) vs. time after high water, 20.04.94 | i |
| Figure 1b | Resultant velocity ( $\overline{V}_T$ ) vs. time after high water, 22.04.94 | i |
| Figure 1c | Resultant velocity ( $\overline{V}_T$ ) vs. time after high water, 25.04.94 | i |
| Figure 2a | Average vertical velocity vs. depth, box 1N . . | ii |
| Figure 2b | Average vertical velocity vs. depth, box 2N . . | ii |
| Figure 2c | Average vertical velocity vs. depth, box 3N . . | ii |
| Figure 2d | Average vertical velocity vs. depth, box 4N . . | ii |
| Figure 2e | Average vertical velocity vs. depth, box 5N . . | ii |
| Figure 2f | Average vertical velocity vs. depth, box 6N . . | iii |
| Figure 2g | Average vertical velocity vs. depth, box 7N . . | iii |
| Figure 2h | Average vertical velocity vs. depth, box 1S . . | iii |
| Figure 2i | Average vertical velocity vs. depth, box 2S . . | iii |
| Figure 2j | Average vertical velocity vs. depth, box 3S . . | iii |
| Figure 3a | $\overline{V}_T.\overline{S}$ vs. time after high water, 20.04.94 . . | iv |
| Figure 3b | $\overline{V}_T.\overline{S}$ vs. time after high water, 22.04.94 . . | iv |
| Figure 3c | $\overline{V}_T.\overline{S}$ vs. time after high water, 25.04.94 . . | iv |
| Figure 4a | Average vertical salt flux vs. depth, box 1N . . | v |
| Figure 4b | Average vertical salt flux vs. depth, box 2N . . | v |
| Figure 4c | Average vertical salt flux vs. depth, box 3N . . | v |
| Figure 4d | Average vertical salt flux vs. depth, box 4N . . | v |
| Figure 4e | Average vertical salt flux vs. depth, box 5N . . | v |
| Figure 4f | Average vertical salt flux vs. depth, box 6N . . | vi |
| Figure 4g | Average vertical salt flux vs. depth, box 7N . . | vi |
| Figure 4h | Average vertical salt flux vs. depth, box 1S . . | vi |
| Figure 4i | Average vertical salt flux vs. depth, box 2S . . | vi |

| | | |
|---|---|---|
| Figure 4j | Average vertical salt flux vs. depth, box 3S . . | vi |
| Table 1 | Excess / deficit volume fluxes for boxes traversing the front . . . . . | vii |
| Figure 5a | $\bar{u}$ vs. time after high water, 20.04.94 . . . | viii |
| Figure 5b | $\bar{v}$ vs. time after high water, 20.04.94 . . . | viii |
| Figure 6a | $\bar{u}$ vs. time after high water, 22.04.94 . . . | ix |
| Figure 6b | $\bar{v}$ vs. time after high water, 22.04.94 . . . | ix |
| Figure 7a | $\bar{u}$ vs. time after high water, 25.04.94 . . . | x |
| Figure 7b | $\bar{v}$ vs. time after high water, 25.04.94 . . . | x |
| Table 2 | Longitudinal equation of motion . . . | xi |
| Table 3 | Lateral equation of motion . . . . | xiii |
| Figure 8a | Slice-averaged u vs. depth, box 1N . . . | xv |
| Figure 8b | Slice-averaged v vs. depth, box 1N . . . | xv |
| Figure 9a | Slice-averaged u vs. depth, box 2N . . . | xv |
| Figure 9b | Slice-averaged v vs. depth, box 2N . . . | xv |
| Figure 10a | Slice-averaged u vs. depth, box 3N . . . | xvi |
| Figure 10b | Slice-averaged v vs. depth, box 3N . . . | xvi |
| Figure 11a | Slice-averaged u vs. depth, box 4N . . . | xvi |
| Figure 11b | Slice-averaged v vs. depth, box 4N . . . | xvi |
| Figure 12a | Slice-averaged u vs. depth, box 5N . . . | xvii |
| Figure 12b | Slice-averaged v vs. depth, box 5N . . . | xvii |
| Figure 13a | Slice-averaged u vs. depth, box 6N . . . | xvii |
| Figure 13b | Slice-averaged v vs. depth, box 6N . . . | xvii |
| Figure 14a | Slice-averaged u vs. depth, box 7N . . . | xviii |
| Figure 14b | Slice-averaged v vs. depth, box 7N . . . | xviii |
| Figure 15a | Slice-averaged u vs. depth, box 1S . . . | xviii |
| Figure 15b | Slice-averaged v vs. depth, box 1S . . . | xviii |
| Figure 16a | Slice-averaged u vs. depth, box 2S . . . | xix |
| Figure 16b | Slice-averaged v vs. depth, box 2S . . . | xix |
| Figure 17a | Slice-averaged u vs. depth, box 3S . . . | xix |
| Figure 17b | Slice-averaged v vs. depth, box 3S . . . | xix |
| International equation of state of sea water . . . . | | xx |

| | | |
|---|---|---|
| Table 4 | Curvature term estimates for Tamar and Lynher Rivers | xxi |
| Table 5 | Primary longitudinal momentum balance . . | xxiii |
| Table 6 | Primary lateral momentum balance . . . | xxv |
| Table 7 | Richardson numbers, vertical eddy viscosities, vertical eddy diffusivities, and flux Richardson numbers . | xxxvii |

*Figure 1a Resultant velocity ( $\overline{V}_T$ ) vs. time after high water, 20.04.94*

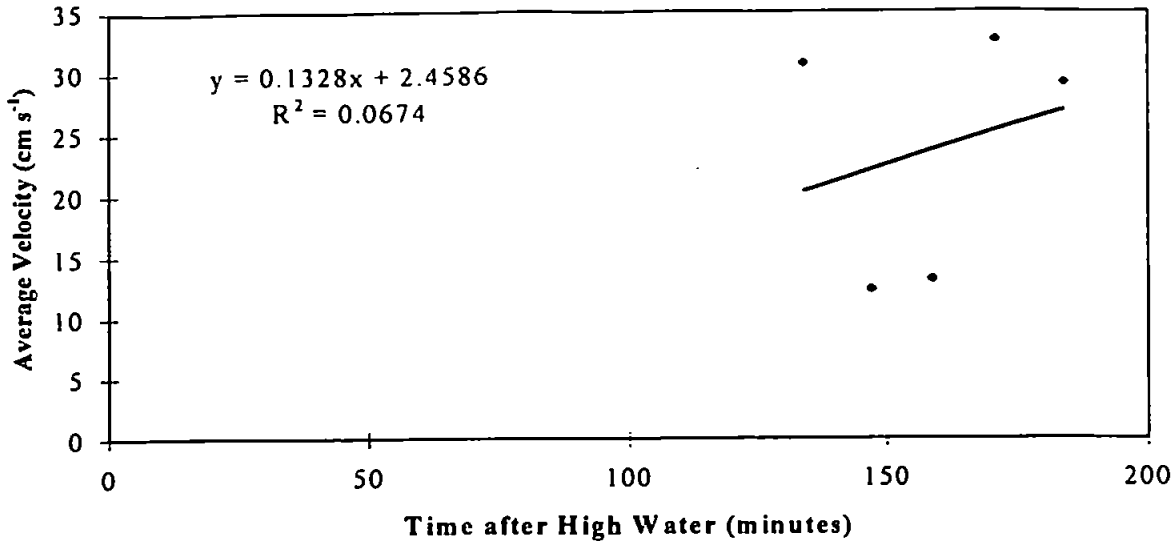


*Figure 1b Resultant velocity ( $\overline{V}_T$ ) vs. time after high water, 22.04.94*

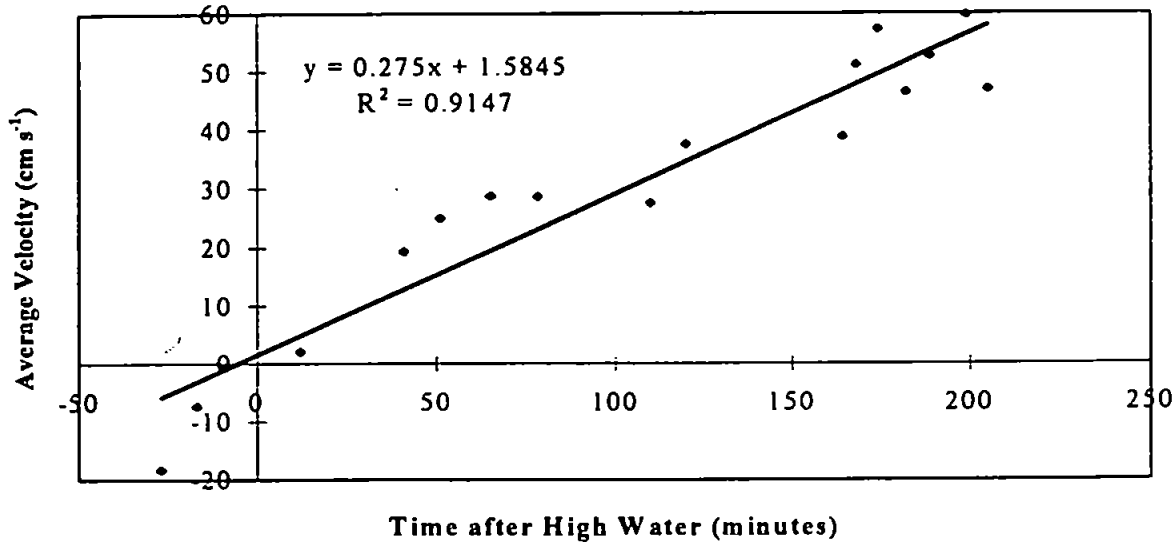


*Figure 1c Resultant velocity ( $\overline{V}_T$ ) vs. time after high water, 25.04.94*

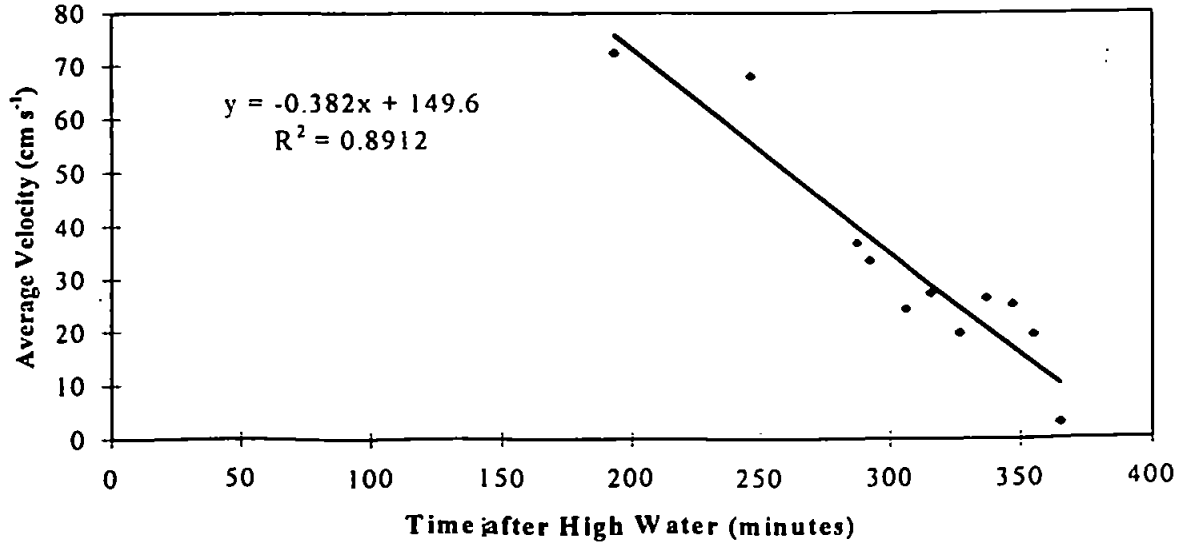

*Figure 2a Average vertical velocity vs. depth, box 1N*

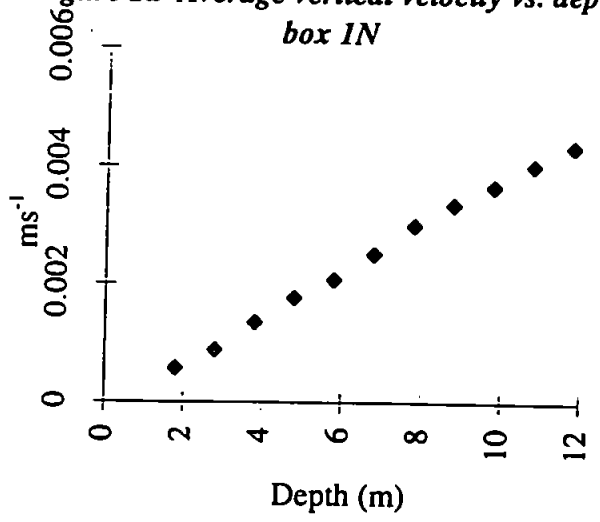


*Figure 2b Average vertical velocity vs. depth, box 2N*

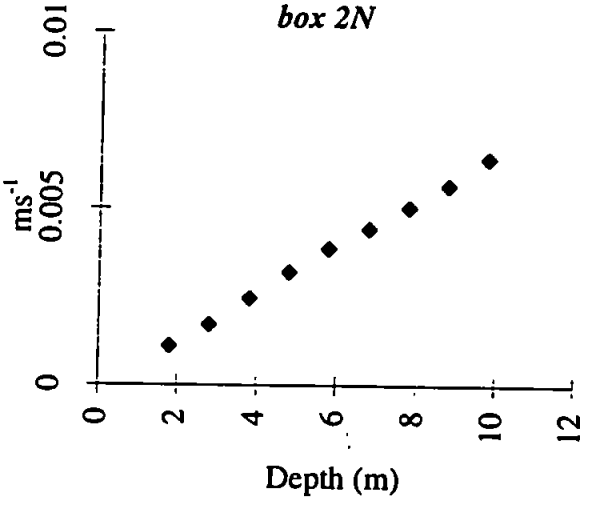


*Figure 2c Average vertical velocity vs. depth, box 3N*

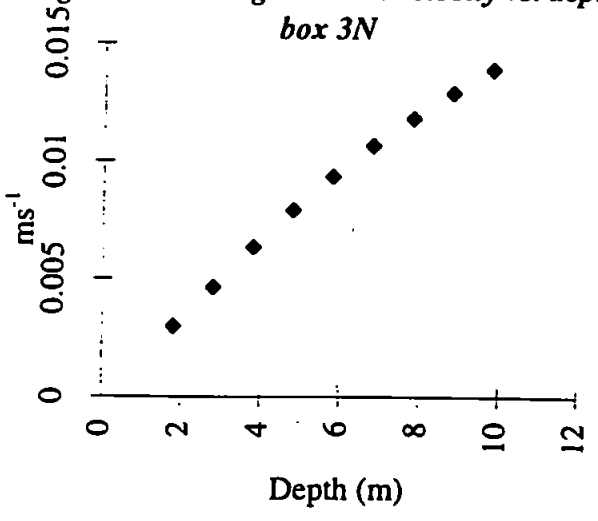


*Figure 2d Average vertical velocity vs. depth, box 4N*

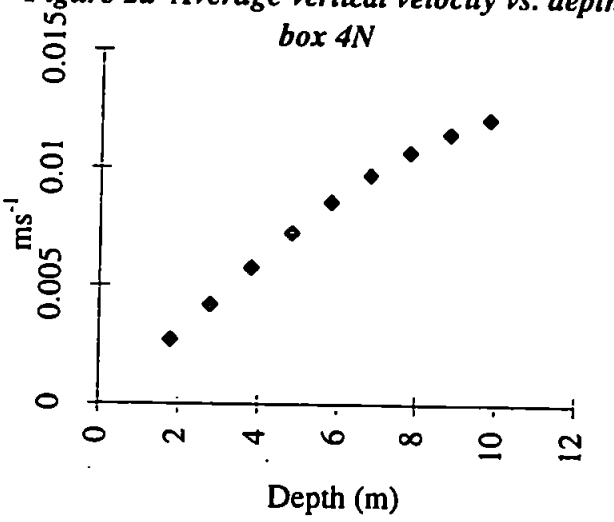


*Figure 2e Average vertical velocity vs. depth, box 5N*

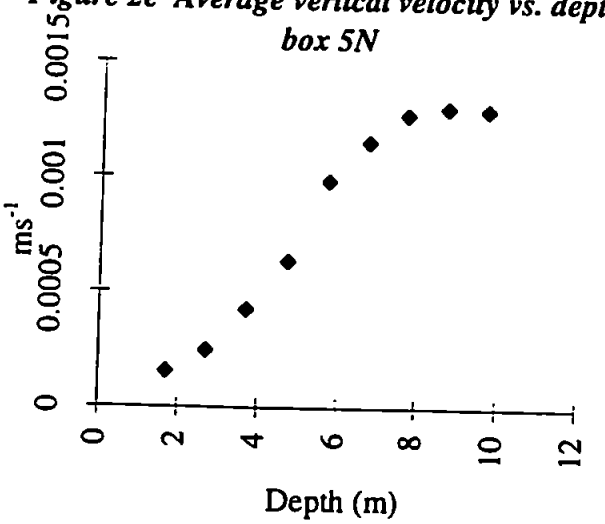

*Figure 2f Average vertical velocity vs. depth, box 6N*

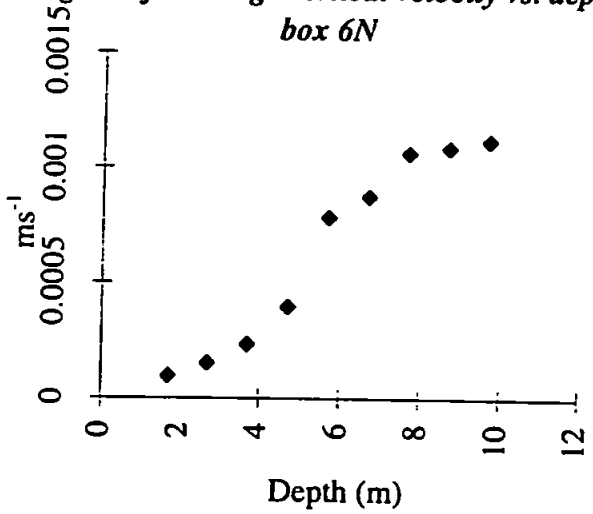


*Figure 2g Average vertical velocity vs. depth, box 7N*

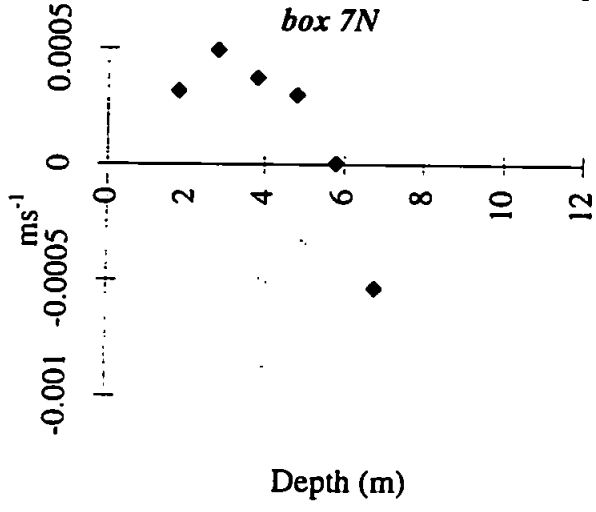


*Figure 2h Average vertical velocity vs. depth, box 1S*

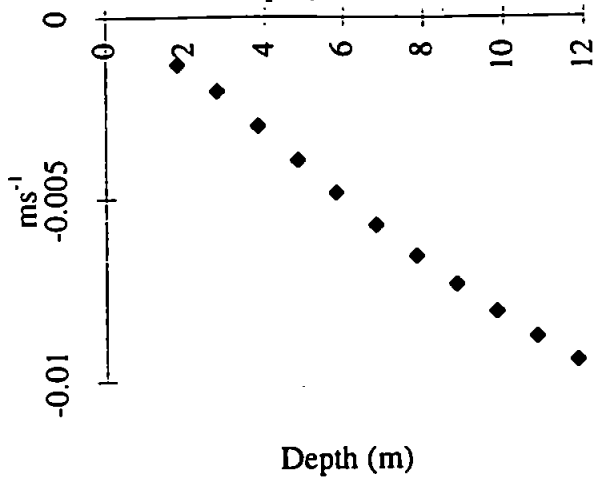


*Figure 2i Average vertical velocity vs. depth, box 2S*

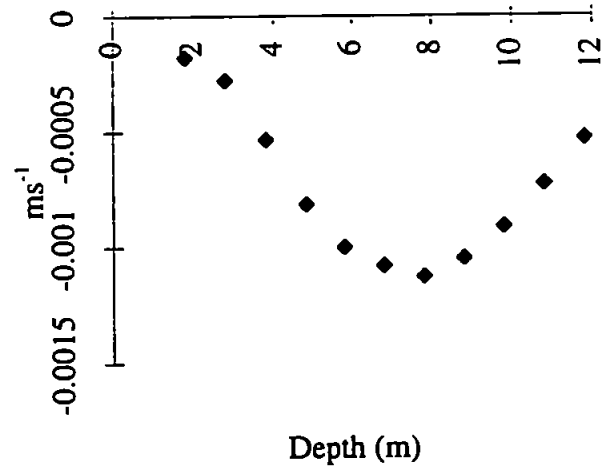


*Figure 2j Average vertical velocity vs. depth, box 3S*

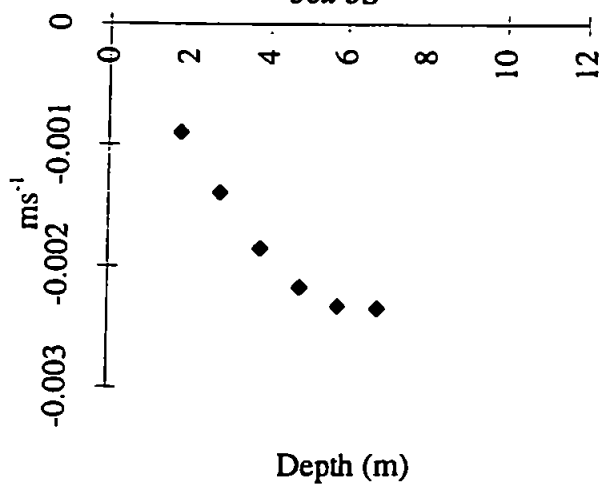

*Figure 3a* $\overline{V}_T.\overline{S}$ *vs. time after high water, 20.04.94*

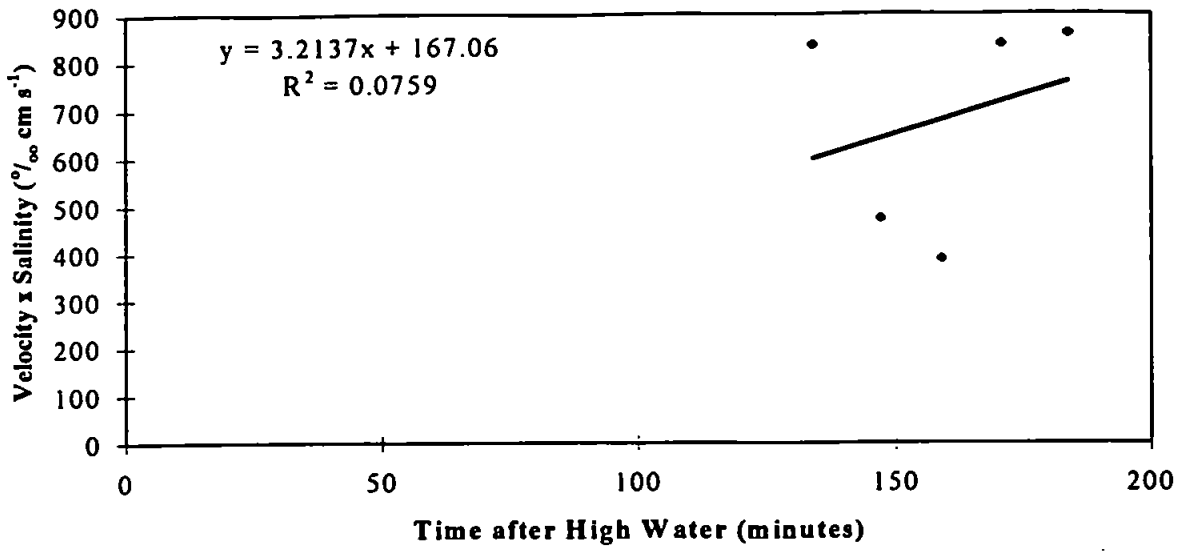


*Figure 3b* $\overline{V}_T.\overline{S}$ *vs. time after high water, 22.04.94*

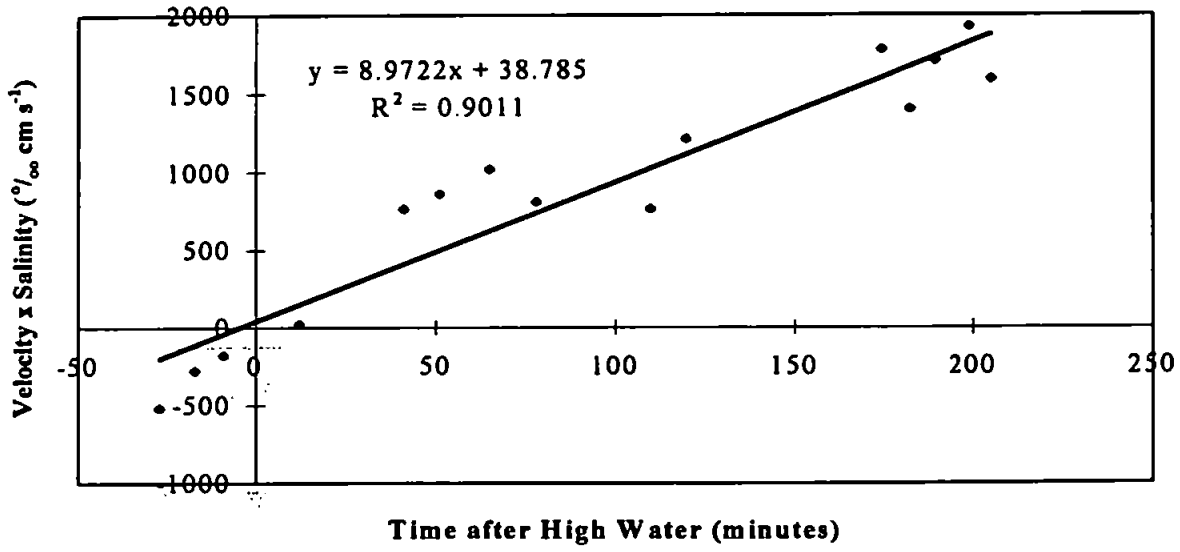


*Figure 3c* $\overline{V}_T.\overline{S}$ *vs. time after high water, 25.04.94*

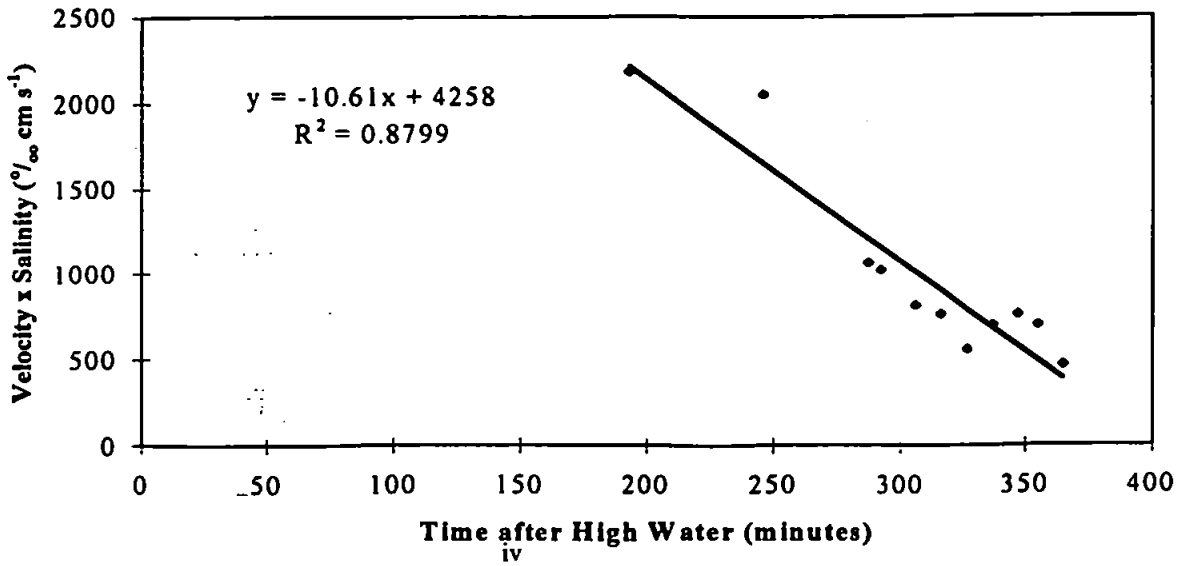

*Figure 4a Average vertical salt flux vs. depth, box 1N*

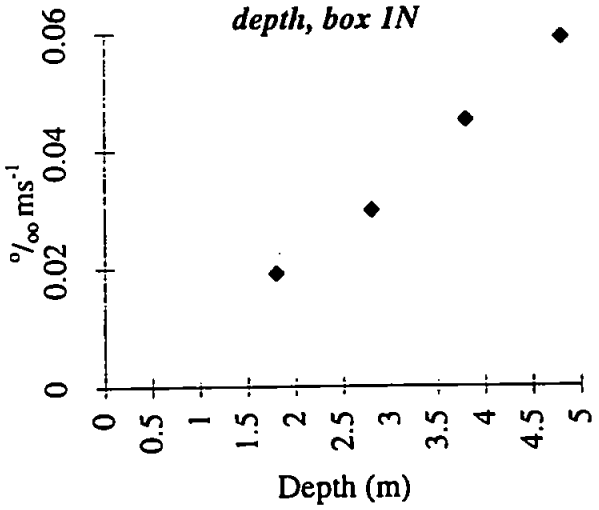


*Figure 4b Average vertical salt flux vs. depth, box 2N*

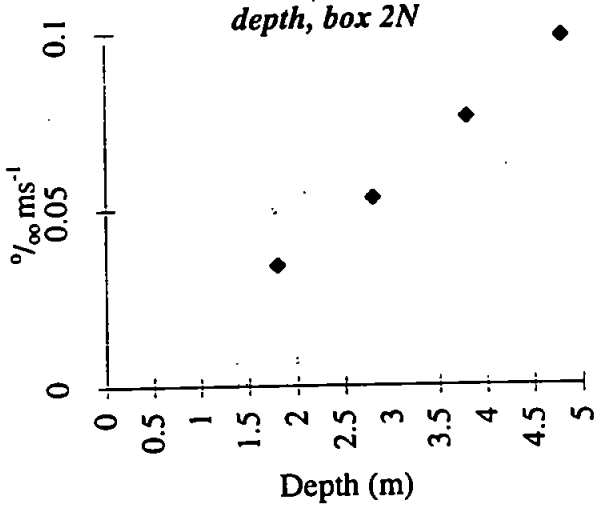


*Figure 4c Average vertical salt flux vs. depth, box 3N*

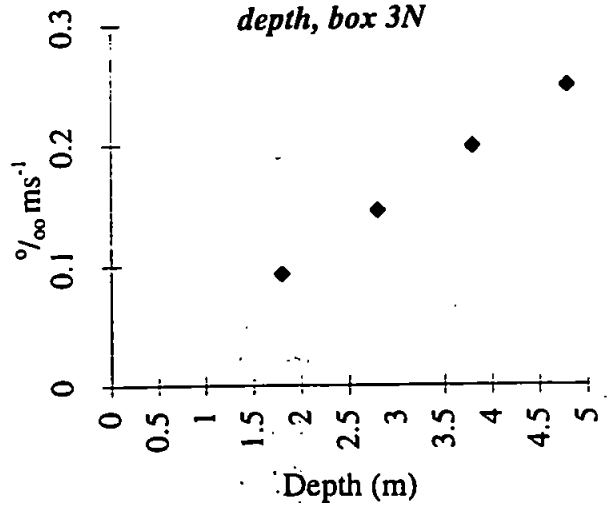


*Figure 4d Average vertical salt flux vs. depth, box 4N*

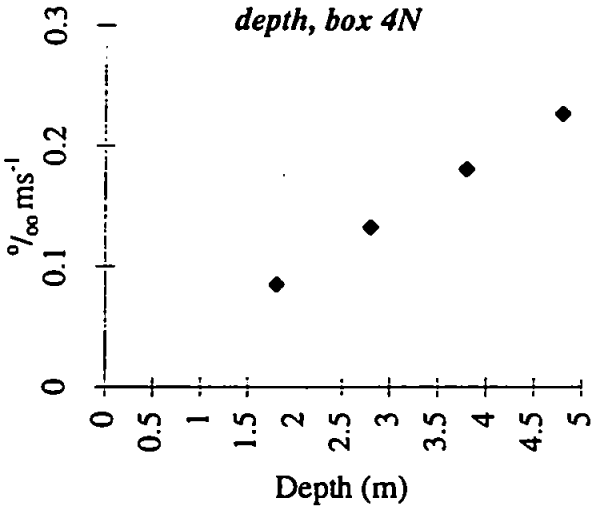


*Figure 4e Average vertical salt flux vs. depth, box 5N*

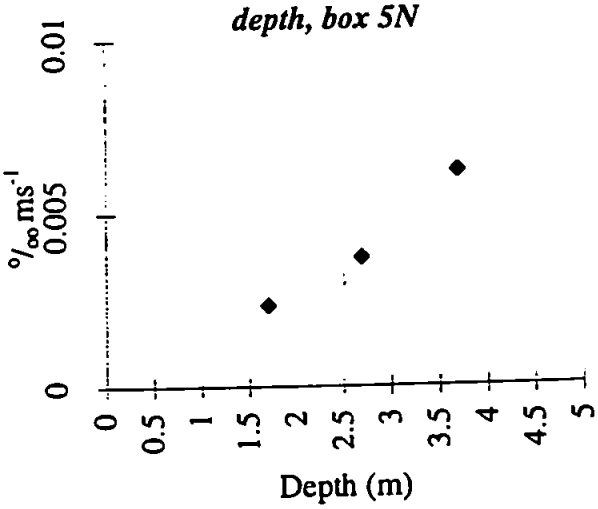

*Figure 4f Average vertical salt flux vs. depth, box 6N*

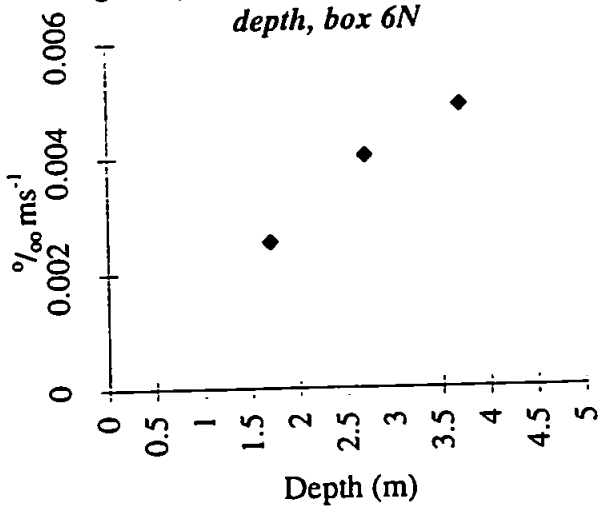


*Figure 4g Average vertical salt flux vs. depth, box 7N*

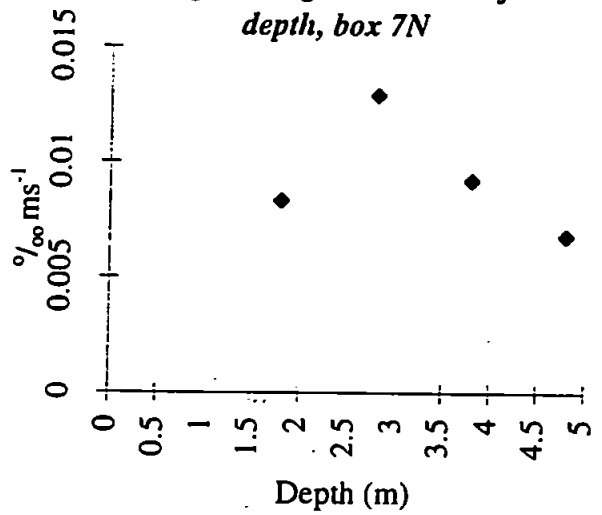


*Figure 4h Average vertical salt flux vs. depth, box 1S*

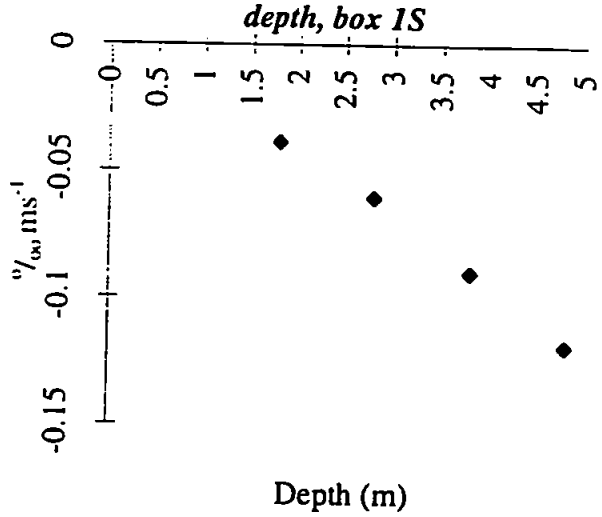


*Figure 4i Average vertical salt flux vs. depth, box 2S*

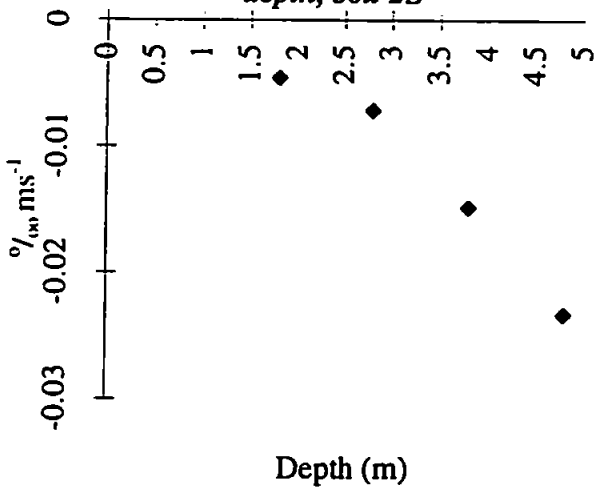


*Figure 4j Average vertical salt flux vs. depth, box 3S*

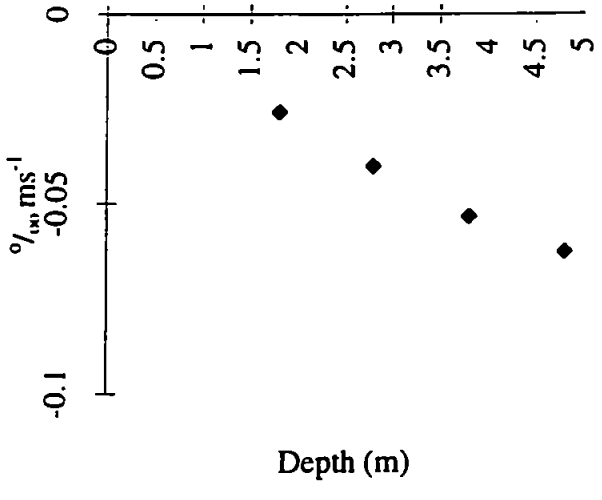

*Table 1 Excess/deficit volume fluxes for boxes traversing the front*

+ = volume flux excess, - = volume flux deficit

| Box 2N Slice | Volume flux in Volume A ($m^3 s^{-1}$) | Volume flux in Volume B ($m^3 s^{-1}$) | Box 4N Slice | Volume flux in Volume A ($m^3 s^{-1}$) | Volume flux in Volume B ($m^3 s^{-1}$) |
|---|---|---|---|---|---|
| 0 | -99.3 | -1508.9 | 0 | 2.7 | -1984.9 |
| 1 | 56 | -1.1 | 1 | 55.1 | 80.3 |
| 2 | 43.5 | 326.9 | 2 | 80.6 | 677 |
| 3 | 108.1 | -246.9 | 3 | 37 | -65.1 |
| 4 | 48.2 | 350.2 | 4 | 50.5 | 347 |
| 5 | 70.2 | 70 | 5 | 67.2 | -171.5 |
| 6 | 52.2 | 240.3 | 6 | 48.2 | 902.1 |
| 7 | 83.3 | 103.3 | 7 | 33 | 56.1 |
| 8 | 46.2 | -241.6 | 8 | 51.2 | 184.9 |

| Box 3N Slice | Volume flux in Volume A ($m^3 s^{-1}$) | Volume flux in Volume B ($m^3 s^{-1}$) | Box 4N Slice | Volume flux in Volume 1 ($m^3 s^{-1}$) | Volume flux in Volume 2 ($m^3 s^{-1}$) | Volume flux in Volume 3 ($m^3 s^{-1}$) |
|---|---|---|---|---|---|---|
| 0 | -183.5 | -1370.3 | 0 | -295 | -2048.7 | -603.3 |
| 1 | 77.3 | 71.3 | 1 | -38.8 | 80 | 175.8 |
| 2 | 164.5 | 419.5 | 2 | -37.6 | -11.6 | 95.2 |
| 3 | 67.4 | -193.8 | 3 | -102.1 | 88.2 | 278.2 |
| 4 | 92.7 | 422.1 | 4 | 51.8 | 399.4 | 308.8 |
| 5 | 98.6 | 155.8 | 5 | 14.6 | 99.5 | 1.2 |
| 6 | 89 | 482.9 | 6 | | | |
| 7 | 16 | 115.5 | | | | |
| 8 | 51.8 | -117.8 | | | | |

*Figure 5a* $\bar{u}$ *vs. time after high water, 20.04.94*

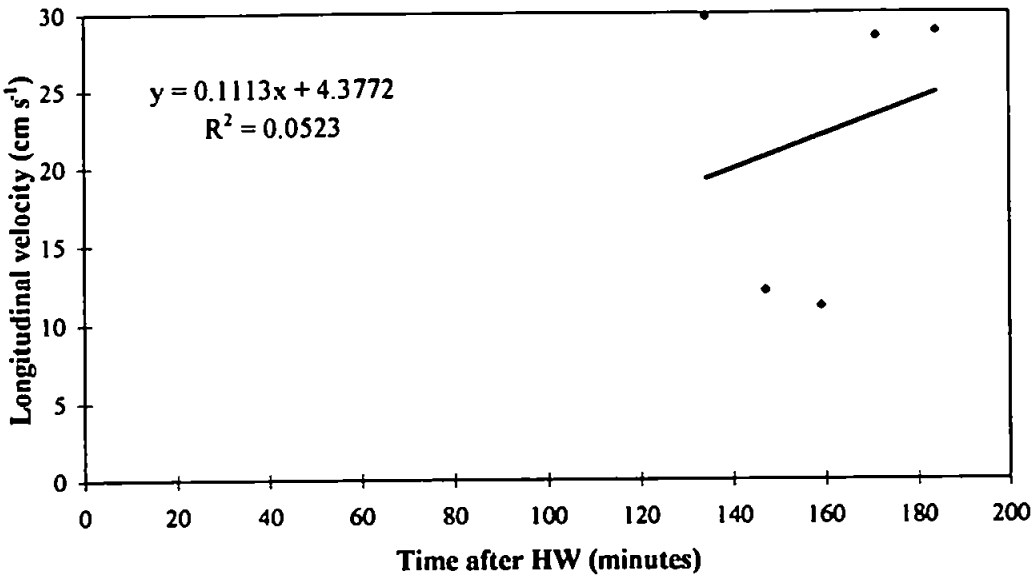


*Figure 5b* $\bar{v}$ *vs. time after high water, 20.04.94*

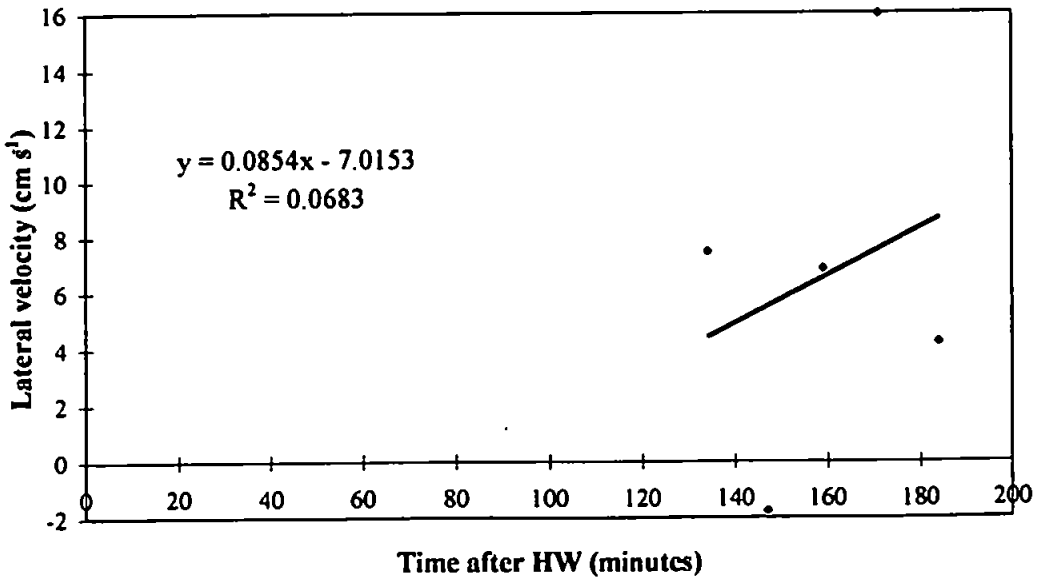

*Figure 6a* $\bar{u}$ *vs. time after high water, 22.04.94*

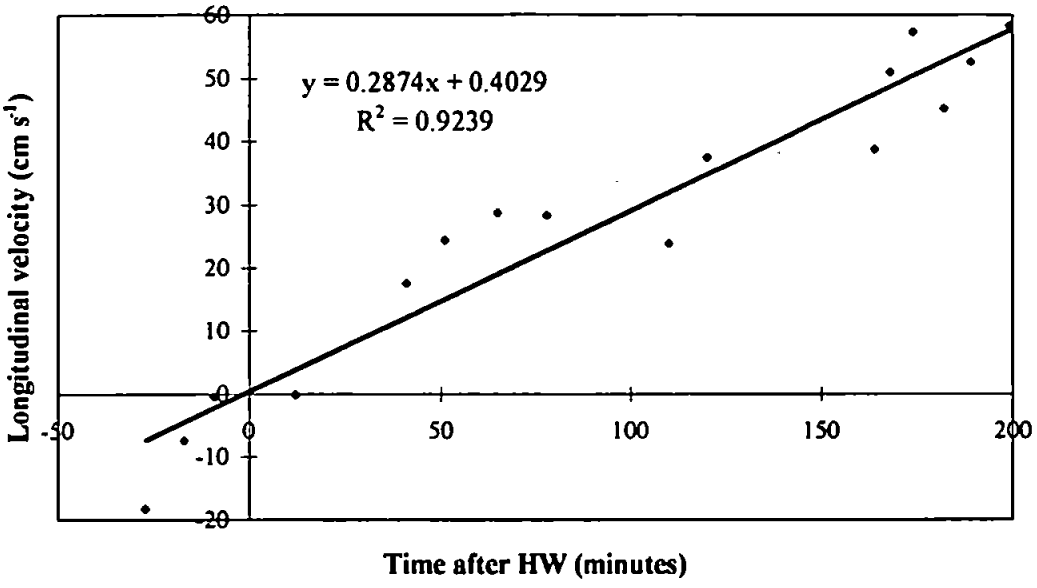


*Figure 6b* $\bar{v}$ *vs. time after high water, 22.04.94*

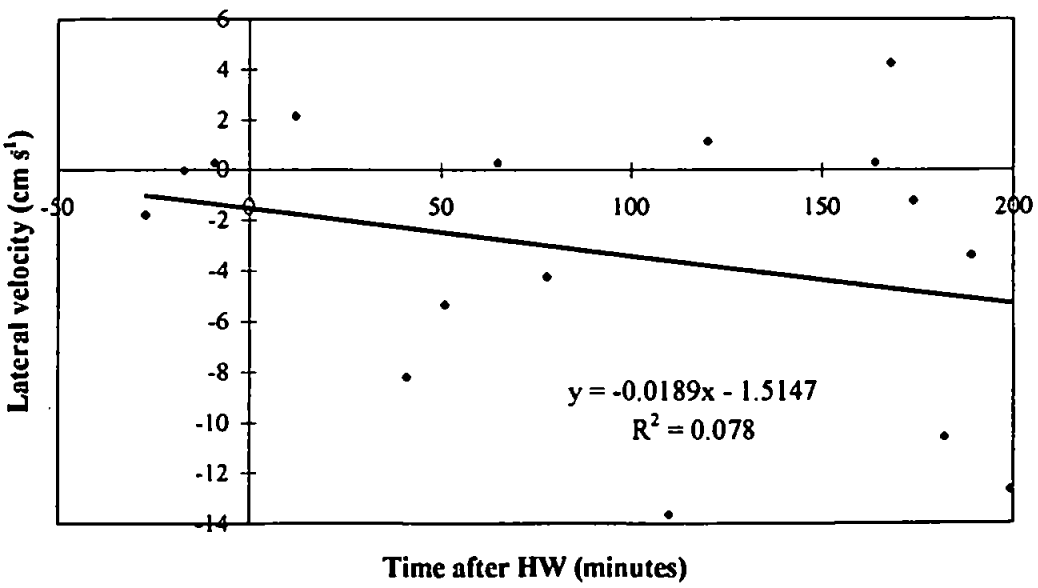

*Figure 7a* $\bar{u}$ *vs. time after high water, 25.04.94*

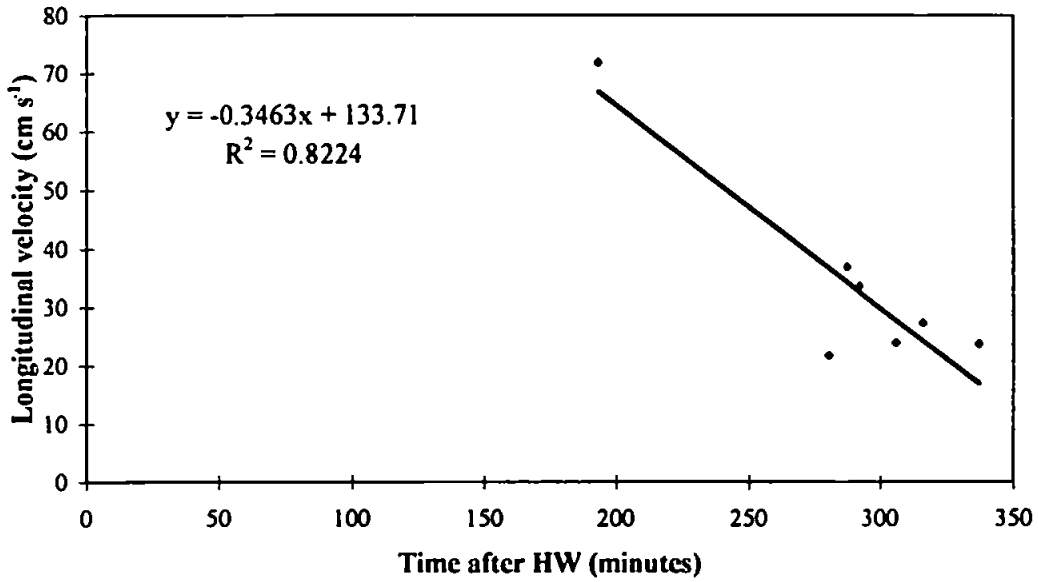


*Figure 7b* $\bar{v}$ *vs. time after high water, 25.04.94*

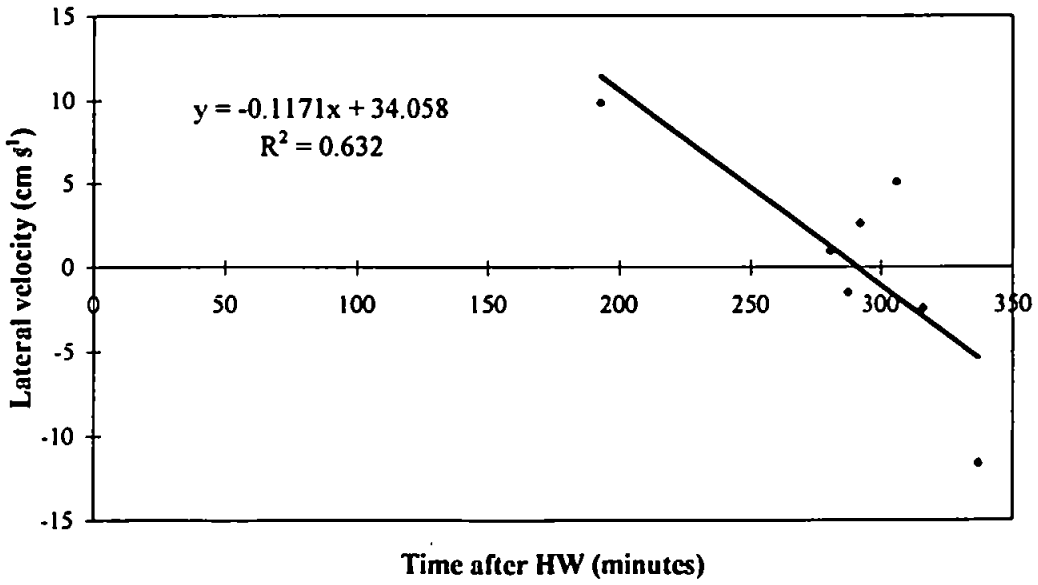

## *Table 2 Longitudinal equation of motion*

| Box 1N | dU/dt | U.dU/dx | V.dU/dy | W.dU/dz | 1/dens.dP/dx | g.d elev/dx | f.V | d/dx(u'.u') | d/dy(u'.v') | d/dz(u'.w') |
|---|---|---|---|---|---|---|---|---|---|---|
| Slice | ($m s^{-2}$) | ($m s^{-2}$) | ($m s^{-2}$) | ($m s^{-2}$) | ($m s^{-2}$) | ($m s^{-2}$) | ($m s^{-2}$) | ($m s^{-2}$) | ($m s^{-2}$) | ($m s^{-2}$) |
| 0 | 4.79E-05 | -2.74E-05 | 6.23E-06 | 0.00E+00 | -5.25E-06 | -5.59E-06 | 1.07E-06 | -2.75E-06 | -1.21E-05 | 0.00E+00 |
| 1 | 4.79E-05 | -2.74E-05 | 6.23E-06 | -2.39E-06 | -8.16E-06 | -5.59E-06 | 1.07E-06 | -2.75E-06 | -1.21E-05 | 5.30E-06 |
| 2 | 4.79E-05 | -2.13E-05 | 9.66E-06 | -1.82E-06 | -1.08E-05 | -5.59E-06 | 5.52E-08 | -3.46E-05 | -6.33E-06 | 2.30E-05 |
| 3 | 4.79E-05 | -2.38E-05 | 1.42E-05 | 9.54E-08 | -1.23E-05 | -5.59E-06 | 1.31E-06 | -3.37E-05 | -1.59E-05 | 3.04E-05 |
| 4 | 4.79E-05 | -2.36E-05 | 3.96E-06 | 3.90E-06 | -1.49E-05 | -5.59E-06 | 2.07E-06 | -3.44E-05 | -2.15E-05 | 4.64E-05 |
| 5 | 4.79E-05 | -1.58E-05 | -5.99E-06 | 9.00E-06 | -1.73E-05 | -5.59E-06 | 1.31E-06 | -3.10E-05 | -1.55E-05 | 3.55E-05 |
| 6 | 4.79E-05 | -1.87E-05 | -3.94E-06 | 1.62E-05 | -1.96E-05 | -5.59E-06 | 1.84E-06 | -3.90E-05 | -1.90E-05 | 4.35E-05 |
| 7 | 4.79E-05 | -2.18E-05 | -2.92E-06 | 2.58E-05 | -2.20E-05 | -5.59E-06 | 9.13E-07 | -3.85E-05 | -2.20E-05 | 4.00E-05 |
| 8 | 4.79E-05 | -2.08E-05 | -4.34E-05 | 3.60E-05 | -2.43E-05 | -5.59E-06 | -8.39E-07 | -4.01E-05 | -2.49E-05 | 7.44E-05 |
| 9 | 4.79E-05 | -8.33E-06 | -4.65E-05 | 4.71E-05 | -2.67E-05 | -5.59E-06 | -2.84E-06 | -2.98E-05 | -2.45E-05 | 4.35E-05 |
| 10 | 4.79E-05 | -5.30E-06 | -4.67E-05 | 6.02E-05 | -2.90E-05 | -5.59E-06 | -3.13E-06 | -3.21E-05 | -2.29E-05 | 3.03E-05 |
| | | | | | | | | | | |
| Box 2N | dU/dt | U.dU/dx | V.dU/dy | W.dU/dz | 1/dens.dP/dx | g.d elev/dx | f.V | d/dx(u'.u') | d/dy(u'.v') | d/dz(u'.w') |
| Slice | ($m s^{-2}$) | ($m s^{-2}$) | ($m s^{-2}$) | ($m s^{-2}$) | ($m s^{-2}$) | ($m s^{-2}$) | ($m s^{-2}$) | ($m s^{-2}$) | ($m s^{-2}$) | ($m s^{-2}$) |
| 0 | 4.79E-05 | 1.14E-04 | -8.83E-06 | 0.00E+00 | 4.41E-05 | -1.61E-04 | -3.64E-06 | -3.79E-05 | -1.91E-06 | 0.00E+00 |
| 1 | 4.79E-05 | 1.14E-04 | -8.83E-06 | -3.87E-06 | 6.85E-05 | -1.61E-04 | -3.64E-06 | -3.79E-05 | -1.91E-06 | -2.06E-05 |
| 2 | 4.79E-05 | 1.10E-04 | -1.81E-05 | -6.02E-06 | 1.00E-04 | -1.61E-04 | -4.57E-06 | -4.26E-05 | -9.69E-06 | -2.50E-05 |
| 3 | 4.79E-05 | 1.08E-04 | -1.76E-05 | -8.65E-06 | 1.34E-04 | -1.61E-04 | -4.26E-06 | -3.11E-05 | -5.14E-06 | -7.07E-05 |
| 4 | 4.79E-05 | 1.09E-04 | -2.52E-05 | -1.13E-05 | 1.62E-04 | -1.61E-04 | -3.89E-06 | -4.62E-05 | -1.00E-05 | -6.89E-05 |
| 5 | 4.79E-05 | 1.10E-04 | -3.11E-05 | -1.36E-05 | 1.92E-04 | -1.61E-04 | -2.83E-06 | -2.77E-05 | -2.31E-06 | -1.17E-04 |
| 6 | 4.79E-05 | 1.06E-04 | -5.38E-05 | -1.56E-05 | 2.22E-04 | -1.61E-04 | -1.84E-06 | -3.36E-05 | 5.09E-07 | -1.14E-04 |
| 7 | 4.79E-05 | 1.14E-04 | -8.04E-05 | -1.77E-05 | 2.52E-04 | -1.61E-04 | -6.94E-07 | -5.15E-05 | -2.66E-06 | -1.01E-04 |
| 8 | 4.79E-05 | 1.13E-04 | -1.10E-04 | -1.99E-05 | 2.82E-04 | -1.61E-04 | -1.48E-07 | -2.13E-05 | -1.14E-05 | -1.20E-04 |
| 9 | 4.79E-05 | 1.15E-04 | | | 3.12E-04 | | | | | |
| 10 | 4.79E-05 | | | | 3.42E-04 | | | | | |
| | | | | | | | | | | |
| Box 3N | dU/dt | U.dU/dx | V.dU/dy | W.dU/dz | 1/dens.dP/dx | g.d elev/dx | f.V | d/dx(u'.u') | d/dy(u'.v') | d/dz(u'.w') |
| Slice | ($m s^{-2}$) | ($m s^{-2}$) | ($m s^{-2}$) | ($m s^{-2}$) | ($m s^{-2}$) | ($m s^{-2}$) | ($m s^{-2}$) | ($m s^{-2}$) | ($m s^{-2}$) | ($m s^{-2}$) |
| 0 | 4.79E-05 | 1.14E-04 | 1.57E-05 | 0.00E+00 | 4.40E-05 | -1.75E-04 | 1.90E-06 | -3.79E-05 | -7.19E-06 | 0.00E+00 |
| 1 | 4.79E-05 | 1.14E-04 | 1.57E-05 | -1.95E-05 | 6.85E-05 | -1.75E-04 | 1.90E-06 | -3.79E-05 | -7.19E-06 | -4.95E-06 |
| 2 | 4.79E-05 | 1.10E-04 | 6.80E-06 | -3.04E-05 | 1.00E-04 | -1.75E-04 | 2.14E-07 | -4.26E-05 | -1.24E-05 | -4.30E-06 |
| 3 | 4.79E-05 | 1.08E-04 | 2.72E-05 | -4.15E-05 | 1.34E-04 | -1.75E-04 | -2.27E-07 | -3.11E-05 | -1.02E-05 | -5.98E-05 |
| 4 | 4.79E-05 | 1.09E-04 | 2.78E-05 | -5.19E-05 | 1.62E-04 | -1.75E-04 | -5.30E-07 | -4.62E-05 | -1.34E-05 | -6.07E-05 |
| 5 | 4.79E-05 | 1.10E-04 | 1.84E-05 | -6.14E-05 | 1.92E-04 | -1.75E-04 | 3.33E-07 | -2.77E-05 | -4.76E-06 | -9.93E-05 |
| 6 | 4.79E-05 | 1.06E-04 | 2.17E-05 | -7.00E-05 | 2.22E-04 | -1.75E-04 | -9.23E-08 | -3.36E-05 | -7.70E-06 | -1.12E-04 |
| 7 | 4.79E-05 | 1.14E-04 | -9.07E-07 | -7.76E-05 | 2.52E-04 | -1.75E-04 | 2.74E-07 | -5.15E-05 | -1.51E-05 | -9.38E-05 |
| 8 | 4.79E-05 | 1.13E-04 | 4.34E-06 | -8.47E-05 | 2.82E-04 | -1.75E-04 | -9.31E-07 | -2.13E-05 | -2.88E-05 | -1.39E-04 |
| 9 | 4.79E-05 | 1.15E-04 | | | 3.12E-04 | | | | | |
| 10 | 4.79E-05 | | | | 3.42E-04 | | | | | |
| | | | | | | | | | | |
| Box 4N | dU/dt | U.dU/dx | V.dU/dy | W.dU/dz | 1/dens.dP/dx | g.d elev/dx | f.V | d/dx(u'.u') | d/dy(u'.v') | d/dz(u'.w') |
| Slice | ($m s^{-2}$) | ($m s^{-2}$) | ($m s^{-2}$) | ($m s^{-2}$) | ($m s^{-2}$) | ($m s^{-2}$) | ($m s^{-2}$) | ($m s^{-2}$) | ($m s^{-2}$) | ($m s^{-2}$) |
| 0 | 4.79E-05 | 1.27E-04 | 1.57E-05 | 0.00E+00 | 3.90E-05 | -2.02E-04 | -4.69E-07 | -2.09E-05 | -7.19E-06 | 0.00E+00 |
| 1 | 4.79E-05 | 1.27E-04 | 1.57E-05 | -5.17E-06 | 6.07E-05 | -2.02E-04 | -4.69E-07 | -2.09E-05 | -7.19E-06 | -1.65E-05 |
| 2 | 4.79E-05 | 1.19E-04 | 6.80E-06 | -1.89E-05 | 8.75E-05 | -2.02E-04 | -1.86E-06 | -3.37E-05 | -1.24E-05 | 4.00E-06 |
| 3 | 4.79E-05 | 1.20E-04 | 2.72E-05 | -4.08E-05 | 1.17E-04 | -2.02E-04 | -2.10E-06 | -3.76E-05 | -1.02E-05 | -2.35E-05 |
| 4 | 4.79E-05 | 1.19E-04 | 2.78E-05 | -6.99E-05 | 1.41E-04 | -2.02E-04 | -1.94E-06 | -4.07E-05 | -1.34E-05 | -1.18E-05 |
| 5 | 4.79E-05 | 1.15E-04 | 1.84E-05 | -1.05E-04 | 1.67E-04 | -2.02E-04 | -9.84E-07 | -2.38E-05 | -4.76E-06 | -1.43E-05 |
| 6 | 4.79E-05 | 1.09E-04 | 2.17E-05 | -1.44E-04 | 1.93E-04 | -2.02E-04 | -1.42E-07 | -3.52E-05 | -7.70E-06 | 1.66E-05 |
| 7 | 4.79E-05 | 1.06E-04 | -9.07E-07 | -1.86E-04 | 2.20E-04 | -2.02E-04 | 1.07E-06 | -2.72E-05 | -1.51E-05 | 5.87E-05 |
| 8 | 4.79E-05 | 9.61E-05 | 4.34E-06 | -2.29E-04 | 2.46E-04 | -2.02E-04 | 1.55E-06 | -1.84E-05 | -2.88E-05 | 8.59E-05 |
| 9 | 4.79E-05 | 9.40E-05 | | | 2.72E-04 | | | | | |
| 10 | 4.79E-05 | | | | 2.98E-04 | | | | | |
| | | | | | | | | | | |
| Box 5N | dU/dt | U.dU/dx | V.dU/dy | W.dU/dz | 1/dens.dP/dx | g.d elev/dx | f.V | d/dx(u'.u') | d/dy(u'.v') | d/dz(u'.w') |
| Slice | ($m s^{-2}$) | ($m s^{-2}$) | ($m s^{-2}$) | ($m s^{-2}$) | ($m s^{-2}$) | ($m s^{-2}$) | ($m s^{-2}$) | ($m s^{-2}$) | ($m s^{-2}$) | ($m s^{-2}$) |
| 0 | 1.86E-05 | 6.77E-05 | -2.85E-05 | 0.00E+00 | 3.51E-05 | -1.03E-04 | -2.49E-06 | 1.10E-05 | -3.29E-06 | 0.00E+00 |
| 1 | 1.86E-05 | 6.77E-05 | -2.85E-05 | -2.88E-07 | 5.58E-05 | -1.03E-04 | -2.49E-06 | 1.10E-05 | -3.29E-06 | -2.04E-05 |
| 2 | 1.86E-05 | 6.18E-05 | -4.81E-05 | -4.57E-07 | 8.54E-05 | -1.03E-04 | 2.47E-06 | 3.00E-08 | -1.45E-05 | 2.83E-06 |
| 3 | 1.86E-05 | 6.65E-05 | -8.43E-05 | -7.88E-07 | 1.09E-04 | -1.03E-04 | 6.35E-06 | -5.29E-06 | -1.59E-05 | 2.16E-05 |
| 4 | 1.86E-05 | 7.17E-05 | -1.47E-04 | -1.18E-06 | 1.34E-04 | -1.03E-04 | 1.26E-05 | -2.10E-05 | -1.37E-05 | 7.41E-05 |
| 5 | 1.86E-05 | 7.62E-05 | -1.41E-04 | -1.83E-06 | 1.59E-04 | -1.03E-04 | 1.35E-05 | -2.07E-05 | -1.38E-07 | 2.62E-05 |
| 6 | 1.86E-05 | 7.07E-05 | -1.21E-04 | -2.15E-06 | 1.84E-04 | -1.03E-04 | 1.43E-05 | -4.92E-05 | -8.99E-06 | 2.52E-05 |
| 7 | 1.86E-05 | 7.27E-05 | -1.06E-04 | -2.37E-06 | 2.09E-04 | -1.03E-04 | 1.20E-05 | -3.07E-05 | -2.98E-06 | -4.35E-05 |
| 8 | 1.86E-05 | 6.36E-05 | -9.69E-05 | -2.43E-06 | 2.34E-04 | -1.03E-04 | 9.96E-06 | -3.07E-05 | -1.29E-05 | -6.06E-05 |
| 9 | 1.86E-05 | | -7.10E-05 | | 2.59E-04 | | | | | |
| 10 | 1.86E-05 | | -3.96E-05 | | 2.84E-04 | | | | | |

*Table 2 continued*

| Box 6N | dU/dt | U.dU/dx | V.dU/dy | W.dU/dz | 1/dens.dP/dx | g.d elev/dx | f.V | d/dx(u'.u') | d/dy(u'.v') | d/dz(u'.w') |
|---|---|---|---|---|---|---|---|---|---|---|
| Slice | ($m s^{-2}$) | ($m s^{-2}$) | ($m s^{-2}$) | ($m s^{-2}$) | ($m s^{-2}$) | ($m s^{-2}$) | ($m s^{-2}$) | ($m s^{-2}$) | ($m s^{-2}$) | ($m s^{-2}$) |
| 0 | 1.86E-05 | 7.37E-05 | -2.85E-05 | 0.00E+00 | 9.55E-07 | -9.91E-05 | -2.45E-06 | 3.52E-05 | -3.29E-06 | 0.00E+00 |
| 1 | 1.86E-05 | 7.37E-05 | -2.85E-05 | -3.06E-07 | 1.52E-06 | -9.91E-05 | -2.45E-06 | 3.52E-05 | -3.29E-06 | -2.56E-07 |
| 2 | 1.86E-05 | 7.48E-05 | -4.81E-05 | -4.86E-07 | 5.14E-06 | -9.91E-05 | 2.10E-06 | 1.75E-05 | -1.45E-05 | 4.83E-05 |
| 3 | 1.86E-05 | 7.14E-05 | -8.43E-05 | -7.49E-07 | 6.65E-06 | -9.91E-05 | 5.66E-06 | 1.22E-05 | -1.59E-05 | 9.69E-05 |
| 4 | 1.86E-05 | 6.59E-05 | -1.47E-04 | -1.27E-06 | 8.70E-06 | -9.91E-05 | 1.11E-05 | 1.48E-05 | -1.37E-05 | 1.64E-04 |
| 5 | 1.86E-05 | 6.22E-05 | -1.41E-04 | -2.51E-06 | 1.08E-05 | -9.91E-05 | 1.15E-05 | 8.15E-07 | -1.38E-07 | 1.62E-04 |
| 6 | 1.86E-05 | 6.26E-05 | -1.21E-04 | -2.80E-06 | 1.28E-05 | -9.91E-05 | 1.26E-05 | -1.95E-05 | -8.99E-06 | 1.70E-04 |
| 7 | 1.86E-05 | 7.21E-05 | -1.06E-04 | -3.41E-06 | 1.49E-05 | -9.91E-05 | 1.06E-05 | 5.12E-06 | -2.98E-06 | 1.11E-04 |
| 8 | 1.86E-05 | 5.84E-05 | -9.69E-05 | -3.48E-06 | 1.69E-05 | -9.91E-05 | 9.40E-06 | -1.17E-05 | -1.29E-05 | 1.40E-04 |
| 9 | 1.86E-05 | | -7.10E-05 | | 1.89E-05 | | | | | |
| 10 | 1.86E-05 | | -3.96E-05 | | 2.10E-05 | | | | | |

| Box 7N | dU/dt | U.dU/dx | V.dU/dy | W.dU/dz | 1/dens.dP/dx | g.d elev/dx | f.V | d/dx(u'.u') | d/dy(u'.v') | d/dz(u'.w') |
|---|---|---|---|---|---|---|---|---|---|---|
| Slice | ($m s^{-2}$) | ($m s^{-2}$) | ($m s^{-2}$) | ($m s^{-2}$) | ($m s^{-2}$) | ($m s^{-2}$) | ($m s^{-2}$) | ($m s^{-2}$) | ($m s^{-2}$) | ($m s^{-2}$) |
| 0 | -5.77E-05 | 3.79E-04 | -7.59E-04 | 0.00E+00 | 1.31E-05 | 3.06E-04 | 2.13E-05 | 1.56E-04 | -1.54E-05 | 0.00E+00 |
| 1 | -5.77E-05 | 3.79E-04 | -7.59E-04 | -2.24E-06 | 2.04E-05 | 3.06E-04 | 2.13E-05 | 1.56E-04 | -1.54E-05 | -5.04E-06 |
| 2 | -5.77E-05 | 3.71E-04 | -6.44E-04 | -3.48E-06 | 2.77E-05 | 3.06E-04 | 1.89E-05 | 1.37E-04 | -5.66E-05 | -6.09E-05 |
| 3 | -5.77E-05 | 3.62E-04 | -6.17E-04 | -2.63E-06 | 3.52E-05 | 3.06E-04 | 1.79E-05 | 1.28E-04 | -3.59E-05 | -9.98E-05 |
| 4 | -5.77E-05 | 3.43E-04 | -5.34E-04 | -2.11E-06 | 4.24E-05 | 3.06E-04 | 1.46E-05 | 1.19E-04 | -1.06E-05 | -1.91E-04 |
| 5 | -5.77E-05 | 3.26E-04 | -3.96E-04 | -2.79E-08 | 4.97E-05 | 3.06E-04 | 1.10E-05 | 1.08E-04 | -2.36E-05 | -3.01E-04 |
| 6 | -5.77E-05 | 2.99E-04 | | | 5.71E-05 | | | | | |
| 7 | -5.77E-05 | 2.90E-04 | | | 6.44E-05 | | | | | |
| 8 | -5.77E-05 | | | | 7.17E-05 | | | | | |
| 9 | -5.77E-05 | | | | 7.91E-05 | | | | | |
| 10 | -5.77E-05 | | | | 8.64E-05 | | | | | |

| Box 1S | dU/dt | U.dU/dx | V.dU/dy | W.dU/dz | 1/dens.dP/dx | g.d elev/dx | f.V | d/dx(u'.u') | d/dy(u'.v') | d/dz(u'.w') |
|---|---|---|---|---|---|---|---|---|---|---|
| Slice | ($m s^{-2}$) | ($m s^{-2}$) | ($m s^{-2}$) | ($m s^{-2}$) | ($m s^{-2}$) | ($m s^{-2}$) | ($m s^{-2}$) | ($m s^{-2}$) | ($m s^{-2}$) | ($m s^{-2}$) |
| 0 | 4.79E-05 | 4.41E-07 | -1.52E-05 | 0.00E+00 | -4.58E-06 | -4.12E-05 | -4.11E-06 | -1.62E-05 | 2.47E-05 | 0.00E+00 |
| 1 | 4.79E-05 | 4.41E-07 | -1.52E-05 | 3.45E-08 | -7.12E-06 | -4.12E-05 | -4.11E-06 | -1.62E-05 | 2.47E-05 | 2.51E-06 |
| 2 | 4.79E-05 | -9.68E-06 | -3.07E-05 | 1.05E-05 | -8.52E-06 | -4.12E-05 | -5.17E-06 | -2.23E-06 | 2.43E-05 | 4.48E-06 |
| 3 | 4.79E-05 | -6.64E-06 | -3.61E-05 | 2.59E-05 | -9.66E-06 | -4.12E-05 | -4.58E-06 | 6.03E-06 | 1.25E-05 | -3.29E-06 |
| 4 | 4.79E-05 | 1.19E-06 | -5.12E-05 | 4.15E-05 | -1.16E-05 | -4.12E-05 | -4.86E-06 | 2.56E-06 | 1.02E-05 | -4.23E-06 |
| 5 | 4.79E-05 | -3.66E-06 | -4.87E-05 | 5.23E-05 | -1.33E-05 | -4.12E-05 | -4.33E-06 | 6.22E-06 | 1.23E-05 | -1.62E-05 |
| 6 | 4.79E-05 | 5.51E-06 | -6.06E-05 | 5.41E-05 | -1.49E-05 | -4.12E-05 | -2.82E-06 | 1.13E-05 | 2.28E-05 | -2.77E-05 |
| 7 | 4.79E-05 | 5.43E-06 | -3.76E-05 | 4.25E-05 | -1.66E-05 | -4.12E-05 | -2.29E-06 | 1.43E-05 | 1.65E-05 | -3.35E-05 |
| 8 | 4.79E-05 | 4.02E-07 | -2.38E-05 | 1.37E-05 | -1.83E-05 | -4.12E-05 | -1.46E-06 | 7.25E-06 | 1.94E-05 | -6.82E-06 |
| 9 | 4.79E-05 | -6.19E-06 | -9.41E-06 | -3.53E-05 | -1.99E-05 | -4.12E-05 | -9.41E-07 | 1.41E-05 | 1.91E-05 | 2.99E-05 |
| 10 | 4.79E-05 | 2.30E-07 | -5.48E-06 | -1.07E-04 | -2.16E-05 | -4.12E-05 | -6.03E-07 | 2.64E-06 | 1.87E-05 | 1.05E-04 |

| Box 2S | dU/dt | U.dU/dx | V.dU/dy | W.dU/dz | 1/dens.dP/dx | g.d elev/dx | f.V | d/dx(u'.u') | d/dy(u'.v') | d/dz(u'.w') |
|---|---|---|---|---|---|---|---|---|---|---|
| Slice | ($m s^{-2}$) | ($m s^{-2}$) | ($m s^{-2}$) | ($m s^{-2}$) | ($m s^{-2}$) | ($m s^{-2}$) | ($m s^{-2}$) | ($m s^{-2}$) | ($m s^{-2}$) | ($m s^{-2}$) |
| 0 | 4.79E-05 | 2.08E-05 | -1.52E-05 | 0.00E+00 | 9.78E-06 | -1.01E-04 | -6.54E-06 | 6.39E-06 | 2.47E-05 | 0.00E+00 |
| 1 | 4.79E-05 | 2.08E-05 | -1.52E-05 | -2.18E-07 | 1.52E-05 | -1.01E-04 | -6.54E-06 | 6.39E-06 | 2.47E-05 | -5.22E-06 |
| 2 | 4.79E-05 | 1.80E-05 | -3.07E-05 | 8.01E-07 | 2.35E-05 | -1.01E-04 | -7.17E-06 | 1.01E-05 | 2.43E-05 | -7.29E-08 |
| 3 | 4.79E-05 | 7.08E-06 | -3.61E-05 | 3.07E-06 | 3.36E-05 | -1.01E-04 | -7.40E-06 | 6.98E-06 | 1.25E-05 | 1.86E-05 |
| 4 | 4.79E-05 | -2.78E-05 | -5.12E-05 | 6.00E-06 | 4.02E-05 | -1.01E-04 | -8.06E-06 | 1.19E-05 | 1.02E-05 | 5.56E-05 |
| 5 | 4.79E-05 | -4.50E-05 | -4.87E-05 | 7.74E-06 | 4.82E-05 | -1.01E-04 | -7.30E-06 | 1.47E-05 | 1.23E-05 | 5.66E-05 |
| 6 | 4.79E-05 | -6.73E-05 | -6.06E-05 | 7.42E-06 | 5.61E-05 | -1.01E-04 | -5.13E-06 | 7.54E-06 | 2.28E-05 | 8.19E-05 |
| 7 | 4.79E-05 | -8.23E-05 | -3.76E-05 | 5.37E-06 | 6.40E-05 | -1.01E-04 | -4.13E-06 | 1.17E-05 | 1.65E-05 | 7.12E-05 |
| 8 | 4.79E-05 | -9.71E-05 | -2.38E-05 | 1.47E-06 | 7.19E-05 | -1.01E-04 | -1.97E-06 | -4.58E-06 | 1.94E-05 | 8.38E-05 |
| 9 | 4.79E-05 | -6.66E-05 | -9.41E-06 | -2.92E-06 | 7.98E-05 | -1.01E-04 | -1.20E-06 | 1.07E-05 | 1.91E-05 | 2.12E-05 |
| 10 | 4.79E-05 | -7.06E-05 | -5.48E-06 | -6.59E-06 | 8.77E-05 | -1.01E-04 | -1.57E-07 | 8.37E-06 | 1.87E-05 | 2.08E-05 |

| Box 3S | dU/dt | U.dU/dx | V.dU/dy | W.dU/dz | 1/dens.dP/dx | g.d elev/dx | f.V | d/dx(u'.u') | d/dy(u'.v') | d/dz(u'.w') |
|---|---|---|---|---|---|---|---|---|---|---|
| Slice | ($m s^{-2}$) | ($m s^{-2}$) | ($m s^{-2}$) | ($m s^{-2}$) | ($m s^{-2}$) | ($m s^{-2}$) | ($m s^{-2}$) | ($m s^{-2}$) | ($m s^{-2}$) | ($m s^{-2}$) |
| 0 | -5.77E-05 | 8.89E-05 | 1.49E-05 | 0.00E+00 | 3.14E-05 | 9.11E-05 | 5.69E-06 | -1.66E-04 | 3.06E-06 | 0.00E+00 |
| 1 | -5.77E-05 | 8.89E-05 | 1.49E-05 | 1.88E-06 | 4.89E-05 | 9.11E-05 | 5.69E-06 | -1.66E-04 | 3.06E-06 | -1.93E-05 |
| 2 | -5.77E-05 | 8.52E-05 | 1.07E-05 | 1.09E-05 | 6.73E-05 | 9.11E-05 | 3.74E-06 | -1.87E-04 | 5.62E-06 | -2.28E-05 |
| 3 | -5.77E-05 | 4.94E-05 | 1.24E-05 | 2.50E-05 | 8.60E-05 | 9.11E-05 | 1.84E-06 | -1.34E-04 | -6.60E-06 | -6.35E-05 |
| 4 | -5.77E-05 | 5.85E-05 | 1.62E-05 | 4.16E-05 | 1.04E-04 | 9.11E-05 | 3.71E-07 | -1.71E-04 | 6.51E-06 | -8.87E-05 |
| 5 | -5.77E-05 | 4.55E-05 | 3.09E-05 | 5.79E-05 | 1.22E-04 | 9.11E-05 | -1.75E-06 | -1.69E-04 | -1.91E-06 | -1.21E-04 |
| 6 | -5.77E-05 | 5.32E-05 | | | 1.40E-04 | | | | | |
| 7 | -5.77E-05 | 2.39E-05 | | | 1.59E-04 | | | | | |
| 8 | -5.77E-05 | | | | 1.77E-04 | | | | | |
| 9 | -5.77E-05 | | | | 1.95E-04 | | | | | |
| 10 | -5.77E-05 | | | | 2.13E-04 | | | | | |

*Table 3 Lateral equation of motion*

| Box 1N | dV/dt | U.dV/dx | V.dV/dy | W.dV/dz | 1/dens.dP/dy | g.d elev/dy | f.U | d/dx(v'.u') | d/dy(v'.v') | d/dz(v'.w') |
|---|---|---|---|---|---|---|---|---|---|---|
| Slice | ($m s^{-2}$) | ($m s^{-2}$) | ($m s^{-2}$) | ($m s^{-2}$) | ($m s^{-2}$) | ($m s^{-2}$) | ($m s^{-2}$) | ($m s^{-2}$) | ($m s^{-2}$) | ($m s^{-2}$) |
| 0 | -3.15E-06 | 3.56E-07 | -4.38E-06 | 0.00E+00 | -2.36E-05 | 6.61E-05 | -8.49E-06 | -6.13E-06 | -2.07E-05 | 0.00E+00 |
| 1 | -3.15E-06 | 3.56E-07 | -4.38E-06 | 8.74E-07 | -3.67E-05 | 6.61E-05 | -8.49E-06 | -6.13E-06 | -2.07E-05 | 1.22E-05 |
| 2 | -3.15E-06 | -1.07E-08 | -4.71E-06 | 1.74E-06 | -4.93E-05 | 6.61E-05 | -8.41E-06 | -5.63E-06 | -1.13E-05 | 1.46E-05 |
| 3 | -3.15E-06 | 1.96E-06 | -2.60E-06 | 2.26E-06 | -6.24E-05 | 6.61E-05 | -9.33E-06 | -3.12E-06 | -1.82E-05 | 2.85E-05 |
| 4 | -3.15E-06 | 4.58E-06 | 6.49E-07 | 1.16E-06 | -7.52E-05 | 6.61E-05 | -9.36E-06 | -2.41E-05 | -1.98E-05 | 5.91E-05 |
| 5 | -3.15E-06 | -5.04E-06 | -7.81E-07 | -2.26E-06 | -8.81E-05 | 6.61E-05 | -9.11E-06 | -1.14E-05 | -8.50E-06 | 6.22E-05 |
| 6 | -3.15E-06 | -7.38E-06 | -2.28E-07 | -8.93E-06 | -1.01E-04 | 6.61E-05 | -7.61E-06 | -1.44E-05 | -1.08E-05 | 8.74E-05 |
| 7 | -3.15E-06 | -8.85E-06 | -5.08E-06 | -2.03E-05 | -1.14E-04 | 6.61E-05 | -7.26E-06 | -1.30E-05 | -1.66E-05 | 1.22E-04 |
| 8 | -3.15E-06 | -1.56E-05 | -1.22E-05 | -3.58E-05 | -1.27E-04 | 6.61E-05 | -6.21E-06 | -1.62E-05 | -2.56E-06 | 1.52E-04 |
| 9 | -3.15E-06 | -9.93E-06 | -1.77E-05 | -5.61E-05 | -1.40E-04 | 6.61E-05 | -4.87E-06 | -1.15E-05 | -5.61E-06 | 1.82E-04 |
| 10 | -3.15E-06 | -5.32E-06 | -2.28E-05 | -8.30E-05 | -1.53E-04 | 6.61E-05 | -3.16E-06 | -2.35E-05 | -1.32E-05 | 2.41E-04 |

| Box 2N | dV/dt | U.dV/dx | V.dV/dy | W.dV/dz | 1/dens.dP/dy | g.d elev/dy | f.U | d/dx(v'.u') | d/dy(v'.v') | d/dz(v'.w') |
|---|---|---|---|---|---|---|---|---|---|---|
| Slice | ($m s^{-2}$) | ($m s^{-2}$) | ($m s^{-2}$) | ($m s^{-2}$) | ($m s^{-2}$) | ($m s^{-2}$) | ($m s^{-2}$) | ($m s^{-2}$) | ($m s^{-2}$) | ($m s^{-2}$) |
| 0 | -3.15E-06 | 4.60E-05 | -7.44E-05 | 0.00E+00 | -4.54E-05 | 6.92E-05 | 3.24E-05 | -2.08E-05 | -3.87E-06 | 0.00E+00 |
| 1 | -3.15E-06 | 4.60E-05 | -7.44E-05 | -2.33E-06 | -7.06E-05 | 6.92E-05 | 3.24E-05 | -2.08E-05 | -3.87E-06 | 2.76E-05 |
| 2 | -3.15E-06 | 4.77E-05 | -8.95E-05 | 9.39E-08 | -9.49E-05 | 6.92E-05 | 3.15E-05 | -1.15E-05 | -1.12E-05 | 6.18E-05 |
| 3 | -3.15E-06 | 4.54E-05 | -9.79E-05 | 5.48E-06 | -1.20E-04 | 6.92E-05 | 3.14E-05 | -6.90E-06 | -1.27E-05 | 8.88E-05 |
| 4 | -3.15E-06 | 4.54E-05 | -8.70E-05 | 1.41E-05 | -1.45E-04 | 6.92E-05 | 3.10E-05 | -5.40E-06 | -1.61E-05 | 9.65E-05 |
| 5 | -3.15E-06 | 4.30E-05 | -6.87E-05 | 2.54E-05 | -1.69E-04 | 6.92E-05 | 3.04E-05 | -7.00E-06 | 1.16E-05 | 6.85E-05 |
| 6 | -3.15E-06 | 4.43E-05 | -9.79E-05 | 3.88E-05 | -1.94E-04 | 6.92E-05 | 3.04E-05 | -1.92E-07 | 9.06E-06 | 1.04E-04 |
| 7 | -3.15E-06 | 5.78E-05 | -1.17E-04 | 5.49E-05 | -2.19E-04 | 6.92E-05 | 2.97E-05 | 5.74E-06 | 1.53E-05 | 1.06E-04 |
| 8 | -3.15E-06 | 8.16E-05 | -1.58E-04 | 7.40E-05 | -2.43E-04 | 6.92E-05 | 2.94E-05 | -4.44E-06 | 5.61E-06 | 1.49E-04 |
| 9 | -3.15E-06 | 6.71E-05 | | | -2.68E-04 | | | -2.14E-06 | | |
| 10 | -3.15E-06 | | | | -2.93E-04 | | | | | |

| Box 3N | dV/dt | U.dV/dx | V.dV/dy | W.dV/dz | 1/dens.dP/dy | g.d elev/dy | f.U | d/dx(v'.u') | d/dy(v'.v') | d/dz(v'.w') |
|---|---|---|---|---|---|---|---|---|---|---|
| Slice | ($m s^{-2}$) | ($m s^{-2}$) | ($m s^{-2}$) | ($m s^{-2}$) | ($m s^{-2}$) | ($m s^{-2}$) | ($m s^{-2}$) | ($m s^{-2}$) | ($m s^{-2}$) | ($m s^{-2}$) |
| 0 | -3.15E-06 | 4.60E-05 | -4.30E-04 | 0.00E+00 | -6.82E-05 | 4.56E-04 | 3.63E-05 | -2.08E-05 | -1.60E-05 | 0.00E+00 |
| 1 | -3.15E-06 | 4.60E-05 | -4.30E-04 | -2.18E-05 | -1.06E-04 | 4.56E-04 | 3.63E-05 | -2.08E-05 | -1.60E-05 | 5.97E-05 |
| 2 | -3.15E-06 | 4.77E-05 | -3.99E-04 | -3.65E-05 | -1.43E-04 | 4.56E-04 | 3.52E-05 | -1.15E-05 | -1.97E-05 | 7.43E-05 |
| 3 | -3.15E-06 | 4.54E-05 | -3.53E-04 | -2.86E-05 | -1.79E-04 | 4.56E-04 | 3.48E-05 | -6.90E-06 | -1.75E-05 | 5.26E-05 |
| 4 | -3.15E-06 | 4.54E-05 | -2.78E-04 | 1.13E-06 | -2.17E-04 | 4.56E-04 | 3.42E-05 | -5.40E-06 | -3.10E-05 | -1.97E-06 |
| 5 | -3.15E-06 | 4.30E-05 | -2.29E-04 | 3.26E-05 | -2.54E-04 | 4.56E-04 | 3.37E-05 | -7.00E-06 | -1.04E-05 | -6.14E-05 |
| 6 | -3.15E-06 | 4.43E-05 | -1.85E-04 | 3.09E-05 | -2.91E-04 | 4.56E-04 | 3.25E-05 | -1.92E-07 | -9.59E-06 | -7.43E-05 |
| 7 | -3.15E-06 | 5.78E-05 | -1.65E-04 | -5.01E-05 | -3.28E-04 | 4.56E-04 | 3.13E-05 | 5.74E-06 | -8.06E-06 | 4.06E-06 |
| 8 | -3.15E-06 | 8.16E-05 | -1.20E-04 | -2.65E-04 | -3.65E-04 | 4.56E-04 | 3.06E-05 | -4.44E-06 | -7.38E-06 | 1.97E-04 |
| 9 | -3.15E-06 | 6.71E-05 | | | -4.03E-04 | | | -2.14E-06 | | |
| 10 | -3.15E-06 | | | | -4.40E-04 | | | | | |

| Box 4N | dV/dt | U.dV/dx | V.dV/dy | W.dV/dz | 1/dens.dP/dy | g.d elev/dy | f.U | d/dx(v'.u') | d/dy(v'.v') | d/dz(v'.w') |
|---|---|---|---|---|---|---|---|---|---|---|
| Slice | ($m s^{-2}$) | ($m s^{-2}$) | ($m s^{-2}$) | ($m s^{-2}$) | ($m s^{-2}$) | ($m s^{-2}$) | ($m s^{-2}$) | ($m s^{-2}$) | ($m s^{-2}$) | ($m s^{-2}$) |
| 0 | -3.15E-06 | 1.10E-04 | -4.30E-04 | 0.00E+00 | -6.82E-05 | 3.59E-04 | 3.75E-05 | 1.10E-05 | -1.60E-05 | 0.00E+00 |
| 1 | -3.15E-06 | 1.10E-04 | -4.30E-04 | -2.00E-05 | -1.06E-04 | 3.59E-04 | 3.75E-05 | 1.10E-05 | -1.60E-05 | 5.78E-05 |
| 2 | -3.15E-06 | 1.11E-04 | -3.99E-04 | -1.25E-05 | -1.43E-04 | 3.59E-04 | 3.66E-05 | 1.70E-05 | -1.97E-05 | 5.40E-05 |
| 3 | -3.15E-06 | 1.05E-04 | -3.53E-04 | 4.42E-06 | -1.79E-04 | 3.59E-04 | 3.63E-05 | 2.34E-05 | -1.75E-05 | 2.51E-05 |
| 4 | -3.15E-06 | 9.25E-05 | -2.78E-04 | 2.78E-05 | -2.17E-04 | 3.59E-04 | 3.55E-05 | 2.62E-05 | -3.10E-05 | -1.17E-05 |
| 5 | -3.15E-06 | 7.75E-05 | -2.29E-04 | 5.33E-05 | -2.54E-04 | 3.59E-04 | 3.45E-05 | 2.17E-05 | -1.04E-05 | -4.90E-05 |
| 6 | -3.15E-06 | 4.79E-05 | -1.85E-04 | 7.71E-05 | -2.91E-04 | 3.59E-04 | 3.27E-05 | 2.14E-05 | -9.59E-06 | -4.90E-05 |
| 7 | -3.15E-06 | 3.52E-05 | -1.65E-04 | 9.60E-05 | -3.28E-04 | 3.59E-04 | 3.05E-05 | 2.65E-05 | -8.06E-06 | -4.24E-05 |
| 8 | -3.15E-06 | 2.01E-05 | -1.20E-04 | 1.07E-04 | -3.65E-04 | 3.59E-04 | 2.89E-05 | 2.35E-05 | -7.38E-06 | -4.27E-05 |
| 9 | -3.15E-06 | 7.21E-06 | | | -4.03E-04 | | | 2.95E-05 | | |
| 10 | -3.15E-06 | | | | -4.40E-04 | | | | | |

| Box 5N | dV/dt | U.dV/dx | V.dV/dy | W.dV/dz | 1/dens.dP/dy | g.d elev/dy | f.U | d/dx(v'.u') | d/dy(v'.v') | d/dz(v'.w') |
|---|---|---|---|---|---|---|---|---|---|---|
| Slice | ($m s^{-2}$) | ($m s^{-2}$) | ($m s^{-2}$) | ($m s^{-2}$) | ($m s^{-2}$) | ($m s^{-2}$) | ($m s^{-2}$) | ($m s^{-2}$) | ($m s^{-2}$) | ($m s^{-2}$) |
| 0 | 1.42E-05 | 3.82E-05 | -3.31E-05 | 0.00E+00 | 9.36E-05 | -1.61E-04 | 2.43E-05 | -3.52E-06 | 2.76E-05 | 0.00E+00 |
| 1 | 1.42E-05 | 3.82E-05 | -3.31E-05 | 4.25E-06 | 1.49E-04 | -1.61E-04 | 2.43E-05 | -3.52E-06 | 2.76E-05 | -5.93E-05 |
| 2 | 1.42E-05 | 1.44E-05 | -6.62E-05 | 8.64E-06 | 2.24E-04 | -1.61E-04 | 2.39E-05 | -3.50E-06 | 1.97E-05 | -7.36E-05 |
| 3 | 1.42E-05 | 1.82E-05 | -1.24E-04 | 1.54E-05 | 2.85E-04 | -1.61E-04 | 2.28E-05 | -1.10E-05 | 1.12E-05 | -7.10E-05 |
| 4 | 1.42E-05 | 1.31E-05 | -2.45E-04 | 1.96E-05 | 3.50E-04 | -1.61E-04 | 2.35E-05 | -2.43E-05 | -9.32E-06 | 1.91E-05 |
| 5 | 1.42E-05 | 8.59E-06 | -1.96E-04 | 1.87E-05 | 4.15E-04 | -1.61E-04 | 2.37E-05 | -3.23E-05 | -9.71E-06 | -8.11E-05 |
| 6 | 1.42E-05 | -8.37E-06 | -1.54E-04 | 6.72E-07 | 4.80E-04 | -1.61E-04 | 2.33E-05 | -3.46E-05 | -1.45E-05 | -1.46E-04 |
| 7 | 1.42E-05 | -1.45E-05 | -8.81E-05 | -3.11E-05 | 5.45E-04 | -1.61E-04 | 2.30E-05 | -3.11E-05 | -2.68E-06 | -2.53E-04 |
| 8 | 1.42E-05 | -1.31E-05 | -7.45E-05 | -7.29E-05 | 6.10E-04 | -1.61E-04 | 2.22E-05 | -3.27E-05 | -1.13E-05 | -2.80E-04 |
| 9 | 1.42E-05 | | -3.99E-05 | | 6.74E-04 | | | | -1.11E-05 | |
| 10 | 1.42E-05 | | -2.48E-05 | | 7.39E-04 | | | | -1.86E-05 | |

*Table 3 continued*

| Box 6N | dV/dt | U.dV/dx | V.dV/dy | W.dV/dz | 1/dens.dP/dy | g.d elev/dy | f.U | d/dx(v'.u') | d/dy(v'.v') | d/dz(v'.w') |
|---|---|---|---|---|---|---|---|---|---|---|
| Slice | ($m s^{-2}$) | ($m s^{-2}$) | ($m s^{-2}$) | ($m s^{-2}$) | ($m s^{-2}$) | ($m s^{-2}$) | ($m s^{-2}$) | ($m s^{-2}$) | ($m s^{-2}$) | ($m s^{-2}$) |
| 0 | 1.42E-05 | 3.90E-05 | -3.31E-05 | 0.00E+00 | 9.37E-05 | -1.53E-04 | 2.46E-05 | -1.31E-05 | 2.76E-05 | 0.00E+00 |
| 1 | 1.42E-05 | 3.90E-05 | -3.31E-05 | 2.44E-06 | 1.49E-04 | -1.53E-04 | 2.46E-05 | -1.31E-05 | 2.76E-05 | -5.75E-05 |
| 2 | 1.42E-05 | 8.49E-06 | -6.62E-05 | 4.71E-06 | 2.24E-04 | -1.53E-04 | 2.47E-05 | -1.33E-05 | 1.97E-05 | -6.34E-05 |
| 3 | 1.42E-05 | 8.63E-06 | -1.24E-04 | 7.36E-06 | 2.85E-04 | -1.53E-04 | 2.32E-05 | -1.71E-05 | 1.12E-05 | -5.61E-05 |
| 4 | 1.42E-05 | -5.25E-06 | -2.45E-04 | 1.06E-05 | 3.50E-04 | -1.53E-04 | 2.30E-05 | -3.44E-05 | -9.32E-06 | 4.85E-05 |
| 5 | 1.42E-05 | -1.40E-05 | -1.96E-04 | 1.32E-05 | 4.15E-04 | -1.53E-04 | 2.25E-05 | -4.00E-05 | -9.71E-06 | -5.27E-05 |
| 6 | 1.42E-05 | -2.64E-05 | -1.54E-04 | 1.56E-06 | 4.80E-04 | -1.53E-04 | 2.25E-05 | -4.42E-05 | -1.45E-05 | -1.27E-04 |
| 7 | 1.42E-05 | -3.20E-05 | -8.81E-05 | -1.96E-05 | 5.45E-04 | -1.53E-04 | 2.30E-05 | -4.08E-05 | -2.68E-06 | -2.46E-04 |
| 8 | 1.42E-05 | -1.93E-05 | -7.45E-05 | -4.75E-05 | 6.10E-04 | -1.53E-04 | 2.17E-05 | -3.33E-05 | -1.13E-05 | -3.07E-04 |
| 9 | 1.42E-05 | | -3.99E-05 | | 6.75E-04 | | | | -1.11E-05 | |
| 10 | 1.42E-05 | | -2.48E-05 | | 7.39E-04 | | | | -1.86E-05 | |

| Box 7N | dV/dt | U.dV/dx | V.dV/dy | W.dV/dz | 1/dens.dP/dy | g.d elev/dy | f.U | d/dx(v'.u') | d/dy(v'.v') | d/dz(v'.w') |
|---|---|---|---|---|---|---|---|---|---|---|
| Slice | ($m s^{-2}$) | ($m s^{-2}$) | ($m s^{-2}$) | ($m s^{-2}$) | ($m s^{-2}$) | ($m s^{-2}$) | ($m s^{-2}$) | ($m s^{-2}$) | ($m s^{-2}$) | ($m s^{-2}$) |
| 0 | -1.95E-05 | 6.89E-05 | -6.09E-04 | 0.00E+00 | 9.70E-06 | 6.69E-04 | 4.51E-05 | -7.53E-05 | -8.86E-05 | 0.00E+00 |
| 1 | -1.95E-05 | 6.89E-05 | -6.09E-04 | -2.51E-06 | 1.51E-05 | 6.69E-04 | 4.51E-05 | -7.53E-05 | -8.86E-05 | -2.88E-06 |
| 2 | -1.95E-05 | 7.21E-05 | -4.85E-04 | -7.37E-06 | 1.76E-05 | 6.69E-04 | 4.39E-05 | -1.03E-04 | -7.90E-05 | -1.09E-04 |
| 3 | -1.95E-05 | 6.89E-05 | -4.96E-04 | -8.18E-06 | 1.95E-05 | 6.69E-04 | 4.43E-05 | -9.47E-05 | -8.35E-05 | -9.96E-05 |
| 4 | -1.95E-05 | 7.76E-05 | -3.71E-04 | -8.66E-06 | 2.36E-05 | 6.69E-04 | 4.20E-05 | -7.80E-05 | -1.22E-04 | -2.13E-04 |
| 5 | -1.95E-05 | 7.85E-05 | -2.37E-04 | -1.42E-07 | 2.68E-05 | 6.69E-04 | 4.14E-05 | -8.71E-05 | -1.11E-04 | -3.60E-04 |
| 6 | -1.95E-05 | 3.71E-05 | | | 3.00E-05 | | | -7.53E-05 | | |
| 7 | -1.95E-05 | 3.73E-05 | | | 3.33E-05 | | | -9.56E-05 | | |
| 8 | -1.95E-05 | | | | 3.65E-05 | | | | | |
| 9 | -1.95E-05 | | | | 3.97E-05 | | | | | |
| 10 | -1.95E-05 | | | | 4.30E-05 | | | | | |

| Box 1S | dV/dt | U.dV/dx | V.dV/dy | W.dV/dz | 1/dens.dP/dy | g.d elev/dy | f.U | d/dx(v'.u') | d/dy(v'.v') | d/dz(v'.w') |
|---|---|---|---|---|---|---|---|---|---|---|
| Slice | ($m s^{-2}$) | ($m s^{-2}$) | ($m s^{-2}$) | ($m s^{-2}$) | ($m s^{-2}$) | ($m s^{-2}$) | ($m s^{-2}$) | ($m s^{-2}$) | ($m s^{-2}$) | ($m s^{-2}$) |
| 0 | -3.15E-06 | -1.32E-07 | -4.17E-06 | 0.00E+00 | -2.37E-05 | -1.66E-05 | 2.28E-05 | 1.47E-05 | 1.02E-05 | 0.00E+00 |
| 1 | -3.15E-06 | -1.32E-07 | -4.17E-06 | 6.66E-06 | -3.68E-05 | -1.66E-05 | 2.28E-05 | 1.47E-05 | 1.02E-05 | 6.49E-06 |
| 2 | -3.15E-06 | 2.24E-06 | -2.30E-05 | 2.16E-06 | -4.57E-05 | -1.66E-05 | 2.32E-05 | 1.13E-05 | 1.16E-05 | 3.79E-05 |
| 3 | -3.15E-06 | 1.82E-06 | -2.74E-05 | -6.49E-06 | -5.37E-05 | -1.66E-05 | 2.29E-05 | 1.13E-05 | 1.21E-05 | 5.92E-05 |
| 4 | -3.15E-06 | -2.98E-07 | -4.52E-05 | -1.81E-05 | -6.46E-05 | -1.66E-05 | 2.08E-05 | 1.93E-05 | 2.43E-05 | 8.35E-05 |
| 5 | -3.15E-06 | 1.09E-06 | -4.39E-05 | -3.02E-05 | -7.44E-05 | -1.66E-05 | 1.93E-05 | 1.80E-05 | 1.42E-05 | 1.16E-04 |
| 6 | -3.15E-06 | -1.79E-06 | -5.42E-05 | -4.04E-05 | -8.43E-05 | -1.66E-05 | 1.80E-05 | 1.69E-05 | 1.43E-05 | 1.51E-04 |
| 7 | -3.15E-06 | -2.42E-06 | -3.12E-05 | -4.66E-05 | -9.41E-05 | -1.66E-05 | 1.76E-05 | 1.82E-05 | 4.38E-06 | 1.54E-04 |
| 8 | -3.15E-06 | -1.65E-07 | -2.40E-05 | -4.64E-05 | -1.04E-04 | -1.66E-05 | 1.79E-05 | 1.35E-05 | 5.96E-06 | 1.57E-04 |
| 9 | -3.15E-06 | 1.80E-06 | -5.33E-06 | -3.84E-05 | -1.14E-04 | -1.66E-05 | 1.81E-05 | 9.72E-06 | 7.38E-06 | 1.40E-04 |
| 10 | -3.15E-06 | -5.84E-08 | -2.79E-06 | -2.07E-05 | -1.24E-04 | -1.66E-05 | 1.78E-05 | 1.32E-05 | 5.35E-06 | 1.31E-04 |

| Box 2S | dV/dt | U.dV/dx | V.dV/dy | W.dV/dz | 1/dens.dP/dy | g.d elev/dy | f.U | d/dx(v'.u') | d/dy(v'.v') | d/dz(v'.w') |
|---|---|---|---|---|---|---|---|---|---|---|
| Slice | ($m s^{-2}$) | ($m s^{-2}$) | ($m s^{-2}$) | ($m s^{-2}$) | ($m s^{-2}$) | ($m s^{-2}$) | ($m s^{-2}$) | ($m s^{-2}$) | ($m s^{-2}$) | ($m s^{-2}$) |
| 0 | -3.15E-06 | 5.10E-06 | -4.17E-06 | 0.00E+00 | -2.37E-05 | -2.82E-05 | 2.96E-05 | 1.43E-05 | 1.02E-05 | 0.00E+00 |
| 1 | -3.15E-06 | 5.10E-06 | -4.17E-06 | 1.37E-06 | -3.68E-05 | -2.82E-05 | 2.96E-05 | 1.43E-05 | 1.02E-05 | 1.18E-05 |
| 2 | -3.15E-06 | 4.38E-06 | -2.30E-05 | 6.92E-07 | -4.57E-05 | -2.82E-05 | 3.06E-05 | 7.52E-06 | 1.16E-05 | 4.53E-05 |
| 3 | -3.15E-06 | 2.33E-05 | -2.74E-05 | -1.03E-06 | -5.37E-05 | -2.82E-05 | 3.01E-05 | 1.25E-05 | 1.21E-05 | 3.56E-05 |
| 4 | -3.15E-06 | 4.88E-05 | -4.52E-05 | -4.56E-06 | -6.46E-05 | -2.82E-05 | 2.85E-05 | 1.66E-05 | 2.43E-05 | 2.75E-05 |
| 5 | -3.15E-06 | 3.12E-05 | -4.39E-05 | -8.54E-06 | -7.44E-05 | -2.82E-05 | 2.76E-05 | 1.14E-05 | 1.42E-05 | 7.40E-05 |
| 6 | -3.15E-06 | 9.33E-06 | -5.42E-05 | -1.16E-05 | -8.43E-05 | -2.82E-05 | 2.63E-05 | 1.20E-05 | 1.43E-05 | 1.20E-04 |
| 7 | -3.15E-06 | -3.74E-05 | -3.12E-05 | -1.38E-05 | -9.42E-05 | -2.82E-05 | 2.62E-05 | 7.38E-06 | 4.38E-06 | 1.70E-04 |
| 8 | -3.15E-06 | -7.70E-05 | -2.40E-05 | -1.36E-05 | -1.04E-04 | -2.82E-05 | 2.67E-05 | 2.27E-06 | 5.96E-06 | 2.15E-04 |
| 9 | -3.15E-06 | -6.25E-05 | -5.33E-06 | -1.18E-05 | -1.14E-04 | -2.82E-05 | 2.68E-05 | 4.48E-07 | 7.38E-06 | 1.90E-04 |
| 10 | -3.15E-06 | -7.41E-05 | -2.79E-06 | -8.87E-06 | -1.24E-04 | -2.82E-05 | 2.62E-05 | -1.87E-06 | 5.35E-06 | 2.11E-04 |

| Box 3S | dV/dt | U.dV/dx | V.dV/dy | W.dV/dz | 1/dens.dP/dy | g.d elev/dy | f.U | d/dx(v'.u') | d/dy(v'.v') | d/dz(v'.w') |
|---|---|---|---|---|---|---|---|---|---|---|
| Slice | ($m s^{-2}$) | ($m s^{-2}$) | ($m s^{-2}$) | ($m s^{-2}$) | ($m s^{-2}$) | ($m s^{-2}$) | ($m s^{-2}$) | ($m s^{-2}$) | ($m s^{-2}$) | ($m s^{-2}$) |
| 0 | -1.95E-05 | 7.57E-05 | -7.68E-07 | 0.00E+00 | -1.16E-05 | -1.80E-04 | 3.80E-05 | 5.89E-05 | 3.89E-05 | 0.00E+00 |
| 1 | -1.95E-05 | 7.57E-05 | -7.68E-07 | 8.79E-06 | -1.80E-05 | -1.80E-04 | 3.80E-05 | 5.89E-05 | 3.89E-05 | -2.36E-06 |
| 2 | -1.95E-05 | 5.80E-05 | -2.65E-06 | 1.75E-05 | -2.04E-05 | -1.80E-04 | 3.67E-05 | 5.31E-05 | 4.46E-05 | 1.22E-05 |
| 3 | -1.95E-05 | 5.19E-05 | -3.76E-06 | 2.84E-05 | -2.17E-05 | -1.80E-04 | 3.62E-05 | 5.74E-05 | 6.36E-05 | -1.29E-05 |
| 4 | -1.95E-05 | 5.31E-05 | -1.32E-05 | 3.93E-05 | -2.64E-05 | -1.80E-04 | 3.52E-05 | 7.75E-05 | 4.38E-05 | -1.02E-05 |
| 5 | -1.95E-05 | 2.55E-05 | -2.97E-05 | 4.87E-05 | -2.97E-05 | -1.80E-04 | 3.14E-05 | 5.49E-05 | 5.70E-05 | 4.11E-05 |
| 6 | -1.95E-05 | 4.39E-06 | | | -3.30E-05 | | | 5.38E-05 | | |
| 7 | -1.95E-05 | | | | -3.63E-05 | | | 6.25E-05 | | |
| 8 | -1.95E-05 | | | | -3.97E-05 | | | | | |
| 9 | -1.95E-05 | | | | -4.30E-05 | | | | | |
| 10 | -1.95E-05 | | | | -4.63E-05 | | | | | |

*Figure 8a Slice-averaged u vs. depth, box 1N*

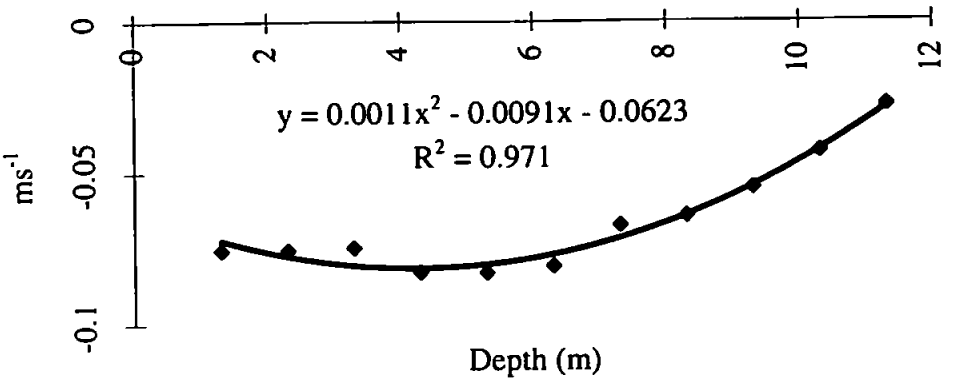


*Figure 8b Slice-averaged v vs. depth, box 1N*

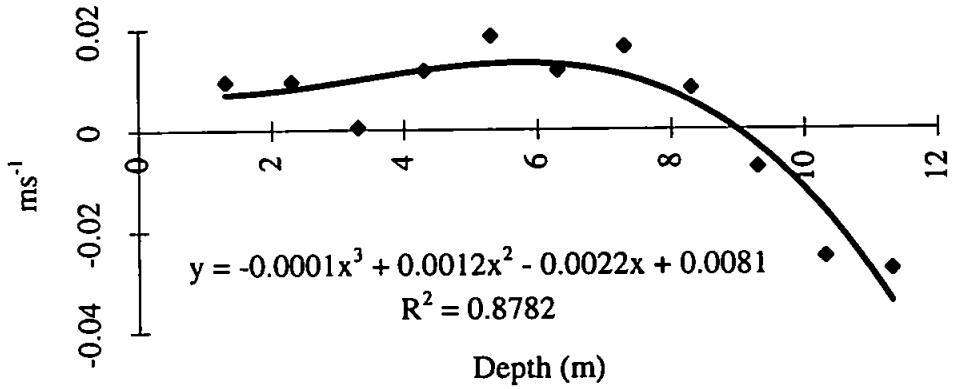


*Figure 9a Slice-averaged u vs. depth, box 2N*

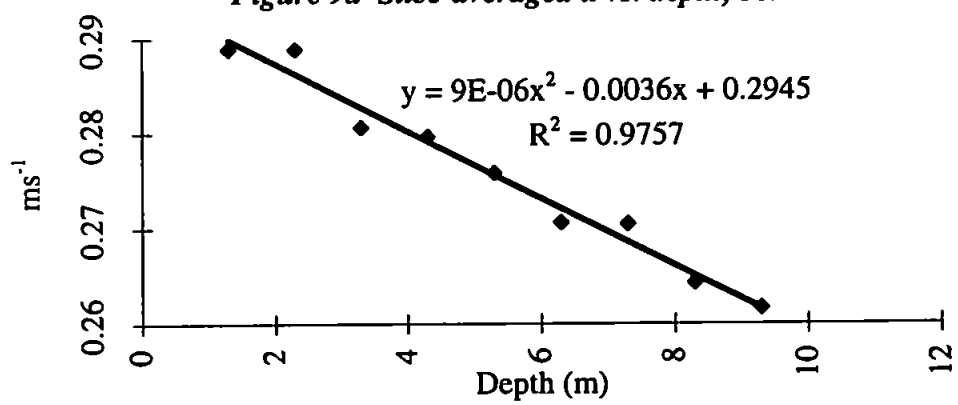


*Figure 9b Slice-averaged v vs. depth, box 1N*

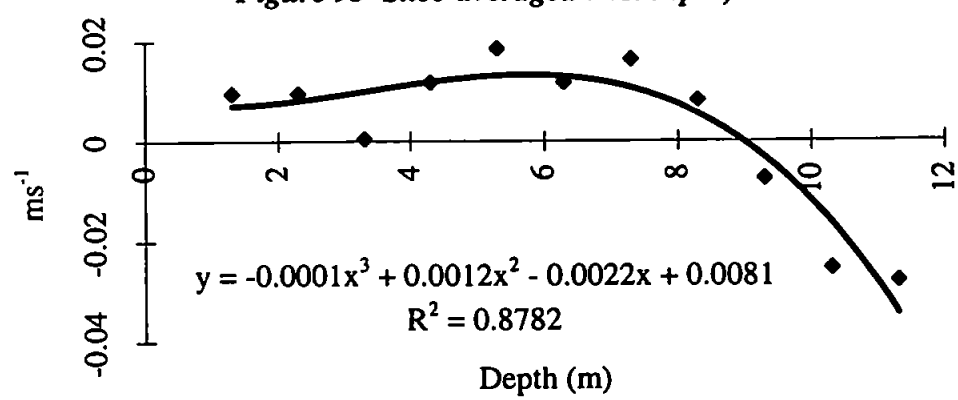

*Figure 10a Slice-averaged u vs. depth, box 3N*

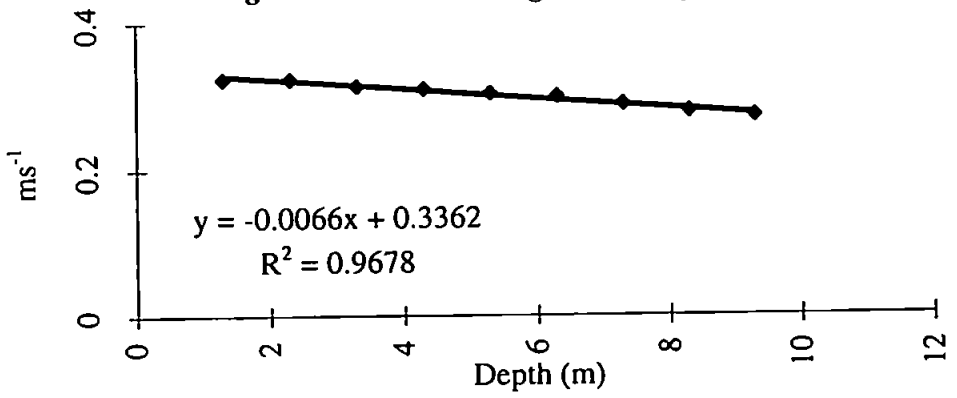


*Figure 10b Slice-averaged v vs. depth, box 3N*

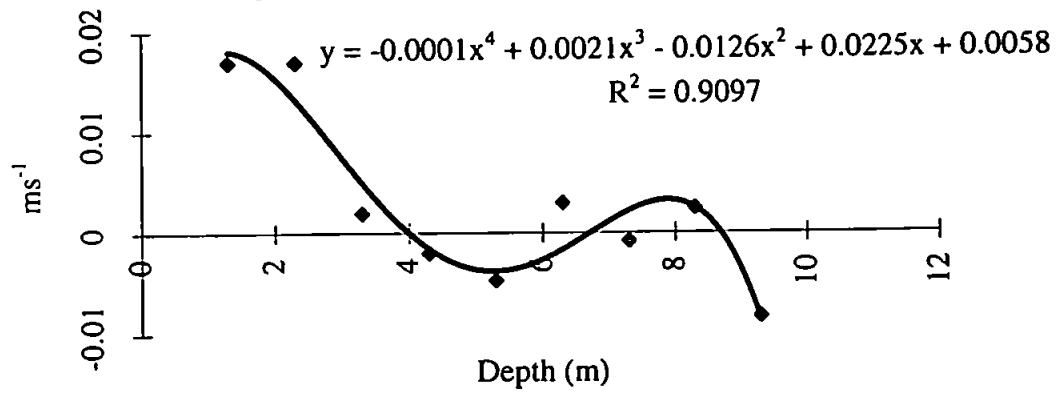


*Figure 11a Slice-averaged u vs. depth, box 4N*

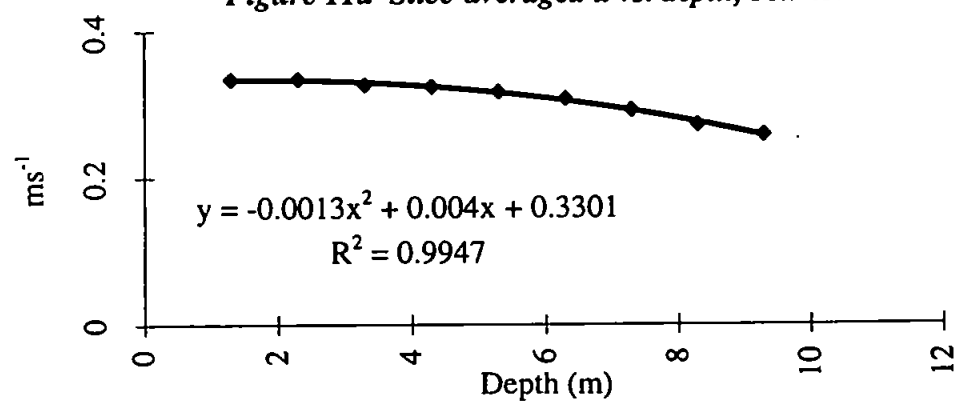


*Figure 11b Slice-averaged v vs. depth, box 4N*

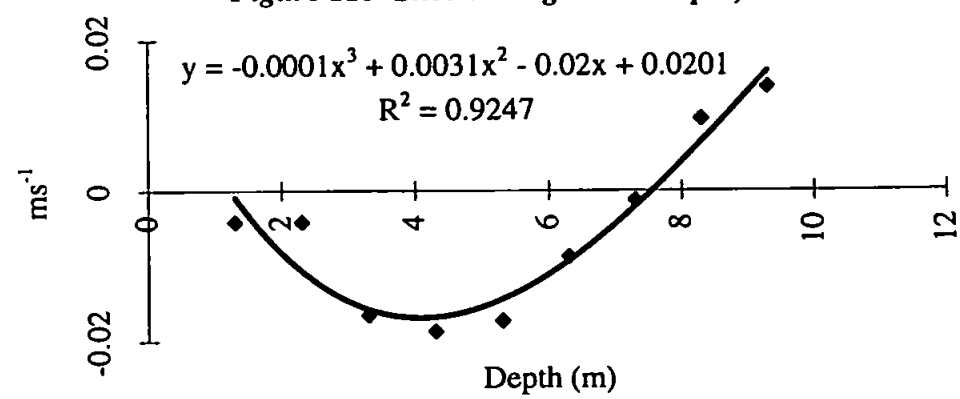

*Figure 12a Slice-averaged u vs. depth, box 5N*

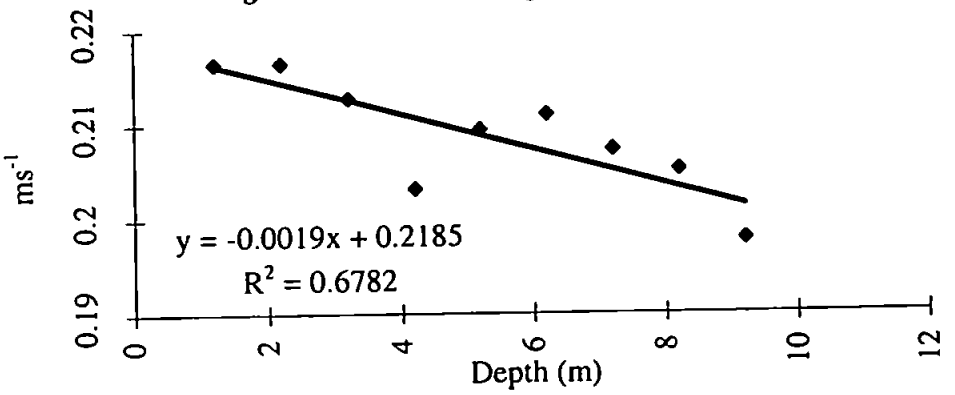


*Figure 12b Slice-averaged v vs. depth, box 5N*

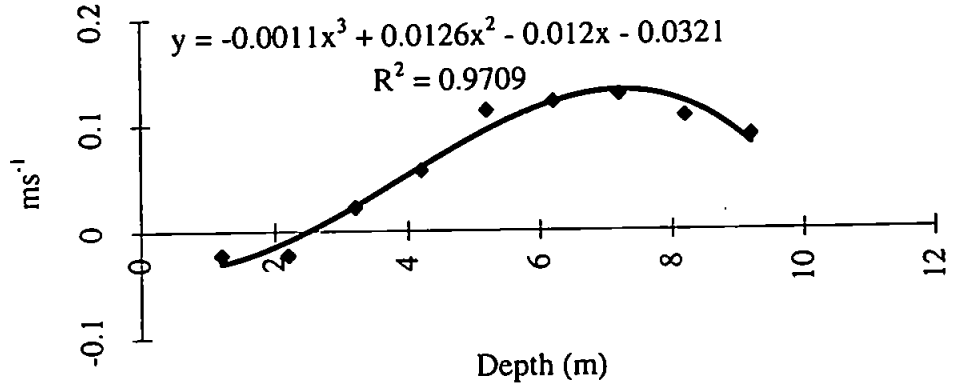


*Figure 13a Slice-averaged u vs. depth, box 6N*

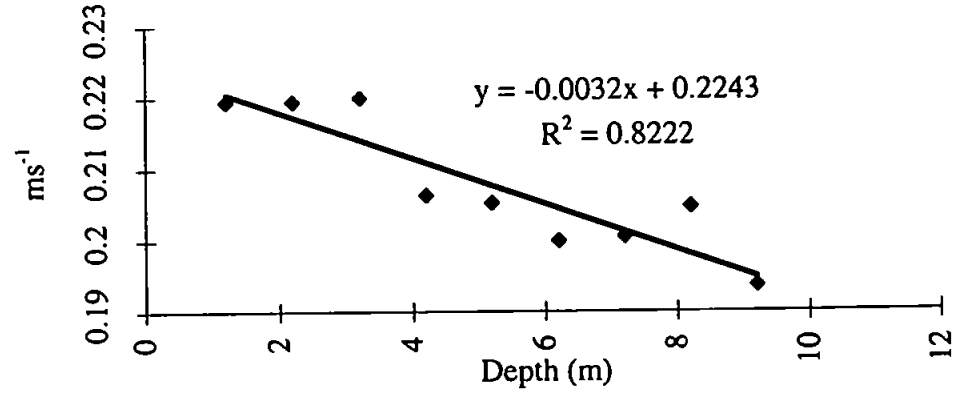


*Figure 13b Slice-averaged v vs. depth, box 6N*

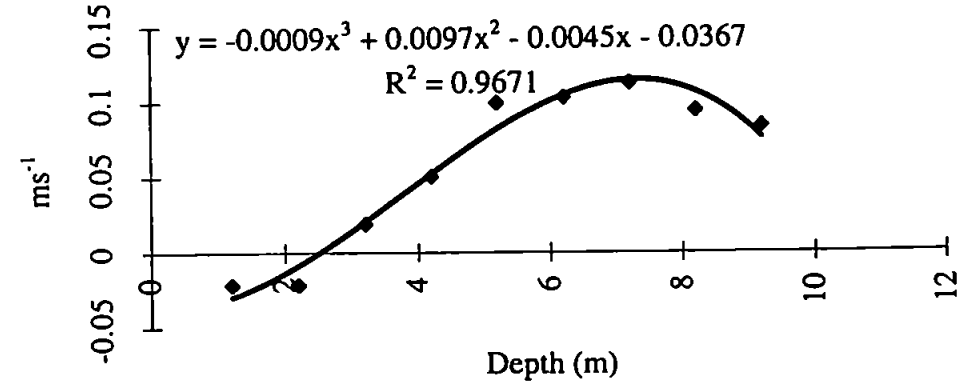

*Figure 14a Slice-averaged u vs. depth, box 7N*

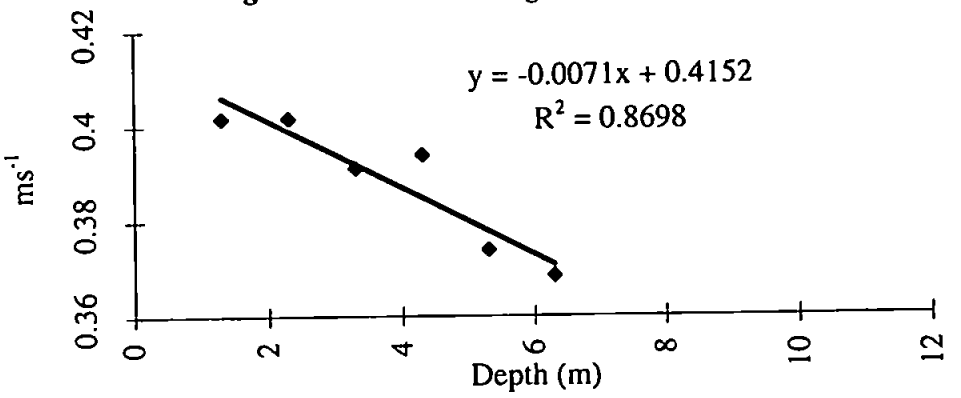


*Figure 14b Slice-averaged v vs. depth, box 7N*

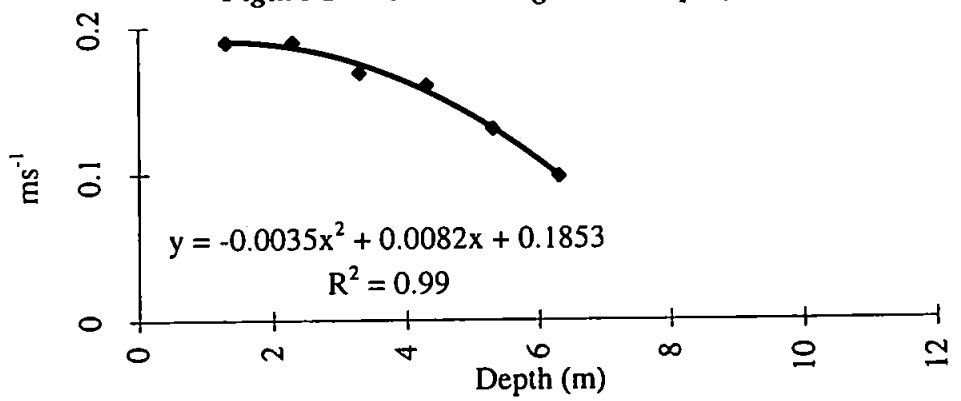


*Figure 15a Slice-averaged u vs. depth, box 1S*

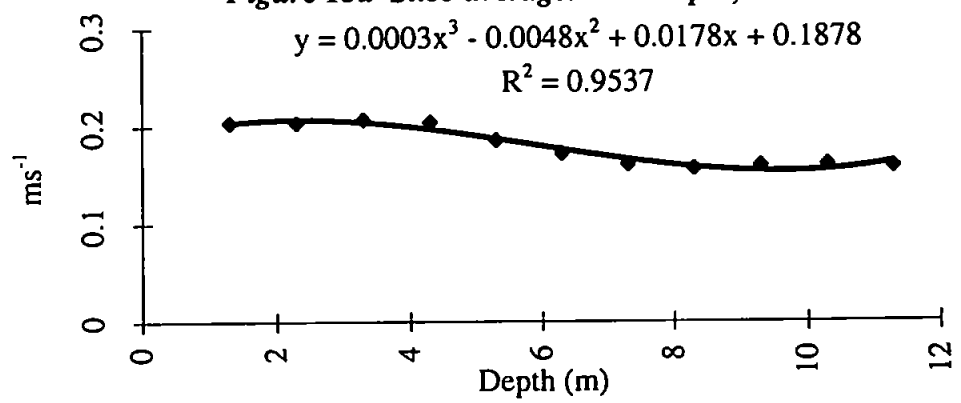


*Figure 15b Slice-averaged v vs. depth, box 1S*

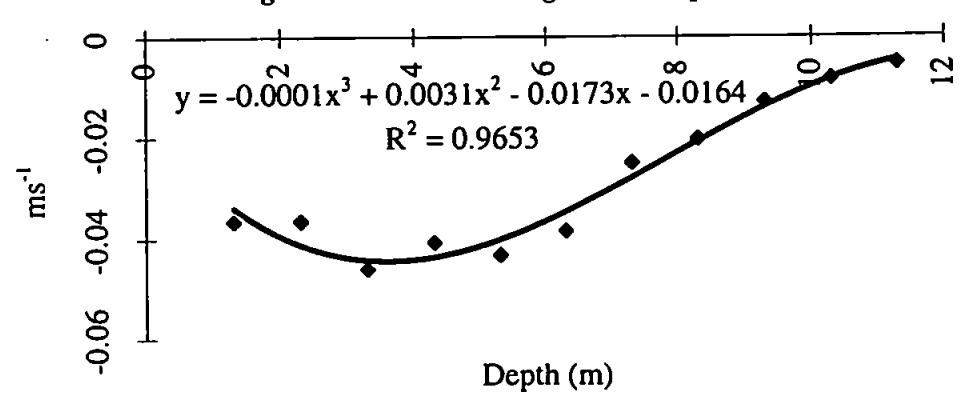

*Figure 16a Slice-averaged u vs. depth, box 2S*

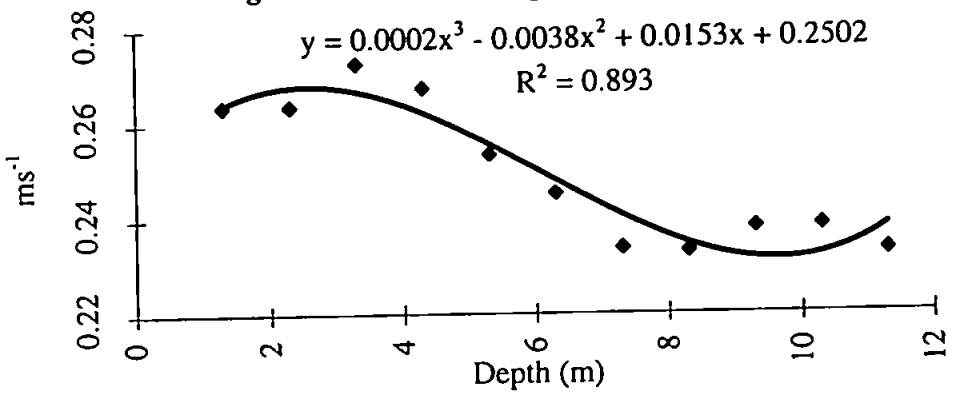


*Figure 16b Slice-averaged v vs. depth, box 2S*

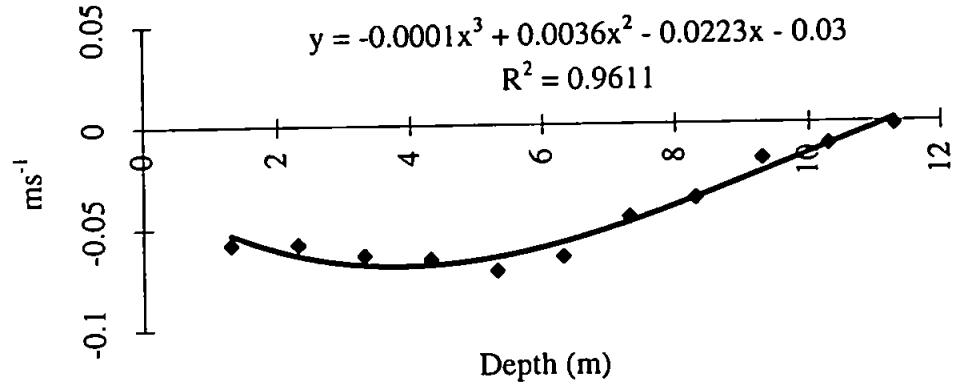


*Figure 17a Slice-averaged u vs. depth, box 3S*

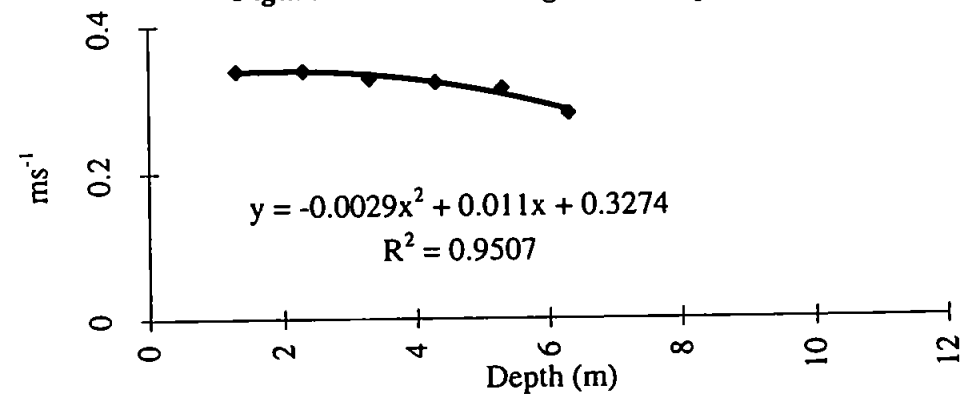


*Figure 17b Slice-averaged v vs. depth, box 3S*

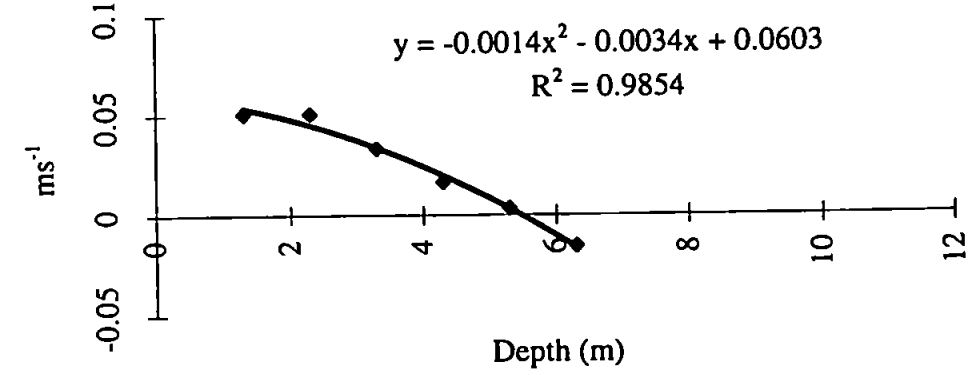

## *INTERNATIONAL EQUATION OF STATE OF SEAWATER (1980)*

$$\rho = + (999.842594 + 6.793952 \times 10^{-2} \times T) - (9.095290 \times 10^{-3} \times T^2) +$$

$$(1.001685 \times 10^{-4} \times T^3) - (1.120083 \times 10^{-6} \times T^4) + (6.536332 \times 10^{-9} \times T^5) +$$

$$(8.24493 \times 10^{-1} \times S) - (4.0899 \times 10^{-3} \times T \times S) + (7.6438 \times 10^{-5} \times T^2 \times S) -$$

$$(8.2467 \times 10^{-7} \times T^3 \times S) + (5.3875 \times 10^{-9} \times T^4 \times S) - (5.72466 \times 10^{-3} \times S^{3/2}) +$$

$$(1.0227 \times 10^{-4} \times T \times S^{3/2}) - (1.6546 \times 10^{-6} \times T^2 \times S^{3/2}) + (4.8314 \times 10^{-4} \times S^2)$$

where T is temperature, S is salinity and $\rho$ is density.

*Table 4 Curvature term estimates for Tamar and Lynher Rivers*

| *Box 1N* | *Lynher Curvature* | *Tamar Curvature* | *Difference between the two curvature terms* | *Unknown term for comparison* |
|---|---|---|---|---|
| *Slice* | | | | |
| 0 | 2.56E-06 | 3.60E-06 | 1.04E-06 | 6.61E-05 |
| 1 | 2.56E-06 | 3.60E-06 | 1.04E-06 | 6.61E-05 |
| 2 | 1.12E-06 | 4.55E-06 | 3.43E-06 | 6.61E-05 |
| 3 | 1.02E-06 | 6.77E-06 | 5.75E-06 | 6.61E-05 |
| 4 | 3.59E-07 | 9.46E-06 | 9.10E-06 | 6.61E-05 |
| 5 | 7.42E-08 | 1.06E-05 | 1.05E-05 | 6.61E-05 |
| 6 | 2.89E-07 | 1.02E-05 | 9.94E-06 | 6.61E-05 |
| 7 | 2.32E-07 | 8.44E-06 | 8.21E-06 | 6.61E-05 |
| 8 | 5.51E-07 | 6.00E-06 | 5.45E-06 | 6.61E-05 |
| 9 | 5.11E-07 | 4.02E-06 | 3.51E-06 | 6.61E-05 |
| 10 | 1.07E-06 | 2.80E-06 | 1.73E-06 | 6.61E-05 |
| *Box 2N* | *Lynher Curvature* | *Tamar Curvature* | *Difference between the two curvature terms* | *Unknown term for comparison* |
| *Slice* | | | | |
| 0 | 4.14E-05 | 2.09E-05 | -2.05E-05 | 6.92E-05 |
| 1 | 4.14E-05 | 2.09E-05 | -2.05E-05 | 6.92E-05 |
| 2 | 3.45E-05 | 2.08E-05 | -1.37E-05 | 6.92E-05 |
| 3 | 3.55E-05 | 2.08E-05 | -1.47E-05 | 6.92E-05 |
| 4 | 3.05E-05 | 2.11E-05 | -9.37E-06 | 6.92E-05 |
| 5 | 2.47E-05 | 2.10E-05 | -3.66E-06 | 6.92E-05 |
| 6 | 2.28E-05 | 2.34E-05 | 5.93E-07 | 6.92E-05 |
| 7 | 1.49E-05 | 2.25E-05 | 7.57E-06 | 6.92E-05 |
| 8 | 1.20E-05 | 2.24E-05 | 1.04E-05 | 6.92E-05 |
| *Box 3N* | *Lynher Curvature* | *Tamar Curvature* | *Difference between the two curvature terms* | *Unknown term for comparison* |
| *Slice* | | | | |
| 0 | 4.14E-05 | 1.54E-05 | -2.60E-05 | 4.56E-04 |
| 1 | 4.14E-05 | 1.54E-05 | -2.60E-05 | 4.56E-04 |
| 2 | 3.45E-05 | 1.36E-05 | -2.09E-05 | 4.56E-04 |
| 3 | 3.55E-05 | 1.15E-05 | -2.40E-05 | 4.56E-04 |
| 4 | 3.05E-05 | 9.26E-06 | -2.12E-05 | 4.56E-04 |
| 5 | 2.47E-05 | 8.05E-06 | -1.66E-05 | 4.56E-04 |
| 6 | 2.28E-05 | 6.79E-06 | -1.60E-05 | 4.56E-04 |
| 7 | 1.49E-05 | 6.32E-06 | -8.59E-06 | 4.56E-04 |
| 8 | 1.20E-05 | 4.49E-06 | -7.51E-06 | 4.56E-04 |
| *Box 4N* | *Lynher Curvature* | *Tamar Curvature* | *Difference between the two curvature terms* | *Unknown term for comparison* |
| *Slice* | | | | |
| 0 | 4.14E-05 | 1.54E-05 | -2.60E-05 | 3.59E-04 |
| 1 | 4.14E-05 | 1.54E-05 | -2.60E-05 | 3.59E-04 |
| 2 | 3.45E-05 | 1.36E-05 | -2.09E-05 | 3.59E-04 |
| 3 | 3.55E-05 | 1.15E-05 | -2.40E-05 | 3.59E-04 |
| 4 | 3.05E-05 | 9.26E-06 | -2.12E-05 | 3.59E-04 |
| 5 | 2.47E-05 | 8.05E-06 | -1.66E-05 | 3.59E-04 |
| 6 | 2.28E-05 | 6.79E-06 | -1.60E-05 | 3.59E-04 |
| 7 | 1.49E-05 | 6.32E-06 | -8.59E-06 | 3.59E-04 |
| 8 | 1.20E-05 | 4.49E-06 | -7.51E-06 | 3.59E-04 |

*Table 4 continued*

| *Box 5N* | *Lynher Curvature* | *Tamar Curvature* | *Difference between the two curvature terms* | *Unknown term for comparison* |
|---|---|---|---|---|
| *Slice* | | | | |
| 0 | 9.49E-06 | 1.52E-05 | 5.70E-06 | -1.61E-04 |
| 1 | 9.49E-06 | 1.52E-05 | 5.70E-06 | -1.61E-04 |
| 2 | 1.14E-05 | 1.55E-05 | 4.03E-06 | -1.61E-04 |
| 3 | 8.03E-06 | 1.44E-05 | 6.34E-06 | -1.61E-04 |
| 4 | 7.69E-06 | 1.63E-05 | 8.60E-06 | -1.61E-04 |
| 5 | 6.60E-06 | 1.63E-05 | 9.73E-06 | -1.61E-04 |
| 6 | 7.07E-06 | 1.58E-05 | 8.78E-06 | -1.61E-04 |
| 7 | 5.18E-06 | 1.67E-05 | 1.15E-05 | -1.61E-04 |
| 8 | 4.92E-06 | 1.67E-05 | 1.17E-05 | -1.61E-04 |
| 9 | 3.72E-06 | 1.65E-05 | 1.28E-05 | -1.61E-04 |
| 10 | 4.81E-06 | 1.10E-05 | 6.20E-06 | -1.61E-04 |
| | | | | |
| *Box 6N* | *Lynher Curvature* | *Tamar Curvature* | *Difference between the two curvature terms* | *Unknown term for comparison* |
| *Slice* | | | | |
| 0 | 9.49E-06 | 1.52E-05 | 5.70E-06 | -1.53E-04 |
| 1 | 9.49E-06 | 1.52E-05 | 5.70E-06 | -1.53E-04 |
| 2 | 1.14E-05 | 1.55E-05 | 4.03E-06 | -1.53E-04 |
| 3 | 8.03E-06 | 1.44E-05 | 6.34E-06 | -1.53E-04 |
| 4 | 7.69E-06 | 1.63E-05 | 8.60E-06 | -1.53E-04 |
| 5 | 6.60E-06 | 1.63E-05 | 9.73E-06 | -1.53E-04 |
| 6 | 7.07E-06 | 1.58E-05 | 8.78E-06 | -1.53E-04 |
| 7 | 5.18E-06 | 1.67E-05 | 1.15E-05 | -1.53E-04 |
| 8 | 4.92E-06 | 1.67E-05 | 1.17E-05 | -1.53E-04 |
| 9 | 3.72E-06 | 1.65E-05 | 1.28E-05 | -1.53E-04 |
| 10 | 4.81E-06 | 1.10E-05 | 6.20E-06 | -1.53E-04 |
| | | | | |
| *Box 7N* | *Lynher Curvature* | *Tamar Curvature* | *Difference between the two curvature terms* | *Unknown term for comparison* |
| *Slice* | | | | |
| 0 | 1.49E-06 | 6.41E-05 | 6.26E-05 | 6.69E-04 |
| 1 | 1.49E-06 | 6.41E-05 | 6.26E-05 | 6.69E-04 |
| 2 | 1.64E-06 | 5.92E-05 | 5.75E-05 | 6.69E-04 |
| 3 | 2.89E-06 | 5.99E-05 | 5.70E-05 | 6.69E-04 |
| 4 | 1.25E-06 | 5.47E-05 | 5.34E-05 | 6.69E-04 |
| 5 | 1.98E-06 | 5.20E-05 | 5.00E-05 | 6.69E-04 |

*Table 5 Primary longitudinal momentum balance*

| Box 1N | du/dt | u.du/dx | v.du/dy | w.du/dz | 1/d.dP/dx | g.dE/dx | f.v | d/dx(u'.u') | d/dy(u'.v') | d/dz(u'.w') |
|---|---|---|---|---|---|---|---|---|---|---|
| 0 | 1 | 2 | | | | | | | 3 | |
| 1 | 1 | 2 | | | | | | | 3 | |
| 2 | 1 | | | | | | | 2 | | |
| 3 | 1 | 4 | | | | | | 2 | 5 | 3 |
| 4 | 1 | 4 | | | 6 | | | 3 | 5 | 2 |
| 5 | 1 | 5 | | | 4 | | | 3 | 6 | 2 |
| 6 | 1 | 6 | | | 4 | | | 3 | 5 | 2 |
| 7 | 1 | 7 | | 4 | 5 or 6 | | | 3 | 5 or 6 | 2 |
| 8 | 2 | 8 | 3 | 5 | 7 | | | 4 | 6 | 1 |
| 9 | 1 | | 3 | 2 | 6 | | | 5 | 7 | 4 |
| 10 | 2 | | 3 | 1 | 6 | | | 4 | 7 | 5 |
| Box 2N | | | | | | | | | | |
| 0 | 3 | 2 | | | | 1 | | | | |
| 1 | 4 | 2 | | | 3 | 1 | | 5 | | 6 |
| 2 | 4 | 2 | 7 | | 3 | 1 | | 5 | | 6 |
| 3 | 5 | 3 | 7 | | 2 | 1 | | 6 | | 4 |
| 4 | | | | | 1 | 2 | | | | |
| 5 | 5 | 4 | 6 | | 1 | 2 | | 7 | | 3 |
| 6 | | 4 | 5 | | 1 | 2 | | | | 3 |
| 7 | | 3 | 5 | | 1 | 2 | | | | 4 |
| 8 | | 4 | | | 1 | 3 | | | | 2 |
| Box 3N | | | | | | | | | | |
| 0 | 3 | 2 | | | 4 | 1 | | 5 | | |
| 1 | | 2 | | | 3 | 1 | | | | |
| 2 | 4 | 2 | | 6 | 3 | 1 | | 5 | | |
| 3 | | 3 | | | 2 | 1 | | | | 4 |
| 4 | | | | | 2 | 1 | | | | |
| 5 | | | | | 1 | 2 | | | | |
| 6 | 6 | 4 | | 5 | 1 | 2 | | | | 3 |
| 7 | | 3 | | 5 | 1 | 2 | | | | 4 |
| 8 | | 4 | | 5 | 1 | 2 | | | | 3 |
| Box 4N | | | | | | | | | | |
| 0 | 3 | 2 | | | 4 | 1 | | | | |
| 1 | | 2 | | | 3 | 1 | | | | |
| 2 | | 2 | | | 3 | 1 | | | | |
| 3 | | 2 | | | 3 | 1 | | | | |
| 4 | | 3 | | 4 | 2 | 1 | | | | |
| 5 | 5 | 3 | | 4 | 2 | 1 | | 6 | | |
| 6 | | | | | 2 | 1 | | | | |
| 7 | | | | | 1 | 2 | | | | |
| 8 | | | | 2 | 1 | | | | | |
| Box 5N | | | | | | | | | | |
| 0 | | 2 | | | 3 | 1 | | | | |
| 1 | | 2 | 4 | | 3 | 1 | | | | |
| 2 | | 3 | 4 | | 2 | 1 | | | | |
| 3 | | | | | 1 | 2 | | | | |
| 4 | | | 1 | | 2 | | | | | |
| 5 | | 4 | 2 | | 1 | 3 | | | | 5 |
| 6 | | 4 | 2 | | 1 | 3 | | 5 | | 6 |
| 7 | | | 2 | | 1 | 3 | | | | |
| 8 | | 4 | 3 | | 1 | 2 | | 6 | | 5 |

*Table 5 continued*

| Box 6N | du/dt | u.du/dx | v.du/dy | w.du/dz | 1/d.dP/dx | g.dE/dx | f.v | d/dx(u'.u') | d/dy(u'.v') | d/dz(u'.w') |
|---|---|---|---|---|---|---|---|---|---|---|
| 0 | | 2 | | | | 1 | | 3 | | |
| 1 | | 2 | | | | 1 | | 3 | | |
| 2 | 5 | 2 | 4 | | | 1 | | | | 3 |
| 3 | | | | | | 1 | | | | 2 |
| 4 | 5 | 4 | 2 | | | 3 | | | | 1 |
| 5 | 5 | 4 | 2 | | | 3 | | | | 1 |
| 6 | | 4 | 2 | | | 3 | | 5 | | 1 |
| 7 | | | 2 | | | | | | | 1 |
| 8 | | 4 | 3 | | | 2 | | | | 1 |
| Box 7N | | | | | | | | | | |
| 0 | 5 | 2 | 1 | | | 3 | | 4 | | |
| 1 | 5 | 2 | 1 | | | 3 | | 4 | | |
| 2 | | 2 | 1 | | | 3 | | | | |
| 3 | 6 | 2 | 1 | | | 3 | | 4 | | 5 |
| 4 | 6 | 2 | 1 | | | 3 | | 4 | | 5 |
| 5 | 6 | 2 | 1 | | | 3 | | 4 | | 5 |
| Box 1S | | | | | | | | | | |
| 0 | 1 | | | | | 2 | | | | |
| 1 | 1 | | | | | 2 | | | | |
| 2 | 1 | | 3 | | | 2 | | | 4 | |
| 3 | 1 | | 3 | 4 | | 2 | | | | |
| 4 | 2 | | 1 | 3 | | 4 | | | | |
| 5 | 3 | | 2 | 1 | | 4 | | | | 5 |
| 6 | 3 | | 1 | 2 | | 4 | | | | |
| 7 | 1 | | 4 | 2 | 6 | 3 | | 8 | 7 | 5 |
| 8 | 1 | | | | | 2 | | | | |
| 9 | 1 | | | 3 | | 2 | | | | 4 |
| 10 | | | | 1 | | | | | | 2 |
| Box 2S | | | | | | | | | | |
| 0 | 2 | 4 | | | | 1 | | | 3 | |
| 1 | 2 | 4 | | | | 1 | | | 3 | |
| 2 | 2 | 6 | 3 | | 5 | 1 | | | 4 | |
| 3 | 2 | 8 | 3 | | 4 | 1 | 7 | | 6 | 5 |
| 4 | 4 | | 3 | | 5 | 1 | | | | 2 |
| 5 | 5 | 6 | 3 | | 4 | 1 | | 7 | 8 | 2 |
| 6 | | | | | | 1 | | | | 2 |
| 7 | 5 | 2 | | | 4 | 1 | | | | 3 |
| 8 | 5 | 2 | | | 4 | 1 | | | | 3 |
| 9 | 4 | 3 | | | 2 | 1 | | | 6 | 5 |
| 10 | 4 | 3 | | | 2 | 1 | | | 6 | 5 |
| Box 3S | | | | | | | | | | |
| 0 | | 3 | | | | 2 | | 1 | | |
| 1 | | 3 | | | | 2 | | 1 | | |
| 2 | | 3 | | | | 2 | | 1 | | |
| 3 | 5 | 6 | | 7 | 3 | 2 | | 1 | | 4 |
| 4 | 6 | 5 | 8 | 7 | 2 | 3 | | 1 | | 4 |
| 5 | 6 | 7 | 8 | 5 | 2 | 4 | | 1 | | 3 |

## *Table 6 Primary lateral momentum balance*

| Box 1N | dv/dt | u.dv/dx | v.dv/dy | w.dv/dz | 1/d.dP/dy | g.dE/dy | f.u | d/dx(v'.u') | d/dy(v'.v') | d/dz(v'.w') |
|---|---|---|---|---|---|---|---|---|---|---|
| 0 | | | | | 2 | 1 | 4 | | 3 | |
| 1 | | | | | 2 | 1 | 5 | | 3 | 4 |
| 2 | | | | | 2 | 1 | 5 | | 4 | 3 |
| 3 | | | | | 2 | 1 | | | | |
| 4 | | | | | 1 | 2 | | | | |
| 5 | | | | | 1 | 2 | 5 | 4 | 6 | 3 |
| 6 | | | | 6 | 1 | 3 | | 4 | 5 | 2 |
| 7 | | | | | 2 | | | | | 1 |
| 8 | | 6 | 7 | 4 | 2 | 3 | | 5 | | 1 |
| 9 | | 7 | 5 | 4 | 2 | 3 | | 6 | | 1 |
| 10 | | | | 3 | 2 | | | | | 1 |
| Box 2N | | | | | | | | | | |
| 0 | | | 1 | | | 2 | | | | |
| 1 | | 4 | 1 | | 2 | 3 | 5 | | | |
| 2 | | 5 | 2 | | 1 | 3 | | | | 4 |
| 3 | | 5 | 2 | | 1 | 4 | | | | 3 |
| 4 | | 5 | 3 | | 1 | 4 | 6 | | | 2 |
| 5 | | 5 | 3 | 7 | 1 | 2 | 6 | | | 4 |
| 6 | | 5 | 3 | 6 | 1 | 4 | 7 | | | 2 |
| 7 | | 5 | 2 | 6 | 1 | 4 | 7 | | | 3 |
| 8 | | 4 | 2 | 5 | 1 | 6 | 7 | | | 3 |
| Box 3N | | | | | | | | | | |
| 0 | | | 2 | | | 1 | | | | |
| 1 | | | 2 | | | 1 | | | | |
| 2 | | | 2 | | 3 | 1 | | | | 4 |
| 3 | | | 2 | | 3 | 1 | | | | 4 |
| 4 | | 4 | 2 | | 3 | 1 | | | | |
| 5 | | | 3 | | 2 | 1 | | | | |
| 6 | | | 3 | | 2 | 1 | | | | |
| 7 | | 4 | 3 | | 2 | 1 | | | | |
| 8 | | 6 | 5 | 3 | 2 | 1 | | | | 4 |
| Box 4N | | | | | | | | | | |
| 0 | | 3 | 1 | | 4 | 2 | 5 | | | |
| 1 | | 3 | 1 | | 4 | 2 | | | | 5 |
| 2 | | 4 | 1 | | 3 | 2 | | | | 5 |
| 3 | | | 2 | | | 1 | | | | |
| 4 | | 4 | 2 | | 3 | 1 | 5 | | | |
| 5 | | 4 | 3 | 5 | 2 | 1 | | | | |
| 6 | | 6 | 3 | 4 | 2 | 1 | 7 | | | 5 |
| 7 | | 6 | 3 | 4 | 2 | 1 | 7 | | | 5 |
| 8 | | | | | 1 | 2 | | | | |
| Box 5N | | | | | | | | | | |
| 0 | | 3 | 4 | | 2 | 1 | 6 | | 5 | |
| 1 | | | | | 2 | 1 | | | | |
| 2 | | | | | 1 | 2 | | | | 3 |
| 3 | | | 3 | | 1 | 2 | | | | |
| 4 | | | 2 | | 1 | 3 | | | | |
| 5 | | | 2 | | 1 | 3 | | | | 4 |
| 6 | | | 3 | | 1 | 2 | | | | 4 |
| 7 | | | 4 | 5 | 1 | 3 | | | | 2 |
| 8 | | | 4 | 5 | 1 | 3 | | | | 2 |

*Table 6 continued*

| Box 6N | dv/dt | u.dv/dx | v.dv/dy | w.dv/dz | 1/d.dP/dy | g.dE/dy | f.u | d/dx(v'.u') | d/dy(v'.v') | d/dz(v'.w') |
|---|---|---|---|---|---|---|---|---|---|---|
| 0 | | 3 | 4 | | 2 | 1 | 6 | | 5 | |
| 1 | | | | | 2 | 1 | | | | |
| 2 | | | 3 | | 1 | 2 | | | | |
| 3 | | | 3 | | 1 | 2 | | | | |
| 4 | | | 2 | | 1 | 3 | | | | 4 |
| 5 | | | 2 | | 1 | 3 | | | | 4 |
| 6 | | | 2 | | 1 | 3 | | 5 | | 4 |
| 7 | | | 4 | | 1 | 3 | | 5 | | 2 |
| 8 | | | 4 | 5 | 1 | 3 | | 6 | | 2 |
| **Box 7N** | | | | | | | | | | |
| 0 | | | 2 | | | 1 | | | 3 | |
| 1 | | | 2 | | | 1 | | | 3 | |
| 2 | | | 2 | | | 1 | | 4 | | 3 |
| 3 | | | 2 | | | 1 | | 4 | | 3 |
| 4 | | 6 | 2 | | | 1 | 7 | 5 | 4 | 3 |
| 5 | | 6 | 3 | | | 1 | 7 | 5 | 4 | 2 |
| **Box 1S** | | | | | | | | | | |
| 0 | | | | | 1 | | 2 | | | |
| 1 | | | | | 1 | 3 | 2 | 4 | 5 | |
| 2 | | | | | 1 | | | | | 2 |
| 3 | | | | | 2 | | | | | 1 |
| 4 | | | 3 | | 2 | | | | 4 | 1 |
| 5 | | | 3 | | 2 | | | | | 1 |
| 6 | | | 3 | | 2 | | | | | 1 |
| 7 | | | 4 | 3 | 2 | 7 | 6 | 5 | | 1 |
| 8 | | | | 3 | 2 | | | | | 1 |
| 9 | | | | 3 | 2 | | 4 | | | 1 |
| 10 | | | | | 2 | | | | | 1 |
| **Box 2S** | | | | | | | | | | |
| 0 | | | | | | 2 | 1 | | | |
| 1 | | | | | 1 | | 2 | | | |
| 2 | | | | | 1 | | | | | 2 |
| 3 | | | | | 1 | | 3 | | | 2 |
| 4 | | 2 | 3 | | 1 | 5 | 4 | | 7 | 6 |
| 5 | | | | | 1 | | | | | 2 |
| 6 | | | 3 | | 2 | | | | | 1 |
| 7 | | 3 | 4 | | 2 | | | | | 1 |
| 8 | | 3 | | | 2 | 4 | | | | 1 |
| 9 | | 3 | | | 2 | | | | | 1 |
| 10 | | 3 | | | 2 | | | | | 1 |
| **Box 3S** | | | | | | | | | | |
| 0 | | 2 | | | | 1 | | 3 | 4 | |
| 1 | | 2 | | | | 1 | | 3 | 4 | |
| 2 | | 2 | | | | 1 | 5 | 3 | 4 | |
| 3 | | 4 | | | | 1 | | 3 | 2 | |
| 4 | | 3 | | | | 1 | | 2 | 4 | |
| 5 | | | | 4 | | 1 | | 3 | 2 | 5 |

*Table 7 Richardson numbers, vertical eddy viscosities, vertical eddy diffusivities and flux Richardson numbers*

| | | | | | | | | |
|---|---|---|---|---|---|---|---|---|
| EE02 | | | | | | | | |
| BOX | SLICE | Ri u | Ri v | Nzu | Nzv | Kz | Fl Ri u | Fl Ri v |
| 1N | 0 | | | | | | | |
| 1N | 1 | 40.0454 | 298.152 | 0.11599 | 4.05308 | -0.00786 | -2.71439 | -0.57837 |
| 1N | 2 | 165.7 | 181.939 | 0.05465 | -18.3717 | -0.00624 | -18.9116 | 0.06177 |
| 1N | 3 | 140977 | 251.551 | 0.07306 | 0.34466 | -0.0027 | -5206.45 | -1.96933 |
| EE03 | | | | | | | | |
| BOX | SLICE | Ri u | Ri v | Nzu | Nzv | Kz | Fl Ri u | Fl Ri v |
| 1N | 0 | | | | | | | |
| 1N | 1 | 40.0454 | 298.152 | 0.6767 | -0.62562 | 0.0058 | 0.34326 | -2.76433 |
| 1N | 2 | 165.7 | 181.939 | 1.98583 | -2.01745 | 0.00946 | 0.78935 | -0.85313 |
| 1N | 3 | 140977 | 251.551 | 2.24903 | 0.20769 | 0.0246 | 1542.03 | 29.7958 |
| EE04 | | | | | | | | |
| BOX | SLICE | Ri u | Ri v | Nzu | Nzv | Kz | Fl Ri u | Fl Ri v |
| 1N | 0 | | | | | | | |
| 1N | 1 | 40.0454 | 298.152 | 0.29127 | 0.25396 | 0.00297 | 0.40831 | 3.48662 |
| 1N | 2 | 165.7 | 181.939 | 0.26145 | -0.08538 | -0.00916 | -5.80356 | 19.514 |
| 1N | 3 | 140977 | 251.551 | 0.336 | -0.01471 | 0.02625 | 11012.4 | -448.747 |
| EE05 | | | | | | | | |
| BOX | SLICE | Ri u | Ri v | Nzu | Nzv | Kz | Fl Ri u | Fl Ri v |
| 1N | 0 | | | | | | | |
| 1N | 1 | 40.0454 | 298.152 | -0.84466 | 0.67394 | 0.0108 | -0.51199 | 4.77759 |
| 1N | 2 | 165.7 | 181.939 | -0.67046 | 1.00505 | 0.00817 | -2.0194 | 1.47915 |
| 1N | 3 | 140977 | 251.551 | 0.36094 | -1.05433 | 0.01654 | 6460.81 | -3.94659 |
| EE10 | | | | | | | | |
| BOX | SLICE | Ri u | Ri v | Nzu | Nzv | Kz | Fl Ri u | Fl Ri v |
| 2N | 0 | | | | | | | |
| 2N | 1 | 39.0914 | 107.69 | 13.7572 | -0.29243 | -0.0009 | -0.00256 | 0.33191 |
| 2N | 2 | 39.088 | 160742 | 7.17602 | -0.14682 | 0.00057 | 0.00312 | -627.135 |
| 2N | 3 | 39.0862 | 97.3374 | -2.54371 | -0.49293 | -0.00897 | 0.13789 | 1.77202 |
| EE11 | | | | | | | | |
| BOX | SLICE | Ri u | Ri v | Nzu | Nzv | Kz | Fl Ri u | Fl Ri v |
| 2N | 0 | | | | | | | |
| 2N | 1 | 39.0914 | 107.69 | -0.27711 | -0.77988 | 0.02198 | -3.10068 | -3.03507 |
| 2N | 2 | 39.088 | 160742 | -1.46435 | -1.01362 | 0.00091 | -0.02431 | -144.408 |
| 2N | 3 | 39.0862 | 97.3374 | -0.09669 | -190.175 | -0.06661 | 26.9242 | 0.03409 |
| EE12 | | | | | | | | |
| BOX | SLICE | Ri u | Ri v | Nzu | Nzv | Kz | Fl Ri u | Fl Ri v |
| 2N | 0 | | | | | | | |
| 2N | 1 | 39.0914 | 107.69 | -0.3347 | 0.18335 | | | |
| 2N | 2 | 39.088 | 160742 | -0.37588 | 0.13133 | | | |
| 2N | 3 | 39.0862 | 97.3374 | -0.54156 | -0.12458 | | | |
| EE13 | | | | | | | | |
| BOX | SLICE | Ri u | Ri v | Nzu | Nzv | Kz | Fl Ri u | Fl Ri v |
| 2N | 0 | | | | | | | |
| 2N | 1 | 39.0914 | 107.69 | -0.32605 | 0.69965 | -0.08368 | 10.0322 | -12.8792 |
| 2N | 2 | 39.088 | 160742 | -0.47942 | 0.90558 | -0.07601 | 6.19724 | -13491.9 |
| 2N | 3 | 39.0862 | 97.3374 | -4.21546 | 3.66744 | -0.10108 | 0.93718 | -2.68264 |
| EE11 | | | | | | | | |
| BOX | SLICE | Ri u | Ri v | Nzu | Nzv | Kz | Fl Ri u | Fl Ri v |
| 3N | 0 | | | | | | | |
| 3N | 1 | 10.5116 | 8.4017 | -0.27711 | -0.77988 | 0.02198 | -0.83376 | -0.23679 |
| 3N | 2 | 10.5106 | 7.27852 | -1.46435 | -1.01362 | 0.00091 | -0.00654 | -0.00654 |
| 3N | 3 | 10.5103 | 22.1541 | -0.09669 | -190.175 | -0.06661 | 7.23989 | 0.00776 |

*Table 7 continued*

| | | | | | | | | |
|---|---|---|---|---|---|---|---|---|
| EE12 | | | | | | | | |
| BOX | SLICE | Ri u | Ri v | Nzu | Nzv | Kz | Fl Ri u | Fl Ri v |
| 3N | 0 | | | | | | | |
| 3N | 1 | 10.5116 | 8.4017 | -0.3347 | 0.18335 | | | |
| 3N | 2 | 10.5106 | 7.27852 | -0.37588 | 0.13133 | | | |
| 3N | 3 | 10.5103 | 22.1541 | -0.54156 | -0.12458 | | | |
| EE13 | | | | | | | | |
| BOX | SLICE | Ri u | Ri v | Nzu | Nzv | Kz | Fl Ri u | Fl Ri v |
| 3N | 0 | | | | | | | |
| 3N | 1 | 10.5116 | 8.4017 | -0.32605 | 0.69965 | -0.08368 | 2.69764 | -1.00481 |
| 3N | 2 | 10.5106 | 7.27852 | -0.47942 | 0.90558 | -0.07601 | 1.66642 | -0.61092 |
| 3N | 3 | 10.5103 | 22.1541 | -4.21546 | 3.66744 | -0.10108 | 0.25201 | -0.61057 |
| EE14 | | | | | | | | |
| BOX | SLICE | Ri u | Ri v | Nzu | Nzv | Kz | Fl Ri u | Fl Ri v |
| 3N | 0 | | | | | | | |
| 3N | 1 | 10.5116 | 8.4017 | 1.73207 | 0.10858 | 0.02841 | 0.17241 | 2.19818 |
| 3N | 2 | 10.5106 | 7.27852 | 0.4778 | 0.05136 | 0.01467 | 0.32279 | 2.07945 |
| 3N | 3 | 10.5103 | 22.1541 | 0.53176 | 0.04146 | -0.02606 | -0.51505 | -13.9251 |
| EE12 | | | | | | | | |
| BOX | SLICE | Ri u | Ri v | Nzu | Nzv | Kz | Fl Ri u | Fl Ri v |
| 4N | 0 | | | | | | | |
| 4N | 1 | 135.052 | 9.07523 | -0.3347 | 0.18335 | | | |
| 4N | 2 | 24.4637 | 56.0514 | -0.37588 | 0.13133 | | | |
| 4N | 3 | 9.86947 | 837.372 | -0.54156 | -0.12458 | | | |
| EE13 | | | | | | | | |
| BOX | SLICE | Ri u | Ri v | Nzu | Nzv | Kz | Fl Ri u | Fl Ri v |
| 4N | 0 | | | | | | | |
| 4N | 1 | 135.052 | 9.07523 | -0.32605 | 0.69965 | -0.08368 | 34.6591 | -1.08536 |
| 4N | 2 | 24.4637 | 56.0514 | -0.47942 | 0.90558 | -0.07601 | 3.87862 | -4.70467 |
| 4N | 3 | 9.86947 | 837.372 | -4.21546 | 3.66744 | -0.10108 | 0.23664 | -23.0781 |
| EE14 | | | | | | | | |
| BOX | SLICE | Ri u | Ri v | Nzu | Nzv | Kz | Fl Ri u | Fl Ri v |
| 4N | 0 | | | | | | | |
| 4N | 1 | 135.052 | 9.07523 | 1.73207 | 0.10858 | 0.02841 | 2.21509 | 2.3744 |
| 4N | 2 | 24.4637 | 56.0514 | 0.4778 | 0.05136 | 0.01467 | 0.7513 | 16.0137 |
| 4N | 3 | 9.86947 | 837.372 | 0.53176 | 0.04146 | -0.02606 | -0.48365 | -526.335 |
| EE15 | | | | | | | | |
| BOX | SLICE | Ri u | Ri v | Nzu | Nzv | Kz | Fl Ri u | Fl Ri v |
| 4N | 0 | | | | | | | |
| 4N | 1 | 135.052 | 9.07523 | -0.17697 | -1.94147 | -0.01801 | 13.7402 | 0.08416 |
| 4N | 2 | 24.4637 | 56.0514 | -0.28761 | 0.8306 | -0.05163 | 4.39124 | -3.48384 |
| 4N | 3 | 9.86947 | 837.372 | 0.54193 | 0.24624 | 0.16006 | 2.91493 | 544.295 |
| DD03 | | | | | | | | |
| BOX | SLICE | Ri u | Ri v | Nzu | Nzv | Kz | Fl Ri u | Fl Ri v |
| 5N | 0 | | | | | | | |
| 5N | 1 | 1537.9 | 7.02997 | 0.10808 | 0.12842 | -0.00011 | -1.55554 | -0.00598 |
| 5N | 2 | 1536.82 | 4.29915 | -0.87731 | 0.04727 | -0.00116 | 2.03958 | -0.1059 |
| DD04 | | | | | | | | |
| BOX | SLICE | Ri u | Ri v | Nzu | Nzv | Kz | Fl Ri u | Fl Ri v |
| 5N | 0 | | | | | | | |
| 5N | 1 | 1537.9 | 7.02997 | -0.21226 | 0.04151 | 0.00161 | -11.6546 | 0.27242 |
| 5N | 2 | 1536.82 | 4.29915 | 0.26007 | 0.01004 | 0.00132 | 7.77386 | 0.56316 |
| DD05 | | | | | | | | |
| BOX | SLICE | Ri u | Ri v | Nzu | Nzv | Kz | Fl Ri u | Fl Ri v |
| 5N | 0 | | | | | | | |
| 5N | 1 | 1537.9 | 7.02997 | -0.10849 | -0.01007 | -0.00536 | 75.9742 | 3.743 |
| 5N | 2 | 1536.82 | 4.29915 | -0.10218 | -0.02779 | 0.00292 | -43.9664 | -0.45231 |
| DD06 | | | | | | | | |
| BOX | SLICE | Ri u | Ri v | Nzu | Nzv | Kz | Fl Ri u | Fl Ri v |
| 5N | 0 | | | | | | | |
| 5N | 1 | 1537.9 | 7.02997 | 0.93417 | 0.03821 | 0.00089 | 1.4626 | 0.16347 |
| 5N | 2 | 1536.82 | 4.29915 | -0.22164 | 0.01659 | 0.0023 | -15.9188 | 0.59498 |

*Table 7 continued*

| DD04 | | | | | | | | |
|---|---|---|---|---|---|---|---|---|
| BOX | SLICE | Ri u | Ri v | Nzu | Nzv | Kz | Fl Ri u | Fl Ri v |
| 6N | 0 | | | | | | | |
| 6N | 1 | 486.351 | 7.64055 | -0.21226 | 0.04151 | 0.00161 | -3.68569 | 0.29609 |
| 6N | 2 | 486.03 | 5.16059 | 0.26007 | 0.01004 | 0.00132 | 2.45854 | 0.676 |
| DD05 | | | | | | | | |
| BOX | SLICE | Ri u | Ri v | Nzu | Nzv | Kz | Fl Ri u | Fl Ri v |
| 6N | 0 | | | | | | | |
| 6N | 1 | 486.351 | 7.64055 | -0.10849 | -0.01007 | -0.00536 | 24.0263 | 4.06809 |
| 6N | 2 | 486.03 | 5.16059 | -0.10218 | -0.02779 | 0.00292 | -13.9047 | -0.54295 |
| DD06 | | | | | | | | |
| BOX | SLICE | Ri u | Ri v | Nzu | Nzv | Kz | Fl Ri u | Fl Ri v |
| 6N | 0 | | | | | | | |
| 6N | 1 | 486.351 | 7.64055 | 0.93417 | 0.03821 | 0.00089 | 0.46254 | 0.17766 |
| 6N | 2 | 486.03 | 5.16059 | -0.22164 | 0.01659 | 0.0023 | -5.03444 | 0.7142 |
| DD07 | | | | | | | | |
| BOX | SLICE | Ri u | Ri v | Nzu | Nzv | Kz | Fl Ri u | Fl Ri v |
| 6N | 0 | | | | | | | |
| 6N | 1 | 486.351 | 7.64055 | -0.27414 | 0.33711 | -0.00212 | 3.75749 | -0.048 |
| 6N | 2 | 486.03 | 5.16059 | -0.50904 | 0.05808 | 0.00572 | -5.46 | 0.50807 |
| FF05 | | | | | | | | |
| BOX | SLICE | Ri u | Ri v | Nzu | Nzv | Kz | Fl Ri u | Fl Ri v |
| 7N | 0 | | | | | | | |
| 7N | 1 | 5.4363 | 4.32008 | 0.06263 | 0.4537 | -0.01335 | -1.15915 | -0.12715 |
| 7N | 2 | 5.43602 | 1.21462 | 0.04323 | 0.41904 | -0.01475 | -1.85513 | -0.04276 |
| 7N | 3 | 5.43596 | 0.56228 | -0.08868 | 0.34674 | -0.0882 | 5.40657 | -0.14302 |
| FF06 | | | | | | | | |
| BOX | SLICE | Ri u | Ri v | Nzu | Nzv | Kz | Fl Ri u | Fl Ri v |
| 7N | 0 | | | | | | | |
| 7N | 1 | 5.4363 | 4.32008 | -0.66417 | 0.62271 | -6.6E-05 | 0.00054 | -0.00046 |
| 7N | 2 | 5.43602 | 1.21462 | -0.34148 | 0.25336 | 0.00117 | -0.01865 | 0.00562 |
| 7N | 3 | 5.43596 | 0.56228 | -0.40626 | 0.25118 | 0.01508 | -0.20173 | 0.03375 |
| FF07 | | | | | | | | |
| BOX | SLICE | Ri u | Ri v | Nzu | Nzv | Kz | Fl Ri u | Fl Ri v |
| 7N | 0 | | | | | | | |
| 7N | 1 | 5.4363 | 4.32008 | -1.89467 | -1.18256 | 0.01632 | -0.04682 | -0.05962 |
| 7N | 2 | 5.43602 | 1.21462 | -6.46848 | -0.63837 | -0.01167 | 0.00981 | 0.0222 |
| 7N | 3 | 5.43596 | 0.56228 | 0.92675 | -0.40335 | 0.0635 | 0.37245 | -0.08852 |
| FF08 | | | | | | | | |
| BOX | SLICE | Ri u | Ri v | Nzu | Nzv | Kz | Fl Ri u | Fl Ri v |
| 7N | 0 | | | | | | | |
| 7N | 1 | 5.4363 | 4.32008 | -3.33786 | 2.77557 | 0.2335 | -0.3803 | 0.36343 |
| 7N | 2 | 5.43602 | 1.21462 | -0.29471 | 0.10415 | -0.21992 | 4.0565 | -2.56475 |
| 7N | 3 | 5.43596 | 0.56228 | 1.51314 | 0.24784 | -0.12746 | -0.45789 | -0.28916 |
| EE05 | | | | | | | | |
| BOX | SLICE | Ri u | Ri v | Nzu | Nzv | Kz | Fl Ri u | Fl Ri v |
| 1S | 0 | | | | | | | |
| 1S | 1 | 1222960 | 32.9019 | -0.84466 | 0.67394 | 0.0108 | -15635.8 | 0.52722 |
| 1S | 2 | 32.1987 | 758.528 | -0.67046 | 1.00505 | 0.00817 | -0.39241 | 6.16676 |
| 1S | 3 | 11.4047 | 181.067 | 0.36094 | -1.05433 | 0.01654 | 0.52266 | -2.84076 |
| EE06 | | | | | | | | |
| BOX | SLICE | Ri u | Ri v | Nzu | Nzv | Kz | Fl Ri u | Fl Ri v |
| 1S | 0 | | | | | | | |
| 1S | 1 | 1222960 | 32.9019 | 7.39419 | 0.10136 | 0.00768 | 1269.44 | 2.49132 |
| 1S | 2 | 32.1987 | 758.528 | -1.68672 | 0.11197 | 0.00687 | -0.13123 | 46.5721 |
| 1S | 3 | 11.4047 | 181.067 | -0.15616 | 0.13579 | 0.03077 | -2.24729 | 41.0307 |

*Table 7 continued*

| EE07 | | | | | | | | |
|---|---|---|---|---|---|---|---|---|
| BOX | SLICE | Ri u | Ri v | Nzu | Nzv | Kz | Fl Ri u | Fl Ri v |
| 1S | 0 | | | | | | | |
| 1S | 1 | 1222960 | 32.9019 | 0.4409 | 2.90038 | -0.00918 | -25469 | -0.10416 |
| 1S | 2 | 32.1987 | 758.528 | -0.22448 | 73.1049 | -0.00052 | 0.07392 | -0.00535 |
| 1S | 3 | 11.4047 | 181.067 | -0.06198 | 0.53132 | -0.00135 | 0.24781 | -0.45897 |
| EE08 | | | | | | | | |
| BOX | SLICE | Ri u | Ri v | Nzu | Nzv | Kz | Fl Ri u | Fl Ri v |
| 1S | 0 | | | | | | | |
| 1S | 1 | 1222960 | 32.9019 | -0.59042 | -0.11228 | -0.00044 | 909.667 | 0.12869 |
| 1S | 2 | 32.1987 | 758.528 | -0.31739 | 0.01094 | 0.00047 | -0.04767 | 32.593 |
| 1S | 3 | 11.4047 | 181.067 | 0.59863 | -0.03813 | 0.0058 | 0.11057 | -27.5625 |
| EE06 | | | | | | | | |
| BOX | SLICE | Ri u | Ri v | Nzu | Nzv | Kz | Fl Ri u | Fl Ri v |
| 2S | 0 | | | | | | | |
| 2S | 1 | 480.669 | 12.2244 | 7.39419 | 0.10136 | 0.00768 | 0.49894 | 0.92562 |
| 2S | 2 | 85.906 | 115.195 | -1.68672 | 0.11197 | 0.00687 | -0.35013 | 7.07274 |
| 2S | 3 | 21.6516 | 192.566 | -0.15616 | 0.13579 | 0.03077 | -4.26644 | 43.6365 |
| EE07 | | | | | | | | |
| BOX | SLICE | Ri u | Ri v | Nzu | Nzv | Kz | Fl Ri u | Fl Ri v |
| 2S | 0 | | | | | | | |
| 2S | 1 | 480.669 | 12.2244 | 0.4409 | 2.90038 | -0.00918 | -10.0103 | -0.0387 |
| 2S | 2 | 85.906 | 115.195 | -0.22448 | 73.1049 | -0.00052 | 0.19721 | -0.00081 |
| 2S | 3 | 21.6516 | 192.566 | -0.06198 | 0.53132 | -0.00135 | 0.47047 | -0.48812 |
| EE08 | | | | | | | | |
| BOX | SLICE | Ri u | Ri v | Nzu | Nzv | Kz | Fl Ri u | Fl Ri v |
| 2S | 0 | | | | | | | |
| 2S | 1 | 480.669 | 12.2244 | -0.59042 | -0.11228 | -0.00044 | 0.35753 | 0.04781 |
| 2S | 2 | 85.906 | 115.195 | -0.31739 | 0.01094 | 0.00047 | -0.12719 | 4.94979 |
| 2S | 3 | 21.6516 | 192.566 | 0.59863 | -0.03813 | 0.0058 | 0.20992 | -29.3129 |
| EE09 | | | | | | | | |
| BOX | SLICE | Ri u | Ri v | Nzu | Nzv | Kz | Fl Ri u | Fl Ri v |
| 2S | 0 | | | | | | | |
| 2S | 1 | 480.669 | 12.2244 | 0.56043 | -3.88669 | -0.00423 | -3.62843 | 0.01331 |
| 2S | 2 | 85.906 | 115.195 | 0.77617 | 0.58591 | -2.2E-05 | -0.00245 | -0.00435 |
| 2S | 3 | 21.6516 | 192.566 | 0.23745 | 0.32458 | -0.01753 | -1.5982 | -10.3988 |
| FF12 | | | | | | | | |
| BOX | SLICE | Ri u | Ri v | Nzu | Nzv | Kz | Fl Ri u | Fl Ri v |
| 3S | 0 | | | | | | | |
| 3S | 1 | 97.0049 | 4.45757 | -0.59748 | 0.31318 | -0.0004 | 0.06506 | -0.0057 |
| 3S | 2 | 7.05819 | 2.71063 | -1.42949 | 0.18512 | -0.00456 | 0.02251 | -0.06676 |
| 3S | 3 | 2.35755 | 1.82061 | -2.75673 | 0.1304 | -0.01513 | 0.01294 | -0.21123 |
| FF13 | | | | | | | | |
| BOX | SLICE | Ri u | Ri v | Nzu | Nzv | Kz | Fl Ri u | Fl Ri v |
| 3S | 0 | | | | | | | |
| 3S | 1 | 97.0049 | 4.45757 | 0.70183 | 0.41702 | 0.01494 | 2.0646 | 0.15967 |
| 3S | 2 | 7.05819 | 2.71063 | 0.1339 | 0.27959 | -0.0074 | -0.39017 | -0.07176 |
| 3S | 3 | 2.35755 | 1.82061 | 0.4599 | 0.45981 | -0.01771 | -0.09081 | -0.07014 |
| FF14 | | | | | | | | |
| BOX | SLICE | Ri u | Ri v | Nzu | Nzv | Kz | Fl Ri u | Fl Ri v |
| 3S | 0 | | | | | | | |
| 3S | 1 | 97.0049 | 4.45757 | 0.79334 | 0.05284 | -0.01793 | -2.19189 | -1.51222 |
| 3S | 2 | 7.05819 | 2.71063 | 0.38349 | 0.03671 | -0.01521 | -0.27999 | -1.12315 |
| 3S | 3 | 2.35755 | 1.82061 | 0.2178 | 0.40328 | -0.04279 | -0.46313 | -0.19316 |
| FF15 | | | | | | | | |
| BOX | SLICE | Ri u | Ri v | Nzu | Nzv | Kz | Fl Ri u | Fl Ri v |
| 3S | 0 | | | | | | | |
| 3S | 1 | 97.0049 | 4.45757 | -1.1398 | -0.52818 | -0.01852 | 1.57619 | 0.1563 |
| 3S | 2 | 7.05819 | 2.71063 | 0.58111 | -0.26274 | 0.00262 | 0.03177 | -0.02698 |
| 3S | 3 | 2.35755 | 1.82061 | -0.02422 | -0.54283 | 0.00087 | -0.08485 | -0.00292 |